Université Denis Diderot, Paris 7

Mémoire d'habilitation à diriger des recherches

presenté par

Jean-François Laporte

DSM/IRFU/SPP CEA-Saclay

Reconstruction des muons dans le détecteur ATLAS et étude de la production de paires de bosons au LHC

Soutenue publiquement le 27 mai 2016 devant le jury composé de:

Pr.	J. Ocariz	Président et Rapporteur
Pr.	G. Mikenberg	Rapporteur
Dr.	E. Perez	Rapporteur
Dr.	G. Hamel de Monchenault	Examinateur
Pr.	B. Fuks	Examinateur

Université Denis Diderot, Paris 7

Mémoire d'habilitation à diriger des recherches

presenté par

Jean-François Laporte

DSM/IRFU/SPP CEA-Saclay

Reconstruction of muons in the ATLAS detector
Study of the production of pairs of bosons at the LHC

Soutenue publiquement le 27 mai 2016 devant le jury composé de:

Pr.	J. Ocariz	Président et Rapporteur
Pr.	G. Mikenberg	Rapporteur
Dr.	E. Perez	Rapporteur
Dr.	G. Hamel de Monchenault	Examinateur
Pr.	B. Fuks	Examinateur

A Pascale, Mathilde et Valentine

Résumé

Ce mémoire, écrit en vue de l'obtention de l'habilitation à diriger des recherches de l'Université de Paris VII, présente certaines de mes contributions à la préparation du détecteur ATLAS auprès du collisionneur LHC et aux études de la production de paires de bosons vecteurs sur les données recueillies lors de la première phase du LHC. Après une brève description du collisionneur et du détecteur ATLAS, je présente la problématique de la reconstruction des muons dans ce détecteur. Je décris ensuite le travail effectué sur la description du détecteur, un sujet très important pour la reconstruction. Dans le chapitre suivant, je présente les algorithmes de la chaîne de reconstruction *STACO* qui a été utilisé par les principales analyses de Physique de ATLAS. Les performances de cette chaîne sur des données simulées et réelles sont discutées. Enfin les analyses de la production de paires de ZZ, WZ, WW, $W\gamma$ et $Z\gamma$ sont présentées. Les mesures de sections efficaces sont comparées aux prédictions théoriques, et les limites sur les couplages anomaux à trois bosons sont comparées à celles obtenues auprès des collisionneurs qui ont précédé le LHC. Les limites sur les couplages anomaux sont discutées dans le cadre de la théorie effective des champs.

Mots-clés: ATLAS, reconstruction de muons, production de paires de bosons vecteurs, couplages anomaux à trois bosons

Avis au lecteur: Ce mémoire présente les résultats d'analyses encore préliminaires au moment d'achever sa rédaction (janvier 2016). Ils n'engagent pas la collaboration ATLAS.

Abstract

This memoir presents some of my research activities, written in view of obtaining the "Habilitation à diriger des recherches" delivered by the University of Paris VII. It retraces some of my contributions to the preparation of the ATLAS detector and to the analyses of production of pairs of vector bosons at the LHC on the data collected in the first phase of the LHC. I first introduce the LHC, the ATLAS detector and the problematic of the reconstruction of muons. Next I describe the work that has been done for the description of the detector, a crucial issue for the reconstruction. Then I discuss in some details the algorithms forming the *STACO* chain of the muon reconstruction which has been used by the main ATLAS Physics analyses. The performance of this chain on simulated and real data are presented. Finally the analyses of the production of pairs of ZZ, WZ, WW, $W\gamma$ and $Z\gamma$ are discussed. The cross sections measurements are compared to the theoretical predictions, and the limits on the anomalous Triple Gauge couplings to the limits from the previous generation colliders. The limits on the anomalous couplings are discussed in the Effective Field Theory framework.

Keywords: ATLAS, Muon reconstruction, dibosons Physics, anomalous Triple Gauge couplings

Notice to the reader: This memoir presents the results of analyses still preliminary at the moment of its completion (January 2016). They do not engage the ATLAS collaboration.

Contents

Introduction **3**

1 The LHC, The ATLAS Detector and its Muon Spectrometer **7**
- 1.1 The LHC . . . 8
- 1.2 ATLAS overview . . . 10
- 1.3 Muon Spectrometer . . . 14
- 1.4 Considerations on the Muon Reconstruction in ATLAS . . . 26

2 Detector Description of Muon Spectrometer and ATLAS **31**
- 2.1 AMDB . . . 32
- 2.2 *AGDD* . . . 37
- 2.3 Conclusions . . . 41

3 Muon Reconstruction in ATLAS **43**
- 3.1 Muon Reconstruction in Muon Spectrometer: *Muonboy* . . . 44
- 3.2 Combined Muon reconstruction in ATLAS: *Staco* . . . 51
- 3.3 Muon Tagging in ATLAS: *MuTag* . . . 53

4 Performance of Muon Reconstruction in ATLAS **55**
- 4.1 Performance on simulated samples . . . 56
- 4.2 Performance on test-beam tests on the ATLAS H8 setup . . . 59
- 4.3 Performance from Cosmics Rays Commissioning . . . 63
- 4.4 Performance on Collisions Data . . . 66
- 4.5 Conclusions . . . 68

5 Two Bosons production: Measurements of cross sections and anomalous Triple Gauge couplings **69**
- 5.1 Introduction . . . 70
- 5.2 Two Bosons production at LHC . . . 70
- 5.3 Study of the ZZ Production . . . 78
- 5.4 Study of the WZ Production . . . 95
- 5.5 Study of the WW Production . . . 105
- 5.6 Study of the $W\gamma$ Production . . . 112
- 5.7 Study of the $Z\gamma$ Production . . . 118
- 5.8 Summary and conclusions . . . 126

Concluding remarks **133**

Bibliography **135**

Appendices 149

A Interactions between Electroweak Gauge Bosons **149**
- A.1 Gauge Bosons interactions in the Standard Model . . . 150
- A.2 Neutral Anomalous Triple Gauge Couplings . . . 154

A.3 Charged Anomalous Triple Gauge Couplings 160
A.4 Measurements of Anomalous Triple Gauge Couplings 163
A.5 Global Effective Field Theory analyses 169

B Linear-EFT Dimension-6 Operators 173
B.1 Definitions 173
B.2 O_B 174
B.3 O_W 174

C Coverage studies for Poisson Data when expectation depends quadratically on the parameter 177
C.1 Introduction 177
C.2 Confidence Interval Methods 179
C.3 Results 181
C.4 Summary and conclusion 186
C.5 Additional Material 188

D Muon Momentum Resolution 199
D.1 Deflections in position and direction for a point moving in a plane 200
D.2 Local measurements in MDT 201
D.3 Momentum Measurement Methods 203
D.4 Multiple Scattering contribution 208
D.5 Generalization 210

Introduction

This memoir retraces some of my contributions to the preparation of the ATLAS detector and to the analyses of diboson production at the LHC, the Large Hadron Collider at CERN, on the data collected in the first period of data taking.

The LHC is the most powerful collider ever built. It aims to explore particle interactions down to the unprecedented TeV scale and to elucidate the problem of the Electroweak Symmetry Breaking. The discovery of a new particle in 2012 which, to all appearances, looks to be the long-awaited Higgs boson of the Standard Model of the Particle Physics, rewarded 20 years spent in designing, building and preparing the collider and the four large detectors designed to exploit the data from proton collisions.

The Higgs boson discovery completes the set of the particles of the Standard Model. However there are many arguments both phenomenological and theoretical which plead for the existence of Physics beyond the Standard Model: the non explained natures of the dark matter and of the dark energy, the non explained baryon asymmetry observed in the Universe, the many free parameters of the Model with vastly different values, the strong CP issue, the neutrinos masses so smaller than the quarks masses, the naturality of the observed light mass of the Higgs boson, unique scalar particle in the Model, the missing explanation of the particular Higgs potential and the puzzling metastable state in which, according to the observed top and Higgs boson masses, it apparently places the Universe.

All this makes plausible that the Standard Model is actually an effective description at low energy scales of a Physics at a higher scale. This Physics Beyond the Standard Model could manifest itself in the form of the direct production of new heavy particles in high energy collisions. Even if too heavy to be produced at LHC, the virtual effects of these particles could induce departures from Standard Model predictions in processes involving Standard Model particles only. This last possibility motivates the precision measurements of the Higgs bosons couplings as well as of the couplings between vector bosons, photon, W and Z bosons. These latter couplings are allowed by the non-abelian nature of the Standard Model Gauge symmetries. They are measured in the production of two vector bosons. The measurement of the cross sections of these processes at high energy scales allow to set limits on the anomalous couplings between the vector bosons in particular on the anomalous Triple Gauge Bosons couplings. The leptonic decays of the W and Z bosons in electrons and muons provides attractively clean signatures of these processes.

In this memoir, I will recount my contributions to the analyses of the production of ZZ, WZ, WW, $W\gamma$ and $Z\gamma$ pairs. The measurements of the total cross sections provides challenging tests of the significant higher order QCD and Electroweak corrections that these processes receive. The limits on the anomalous couplings improve significantly, sometimes dramatically, on those obtained at previous colliders. Interpreted in the framework of the Effective Field Theory, they promise a glimpse on effects from a new Physics Beyond the Standard Model.

The final states of the diboson processes are simple and clean with few leptons. They are examples of the many processes to which leptons and in particular high-momentum muons provide robust signatures. For the muon measurements, the ATLAS collaboration chose a Muon Spectrometer based on air-code toroids of exceptional dimensions.

I joined the ATLAS Muon Spectrometer project in 1995. I could contribute to the design, optimization and testing of this complex detector all over the years which from the early technical proposal led to its successful operation right from the LHC inception. Instrumental in the long maturation of the project has been the possibility at a very early stage to rely on software tools allowing realistic evaluations of the performance of the simulation of the various options of the design of the detector which had to be considered over the years, as well as of the performance of the actual detector when it became possible to work on real data from test beams, cosmics rays during the ATLAS commissioning and ultimately on collision data.

The domains concerned by these activities, with which my colleagues and I came to be involved, cover the alignment of the detection units of the detector, the magnetic field, the precise description of the active and passive components of the Detector, and at the heart of all, fed by all the other domains, the reconstruction and identification of a muon in the apparatus. I contributed mainly on one hand, to the description of the Detector and on the other hand, to the muon reconstruction both in Standalone mode, i.e within the Muon Spectrometer only and in Combination mode, i.e using all the sub detectors ATLAS, chiefly the two ATLAS tracking systems, the Inner detector and the Muon Spectrometer.

The challenge of the reconstruction of muon within the Muon Spectrometer is to form a trajectory in a highly inhomogeneous field, from the patterns of few hits in detection units meters apart. These hits can be from a genuine muon but can have actually been generated by the high level background of neutrons and photons induced by the protons collisions. These fake hits spoil true tracks and create fake ones. These fake muons are a scourge that should be fight to the maximum extent at an early stage in the chain of reconstruction. The combination of tracks from the Inner detector and the Muon Spectrometer is comparatively easier. This combination stage provides the bulk of the identification of muons in ATLAS. However an additional tagging algorithm is needed to rescue reconstruction efficiency at low momentum and in weak acceptance spots.

In this memoir I will recount the principles and the performance on simulated and actual data, of a suite of reconstruction algorithms to which I contributed. Suitably integrated in the complex software infrastructure of ATLAS by means of a significant technical work that will be not recounted, this chain was improved and extensively validated over many years. At the eve of the LHC start the ATLAS collaboration based the evaluation of the global performance of the detector on this chain. Since the LHC inception it has be used by the main ATLAS Physics analyses for the first phase of LHC.

This memoir contains five chapters. In the first chapter I briefly present the LHC and the ATLAS detector, with some emphasis on the Muon Spectrometer of ATLAS. The chapter closes with an introduction to the problematic of the reconstruction of the muons in ATLAS .

The chapter 2 describes my contributions to the domain of the description of the detector. Two schemes of very different sophistication levels are discussed. They are at the base of the current description of the active and passive components of the Muon Spectrometer.

The chapter 3 describes in some details, the reconstruction and identification algorithms of a muon in ATLAS to which I contributed, the *Muonboy* Standalone reconstruction, the *Staco* combination algorithm and the *MuTag* tagging algorithm, which all together form the *STACO* chain.

The chapter 4 is an overview the performance of the muon reconstruction in ATLAS established for the *STACO* chain, on simulated data, then on real data from test beam and cosmics rays, and finally on real collisions data.

The final and longest chapter 5 reviews the results of the diboson production analyses to which I contributed. The measurements of the production cross sections and the limits on anomalous Triple

Gauge Bosons couplings are presented and discussed. Limits on anomalous couplings are discussed in the Effective Field Theory framework.

The memoir is completed with few appendices. The appendix A offers a review of the theory of anomalous Triple Gauge Bosons couplings and of their measurements, as well as a discussion of the Effective Field Theory framework. The appendix C examines through a very idealized case some statistical issues relevant for the anomalous couplings measurements. The appendix D contains some back of an envelope calculations of the muon momentum resolution in the Muon Spectrometer.

Chapter 1

The LHC, The ATLAS Detector and its Muon Spectrometer

In this chapter, I wish to set the scene for the discussions, the studies and the results which are presented in this memoir.

In the first section, I briefly present the LHC and its working conditions during the so-called Run 1 period, the first period of the data taking. The analyses presented in the chapter 5 are on data from this period.

Then I present the ATLAS detector, following the journey a muon born at the point of the collision of protons while it crosses all the sub-detectors. The Inner Tracking Detector and the calorimeters are described as well as their interaction with the muon. The Muon Spectrometer is described in more detail. I discuss the guidelines and some important aspects of its design. I briefly review the magnetic field map, material distribution and alignment issues and describe the layout of the detection units and the detection technologies.

Finally I discuss in general terms the issue of the reconstruction of muons in the ATLAS detector, first within the Muon Spectrometer and then combining all the sub-detectors of ATLAS. The main difficulties are discussed and the reconstructions algorithm are briefly outlined.

This last section serves are introduction for the next three chapters, which discuss the issue of the Description of the detector and its relevance for the reconstruction, then present in detail the *Staco* reconstruction chain, and finally review the performance of this chain.

1.1 The LHC

The LHC is the most powerful of the particle accelerators [1, 2]. The collider reuses the 27 km long tunnel which once hosted the LEP. It is the last element of a suite of accelerators displayed in figure 1.1, rising the protons energy up to 450 GeV prior to their injection in the main accelerator which brings them to the collision energy, nominally 7 TeV.

When officially inaugurated end of November 2008, the LHC was a wounded beast. A month earlier, few days after the first very successful protons injections and circulations, a spectacular incident exposing important safety defects, exacted a year long repair campaign. But the LHC was to return with a revenge [1].

By the end of November 2009, it provided first collisions in the detectors and achieved 1.18 TeV beam beating Tevatron by an awesome 200 GeV. At the end of March 2010, LHC performed first collisions at 7 TeV in the center of mass, reaching the energy targeted for the first runs for physics. In April 2011, it overtook the Tevatron instantaneous luminosity record [2].

For a period of more than 1.5 year, the machine instantaneous luminosity steadily improved and at the end of 2011, the detectors had harvested an integrated luminosity of about 5 fb^{-1} . A new period opened up in April 2012, with collisions at 8 TeV in the center of mass. Before the long shutdown in February 2013, ATLAS had collected an integrated luminosity of about 25 fb^{-1} (cf figure 1.2(a)). LHC is due to restart its operations early 2015 with an energy in the center of mass of 13 TeV and increased luminosity.

The high luminosity, made possible by highly focusing closely packed numerous dense protons bunches, comes with a price. Huge number of interactions occur simultaneously in a single crossing of two protons bunches, in average 20.7 interactions in the 2012 period with excursion up to 40 interactions for some fills as shown in figure 1.2(b) [3]. The resulting pile-up of events in time with the triggered bunch-crossing is, depending on the sub-detectors time window sensitivities, worsened by the out-of-time pile-up from neighboring bunch-crossings, following or preceding by small intervals of time (50 ns in 2012 see table 1.1).

By obscuring the event pattern, the pile-up severely impacts the reconstruction of objects especially in the Inner Tracker and Electromagnetic calorimeter most exposed to the high flow of particles. A great deal of work on the reconstruction algorithms is being made to assess and to improve their performance against pile-up [4–7].

The issue and related concerns are not going to alleviate any time soon. It is anticipated that at the restart of the LHC, there will be about 50 interactions per bunch crossing in the conditions of the reference beam configuration [8]. On the longer term, figures as high as 140 interactions per bunch crossing are being contemplated for the High Luminosity LHC project [9].

---

[1] The long and epic History of the LHC and the associated experiments projects has been recently told in great details and in French in [3].

[2] Tevatron ceased operations by September of the same year.

[3] It is the very nature of the LHC idea to compensate by a very high luminosity, an energy in the center of mass limited by the cost saving re-use of the LEP tunnel.

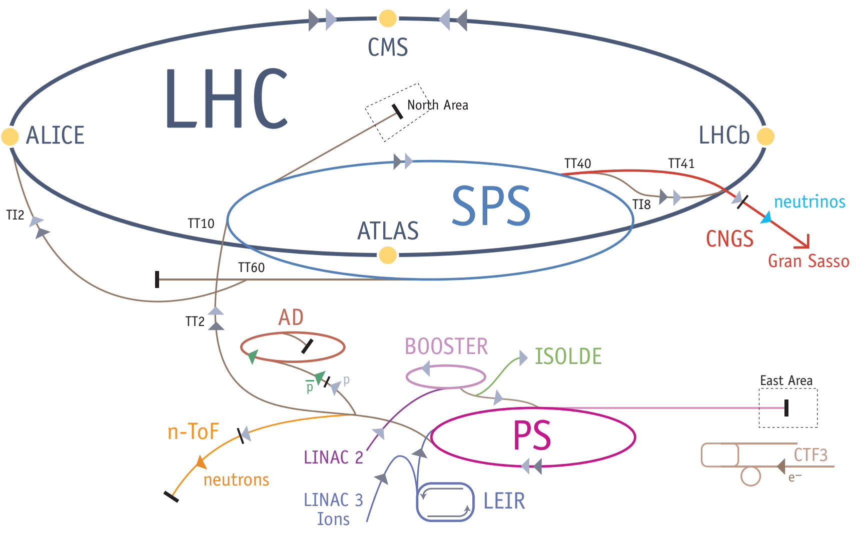

Figure 1.1: LHC accelerators chain

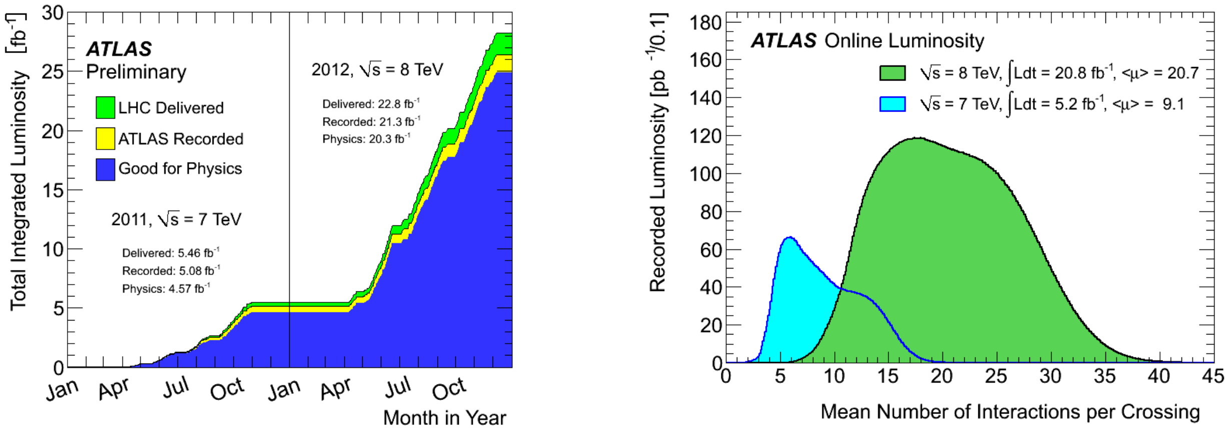

(a) (b)

Figure 1.2: (a) Total Integrated Luminosity and Data Quality in 2011 and 2012: cumulative luminosity versus time delivered to (green), recorded by ATLAS (yellow), and certified to be good quality data (blue) during stable beams and for pp collisions at 7 and 8 TeV center-of-mass energy in 2011 and 2012; (b) Mean number of interactions per crossing for the 2011 and 2012 data

	2010	2011	2012	Nominal
Energy in the center of mass (TeV)	7	7	8	14
Number of bunches	368	1380	1380	2808
Bunch time spacing (ns)	150	75/50	50	25
Delivered Integrated Luminosity (fb^{-1})	0.04	6	23	
Mean number of interactions per bunches crossing	∼2	∼9	∼21	19

Table 1.1: LHC parameters [8]

1.2 ATLAS overview

The ATLAS detector displayed in figure 1.3 is the largest of the general-purpose Particle Physics detectors ever built [10]. Its overall dimensions are defined by its exceptionally large Muon Spectrometer displayed in figure 1.4.

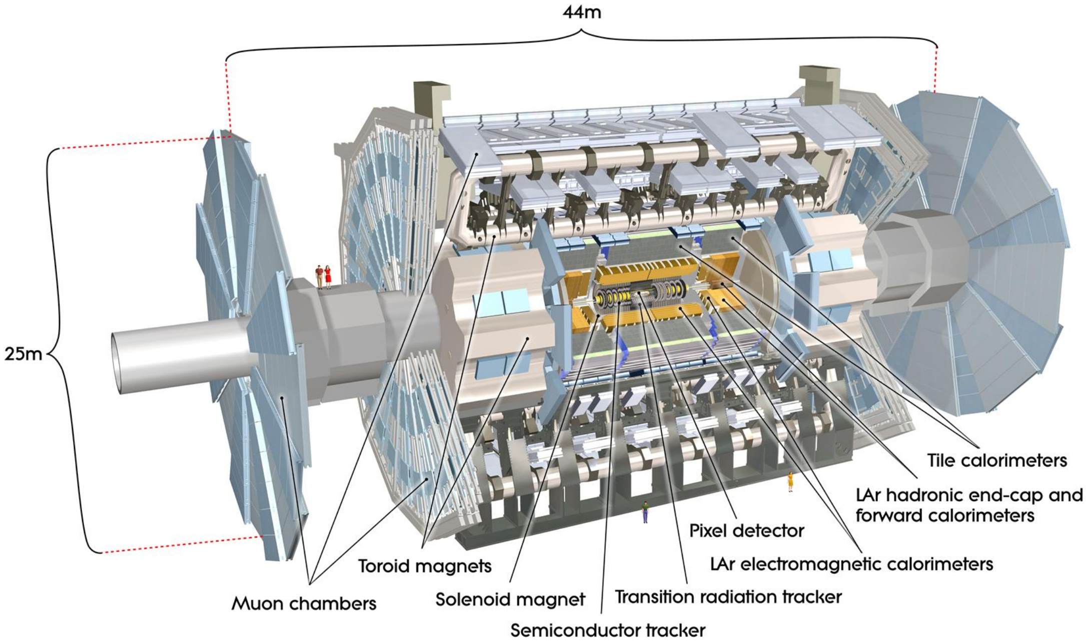

Figure 1.3: Cut-away view of ATLAS Detector with the different sud-systems identified

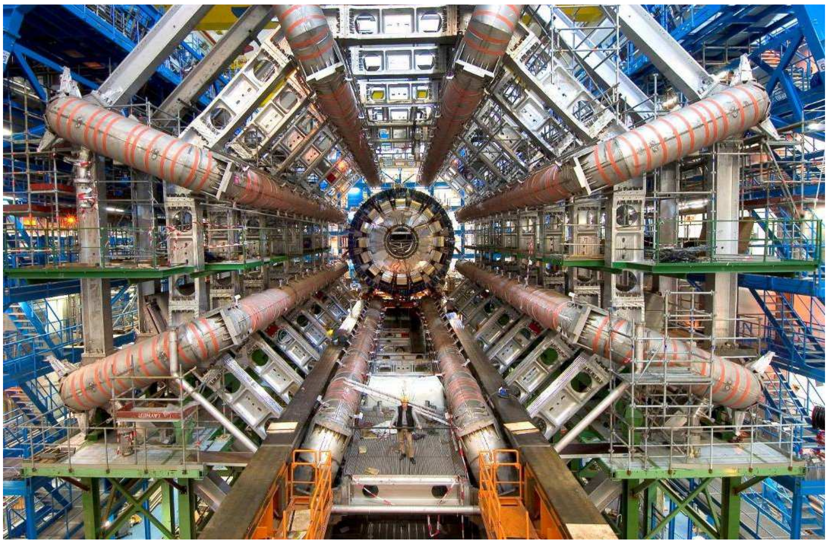

Figure 1.4: The eight barrel toroids magnets installed in the ATLAS Cavern

Notwithstanding its impressively large dimensions, ATLAS has the same onion-like structure than many of the Particle Physics detectors: several detectors layered upon one another surround the nominal zone of interactions of the protons bunches.

Emerging from the central interactions area, a muon will cross all these detectors:

- It will meet first the Inner Tracking Detector (ID) shown in figure 1.5.

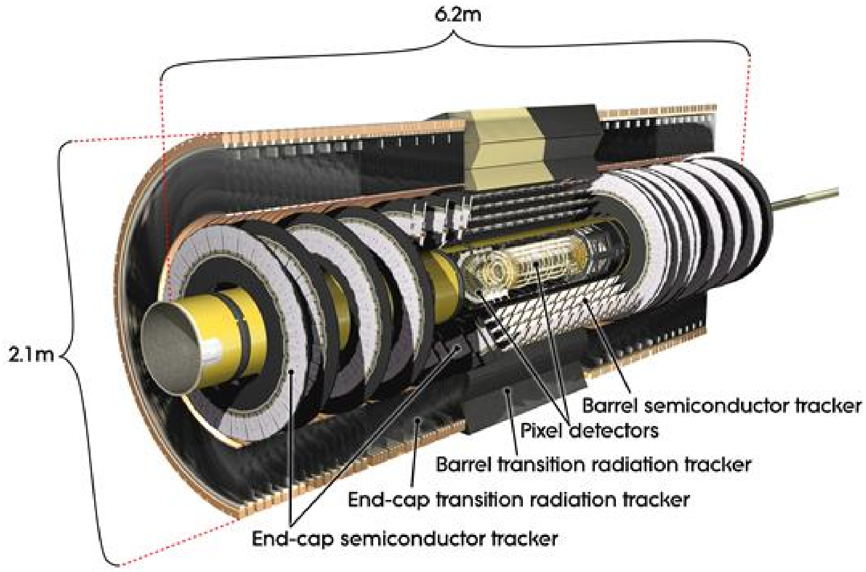

Figure 1.5: ATLAS Inner Tracking Detector

The ID, which covers the η [4] range $[-2.7; 2.7]$, is composed of three sub-detectors: two semiconductor detectors, one using pixels, the Pixel detector, the other using micro-strips, the Semi-Conductor Tracker (SCT), and the Transition Radiation Tracker (TRT). Immersed in a 2 Tesla field of the Central Solenoid (CS), these detectors provide high granularity position measurements along the transversally bent tracks.

Lightweight, these detectors are designed to be as much as possible transparent to the particles emerging from the interaction point (IP). This is particularly true for muons, which are affected only by Multiple Scattering within sub-detector material, let simple, pristine tracks easily reconstructible. Indeed muon tracks are more easily reconstructible than tracks of electrons which are affected also by Bremsstrahlung, or of pions which are affected also by hadronic interactions.

This results in higher performance of the muon reconstruction, as illustrated by the figure 1.6(a) which shows the reconstruction efficiency as a function of η [10]. While the muon reconstruction efficiency is high and fairly uniform, the efficiencies for electron and pions are not only lower but do depend strongly on η in a way reflecting the amount of material in the ID (cf figure 1.6(b)).

This material impacts nevertheless the muon performance by the Multiple scattering effect. It deteriorates the muon momentum resolution shown in figure 1.7 in the intermediate range from $|\eta| \sim 0.7$ to $|\eta| \sim 1.7$. For higher η, the resolution inexorably worsens because not only the

---

[4] ATLAS uses a right-handed coordinate system with its origin at the nominal interaction point (IP) in the center of the detector and the z-axis along the beam pipe. The x-axis points from the IP to the center of the LHC ring, and the y-axis points upward. Cylindrical coordinates (r, ϕ) are used in the transverse plane, ϕ being the azimuthal angle around the beam pipe. The pseudo-rapidity and the transverse momentum are defined in terms of the polar angle θ as $\eta = -\ln(\theta/2)$ and $p_T = p\sin(\theta)$, respectively. The $\eta - \phi$ distance between two particles is defined as $\Delta R = \sqrt{\Delta\eta^2 + \Delta\phi^2}$.

instrumentation reduces (TRT stops at ~ 2.0), but also the measurement lever arm shortens due to the finite length of the solenoid.

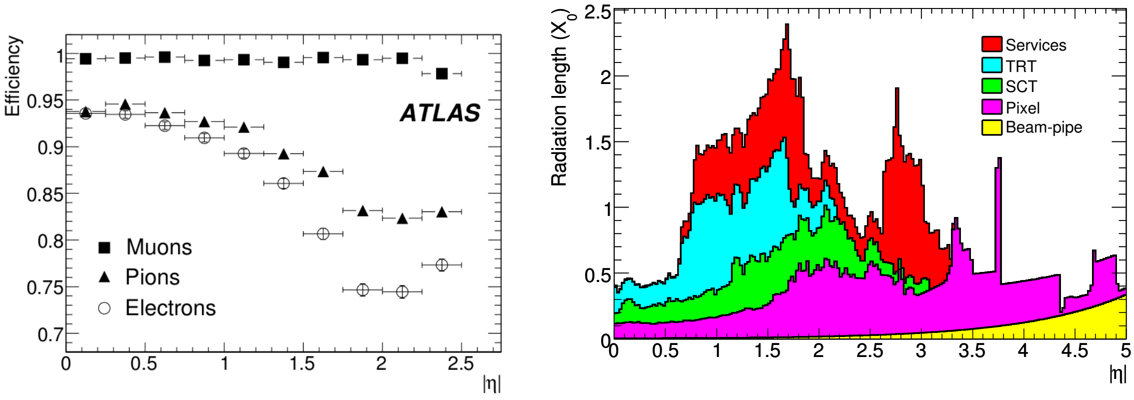

(a)

(b)

Figure 1.6: (a) Track reconstruction efficiencies as a function of $|\eta|$ for muons, pions and electrons with $p_T = 5$ GeV (b) Material distribution in X_0 at the exit of the ID envelope;

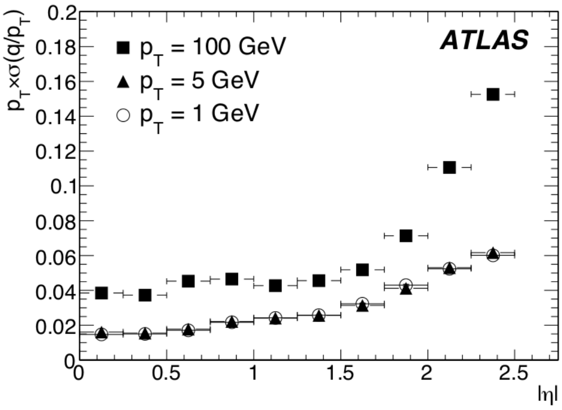

Figure 1.7: Muon momentum resolution as a function of $|\eta|$ for muons with $p_T = 1$, 5 and 100 GeV .

- the muon then meets the Calorimeters system shown in figure 1.8.

The ATLAS Calorimeters cover the range $|\eta| < 4.9$. They are all sampling calorimeters, saving the presampler sections in front of the Liquid Argon Electromagnetic calorimeter, using various absorber materials (lead, steel, copper, tungsten) and various active materials (liquid Argon, scintillator tiles). The complexity of their geometrical structure is also variable, the most sophisticated one being the accordion shape of the Liquid Argon electromagnetic calorimeter.

They are designed to force the incoming electrons, photons and hadrons to generate showers of secondary particles by cascades of successive electromagnetic and hadronic interactions until the initial energy is spread out on low energy particles which are eventually absorbed, for most of them, within the calorimeters themselves.

Much heavier than an electron, a muon does not shower and typically goes through the calorimeters. However, in addition to suffer from a multiple scattering effect much larger than in the ID, a muon does loose energy in the dense material of calorimeters both by ionization and radiative

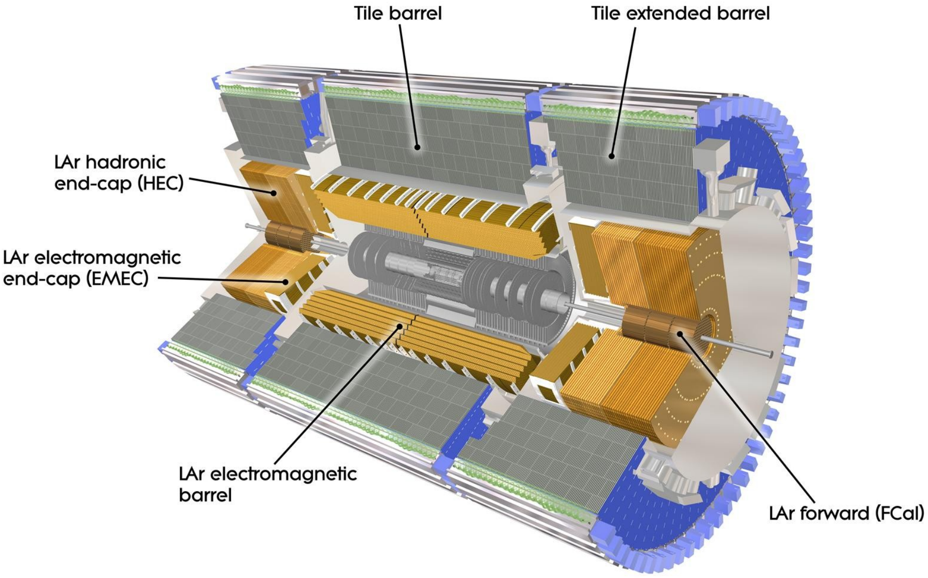

Figure 1.8: ATLAS Calorimeters

processes (cf figure 1.9) and if its energy is too low, lower say than 3 or 4 GeV, it will be absorbed in the calorimeters. The average energy lost per unit length is approximately an affine function of the muon energy. The distribution of the energy actually lost is a Landau distribution with large tail toward large energy loss, reflecting the not so unlikely deposit at one time of a large fraction of the muon energy, i.e a catastrophic energy loss event.

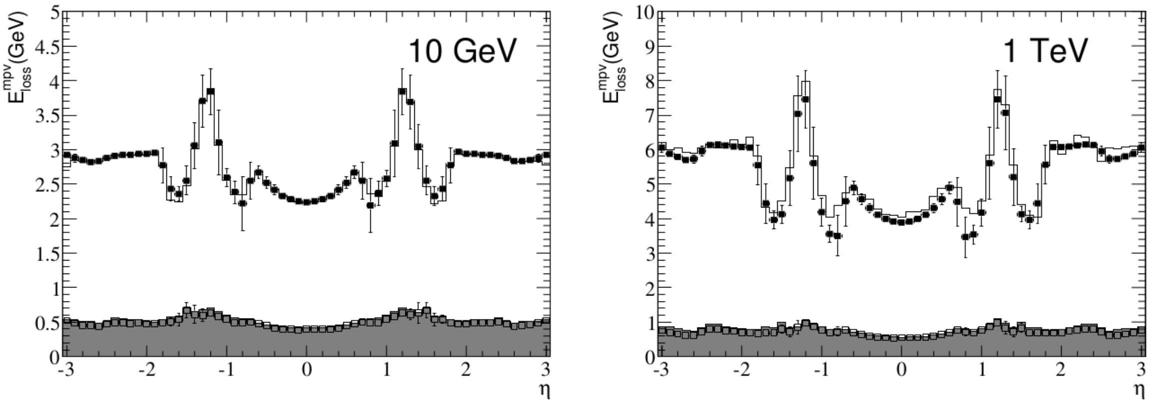

Figure 1.9: Most probable value of the energy loss as parameterized in the geometry of the ATLAS tracking (points) and in GEANT4 [11] for muons of momentum 10 GeV (left) and 1 TeV (right) as a function of pseudo-rapidity. The solid line and points correspond to the energy loss of muons propagating from the beam pipe to the exit of the hadronic calorimeters. The filled histogram and hollow points correspond to the energy loss of muons propagating from the beam pipe to the entrance of the hadronic calorimeters (from [12]).

- Having survived the passage through the calorimeters, a muon, if its energy is high enough, can eventually reach the Muon System that is described in the next section.

1.3 Muon Spectrometer

1.3.1 General considerations on the Design

The Muon Spectrometer, depicted in figures 1.4 and 1.10, is a detector of truly gigantic size: a hollow cylinder 46 meters long, 22 meters large. Yet its function is nothing but standard: estimate the momentum of a muon from the bending of its trajectory in a magnetic field. The field is toroidal so that the lever arm on which the measurement is done, is not decreasing at high η.

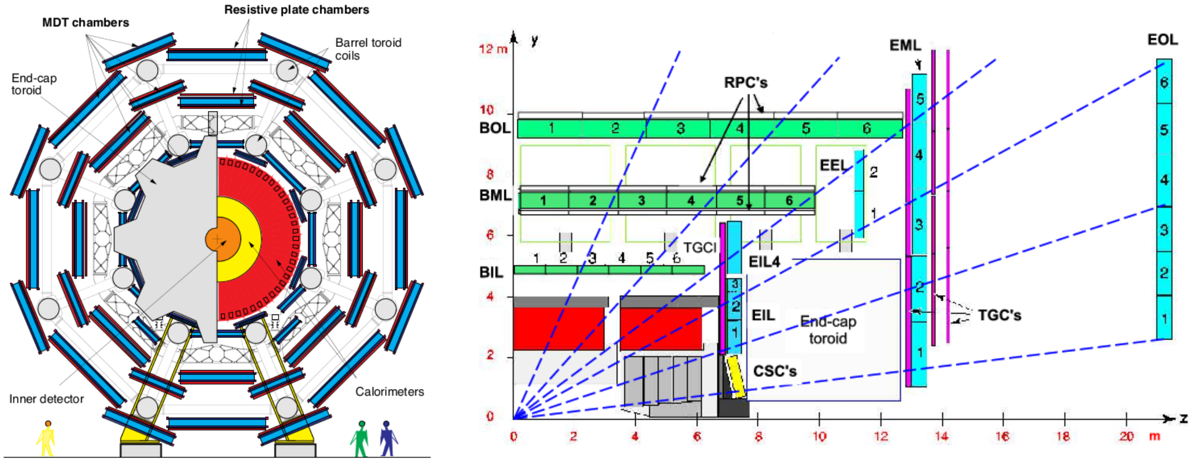

(a)

(b)

Figure 1.10: (a) Schematic view of the ATLAS Muon Spectrometer; cross-section view transverse to the Z direction. (b) R-Z view of the ATLAS Muon Spectrometer

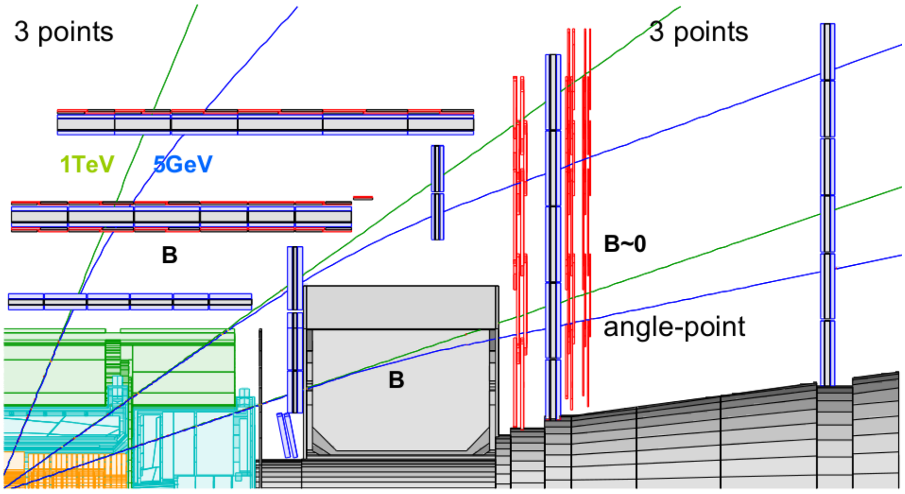

Figure 1.11: Transverse view of the ATLAS Muon Spectrometer showing where the reference methods of momentum measurement apply. Note that these reference methods are only convenient idealizations of the actual measurement algorithm.

The rationale underlying the Muon Spectrometer design is to perform the momentum measurement with the effect of the multiple scattering in the matterial of the apparatus reduced to the extreme. This led to the solution of an air-core toroid with magnetic field supplied by superconducting magnets

[5]. Because these magnets provide field weaker than conventional iron magnets, and therefore have smaller bending power, the level arm of the measurement has to be quite large.

The muon trajectory in an gentle magnetic field forms a smooth arc, the sagitta of which depends on the momentum. The reference method, so called Three-Point method (cf appendix D), to measure the momentum of a muon is to measure this arc by measuring 3 points along this trajectory at the entrance and the exit of the volume where the deflection occurs and somewhere in between within this volume, as shown in the figure 1.11.

Aiming for a 10 % momentum resolution for a 1 TeV muon, and assuming that one can achieve a field of typically ~0.5 T and a precision of ~50 μm on the measurement of the sagitta, it comes that the lever arm should be of the order of 5 m (cf appendix D.3.1). This sets the overall dimensions of the Barrel part of the apparatus: eight superconducting coils, each embedded in its own cryostat (figure 1.4), generate a toroidal field in a cylindrical volume extending from the radius ~5 m where the calorimeters end, to a radius of ~10 m (figure 1.10).

The deflection of the trajectory is measured in position detectors arranged in three set of Stations, the Inner, Medium, and Outer Stations, respectively at the entrance of, within, and at the exit of the deflection volume. To obtain a ~50 μm precision on the sagitta, one needs a precision of ~40 μm on the measurements of the position of each point where the trajectory intersects the Stations. This set the choice of the detection technologies for the measurement of the position in the bending direction as it will be discussed latter.

For mechanical reasons, the schema of the Barrel part of the Muon Spectrometer could not be repeated for the end cap part. The field is still generated by eight superconducting coils but they share a single cryostat Contrary to the Barrel case, there is no measurement Station within the magnetic field volume. There are still three Stations but now the Inner and Medium Station measure the track position respectively before and after the deflection of the trajectory in the end cap toroid. No further deflection occur between the Medium and Outer Stations.

Instead of the Three-Points Method, the momentum measurement relies in the End-Caps on the so called Angle-Point Method (cf figure 1.11): the track angle after the deflection is very precisely measured by the two position measurements in the Medium and Outer Stations and the difference between straight line extrapolation on the plane of the Inner Station and the actual track position measured there gives the track momentum. It can be shown that with Stations of similar performance than those of the Barrel part, this Method needs larger distances between the Stations (cf appendix D.3.2). This sets the larger dimensions of the end sides of the Spectrometer.

The above considerations give the outlines of the Muon Spectrometer. In the next sections I will discuss few aspects of the concrete design of the detector, concerning the magnetic field, the material distribution within the apparatus, the alignment issue and in more detail, the layout of the detection Units.

---

[5] An air-core toroid was part of the ASCOT detector proposal for LHC in the early 90's [13]. ASCOT and an other proposal, EAGLE [14], merged to form the actual ATLAS detector. The originators of the air-core toroid concept, Marc Virchaux and Claude Guyot, were drawing on an earlier proposal that they did with others, of such an apparatus for a Deep Inelastic Scattering (DIS) experiment, the project MuSupra [15]. The idea was to improve on the performance of the spectrometers of the majors DIS experiments of that time, which were mainly Iron spectrometers. Iron allows strong magnetic field in a compact volume at the price of a momentum resolution limited by multiple scattering.

1.3.2 Some consequences of the Design

1.3.2.1 Magnetic Field Map

As discussed above, the field in the Muon Spectrometer is given by 3 Toroids: the Barrel toroid, made of eight coils each in its own cryostat, and two End Cap Toroids, each made of eight coils sharing the same cryostat. The eight End Caps coils are rotated by 22.5°with respect to the Barrel coils [6].

The resulting field departs significantly from an ideal toroidal configuration and shows complex structures, specially in the transition region when the fields from Barrel and End Cap Toroids overlap (cf figure 1.12). This prevents any simple analytical parametrization of the muon trajectory.

Therefore a precise map of the field is a crucial ingredient of the reconstruction program for tracking the trajectory, as well as for corrections of field effect at the level of the detection units.

The Field description is based on a reconstruction of the positions of the coils conductors from the measurements of a set of magnetic probes located mainly on the Stations, taking into account the effect of some magnetic materials around, as well as the influence of the field in the calorimeters nearby the Muon Spectrometer entrance [16].

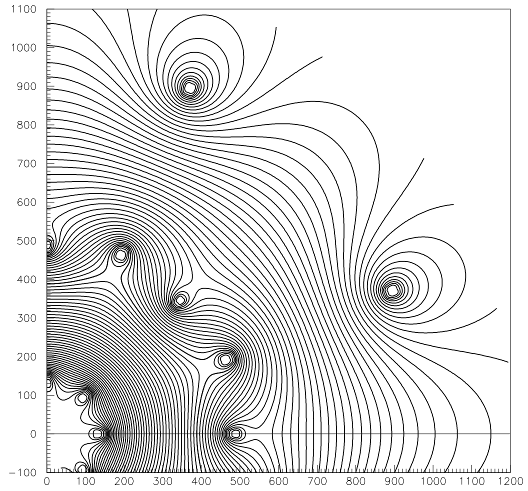

Figure 1.12: Magnetic field map in the transition region. The field lines are shown in a plane perpendicular to the beam axis and located in the middle of an end-cap. The scales are in centimeters.

1.3.2.2 Matter distribution

As discussed in appendix D.4, the multiple scattering effects dominate the momentum resolution at low momentum. Although being based on an air-core Toroid concept, the actual ATLAS Muon Spectrometer is far from being empty.

The matter of detection units themselves provides opportunities for the muon to experience scatterings.

The Coils of all the Toroids place large amount of matter on the muon paths even though they are limited distributed in azimuth. The Struts and the Voussoirs, large bars connecting the coils needed for mechanical integrity, do contribute by ring-like matter spots extending over all the azimuth, although narrow in rapidity.

On the side of the End Cap Toroids, the walls of the cryostat cover all the phase space at high rapidity.

The area of two pillar structures, the feet, which support the weight of the detector and are merged with the two bottom Barrel Toroid coils, (cf figures 1.10(a) and 1.20) is one of the most difficult ones.

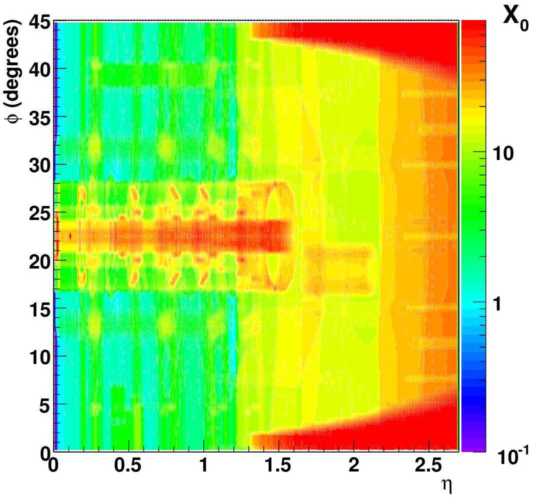

Figure 1.13: Amount of material in units of radiation lengths (X_0) traversed by muons after exiting the calorimeters, as a function of η and ϕ

---

[6] At one time considered, the configuration with both Barrel and End Cap coils lying in the same plane was abandoned since it led to too large low field regions in the regions between coils of the two systems.

In addition to all of this, few spots of matter corresponding to services and supports. are often distributed in a highly non uniform way.

All these contributions make a very contrasted distribution of the matter in η and ϕ as shown in figure 1.13. Furthermore, as discussed in appendix D.4, the influence of the matter on the resolution does depend on the actual position of the matter with respect to the detection units, the more damaging spots being those which are the closest to the Medium Stations. This implies that one does need a fully tridimensional description of the matter distribution to properly take in to account the effects of the multiple scattering on the measurement of the momentum.

1.3.2.3 Alignment of the detection units

We saw that to measure properly the sagitta of a trajectory, a precision of $\sim$40 μm is needed on the positions of the intersections of the track with detection units. As we will see later, technologies exist which allow to reach this precision.

But the relative positioning of the detection units themselves contributes also to the precision on the sagitta. In order that this contribution remains a sub-leading contribution to the overall momentum resolution, the relative position of chambers should be known with an uncertainty better than 30 μm. The detection units are meter wide objects few meters apart. Installation procedures and geometers surveys allow a precision at the mm level, more that an order of magnitude worse than the precision required.

Therefore sophisticated optical systems have been developed to reach this goal [17, 18]. Thanks to an intricate network of optical links connecting the different units, illustrated in figures 1.14(a) and 1.14(b), to special data sets recorded with the Toroids field switched off, and to the tremendous work of my colleague physicists working on this task, the relative and absolute positions of the detection units can be determined with the prescribed precision for almost all of them [19, 20]. The outcomes of the Alignment procedure are important inputs for the reconstruction of the tracks.

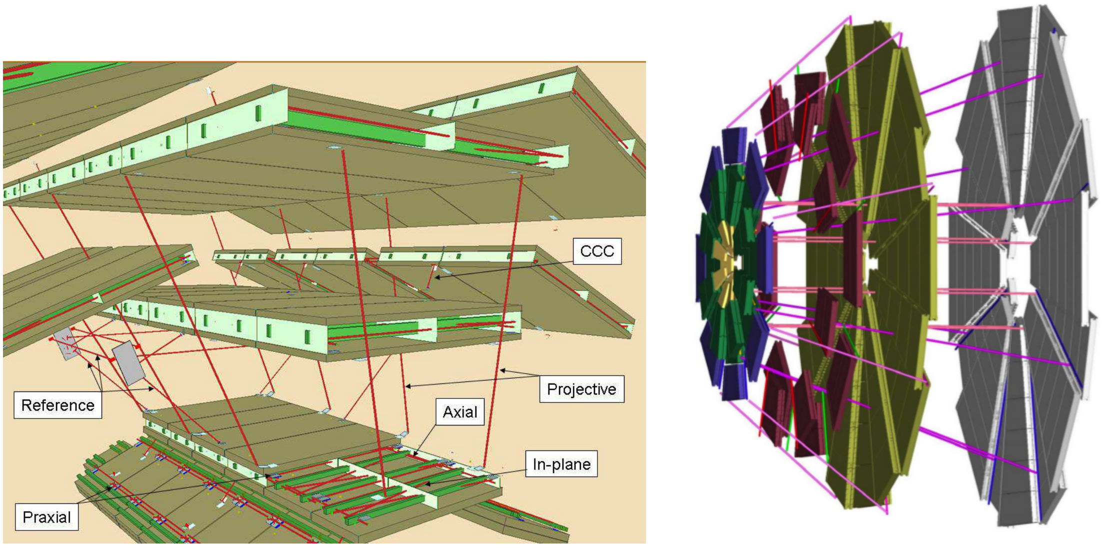

(a) Barrel Optical Alignment System (b) End Cap Optical Alignment System

Figure 1.14: ATLAS Optical Alignment Systems

1.3.3 Stations Layout and Chambers Technologies

1.3.3.1 Stations Layout

The Muon Spectrometer covers the range $|\eta| < 2.7$. The general scheme of a Triplet Inner/Medium/Outer Stations is present everywhere in the layout of the Stations of the Detector, as it is shown in figure 1.15.

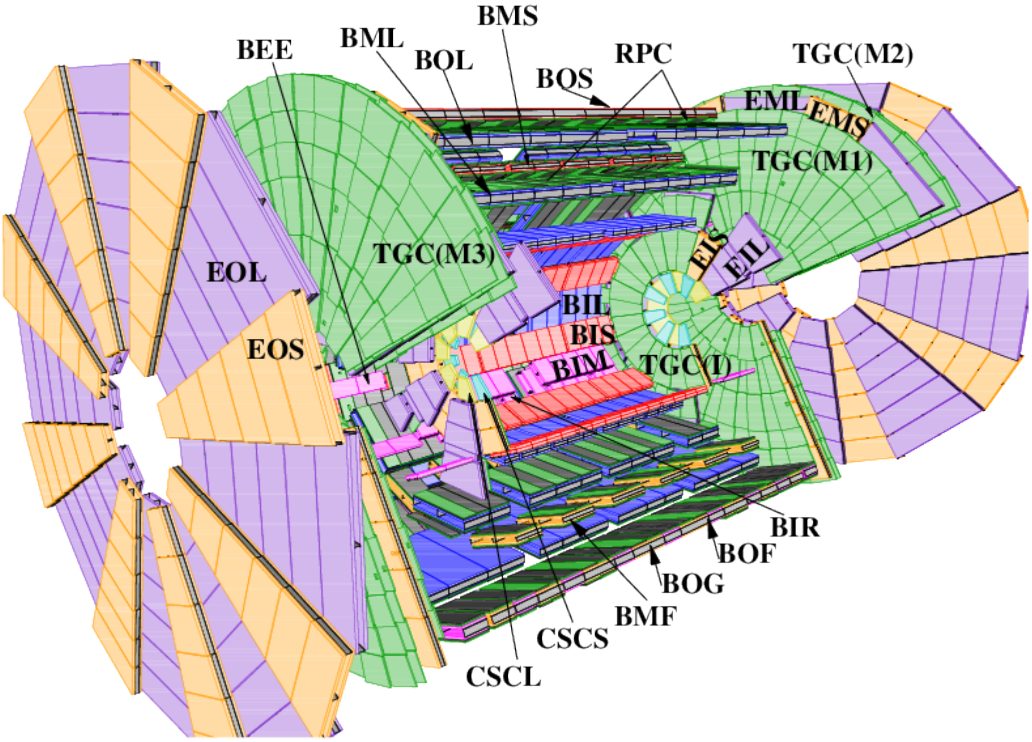

Figure 1.15: View of the Muon Spectrometer Layout giving some examples of the nomenclature of the Chambers.

In azimuth the Toroids define 16 Sectors, each with their set of Stations: eight Large Sectors for Stations in between the Barrel coils, eight Small Sectors for Stations centered on them. The ubiquity of the Station Triplet scheme explains the nomenclature based of a triplet of letters, of most of the names of the Stations: first B or E for Barrel or End Cap Stations, then I, M or O for Inner, Medium or Outer Stations and finally S or L for Small or Large Sectors.

But the Muon Spectrometer Layout is not just three cylinders nested one inside the other. There are many departures from this scheme.

Some departures are astute such as in the transition area between the Barrel and the End Cap parts illustrated by the figure 1.16, where additional Stations, the EEL and EES Stations, are placed to act as Medium Stations in a Triplet which recruits a, in principle, Medium Stations as an Outer Stations.

Some departures are to rescue weak points, such as when the BEE Stations are added in the Small Sectors and forms with the EIS, EMS and EOS a Quadruplet of Stations. The complicate field structure in such region results in cancellation of bending power between the Inner and Medium Stations. The BEE inserted in between these Stations allows to recover the momentum resolution. Unfortunately the alignment of these BEE is specially challenging.

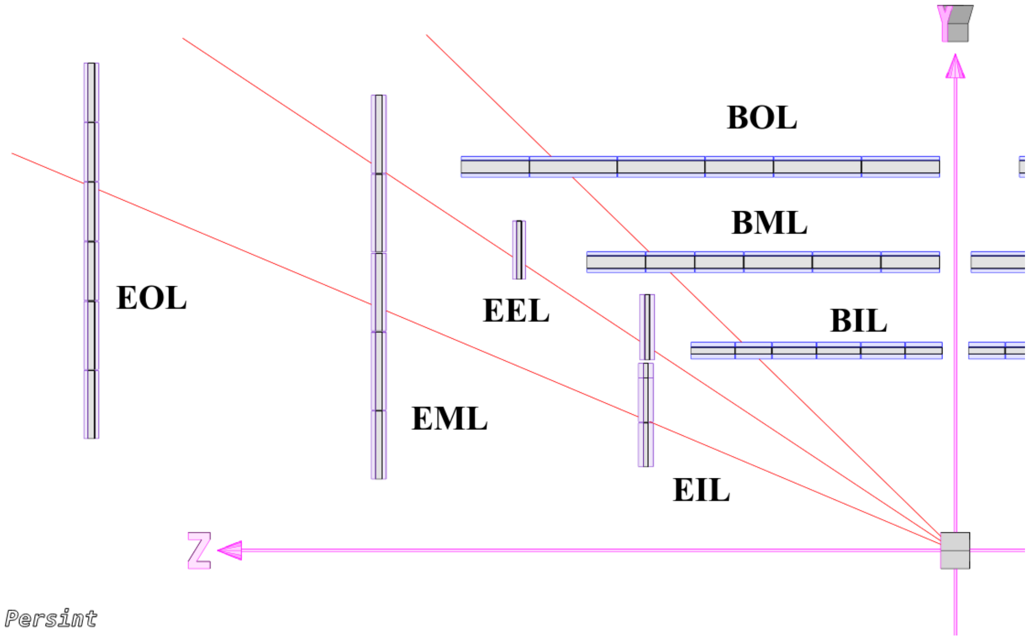

Figure 1.16: Cross-section in the Large Sectors of the Muon Layout. In Barrel, the tracks are measured by the triplet BIL-BML-BOL and in End Cap, by the triplet EIL-EML-EOL. In the transition region, the measurement triplet is EIL-EEL-EML, i.e the Medium EML Station is used as an Outer Station.

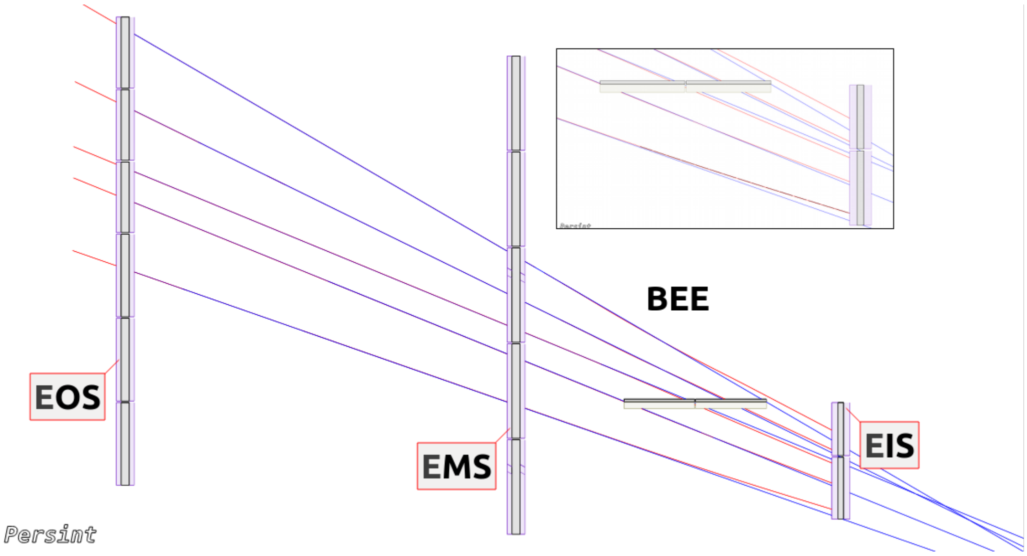

Figure 1.17: Cross-section in the Small Sector. Red Curves starting on the Inner Station are trajectories of muons of 10 GeV p_T. Blue curves crossing the Inner Station are straight lines superimposed on these muon trajectories in the volume between EO and EM Stations. Difference between positions on the Inner Station surface of the Red and Blue curves gives the momentum (Angle-Point Method).

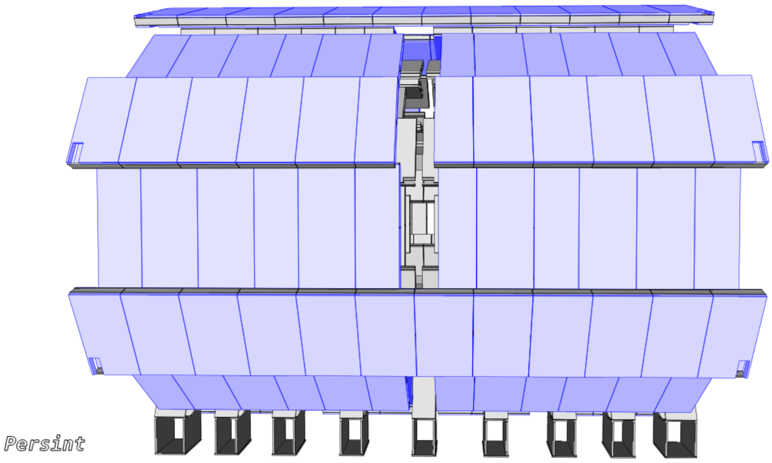

Figure 1.18: View of the allowance space at η ~0. Meter wide passages for service prevents installation of Chambers.

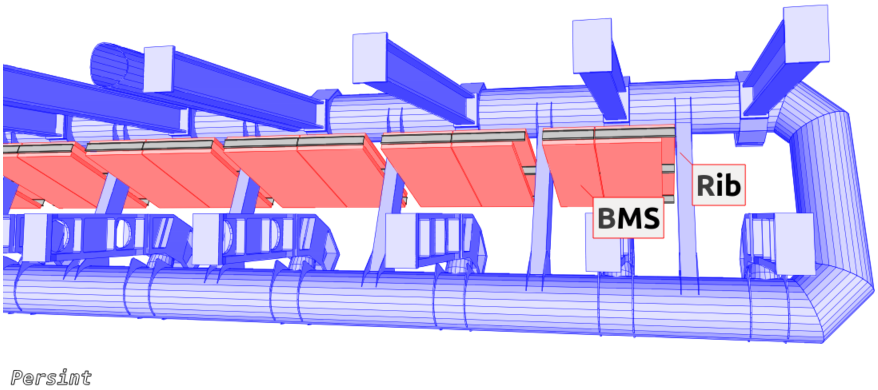

Figure 1.19: Holes are made within the Medium coverage for the Barrel coils ribs.

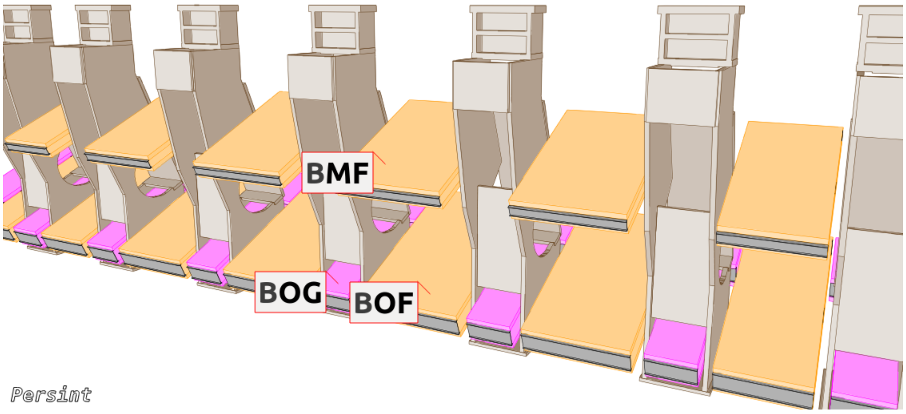

Figure 1.20: In the feet sectors, holes are made in the Medium and Outer Stations coverages.

However its fair to say that most of the departures from the ideal Layout are damaging. They amount for acceptance losses to make room for services.

The worst case is the allowance space in the range $|\eta| < 0.06$, made for the passage of various services. It mainly affects the Large Sectors where all Stations are lost as shown in the figure 1.18.

In other cases, only one of the standard Three Stations along the trajectory of a muon is lost.

Examples are holes made in all the Medium Small Stations to accommodate the Ribs of the Barrel coils as illustrated in the figure 1.19, or made non projectively in both Medium and Outer Stations to make room for the feet structures as shown in the figure 1.20.

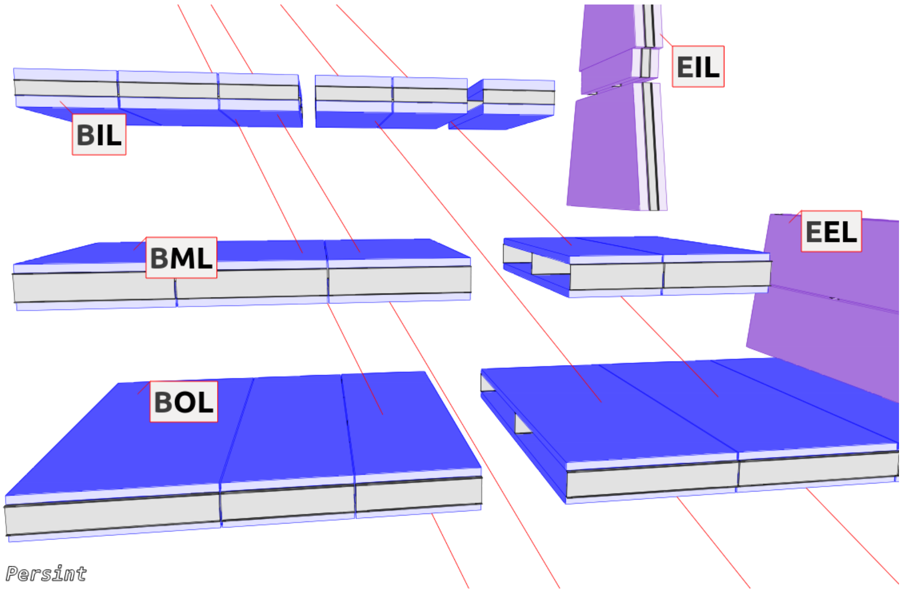

Figure 1.21: In the bottom Large sector between the two feet, a passage for an Elevator is hollowed out in the Medium and Outer Stations. View from the Interaction Point, only one station, the BM or the BO, is missing at once.

A last example of these configurations, are the two large non-projective holes in the bottom Barrel Large Sector around |Z| ~7 m shown in figure 1.21. There, meter wide holes allow room for Elevators needed to access Inner Detector and Calorimeters.

The figure 1.21 shows also trajectory of muons shot from the Interaction Point at different η. As it can be seen for some trajectories, only two points can be measured and the Three-Points method, usual in the Barrel area, can not be applied. However the Muon Spectrometer Stations do measure more than just the track intersection point. Actually they measure a segment of the track, a point and a direction. Therefore for this category of trajectories, the momentum can be measured by comparing the angles of the trajectory on the two Stations. Unfortunately, the resolution obtained with this so called Angle-Angle Method is not as good as the resolution of the standard Three-Points Method (cf appendix D.3.3).

1.3.3.2 Chambers Technologies

A very convenient idealization of the trajectories of the muon in the Muon Spectrometer is to see them as confined in a plane passing by the beam axis.

Indeed emerging from the beam axis, a muon is bent transversally in one direction by the solenoidal field when it crosses the Inner Detector volume. When it crosses the calorimeters volumes, it is bent in the other direction by the return field there. If the fluxes of the Inner Detector field and its return field have canceled each other at the radius of the Muon Spectrometer entrance, then the muon enters in the Muon Spectrometer tangentially aligned on a ray passing by the beam axis.

Then crossing the Muon Spectrometer, bent by a Toroid field its trajectory remains in a plane at constant ϕ, which includes the muon entry point and the beam axis. This idealization of the actual field configuration, is good enough to capture the main picture.

On this basis, one distinguishes first coordinates quantifying positions in the bending plane, i.e η direction, and second coordinate for position perpendicular to this plane, i.e ϕ direction. The measurements of these coordinates are done in Chambers of various kinds, called technologies hereafter. Four types of technologies are present: MDT, RPC, TGC and CSC

1.3.3.2.1 MDT Chambers

The main technology is the Monitored Drift Tubes Chambers technology, the MDT technology. The MDT Chambers are collection of orthoradial [7] tubes typically arranged in three or four Tubes Layers grouped in one or two Multilayers.

The tubes are filled by a mixture of Ar and CO_2 gases under pressure. High voltage is applied between the tube wall and a wire at the center of the tube. Operation principle is illustrated in figure 1.22(b): crossing a tube, the muon ionizes the gas; the ionization electrons drift toward the wire; the time delay between crossing and first arrival of charges on the wire, the drift time, gives a measure of the shortest distance of the muon to the wire, the drift radius. The information from a single tube is thus that the muon trajectory is tangent to a cylinder centered on the tube axis, the radius of which is the drift radius. The resolution on the drift radius is typically 100 μm in average, with a significant dependence on the impact radius shown on figures 1.22(c) [21, 22]. Fluctuations in the deposited ionization charge is responsible for the resolution degradation at small radius [23, 24].

The local magnetic field modifies the trajectory of the drift electrons and therefore the relation between drift radius and arrival time (Lorentz angle effect) [25]. A moderately precise, ~1 cm, estimate of the position of the track along the tube, i.e a measurement of the second coordinate, is needed to correct for this effect. This measurement is also needed to correct for the time of the propagation of the signal along the tube.

A salient feature of the MDT technology is that it is slow. The maximum drift time corresponding to charge deposition at the largest radius, is ~700 ns. While only the charge deposition the closest to the wire does contain impact parameter information, the drift of all deposited charges along the track will take that long. This led to implement in the readout-electronic, a dead-time of 750 ns after the arrival of the first signal. Therefore it could be that the signal expected on some tube for a candidate track has been masked by an earlier signal from a δ-ray, i.e an atomic electron knocked out by the muon from the tube wall, or a neutron or a photon from the high level background radiation [26]. This masking effect is an important feature to be included in the track reconstruction algorithm

---

[7] Orthoradial is used here and later to mean that a circle centered on the beam-axis and passing by the middle of the tube would be tangent to the tubes axis.

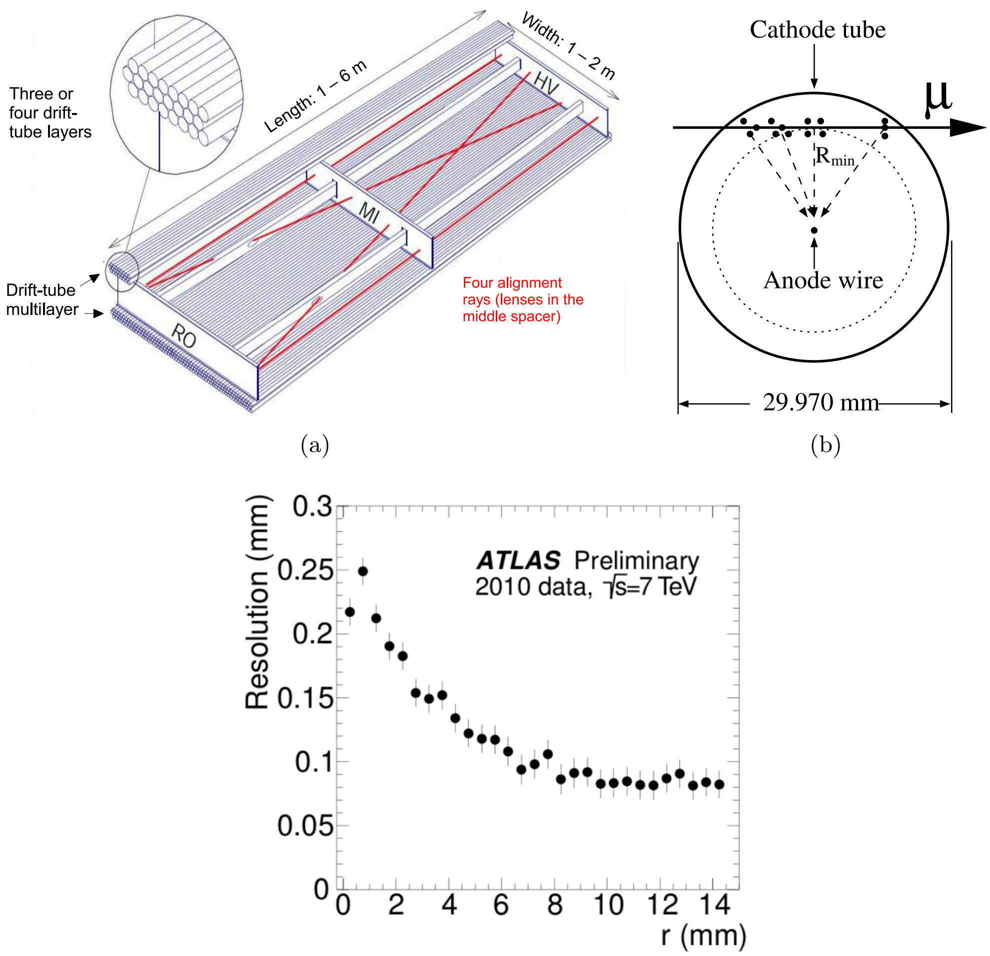

(a) (b)

(c)

Figure 1.22: (a) Mechanical structure of a MDT chamber. Three spacer bars connected by longitudinal beams form an Aluminium space frame, carry two Multilayers of three or four drift Tubes Layers. Four optical alignment rays, two parallel and two diagonal, allow for monitoring of the internal geometry of the chamber; (b) Cross section of a MDT tube. They are Aluminium tubes filled with Ar/CO_2 gas under a 3 bar pressure. A voltage difference of 3080 V is applied between the central tungsten-rhenium wire and the tube wall. (c) Resolution as a function of the impact parameter of the track with respect to the tube wire from [21].

The mechanical simplicity of the MDT technology has permitted the development of very reliable and precise assembly procedures which allowed to reach a precision on the positioning of the wires in the MDT Stations better than 20μm [27, 28], well below the intrinsic drift radius precision. Still MDT Stations are large objects subject to gravitational or thermal deformations. Therefore, they are equipped with internal optical system shown in figure 1.22(a), which monitor these deformations. As the corrections of the positions of the Stations, these deformation corrections have to be included in the reconstruction algorithm of the tracks.

The measurement of the local position and angle of the muon trajectory in an MDT station will consist in fitting a straight line tangent to a set of cylinders centered on the tube axis. The resolutions on the local position and angle of the trajectory obtained in this way are of the order of 40 μm and few hundreds of μrad (cf appendix D.2).

The tubes of the MDT Chambers measure precisely the first coordinate. The MDT Chambers provide this precision measurement over most of volume. Only at high rapidity and only in the innermost Station an other technology is used, the CSC technology, which allows also a second coordinate measurement.

But anywhere else, the second coordinate is measured in Chambers distinct from the MDT Chambers but located in their immediate vicinities. These Chambers are of two types: the RPC and the TGC Chambers. The use of two technologies, the RPC for the lower rapidity range and the TGC for the higher range, has resulted, among other factors, from a compromise between prices (RPC Chambers are less expensive) and rate capabilities (TGC Chambers cope better with the higher background rates of the high η range) [29, 30]. Both Chambers types provide first and second coordinate with a precision in the cm range. Much faster than those of the MDT Chambers, their signals are used in the logic of the Muon Spectrometer Standalone Trigger system [31].

1.3.3.2.2 RPC Chambers

The Resistive Plate Chambers, the RPC Chambers, are used in the Barrel part of the Muon Spectrometer. One or Two of these Chambers are placed on each side of the Medium MDT Stations as shown in figure 1.23(a).

The internal structure of the RPCs is shown in figure 1.23(b). The active volume is a gas gap defined by two resistive planes between which a high voltage difference is applied. A muon crossing this volume generates avalanches along its path. The reading is performed by capacitive coupling on strips planes parallel to the resistive planes. On each side of the gap, strips run in orthogonal directions providing position measurements in both coordinates with a resolution of the order of ∼1 cm. Both first and second coordinates measurements are used in offline reconstruction of tracks.

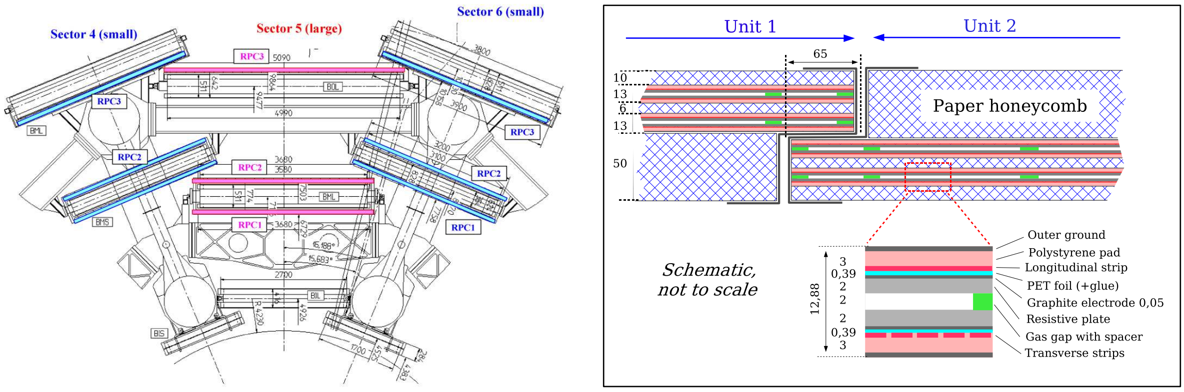

(a) (b)

Figure 1.23: (a) Cross-section through the upper part of the barrel. In the middle chamber layer, RPC1 and RPC2 are below and above their respective MDT partner. In the outer layer, the RPC3 is above the MDT in the large and below the MDT in the small sectors; (b) Cross-section through a RPC, where two units are joined to form a chamber.

1.3.3.2.3 TGC Chambers

The Thin Gap Chambers, the TGC Chambers, are used in the End Cap part of the Muon Spectrometer. They are arranged in four wheels: one covers the End Cap Inner MDT Chambers while the three others are flanking the End Cap Medium MDT Chambers (cf figure 1.10(b) and 1.24(a)). Only these last three are used in the Trigger. They are not matching Small and Large Sectors segmentation of the End Cap MDT Stations but are rather formed of trapezoidal Chambers arranged in concentric rings.

The internal structure of the TGCs is shown on figure 1.24(b). A high electric field is generated between a plane formed by orthoradial anode wires and cathode graphite layers. The wire distance is greater than the anode-cathode distance. Set of wires are grouped to form the signal measuring the first coordinate while some cathode planes are read by strips orthogonal to the wires providing thus the second coordinate. The resolution in both direction is of the order of ∼0.5 cm.

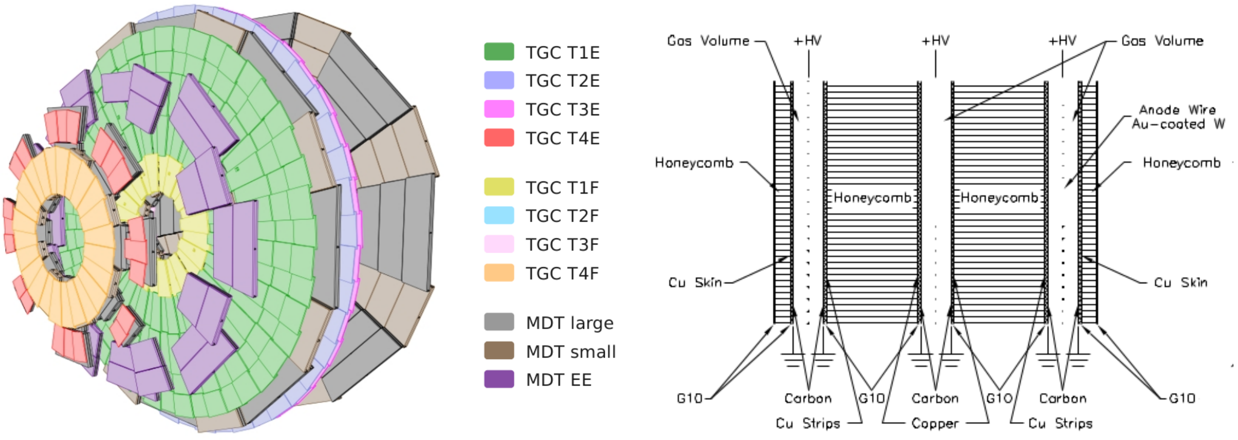

(a) (b)

Figure 1.24: (a) TGC Chambers with the End Cap MDT Chambers; (b) Cross-section of a TGC triplet

1.3.3.2.4 CSC Chambers

The Cathode Strip Chambers, the CSC Chambers, are used at high rapidity in the range $2 < |\eta| < 2.7$ where the rate of incoming tracks would have been too high for the slower MDT technology. Each CSC unit is formed by four CSC planes grouped in trapezoidal units, (cf figures 1.10(b) and 1.25(a)). The internal structure of a CSC plane is shown in figure 1.25(b). CSCs are multi-wire proportional chambers with anode formed by a plane of wires arranged radially, i.e the wires are all parallel to the symmetry axis of the chamber which passes by the beam-axis. These wires are not read. The cathode planes are segmented in strips running in orthogonal directions on each side of the anode plane. While the strips measuring the first coordinate are mm wide, those that measure the second coordinate are cm wide and run parallel to the wires.

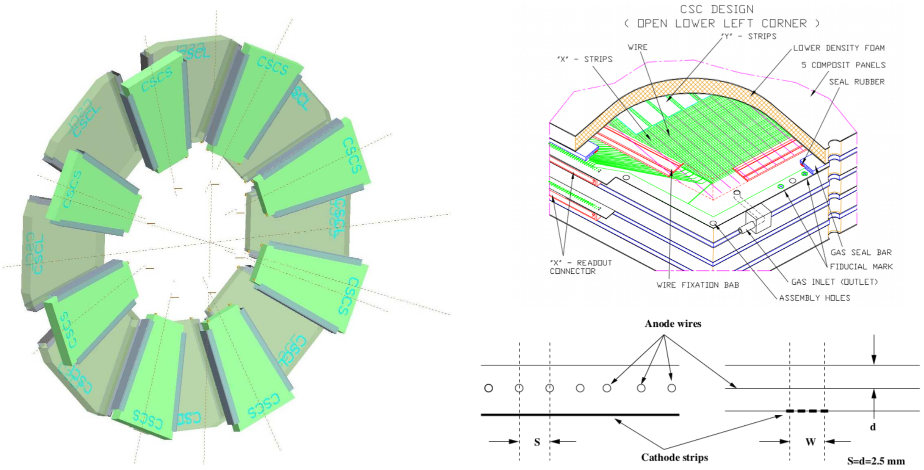

(a) (b)

Figure 1.25: (a) Layout of a CSC end-cap with eight small and eight large chambers; (b) Left: structure of the CSC cells looking down the wires.

The resolution on the second coordinate is of the order of ∼0.5 cm. The position measurement in the first coordinate is done by averaging signals received on the ∼5 first coordinate strips on which the charge distributes. A resolution of the order of ∼60 μm is achieved in this way.

The CSC resolution for first coordinate depend on the angle of incidence of the muon. This is why the CSC Chambers are mounted inclined toward the Interaction Point such that a muon of infinite momentum falling on the center of a CSC Chamber would be perpendicular to the Chamber surface.

1.4 Considerations on the Muon Reconstruction in ATLAS

As we have seen the three main sub-detectors, primarily the two tracker systems, can provide useful informations for the reconstruction of muons in ATLAS.

The reconstruction of muon track in the Inner Detector does not pose specific problems. On the contrary, by the very nature of this particle, the reconstruction efficiency of a muon is very high in the ID with unsurpassable measurements on the angles of the track. However the momentum resolution in the ID is limited by the lever arm of the detector and the magnitude of the magnetic field. A common rough number is that below 100 GeV in p_T, the momentum resolution of a muon in ATLAS is driven by the ID measurements, the identification of the particle itself being always from the Muon Spectrometer measurements. For this sort of comparison, it is relevant to note that the actual ID resolution has a strong rapidity dependence due to the solenoidal configuration of the field and to the mater distribution within the detector. Therefore even in this range of moderate momenta, the momentum measured in the Muon Spectrometer does contribute significantly to the overall measurement at high rapidity [8].

At higher momentum, the measurement of momentum of a muon rests primarily on the Muon Spectrometer. The reconstruction of a muon in this detector presents specific difficulties.

The main point is that the long trajectory of a muon in the detector is sparsely sampled as illustrated on figure 1.26.

The connection of these far distant sampled sections, of these Segments of the track, is made difficult by the highly inhomogeneous magnetic field. The propagation of a candidate muon over the large distance is doomed to be done numerically step by step, analytical means being confined to very rough estimates only.

This large distance propagation is a source of extrapolation errors, all the more important that, given the relatively modest magnetic field, the chased magnetic deflections are small.

A precise knowledge of the Geometry of the detector is mandatory to properly reconstruct muons. As seen above, at high momenta the momentum resolution would be completely spoiled if the reconstruction algorithm does not take into account not only the relative positions of the detection units, but also their internal deformations.

At lower momenta, the scatterings in the matter of the detector can easily mimic magnetic deflections. This is a source of abundant low momentum fake tracks which can only be reduced by adding to the kinematic variables of a candidate track, degrees of freedom accounting for these scatterings. In turn, this requires a precise description of the matter which can be crossed by a muon, from which,

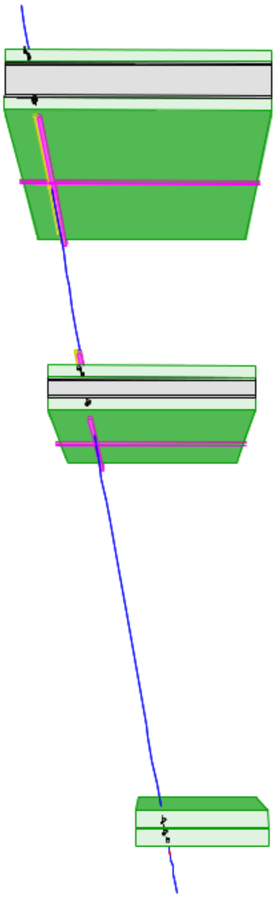

Figure 1.26: A simple reconstructed track within the Muon Spectrometer

---

[8] In a very early version of the Muon Spectrometer, the possibility of an Iron-Core End Cap Toroid was considered and wisely rejected on the basis of these considerations, the standalone resolution from a air-core End Cap Toroid surpassing the performance of the combination of the ID and the iron-core End Cap Toroid [32].

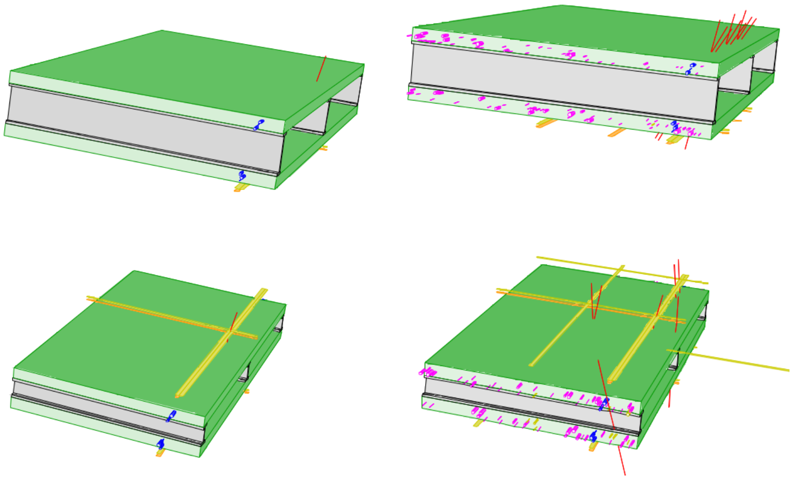
(a) (b)

Figure 1.27: (a) No neutrons and photons background (b) With neutrons and photons background

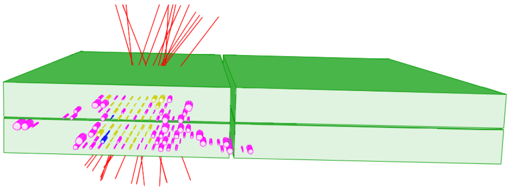

Figure 1.28: Muon track accompanied by shower

for instance, one can define properly located and weighted spots for scattering angles to be fitted along with the kinematic parameters of a candidate track.

Another issue is that there is no (but in the limited corner of the CSC Chambers) true local three-dimensional position measurement. The precise first coordinate measurement of the MDT Chambers is separated physically from the second coordinate measurement from RPC or TGC chambers. Therefore pattern recognition is mandatory to associate these measurements to form a fully three-dimensional local object, the track segment. Due to cost considerations, the redundancy offered by the local detection devices is limited (for instance only the innermost MDT Stations are equipped with four Tubes Layers per Multilayer), the pattern recognition can be badly perturbed by the activity in the vicinity of the true track.

The first source of these perturbing local environments is the neutrons and photons background induced by the interactions of primary hadrons produced in protons interactions, with the calorimeters and shielding. The low energy neutrons and photons which escape the absorption, can produce hits in the active devices. Some of these hits are not correlated tube to tube and simply harm by the confusing combinatory that they induce. The other part produces correlated hit in tubes harmfully mimicking genuine segment of tracks. Examples of the sort of confusion that this source can produce is given in figures 1.27.

An other source of confusion, is illustrated in the figure 1.28. At high momenta, the probability of local showers generated while crossing some dense material increases. These local showers can give many hits in the active devices spoiling the pattern of the genuine hits from the muon, up to the point that the track can not be reconstructed. The resulting effect is a reduction of the track reconstruction efficiency at high momenta.

The reconstruction of a muon in the Muon Spectrometer is naturally performed by fitting its position, angle and momentum at the entrance of the Volume of the Muon Spectrometer. By themselves, these track parameters are of little use for Physics analysis (although they can be of interest for some computation of visible transverse momentum of an event). It is necessary to express this measurement in terms of the parameters of the track as it emerges from the Interaction point.

This operation, the back tracking of the track measured in the Muon Spectrometer, involves propagation in the magnetic fields of the Calorimeters and the Inner Detector. In the process, the muon energy should be updated for the energy that the muon lost when is crossed these volumes in the other direction. This correction can be done with or without the assistance of energies measured in the calorimeters along the muon path, but in all cases it involves a parametrization of some average energy loss based on the nature and dimensions of the matter volumes crossed. The errors of the measurement are to be updated for the uncertainties in the energy loss correction as well as for the uncertainties on possible multiple scattering events which could have occurred on the muon path. All this requires a precise description of the Inner Detector and the Calorimeters, specially of the latter since by far, both energy losses and multiple scattering are more important in them.

The Muon Spectrometer Standalone Reconstruction consists in reconstructing a track from the Muon Spectrometer Stations hits and backtracking its to the beam axis.

At the end of the Standalone Reconstruction, one has a track at the level of the beam axis with all the errors on its parameters. If this track is real, it is very likely that there is also nearby a track which has been reconstructed in the Inner Detector. These two tracks are two independent measurements of the same muon and their combination can improve the precision of the measurement.

A combination procedure can be to perform a common refit of all the primary signals of the detection devices which were used to perform the two independent track measurements. Alternatively one can do a simple statistical combination of the two tracks measurements. Actually under the assumptions that the errors are small enough there is no gain to expect from a common refit with respect to a simple statistical combination. Of course, a so definitive statement is doomed to be wrong sometimes. Still it fails so rarely, in occasions so easy to fix, that it is exact for all practical purposes. The key point is that the track measurements from a sub-detector with the errors in the form of covariance matrix is a faithful and, above all, complete summary of the signals of the basic detection units of the sub-detector.

Because the reconstruction of a muon in the Inner Detector has a very high efficiency, it is very likely, provided that the reconstruction algorithm in the Muon Spectrometer does a decent job, i.e does not produce too much fake tracks, that a back tracked track will be successfully and appropriately combined with an Inner Detector track. The problem is that it happens that there is no Muon Spectrometer track to play the game of the combination. There are two circumstances which limit the reconstruction efficiency within the Muon Spectrometer:

- the coverage of the Muon Spectrometer Layout is imperfect. Specially in the configuration in which Data were collected at first, some places are so poorly covered (EE Stations area) that only one Station is on the path of a muon. There is only one Track Segment in the event and no track can be reconstructed.
- at low momentum, as illustrated in figure 1.29, the trajectory of a muon becomes excessively curved, and soon it is effectively impossible to reconstruct it in its totality. As a consequence, the track reconstruction decreases steeply for p_T below say 7-8 GeV . Still Track Segments can be found in the Innermost Stations at the entrance of the Muon Spectrometer before the muon enters too far in the Muon Spectrometer and starts its uneasy path.

In both circumstances, no full track can be reconstructed. However the identification of the muon is possible, although with a lesser confidence, on the basis of the few segments let by the muon: an Inner Detector track extrapolated in the Muon Spectrometer will be identified as a muon if it matches some track segments there.

Though very efficient, such a "Tagging" identification is less solid than an identification based on the combination of two full tracks. Indeed there is a risk to build fake candidates by associating erroneously one of the many Inner Detector tracks to an unrelated track segment in the Muon Spectrometer. Such an algorithm should be used with care and under strict control.

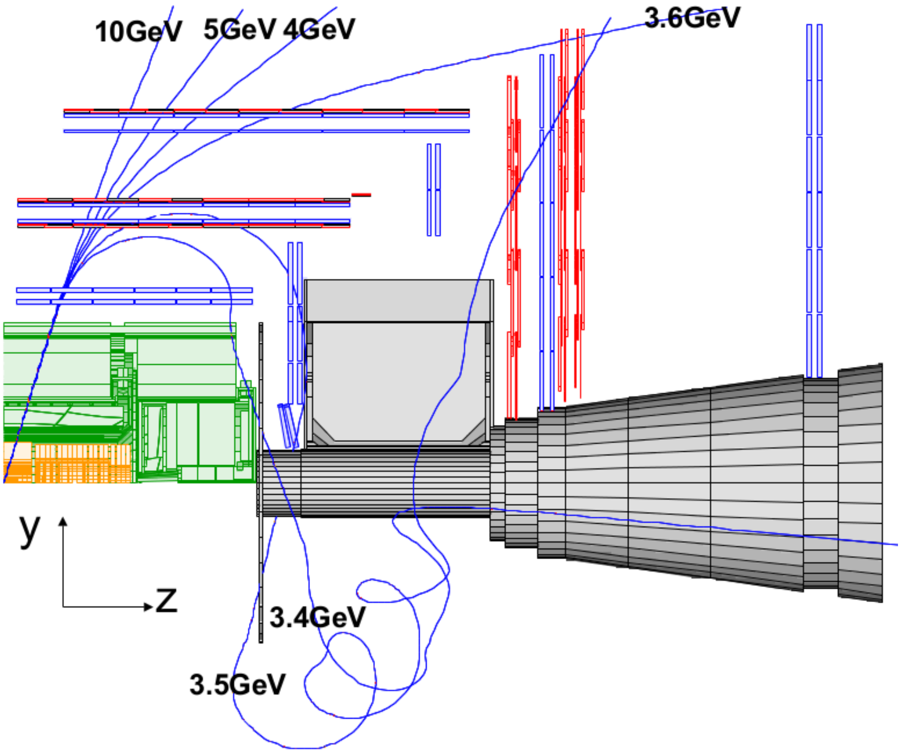

Figure 1.29: Views of some Muon trajectories in the Muon Spectrometer, illustrating the difficulties of reconstructing the trajectories of low momentum muons.

In the chapter 3 I will discuss in some detail three Muon reconstruction algorithms to which I contributed:

- *Muonboy* a Standalone Reconstruction
- *Staco* a Combined Reconstruction of the Muon Spectrometer and Inner Detector tracks
- *MuTag* a Tagging identification algorithm of the Inner Detector tracks

But before I am going to review in the next chapter the work which has been done on the Detector Description, an issue of central importance for the reconstruction

Chapter 2

Detector Description of Muon Spectrometer and ATLAS

To have a precise Description of the detector is a crucial issue for the reconstruction.

Clearly, one needs the positions of the elements of the active units which are fired. This is first needed to arrange these fired elements, these hits, in patterns consistent with the passage of a particle, i.e. in segments of tracks in the active units. Actually a great precision on these positions is needed when in a second stage these segments are assembled in a candidate trajectory in order to measure the minute curvatures of the high momentum muons in the Muon Spectrometer. To fulfill these needs one has only to transmit to the reconstruction algorithm the positions at the same time as one gives it all the other informations concerning the hits, such as say drift times. In this perspective, it is good enough to pass so to say the geometry with the hits.

This scheme was actually the one followed for the very first design studies. This was good enough for a first evaluation of the Muon Spectrometer performance. However while the understanding of the working conditions of the actual detector progressed, it became clear that the issue of the fake muons rate imposed a more ambitious scheme.

Indeed as we have seen, in the Muon Spectrometer the trajectories are sparsely sampled in Stations far apart. In addition, the proton collisions induce significant neutrons and photons backgrounds generating hits here and there all around the apparatus, possibly forming apparently consistent local segments of tracks in Stations. These two circumstances make that the reconstruction algorithm can be fooled and can reconstruct a false track from segments erroneously associated in the same trajectory.

Generally such a fake track is globally inconsistent. Indeed connecting unrelated track segments, its trajectory over the whole detector has a good chance to cross also station units where the hits that one would have expected to find are actually absent. Therefore if the reconstruction program knows all the positions of the active elements fired or silent, it can spot these inconsistent trajectories and reject fake muons.

For the detailed studies of the ATLAS experiment finally approved, the rate of fake muons became a central issue of the reconstruction performance. It became clear that the reconstruction algorithm had to have access to the full geometry of the Detector and had to know about detection units whether they are fired or not. Soon the description was extended to the passive material in the whole ATLAS Detector. This allowed to account for the Multiple Scattering and Energy loss in the Muon Spectrometer and to back track the Muon Spectrometer tracks through the Calorimeters down to beam axis.

The two next sections briefly describe two schemes for the Detector descriptions to which I contributed, the *AMDB* and *AGDD* schemes. The actual descriptions of the Muon Spectrometer for the simulation and the reconstruction are based on these schemes.

2.1 AMDB

Marc Virchaux, Laurent Chevalier and I designed the first version of the ATLAS Muon Detector Description Database (*AMDB*) to fulfill the reconstruction needs. Over the years the design and the power of *AMDB* improved greatly thanks to the involvement of many our ATLAS colleagues among who, Stefania Spagnolo, Daniel Pomarède, Daniel Lellouch, Kétévi A. Assamagan, Florian Bauer, Pierre-François Giraud and Jochem Meyer [33].

AMDB allows to collect and to organize, the thousands of numbers coming from a myriad of disparate sources (Engineers drawings, Excel and paper sheets, people interviews and confessions) that are needed to describe the Muon Spectrometer. Providing in a structured and reliable way the primary numbers on the actual Layout, needed for the Reconstruction and Simulation, *AMDB* played a crucial role in the early developments of these softwares. It was also a means to discuss in effective terms the incorporation of the outputs of the Alignment System Software, being the corrections of the positions of the detection units (Alignment proper) or the correction of their shapes (deformations).

AMDB is fundamentally a format to organize numbers plus some light code to access them. However since these numbers have to be interpreted to be useful, a set of non trivial codes are provided which compute the actual positions of the various described elements. These codes form a set of packages, the *Amdcsimrec* packages, part of the ATLAS software. The different implementations interpreting the same *AMDB* numbers (*Amdcsimrec*, Reconstruction, Simulation, Alignment) were actually checked against each other continuously over all the years of ATLAS preparation. Far to be an unnecessary duplication of work as an average manager would say, any one who has ever had the questionable chance to work on such as complex issue as the Detector Description, will understand that this is a powerful means to debug software as the facts did prove many times in ATLAS.

Working on *AMDB* is a hard job of collecting thousands of numbers dispersed all around. The worker pain is alleviated by the wonderful views of the Detector that he gets in return from the 3D Visualization Software *PERSINT* [34] that Marc Virchaux started to develop at about the same time we started *AMDB*. Here, as elsewhere in this document, I will use these views to illustrated my points.

2.1.1 Brief Description of the Structure of *AMDB*

The *AMDB* format organizes numbers in a flat file describing active and passive materials. Hereafter, I briefly describe the structure of the active material part, i.e of the Stations of the Muon Spectrometer (cf table 2.1). More details can be found in the *AMDB* documentation [33].

`D entry`	type of Station ; lists and defines its components (shapes, dimensions, positions)
`W entry`	internal structure of a Station component (technology dependent)
`H entry`	cut out of a Station; refer to a `D entry`
`P entry`	Station placements; refers to a `D entry`, possibly to a `H entry`
`A entry`	Alignment corrections of a given Station
`B entry`	Deformation corrections of a given Station
`I entry`	Internal Alignment corrections for a given CSC Station

Table 2.1: *AMDB* `Entries` types for the description of Muon Spectrometer Stations

Extensive use of the many similarities that exist between the various Muon Spectrometer Stations in their shapes and in their internal structure, is made in order to reduce the numbers of distinct elements needed for a complete description.

Muon Spectrometer Stations data are organized around a two levels structure: Station or `D entry`, and Inner Structure or `W entry`.

The Station level, the `D entry`, defines the Station in its own local axis system as a stack of units (MDT, RPC, ...) giving the shapes of these elements, their dimensions, their relative positions and for each of them a pointer to the Inner Structure level, to a `W entry`, specifying the details of its internal building.

The shape definition is flexible enough to handle the rectangular shape of MDT Barrel and RPC units (cf figure 2.1(a)), the trapezoidal shape of MDT End Cap and TGC units (cf figure 2.1(b)) or the coffin-like shape of some CSC units (cf figure 1.25(a)).

Many of the physical Stations of the Muon Spectrometer are identically built. They are described by the same `D entry` which, therefore a type of Station, not a physical Station.

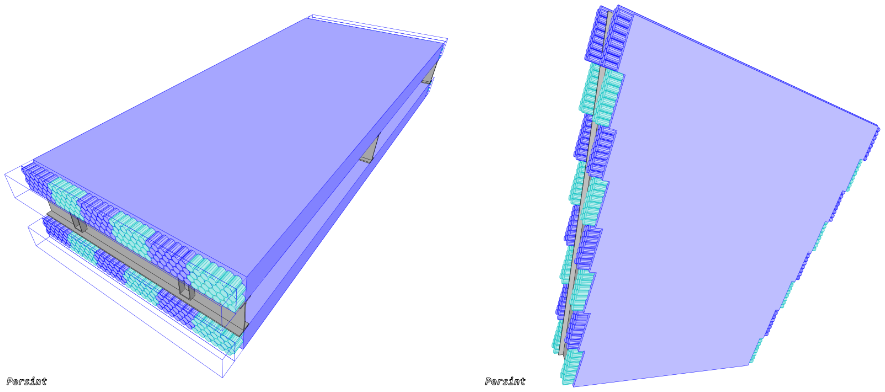

(a) (b)

Figure 2.1: *AMDB* description of a Barrel (a) and End Cap (b) Chambers

The Inner Structure level, the `W entry`, is Technology dependent.

For instance, a `W entry` for a MDT Multilayer contains informations such as the number of Tubes Layers, the values of the inner radius and of the thickness of the wall of the MDT tubes, the pitch of the tubes within a Tubes Layer and the relative positions of the Tubes Layers in the local MDT Multilayer axis system.

The `W entry` for RPC, TGC and CSC Technologies are similar, only sometimes more extended as for instance, in the case of TGC owing to the more complex structure of this Technology. A flavor of the described internal structure for MDT and RPC units is given on figure 2.2

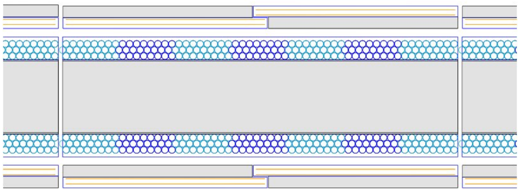

Figure 2.2: *AMDB* internal structure description of a Barrel Chamber

Parallel to the `D entries`, runs an other tree-like structure formed by special entries, the `H entries`, which describe the cutouts that are made in the detection units for e.g. the optical paths of the Alignment System. In the local axis of a Station, a `H entry` defines which elements of a given `D entry` are cut and the parameters of the rectangular beveled volume to be removed (cf figures 2.3). Many of the physical Stations which are identically built, differ only by the actual cutout that is dug in them. In these cases, there are different `H entries` referring to the same `D entry`.

Finally there are the positioning entries, the `P entries`. A `P entry` refers to a particular `D entry` and possibly to a particular `H entry`, and describes the simultaneous positioning of multiple copies of a particular Station type with the same cutout, at a given radius from and position along the beam-axis, in a set of ϕ sectors at once.

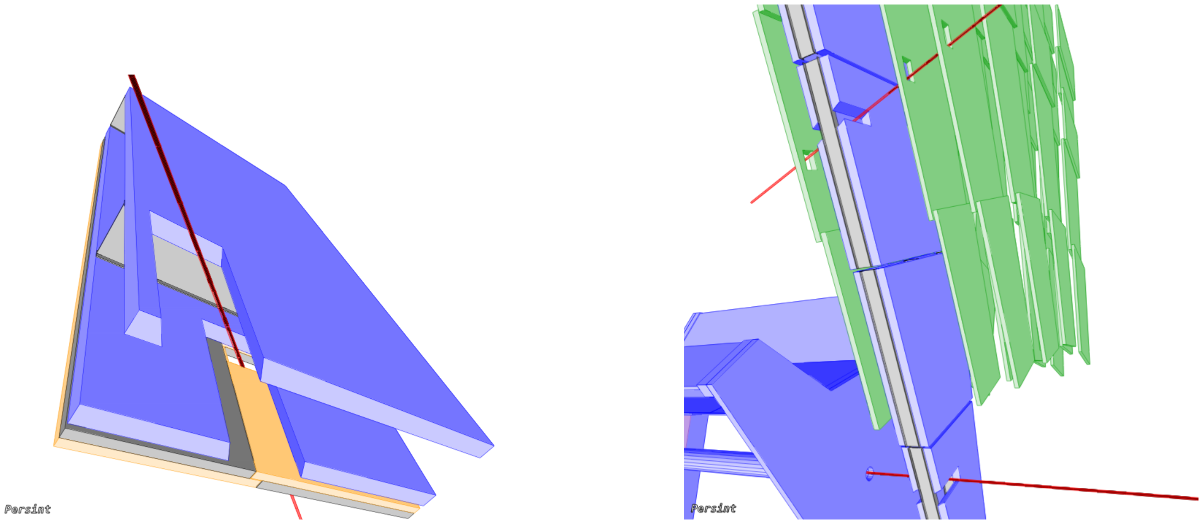

Figure 2.3: Cut outs in MDT, RPC and TGC Chambers in Barrel

A set of identifiers allows to navigate in the tree of the above entries. For instance to each physical Station is associated a name (e.g. BIS, EOL, ...), and two indices specifying its ϕ sector and its rank in the Station segmentation along the beam axis in Barrel region or along the distance to the beam axis in End Cap region.

To this set of identifiers for a physical Station is associated an index pointing to a `D entry`. In turn for a given `D entry` are associated indices pointing to the different elements forming it, and so to the different `W entries`. If a given physical Station is cut out, then the set of its identifiers allows also to reach a `H entry`.

This identifiers scheme, up to insignificant differences, is the one used in the ATLAS Muon Spectrometer software [35].

Coupled with a description of the passive material of the detector not discussed here, the *AMDB* organization of the data of the geometry of the Stations, allowed to perform many of the Muon Spectrometer Layout evaluation and optimization studies such as the optimization of the Number of MDT tubes layers per MDT Multilayer [36] or impacts on Momentum resolution of an imperfect acceptance coverage of various Layouts [37, 38].

2.1.2 Alignment and Deformation in *AMDB*

Some dedicated entries, the `A entries` are designed to carry the outputs of the Alignment System software.

A given `A entry` allows to get the corrections of the position and orientation of a given physical Station as shown on figure 2.4(a). This functionality can be used to generate randomly misaligned layouts as the one shown on figure 2.4(b). These "random" Layouts were extensively used in studies of the effects of misalignment on the resolution on the momentum of a muon or on the mass of a resonance as shown on figures 2.5(a) and 2.5(b) respectively [39–41].

The Alignment system provides also measurements of the deformations of the shapes of the detection units. These outputs are entered in dedicated entries, the `B entries`, of *AMDB*. There are many types of deformations such a banana deformation type or twist deformation type as shown on figures 2.6(a) and 2.6(b) respectively.

Some corrections of the internal arrangement of the elements forming a Station are possible using the `A entry` as illustrated in figure 2.7. This option could be used to describe relative misalignment

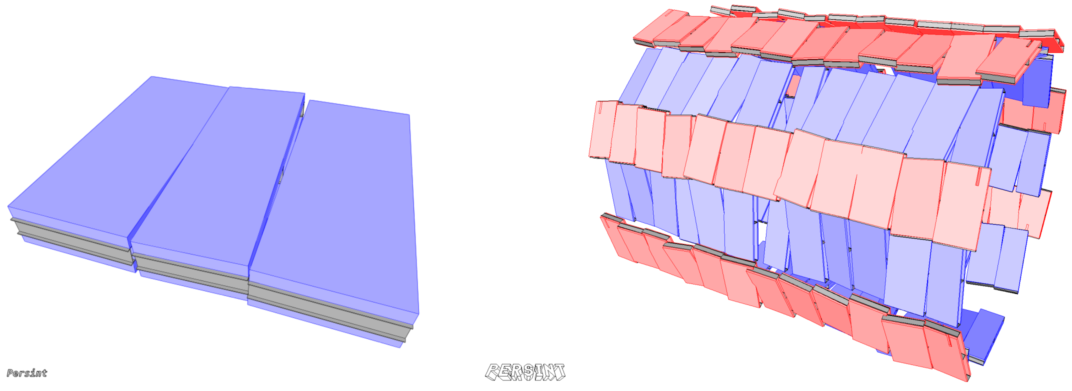

(a) (b)

Figure 2.4: Examples of *AMDB* misalignments; (a) Three Barrel Chambers, the middle one has non nominal positions and orientation (b) Persint view of the Outermost Barrel Stations with random rotations added on their nominal positions; for the effects to be visible, the unrealistically large value of 50 $m$rad has been used for the width of the Gaussian distribution of the added random angles.

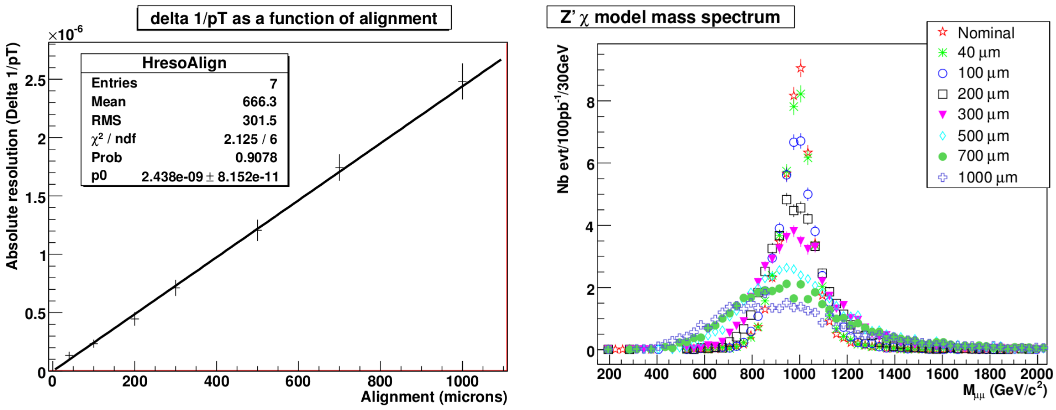

(a) (b)

Figure 2.5: (a) Contribution to the momentum resolution as a function of the misalignment in position (from [40]). (b) Reconstructed invariant mass of Z' events produced with the χ model, decaying in pairs of muons reconstructed with *Staco* Combined Reconstruction, for various misalignment errors (from [39]).

in position and in orientation of the MDT Multilayers forming an actual MDT Station. Such informations on the "As built" geometry of actual MDT chambers have been collected at CERN for about 15% of the MDT Stations in Quality control tests using X-ray tomography [42]. Exploratory studies in the context of a Qualification task [43] did show the interest of these data for the reconstruction and some progress were made in incorporating them in *AMDB*.

The MDT Chambers construction was in general of very high quality, and to ignore in the reconstruction the "As built" MDT geometry, as it was the case for all the Run 1 period, has no major impact.

On the contrary, for the CSC Stations the corrections of the positions and orientations of the internal elements with respect to the nominal design can not be ignored without a major degradation of the performance. These corrections are simple rotations and translations of the planes forming the active layers of the CSC. Although they do not fit either in the `A entry` scheme, they are close enough to be dealt with a very similar but CSC specific entry, the `I entry` and the effects of these corrections are propagated down to reconstruction without a hitch.

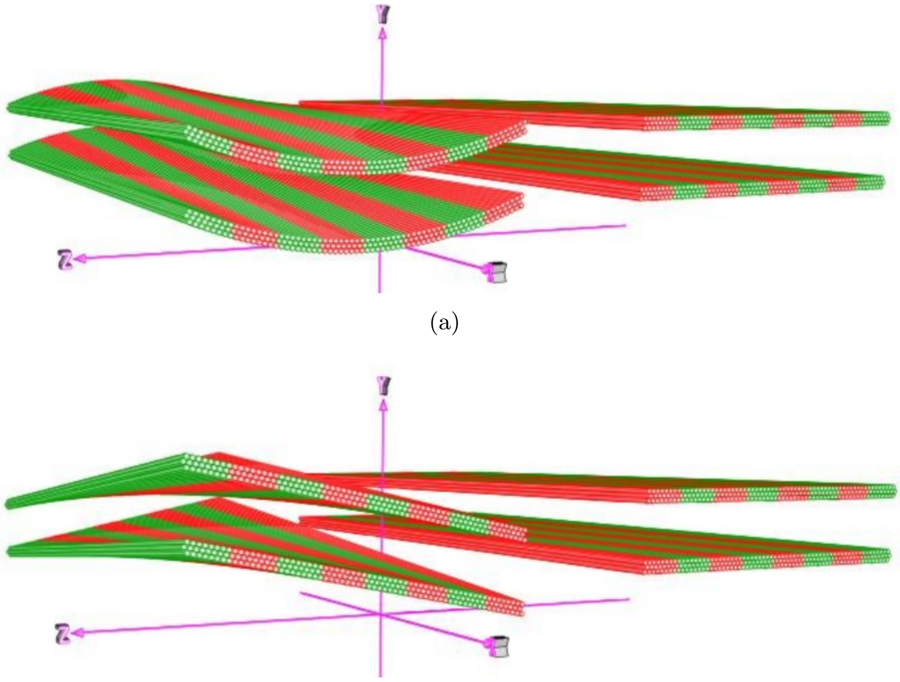

(a)

(b)

Figure 2.6: (a) *AMDB* banana-like deformation: the tubes ends planes sag out and take parabolic shapes; (b) *AMDB* twist deformation: a twist is applied along the tube nominal axis on the Station volume ; deformations is applied on the left Station.

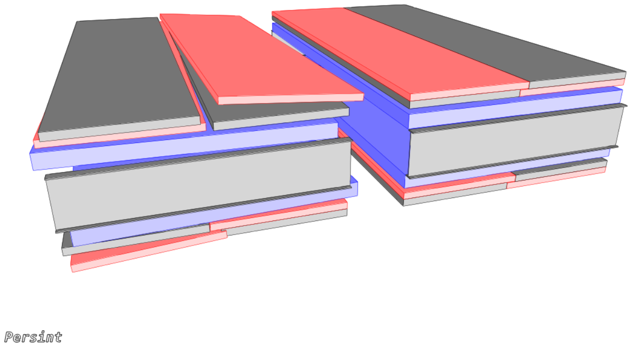

Figure 2.7: Example of *AMDB* misalignment of the internal components of a Barrel Station

2.2 *AGDD*

2.2.1 Early days

At the end of 1999, Marc Virchaux and I joined some of our ATLAS colleagues, among others, Christian Arnault, Stan Bentvelsen, Steven Golfarb, Julius Hrivnac, RD Schaffer and Christophe Lester, in a new Detector Description project, the ATLAS Generic Detector Description (*AGDD*) project, based on XML, the eXtensible Markup Language [44].

Although this use of XML is quite common now-days [45], it was very new at that time and the design and development of *AGDD* has been a very creative and exciting period. Very soon, the basic elements of *AGDD* were in place, almost all the sub-detectors of ATLAS were described at least at the level of solid prototyping, and Visualization, Reconstruction and Simulation applications using these *AGDD* descriptions were available.

Brief description The basic idea of *AGDD* is to have a very explicit description of the Geometry in terms of Geometry primitives and their relations, couched in very human readable XML files, so that the Description of the Geometry is totally independent of the applications that use it.

At the bottom of the elements that *AGDD* defines, are basic volumes such as box or tube. Some of them are shown in figures 2.8. The material of a volume can be defined and chosen within a list of materials, itself defined in a separate section. Also to sort out passive and active volumes, a “sensitivity” status of a given volume can be set.

A bunch of these basic volumes can be placed together in a common axis system. *AGDD* provides various ways to do these placements, some directly inspired from those of *AMDB* (cf figures 2.9). The simplest of the results of this step is an element called `composition` which is essentially the axis system with respect to which the volumes placement is done. Contact with the memory saving *GEANT 4* concept of mother volume, can be made at this stage, by equipping a `composition` with an envelope, a boundary volume which can be a basic *AGDD* volume or a volume resulting from boolean operations, a boolean *AGDD* volume. *AGDD* provides boolean volumes of types `union`, `subtraction` and `intersection`, (cf figures 2.10).

These `compositions` and boolean volumes can be positioned as well along with other *AGDD* volumes . This leads to tree-like structures allowing the description of complex Geometries. Elements named `sections` are provided that allow to map the various sub-detectors domains by encapsulating separately the descriptions of independent large structures.

AGDD applications The syntax and structure of *AGDD* is very effective and user friendly. To write *AGDD* files describing complex structures is actually quite easy. In any respect, it is much easier and efficient than to code the same geometry with C++ objects.

For the Muon Spectrometer, *AMDB* provided the sources for the *AGDD* description and all active and passive elements described in *AMDB* went available in *AGDD* files within a year. The figures 2.11 show for instance the Muon Spectrometer Stations as described in *AGDD*. Soon this was also the case for a large part of the other ATLAS sub-detectors [46–49].

Some applications using AGDD started to be developed.

The first of them were 3D Visualization applications. Along with *GraXML* developed by Julius Hrivnac [50], there was *PERSINT* [34] from Marc Virchaux which, backed with the great experience

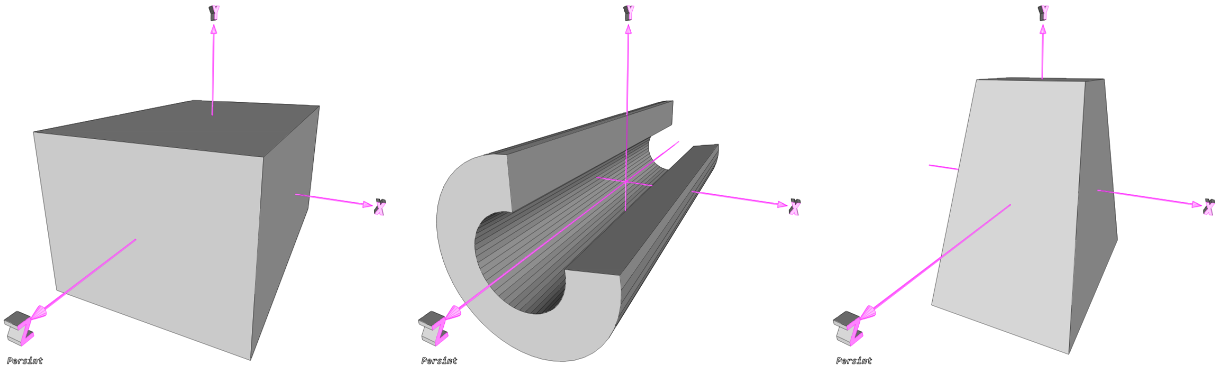

(a) A `box` volume (b) A `tubs` volume (c) A `trd` volume

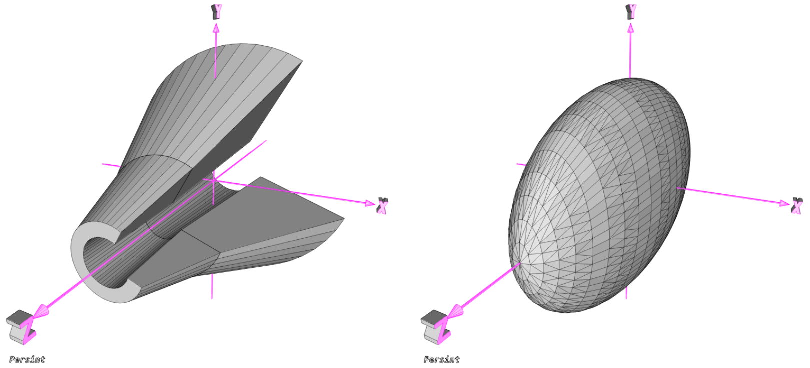

(d) A `pcon` volume (e) A `elipso` volume

Figure 2.8: Examples of *AGDD* basic volumes

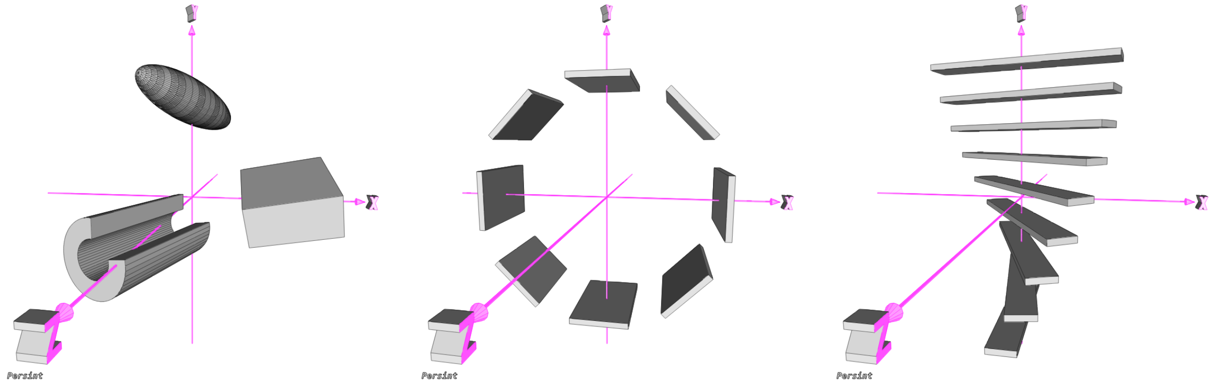

(a) Three volumes positioned and oriented individually (b) Positioning in Phi on eight copies of a single volume (c) Stacking positioning setting only the distance between objects stacked in the Y direction

Figure 2.9: Examples of *AGDD* placements

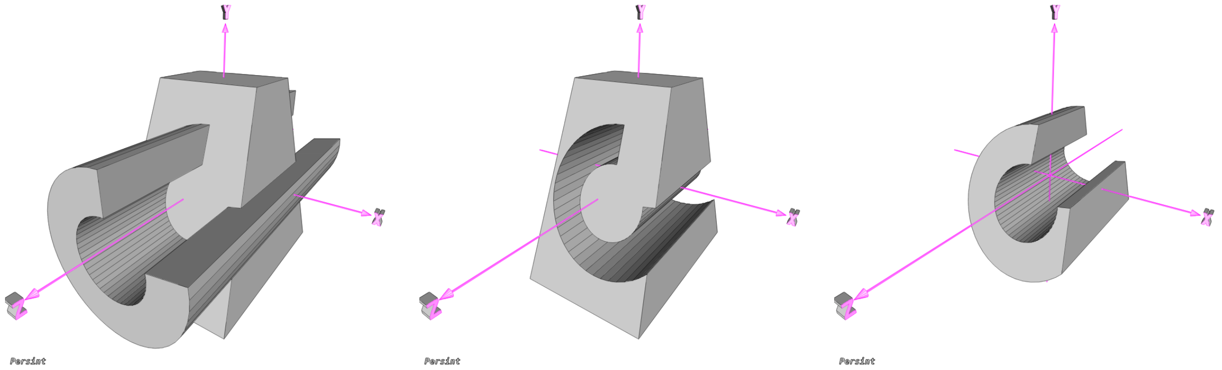

(a) A `union` volume (b) A `subtraction` volume (c) A `intersection` volume

Figure 2.10: Examples of *AGDD* boolean volume

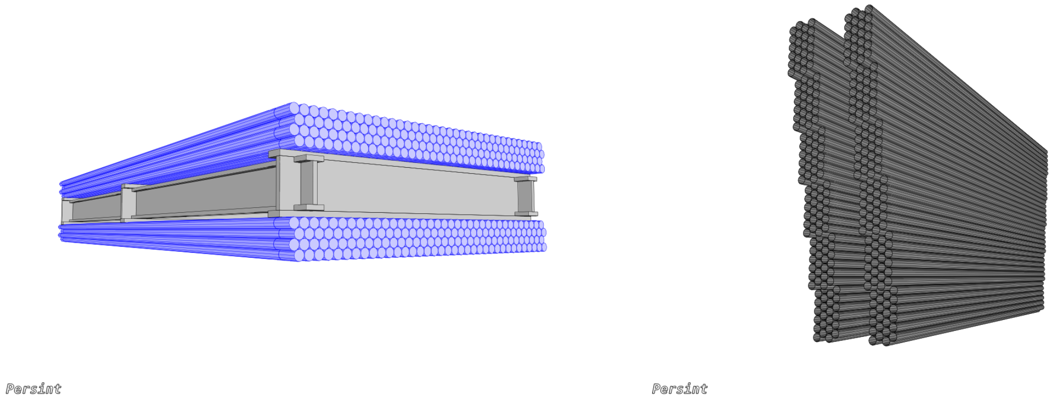

(a) (b)

Figure 2.11: Muon Spectrometer Stations described with AGDD. First a `tubs` element is created. Then multiple copies of it are done to form a Layer `composition` . This layer is copied multiple time to form a Multilayer `composition`. Then this Multilayer is copied twice to form a Station `composition`.

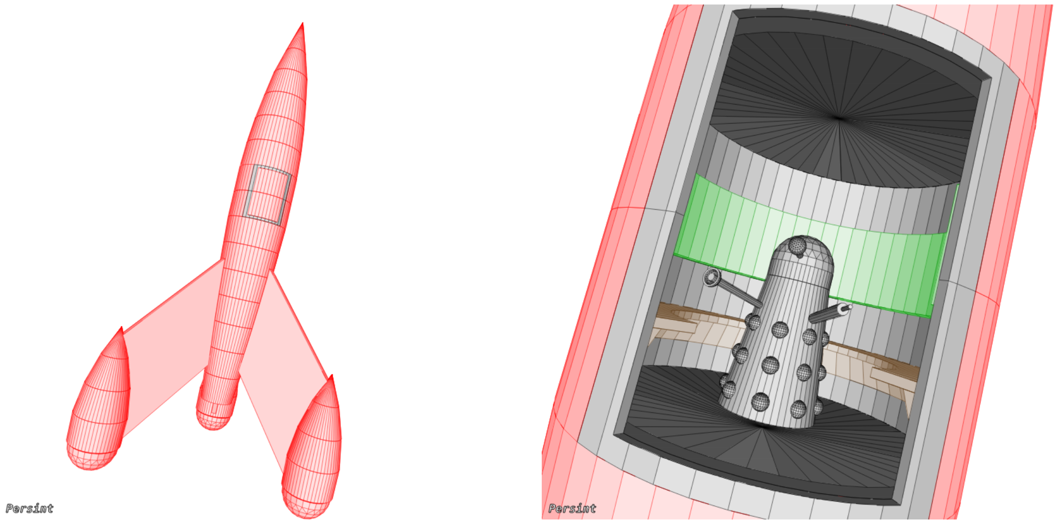

(a) A Rocket (b) A Dalek in the Rocket

Figure 2.12: This too was done with AGDD. With the great power of *AGDD* and *PERSINT* comes the great difficulty to not spend a lot of time on things of questionable interest

from *AMDB*, provided very useful functionalities [1]. They were instrumental for the debugging of an *AGDD* description in construction.

On the reconstruction side, *Muonboy* is the only application which can use directly *AGDD* as far as I know, .

For what concerns simulation, there were some *GEANT 4* applications developed to use *AGDD*. Among them is my own application `G4AGDD` [51]. With `G4AGDD`, I prototyped an automatic building of a *GEANT 4* Geometry from *AGDD* as a proof of principle that its was possible to do this in a sensible way.

The top node of an *AGDD* hierarchical structure represents the "World" in which all the described elements are ultimately placed. The easy way is to read this hierarchy as a tree and to position physically each of the volumes individually. This is particularly inefficient in terms of memory usage. But an *AGDD* hierarchy is not a tree since some volumes are identical up to their positioning within others. This maps the difference *GEANT 4* between Physical and Logical volumes. Taking account of this, the building of a *GEANT 4* geometry can be done efficiently with an algorithm with visits recursively an *AGDD* hierarchy, building on flight when needed, the *GEANT 4* objects alter egos of the *AGDD* ones. This can be reversed and one can translate *GEANT 4* Geometries in *AGDD* Geometries, i.e dump *GEANT 4* Geometries in *AGDD* files. This back and forth game between *AGDD* and *GEANT 4* Geometries can be played with the Geometry of any other packages. For instance I implemented it for the *TGeo* Geometry of *ROOT* [52], translating *AGDD* Geometries in *TGeo* Geometries and vice versa.

2.2.2 Dark ages

The *AGDD* project came to an abrupt end in 2002 when the ATLAS computing management decided that the ATLAS software had to use a Detector Description package, the *GeoModel* [53, 54]. This package is a library of geometrical primitives very close to the *GEANT 4* ones with some memory optimizations.

This decision was both good and bad. It was good since it provided an uniform way to handle geometrical informations for the Reconstruction and Simulation applications.

However for the Detector Description proper, the decision missed the whole point of the idea motivating *AGDD*. We went back to old schemes [55] which identify on one hand, a set of C++ codes each dedicated to a specific task, e.g "Build a Toroid", and on the other hand, primary numbers, stored almost structureless in some format, that are needed to feed these codes.

For active elements of the Muon Spectrometer, this was viable since, as already said, they form a very structured almost regular set of elements. For the passive part of the Muon Spectrometer, this was a very serious handicap since this meant that the passive part had to be handled by a set of specific codes, as numerous as there are dead matter volumes, i.e really a lot, fossilizing a particular level of detail of the description.

To decide to code the passive material of the Muon Spectrometer in C++ objects was necessarily leading to a hardly updatable and maintainable heavy software, doomed to lag behind reality and, ultimately, doomed to stasis.

The *AGDD* description for the dead material of the Muon Spectrometer continued to be refined

---

[1] in particular a tool of detection of clashes between volumes, extremely useful to find minutes inconsistencies which tend to destabilize *GEANT 4* simulations.

for some time. But unfortunately it was used only in *Muonboy*. As it should have been anticipated, the *GeoModel* codes for the Muon Spectrometer dead material started quietly to fossilize.

2.2.3 Renaissance

These *AGDD* dark days ended in 2008 when Andrea Dell'Acqua and Laurent Chevalier, soon joined by Jochem Meyer, decided to cure this appalling situation, and to raise high the *AGDD* banner again, at least for the Muon Spectrometer dead matter [56, 57].

Their fully generic application, `AGDD2Geo`, does build a *GeoModel* Geometry from an *AGDD* Geometry which is then moved to *GEANT 4*. As `G4AGDD` but more efficiently, `AGDD2Geo` can also build directly *GEANT 4* and *TGeo ROOT* Geometries.

At the end of an impressive update of the *AGDD* Geometry, the whole set of elements of the Muon Spectrometer dead matter has been described and included in the ATLAS simulation. This is illustrated by the impressive figure 2.13 from [56], which shines as the old *AGDD* dream come true.

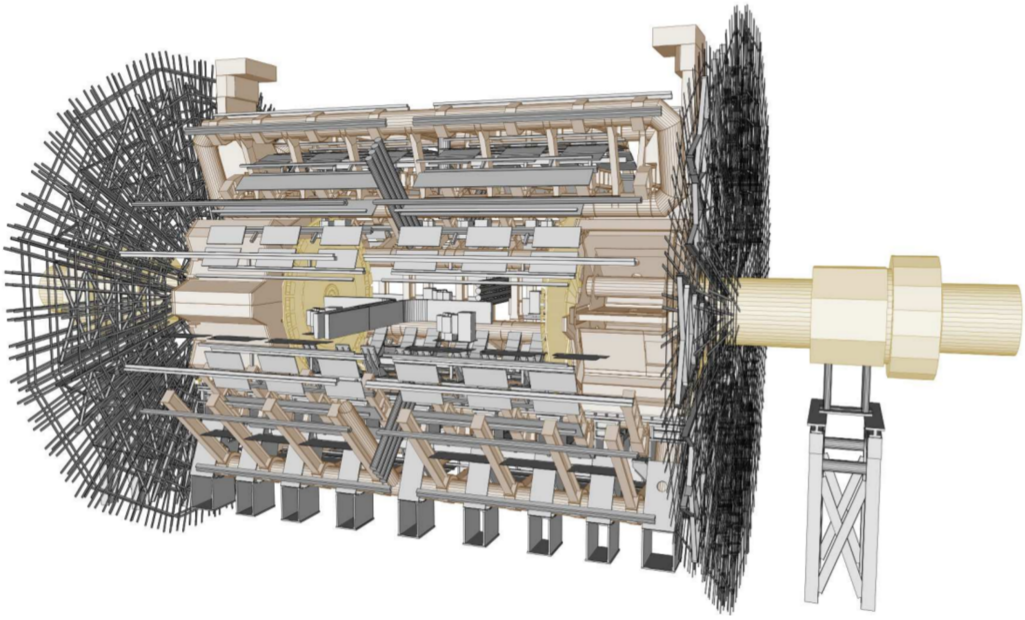

Figure 2.13: Support structures as included in the muon spectrometer detector layout. All volumes are implemented in terms of AGDD-XML elements. (from [56]).

2.3 Conclusions

The detector description is an issue of crucial importance for both simulation and reconstruction. It requires a very significant investment for the few but distinguished individuals who get involved in it.

The development of *AMDB* scheme allowed to address very early the optimization of the Muon Spectrometer and well as to structure the alignment and reconstruction softwares. Since then it provides the only description of the active volumes.

The *AGDD* scheme allows to describe in a very generic and effective way any geometry. After a long eclipse, its sound philosophy now prevails in the ATLAS simulation of the Muon Spectrometer passive material.

Chapter 3

Muon Reconstruction in ATLAS

In this chapter I describe the reconstruction algorithms that form the *STACO* chain.

The core of this chain is the *Muonboy* algorithm. It is described in the section 3.1. This algorithm performs the reconstruction of muon candidates in Standalone mode, i.e from the signal of the devices of the Muon Spectrometer exclusively.

Briefly its strategy is to form in a first stage segments of tracks within the Stations and in a second stage to associate them in a trajectory of a muon candidate, the kinematics of which is fitted to match the segments. As we have seen, due to the low redundancy in the measurements of a muon trajectory, and to the background activity in the detector, there is a risk to associate erroneously unrelated segments and to build a fake muon candidate.

From the very beginning, *Muonboy* has aimed to maintain the rate of these fake muons as low as possible while providing the highest possible efficiency of the reconstruction of true muons. This motivated in particular the important investment in the Detector Description issue as it was discussed in the previous chapter

The second element of the chain is the *Staco* algorithm. It performs the combination of the tracks reconstructed separately in the Inner Detector and in the Muon Spectrometer. It is described in the section 3.2.

In comparison to *Muonboy*, *Staco* is very simple: from the set of tracks reconstructed on one hand within the Muon Spectrometer and on the other hand within the Inner Detector, *Staco* performs a simple statistical combination of the two independent measurements of the parameters of a track.

This simple algorithm works excessively well. That it does so well with only few cuts on the Inner Detector associated tracks and simple cuts on the χ^2s of the combined tracks, is a consequence of the quality of the measurements of the track parameters performed in both sub-detectors and, as importantly, of the high purity of muons reconstructed by *Muonboy*.

Indeed given the huge number of Inner Detector tracks, it is quite easy to identify erroneously one of them as a muon, if one is willing to associate such tracks with any junk objects “reconstructed” from some vague activity in the Muon Spectrometer. Therefore it is excessively important when it comes to the combination of the two sub-detectors that one is extremely strict on the quality of the reconstructed tracks that one assembles.

The last element of the chain is the *MuTag* algorithm. It identifies an Inner Detector track as a muon on the basis of the good matching a Muon Spectrometer segment with the extrapolation of the track. It is described in the section 3.3.

MuTag aims to recover inefficiencies on weak spots of the Muon Spectrometer acceptance and at low momentum. By nature this algorithm is prone to produce fake candidates. Its action is therefore severely limited. It is allowed to run only on the left-overs of the previous stage and strict conditions are put on the matching of the Inner Detector tracks and the Muon Spectrometer segments. In this way the *MuTag* goals are achieved while maintaining a high purity of the muons candidates.

3.1 Muon Reconstruction in Muon Spectrometer: *Muonboy*

As we have seen in details in section 1.4, the reconstruction of muon in the ATLAS Muon Spectrometer has to cope with specific difficulties: sparsely sampled trajectories; high inhomogeneity of the magnetic field; low redundancy of local measurements; high level of neutrons and photons background spoiling true tracks and creating fake ones; complexity of the layout and variety of chambers types ; detector matter highly non uniformly distributed; no local true three-dimensional information.

Muonboy has been designed to cope with these difficulties. Its algorithm, described with more details in the next sections, can be summarized in four main points:

- identification of Regions of Activity (ROA) through the RPC/TGC systems;
- reconstruction of local Track Segments in each Station of these ROAs;
- combination of Track Segments of different Stations to form Muon Track Candidates using three-dimensional tracking in the magnetic field;
- global track fit of the Muon Track Candidates using individual hit information.

3.1.1 Regions Of Activity

Regions of Activity (ROA) in the (η, ϕ) space are found using information from the Trigger Chambers. The size of the ROAs is roughly $\Delta\eta \times \Delta\phi = 0.4 \times 0.4$. They are centered on the intersection of RPC or TGC hit measurements in the two different coordinates, from any Stations belonging to the same sector in ϕ.

All Chambers intersecting with the ROAs are selected for the Muon Track reconstruction.

3.1.2 Track Segment Reconstruction

Track segments are reconstructed by forming pairs of hits, one of the hits belonging to a Multilayer and the other hit to the opposite Multilayer from the same Station or from the Stations contiguous in the η direction. A Track segment is formed using hits from Stations neither from different sectors in ϕ nor from Barrel and End cap simultaneously.

The hit pair is required to point loosely to the interaction vertex in order to suppress background tracks and combinatorial background. All possible candidates of each hit pair are extrapolated to the remaining tubes of the MDT Chamber and matched with the hits in these tubes.

The Track Segments are straight-lines as illustrated in figure 3.1. This, over the thickness of a Multilayer, is an acceptable approximation of the trajectory for any momentum to be reasonably considered.

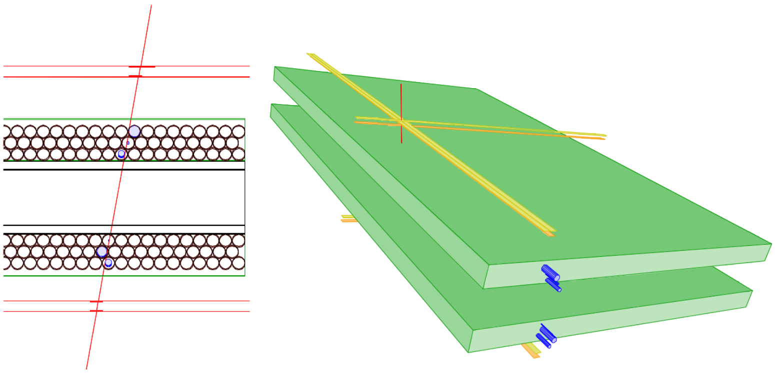

Figure 3.1: *Muonboy* Track Segment

The quality of a segment is evaluated using a "penalty factor" χ^2_P, which deviates from a purely statistical χ^2 (cf figure 3.2) to take into account the following effects:

- masking effect by hit from δ-ray or neutrons and photons background; Tube hits with a drift time shorter than that expected value have a lower contribution to χ^2_P than hits with a drift time longer than the expected value, i.e the absence of an expected hit is less damaging for the likelihood of the candidate in the making, if it is possible that the expected hit has been masked by an earlier hit;
- non uniformity of detection efficiency of individual MDT tubes; The higher the tube efficiency assumed, the larger the contribution to χ^2_P, of tubes which are crossed by the extrapolated candidate track segment, but which do not contain a valid hit.

As we have seen, signal should be corrected for propagation time of the signal along the tube and for the Lorentz angle effect from magnetic field. Both effects require an estimate of the position along the second coordinate. Segments are positioned in this direction using, if available, second coordinate measurements from RPC or TGC Chambers. If there are not such measurements, several positions are tried and the best hypothesis is retained. The resolution of this pure MDT second-coordinate measurement is poor, ~60 cm [1].

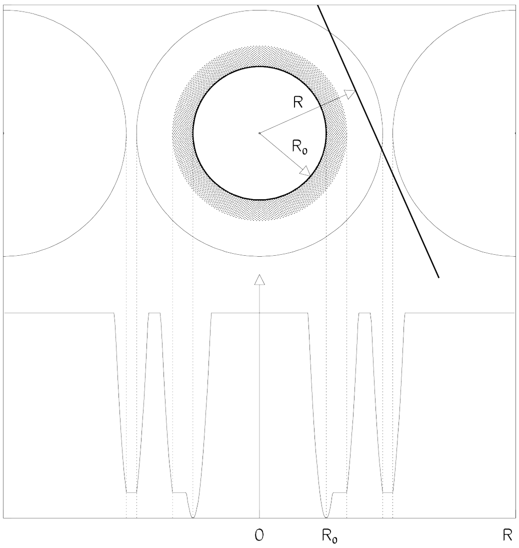

Figure 3.2: Top: sketch of a candidate Track Segment crossing, at a predicted radius R from the wire, a tube where a hit was recorded at radius R0. The thickness of the shaded area corresponds to the dead time assumed for the electronics; in the absence of multi-hit capability, the shaded area would extend from R0 all the way to the tube wall. Bottom: penalty factor χ^2_P vs. impact parameter R. The penalty is highest for R << R0 and R >> R0, as well as in the two empty adjacent tubes. χ^2_P is minimum for R = R0, and only slightly larger for R just above R0 (hit masking). The penalty is also moderate in the space known to be inactive between neighboring tubes.

The steps of the Track Segment search are:

- ROAs in the (η, ϕ) space are identified using information from the Trigger Chambers.
- First the Track Segment are looked only in Stations where second coordinate Chambers can be available, i.e in Outer and Medium Stations in the Barrel and in Inner and Medium Stations in the End Cap. Indeed, in this first search which is called *Strict* search, Track Segments are required to be associated with at least one second-coordinate hit;

---

[1] In commissioning or cosmics running, this is not possible due to the T_0 fit and the Track Segment is positioned at the center of the Station.

- At this stage, Track Segments are also reconstructed in the CSC Chambers, directly in Three Dimensions using the CSC clusters (in both projections) as inputs. All these CSC Track Segments are considered as *Strict*.

- Then starts an second, independent and looser search of Track Segments, called *Loose* search. The *Loose* Track Segments are not required to match second-coordinate hits and the requirements on χ^2_P are less stringent. To avoid too many fakes candidates, this search is performed only within those RPC/TGC ROAs which include at least one *Strict* Track Segments. However to recover some efficiency from regions where RPC/TGC are not available, new ROAs defined by an accumulation of first coordinate hits in Stations without RPC nor TGC associated Chambers, are added to the ROAs set.

The above searches are completed by an other class of Track Segments which are this time allowed to be formed with hits from one Multilayer only. This class is intended to cure inefficiencies at the edges of Stations where the muon can cross only one Multilayer, or due to dead channels. For this class of Track Segments, each Multilayer of a Station is used individually to identify triplets (or quadruplets) of tubes with hits compatible with a straight track. In order to reduce the large number of possible combinations, only the hits left unused by the Track Segments found in above searches are considered and the χ^2_P requirements are more strict.

3.1.3 Track Fit

The track fit is a multi-stages process. First a track candidate is formed using only segments, associating them according to a set of Strategies. From the result of this segment-based fit, the track is refined by first using directly the raw informations used to build the segments, instead of the segments cinematic, and then fitting, along with the track cinematic parameters, few additional angles of scattering at appropriately located and weighted locations, in order to take into account the Multiple scattering effects in crossed matter.

Taking the case of a track fully contained within the Barrel, the segments-based fit stage starts from a *Strict* Track Segment found in the Barrel Outer Stations. Its position and direction are used to derive a first rough estimate of the momentum. This estimate is used to extrapolate first to the Barrel Medium Stations. A “Momentum Scan” is performed around the first rough estimate and several extrapolations are performed for different values of the momentum. Matchings with Track Segments in these Medium Stations are evaluated and the Track Segment with the best matching is included in the candidate track, leading to a second and more accurate estimate of the momentum. The process is repeated with the Barrel Inner Stations and then with all other potentially crossed Stations refining each time the estimate of the momentum. In all these fits full tracking is performed at each step of the minimization procedure. After this stage, a candidate track is kept only if it contains at least two Track Segments.

The above Barrel basic strategy which starts from the Outer Stations and looks first in the Medium Stations and then in the Inner Stations corresponds to the two first strategies listed in table 3.1. In the End Cap, the basic strategy is to start from the Medium Stations, then to look in the Outer Stations and finally in the Inner Stations.

Dedicated strategies cope with the association of Barrel and End Cap Track Segments.

All these strategies are restricted to a same single ϕ sector, large or small. Only for Track Segments at the edges of sectors, some strategies are applied to attempt association between two ϕ sectors.

Finally two last searches are devoted to reconstruct tracks at very high η where the TGC Chambers coverage is limited. These are thus the only searches which can start with *Loose* Track Segments (i.e. without ϕ information), but on the other hand, they have harder cuts (3 Stations required).

Basic Fully Barrel or End Cap strategies				
BOL	⇄	BML	→	BIL or BIR
BOS	⇄	BMS	→	BIS
EML	⇄	EOL	→	EIL or EEL or CSL
EMS	⇄	EOS	→	EES or EIS or CSS
Barrel/End Cap transition strategies				
EML	⇄	EIL	→	EEL or BIL
EMS	⇄	EIS	→	EES or BIS
EMS	⇄	BMS	→	EES or BIS or BOS
EML	⇄	BML	→	EEL or BIL or BOL
BOL	⇄	EIL	→	BIL or EEL or EML
BOS	⇄	EIS	→	BIS or EES or EMS
Mixing ϕ sectors; Restricted to Track Segments at the border of the Station				
BOS	⇄	BML	→	BIL or BIR
BOL	⇄	BMS	→	BIS
EML	⇄	EIS	→	BIS or EEL or CSS
EMS	⇄	EIL	→	BIL or EES or CSL
Start with *Loose* Track Segments, but with harder cuts and not used for cosmics				
EML	⇄	CSL	→	EOL
EMS	⇄	CSS	→	EOS

Table 3.1: Stations Association Strategies (BIM are included inside BIL, BMF inside BMS and BOF/BOG inside BOS); A⇄B → C means that the association starts from a *Strict* Track Segment on A and then looks for association with a Track Segment on B; if this is successful, association is then tried with a Track Segment on C; if not, association is tried starting from a *Strict* Track Segment on A directly looking for a Track Segment on C. If this fails the procedure restarts from a *Strict* Track Segment on B looking for a Track Segment on A; If this is successful, association is then tried with a Track Segment on C; if not, association is tried starting from a *Strict* Track Segment on B directly looking for a Track Segment on C.

Then from the Segments-based fit, a new fit is performed using directly the raw information which were used to build the Segments-based track. Besides to add information to the fit, this allows to sort out, among all the hits, the “good” ones from the “bad” ones, the outliers, which are too far away from the reconstructed path of the muon.

From this stage, tracks are penalized for the “holes” on their predicted trajectory, i.e for the total absence of a predicted hit. This allows an important rejection of fake tracks resulting from accidental association of segments, which, against evidence, should have crossed some Stations which are actually missing.

This refined fit is used to collect dead matter along the track. Crossed volumes are replaced by discrete scattering centers. An optimized procedure merges the neighboring scattering centers collapsing the matter into a set of fewer more manageable (3 to 5 according to the momentum) appropriately located and weighted Scattering spots. To these scattering spots, adjustable angles of scattering are attached. From here, energy loss is also applied at these spots when tracks are propagated in the Magnetic Field.

A final global fit is performed similar to the last one, but this time with energy loss applied and fitting as well the scattering angles for which constrains have been added to the χ^2 function depending on the amount of matter their scattering spots stand for. Eventually, a selection of reconstructed muons is made according to the value of the χ^2 of this last global fit.

The covariances matrices of the track candidates are computed from the variations of the χ^2 when varying the track parameters around the fitted parameters.

3.1.4 Back Tracking

At the end of the previous Track Fit, the parameters of the track are expressed at the Entrance of the Muon Spectrometer. This means that the 5 parameters which have been fitted set the cinematic of the muon where it crosses a cylinder located just after the Calorimeters volumes (cf figure 3.3(a)).

These parameters form a 5-dimension vector $\vec{E}_5$, the fitted value of which is $\vec{E}_5^o$, associated with a 5×5 Covariance matrix $C_{E,5}$ or equivalently its inverse, the Weight matrix, $W_{E,5} = C_{E,5}^{-1}$, so that the compatibility of a given hypothesis $\vec{E}_5$ with the Muon Spectrometer data is quantified by:

$$\chi_5^2(\vec{E}_5) = (\vec{E}_5 - \vec{E}_5^o)^T W_{E,5} (\vec{E}_5 - \vec{E}_5^o) \tag{3.1}$$

Analyses are primarily interested in the parameters of the muon when it emerges from the interaction point. Therefore the track measurement is to be transported from MS Entrance to the vicinity of the beam axis. A new more convenient definition of track parameters, the Perigee Track Representation, is needed which sets the cinematic of the muon at the DCA point, the point at the distance of closest approach where the trajectory is the closest to the beam axis (cf figure 3.3(b)). This defines a 5-dimension parameters vector $\vec{P}_5$, its central value $\vec{P}_5^o$, and the Covariance and Weight 5×5 matrices in this representation $C_{P,5}$ and $W_{P,5} = C_{P,5}^{-1}$. The aim is to compute $\vec{P}_5^o$ and $C_{P,5}$.

Crossing the detector from the interaction point, the muon can have lost energy and can have been scattered specially in the Calorimeters. The errors in the Perigee Representation will reflect both errors on the parameters measured at the MS Entrance and the uncertainties on the energy actually lost and on the multiple scatterings that actually occurred along the trajectory.

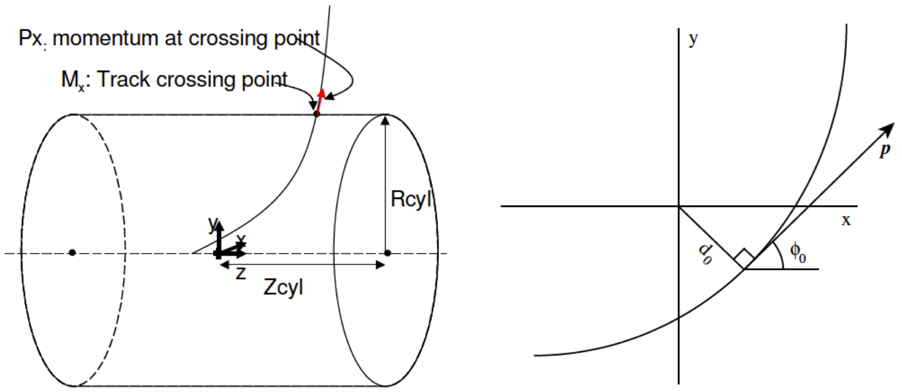

(a) (b)

Figure 3.3: (a) Cylindrical representations on a cylinder defining the entrance of the entrance of the Muon Spectrometer: two parameters to fix the point where the track intersects the cylinder, two parameters to fix the unit vector tangent to the track at this point and the inverse of the momentum multiplied by the charge; (b) Perigee representation: the longitudinal coordinate of the DCA point along the beam-axis, the signed distance perpendicular to the beam axis of the DCA point, two variables for the unit vector tangent to the track and the inverse of momentum multiplied by the charge ;

In *Muonboy*, the *AMDC/AGDD* Detector Description of the Calorimeters volumes is used to collect along the backtracked trajectory, the locations of the Calorimeters volumes crossed or equivalently a set of discrete points where the Energy loss corrections are to be applied (cf figure 3.4). Also, one derives from the collection of these points, the positions of two Scattering Spots sharing the total amount of the crossed material on which the track direction can be changed discontinuously.

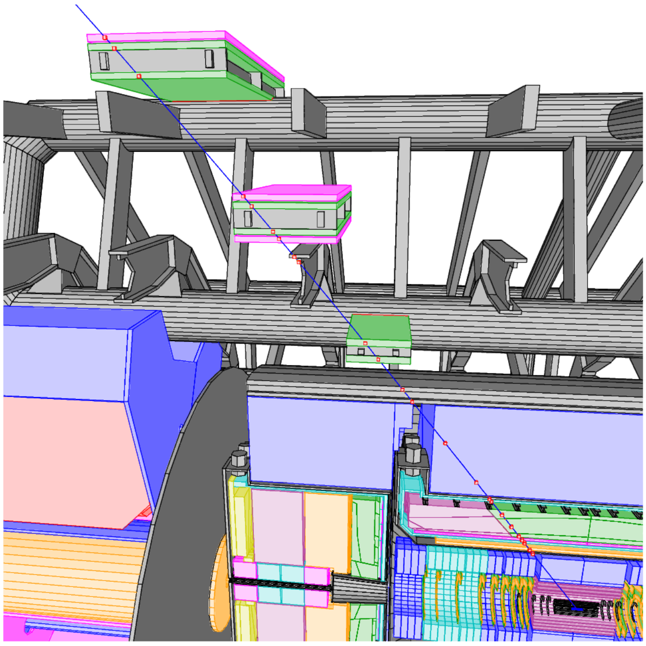

Figure 3.4: Three-dimensional display of a muon track traversing the ATLAS calorimeters and Muon Spectrometer; the small red cubes indicate the centers where multiple scattering was assumed by the reconstruction to occur in the material traversed by the track.

Applying, as the most likely assumptions, the average energy loss correction and no scattering at all, one computes the central value of the parameters vector in the Perigee Representation, $\vec{P}^o_5$, from the central value of the parameters vector in the Track Representation at MS Entrance, $\vec{E}^o_5$.

In order to deal with the errors, the Track Representations are extended to include extra parameters to handle fluctuations of Energy losses and multiple scattering within the Calorimeters. One introduces an Energy Loss Scale Factor, f_{Eloss}, which multiplies the Energy losses on each of the points collected before. To handle multiple scattering, one associates two scattering angles, α_1 and α_2 to the two Scattering Spots.

A representation of the full trajectory is obtained adding to the track parameters at the MS Entrance, the three new Extra parameters f_{Eloss}, α_1 and α_2. This defines 8-dimension parameters vector $\vec{E}_{5+3}$. The elements of the central value vector $\vec{E}^o_{5+3}$ are those of $\vec{E}^o_5$ but for f_{Eloss} which is 1 and α_1 and α_2 which are 0. The Likelihood of a given hypothesis $\vec{E}_{5+3}$ is evaluated by:

$$\chi^2_{5+3}(\vec{E}_{5+3}) = \chi^2_5(\vec{E}_5) + \frac{(f_{Eloss}-1)^2}{\sigma_f^2} + \frac{\alpha_1^2}{\sigma_{\alpha_1}^2} + \frac{\alpha_2^2}{\sigma_{\alpha_2}^2} = (\vec{E}_{5+3} - \vec{E}^o_{5+3})^T W_{E,5+3} (\vec{E}_{5+3} - \vec{E}^o_{5+3}) \tag{3.2}$$

where σ_{α_i} are the multiple scattering distribution widths computed for the equivalent amount of matter associated to each of the two Scattering Spots and σ_f scales the fluctuations of the energy lost and is taken to be 15%. The 8×8 matrix $W_{E,5+3}$ is obtained from $W_{E,5}$ by adding rows and columns for the Extra parameters. Since there is no correlation between track parameters at MS Entrance and the Extra parameters, the elements of the additional rows and columns in $W_{E,5+3}$ are all 0 but the diagonal terms which are equal to $1/\sigma_f^2$ and $1/\sigma_{\alpha_i}^2$.

In the same way, the Perigee Track Representation is extended adding the same three Extra parameters. This defines 8-dimension parameters vector $\vec{P}_{5+3}$. The elements of the central value vector $\vec{E}^o_{P+3}$ are those of $\vec{E}^o_5$ but again for f_{Eloss} which is 1 and α_1 and α_2 which are 0. One can always compute numerically $\vec{P}_{5+3}$ from $\vec{E}_{5+3}$ and vice versa. In the vicinity of $\vec{P}^0_{5+3}$, this relation takes a matricial form, where a Transfer 8×8 matrix $\mathcal{T}$, evaluated numerically, acts as:

$$\vec{E}_{5+3} - \vec{E}^0_{5+3} \simeq \mathcal{T}(\vec{P}_{5+3} - \vec{P}^0_{5+3}) \tag{3.3}$$

Then if the errors are small enough, one can say that the likelihood of a given hypothesis $\vec{P}_{5+3}$ is evaluated by

$$\chi^2(\vec{P}_{5+3}) = \chi^2(\vec{E}_{5+3}) \simeq (\vec{P}_{5+3} - \vec{P}^o_{5+3})^T [\mathcal{T}^T W_{E,5+3} \mathcal{T}] (\vec{P}_{5+3} - \vec{P}^o_{5+3}) \tag{3.4}$$

Therefore the 8×8 matrix $W_{P,5+3} = \mathcal{T}^T W_{E,5+3} \mathcal{T}$ is the Weight matrix in the Extended Perigee Track Representation.

At the end one is interested by the errors on $\vec{P}_5$ and not by those on $\vec{P}_{5+3}$. One obtains the 5×5 Covariance matrix on $\vec{P}_5$ by simply removing from the inverse of $W_{P,5+3}$ the rows and columns concerning any of the f_{Eloss}, α_1 and α_2 parameters.

3.1.5 Energy loss correction in *Muonboy*

The energy loss correction in *Muonboy* is intimately connected with the *AMDC/AGDD* description of all the volumes of ATLAS. The *Muonboy* tracking can collect the intersection of the trajectory of a muon with all these volumes. It is known that for what concerns the multiple scattering, a slab of matter can be exactly replaced with two planes sharing the total amount of matter, with random independent discontinuous angular changes on them [58]. On the other hand, to proceed that way for the energy loss is a discretization approximation. This approximation is worsened when as explained above, the spots are further collapsed in a set of three to five points as done in the Track reconstruction within the Muon Spectrometer. However this procedure is valid since the Energy loss within the Muon Spectrometer is small. For the back tracking within the Calorimeter, the energy loss is much more important and the set of spots on which the Energy loss is applied is not reduced. This insures that the correction remains smooth, or the smoothest possible, all along the trajectory.

The basic *Muonboy* assumption on the Energy loss is that the amount of energy lost per unit length is linear in the momentum

$$\frac{dE}{dx} = -(a + bE) \tag{3.5}$$

reflecting the loss by ionization at low energy and the radiative rise with energy. For a given length l, this leads to

$$E_{out} = E_{in}\alpha + \beta \text{ with } \alpha = \exp(-bl) \text{ and } \beta = (\alpha - 1)a/b \tag{3.6}$$

where E_{in} and E_{out} are the energies of the muon before and after going through the length l. When a slab of matter is replaced by a spot, the parameter α and β are associated to this spot, and the equation (3.6) is used to compute the energy of the outgoing muon from the energy of the incoming muon when it crosses the spot.

The parameters a and b of equation (3.5) were originally derived from [59]. Over the years, specially for the Calorimeters, substantial massage of these parameters has occurred to get satisfactory single muons pulls and satisfactory description of various resonances mass peaks, on the basis of detailed GEANT4 [11] simulations. It is well known that the distribution of the energy losses follows a Landau distribution and that the parameterizations of the energy loss correction face difficulties sometimes termed as choices between Most Probable Value and Mean Value correction [12]. It is fair to say that these fine distinctions are quite moot in the case of the *Muonboy* parametrization which, at the term of the years of “massage”, is justified mainly by the results of the empirical studies mentioned above.

3.2 Combined Muon reconstruction in ATLAS: *Staco*

Staco aims to combine an ID Track and MS track. This combination is a Statistical combination of two independent tracks measurements of the same muon by means of their covariance matrices.

Let assume two Tracks measurements from two independent Data sets, represented in the same Track representation by the 5-dimension parameter vectors, $\vec{P}_1^o$ and $\vec{P}_2^o$, and their covariance matrices, C_1 and C_2, or equivalently by their Weight matrices, the inverses of the covariance matrices, $W_1 = {C_1}^1$ and $W_2 = {C_2}^1$. The compatibility of a Track hypothesis, represented by a parameter vector $\vec{P}$, with the two independent Data sets is quantified by the function

$$\chi^2(\vec{P}) = (\vec{P} - \vec{P}_1^o)^T W_1 (\vec{P} - \vec{P}_1^o) + (\vec{P} - \vec{P}_2^o)^T W_2 (\vec{P} - \vec{P}_2^o) \tag{3.7}$$

which can be written as

$$\chi^2(\vec{P}) = (\vec{P} - \vec{P}_{Cb})^T W_{Cb} (\vec{P} - \vec{P}_{Cb}) + {\chi^2}_{match} \tag{3.8}$$

where

$$\vec{P}_{Cb} = (W_1 + W_2)^{-1} [W_1 \times \vec{P}_1^o + W_2 \times \vec{P}_2^o] \tag{3.9}$$

is the best estimate of the cinematic from the two Track measurements,

$$W_{Cb} = W_1 + W_2 \tag{3.10}$$

is the Weight matrix of the combined measurement, i.e the covariance matrix of the combined measurement is $C_{Cb} = W_{Cb}^{-1}$, and

$${\chi^2}_{match} = (P1 - P2)^T (C_1 + C_2)^{-1} (P1 - P2) \tag{3.11}$$

quantifies the quality of the combination of the two measurements.

The *Staco* algorithm works on the two collections of tracks measured in the ID and of track measured in the MS backtracked to beam axis. Both set of tracks are in Perigee Representation with respect to the Oz axis. All tracks are required to have p_T above 3 GeV. The ID Tracks are first filtered on the basis of quality criteria, e.g one can require a certain number of Pixel or SCT hits.

Then the algorithm forms pairs of ID and MS Tracks requiring first that they point loosely in the same direction. The above Statistical Combination is performed and only the combination with the best ${\chi^2}_{match}$ is kept. If the ${\chi^2}_{match}$ of the best pair is above a certain momentum dependent threshold, the combination is rejected. For the best association to be accepted, a statistical combination is then performed by extrapolating the ID track measurement up to the Muon Spectrometer Entrance and combining the extrapolated measurement with the Muon Spectrometer measurement there. In principle, the ${\chi^2}_{match}$ of this combination and the one of the combination in the ID volume should be identical since the ${\chi^2}_{match}$ is a statement on the compatibility of the two trajectories measured in the Inner Detector and in the Muon Spectrometer and should not depend on the point where one computes it. This is actually true within the numerical precision, for the overwhelming majority of the cases. Still it was found useful to require that the ${\chi^2}_{match}$ of the combination at the Entrance of the Muon Spectrometer does not exceed by too much the ${\chi^2}_{match}$ of the combination in the ID volume. Indeed this prevents the very rare cases where the algorithm errs combining ID and MS Tracks with very unbalanced momenta. If the pair passes this last test, the combination is kept and the Tracks it uses are removed from the sets of ID and MS Tracks. The procedure restarts on the leftovers and stops when no more acceptable combination can be formed.

The standard ID tracks are restricted to the range $|\eta| < 2.5$. Still some ID informations are available up to $|\eta| < 3$. These informations are exploited by a special setting of the ID reconstruction

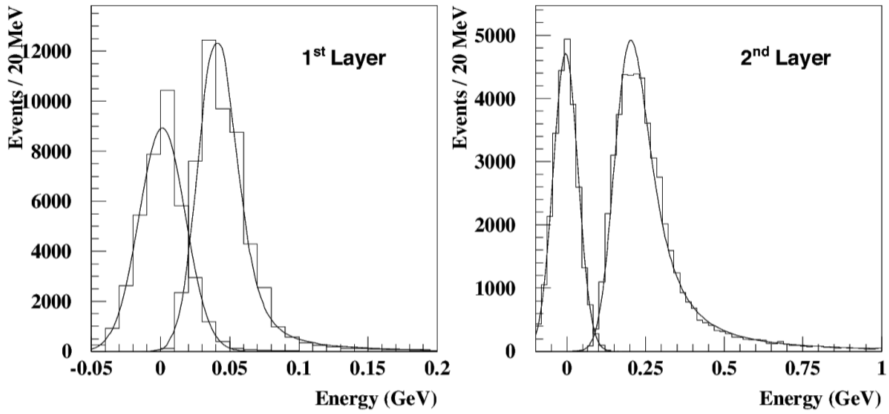

Figure 3.5: Distribution of the muon energy deposited in one electromagnetic Calorimeter cell by 150 GeV muons. The Gaussians on the left of each plot are the distributions of the noise. Left (right): energy deposit in a cell belonging to the first (middle) longitudinal sampling traversed by the muon. The data were collected in the 2004 Combined Test-beam.

running on the leftover hits of the main reconstruction with criteria relaxed on the SCT hits (a minimum of 6 of them are required in the main ID reconstruction; none are required by the special ID reconstruction setting) to go past the $|\eta| < 2.5$ limit. *Staco* uses the set of these so-called Pixel “tracklets” so obtained to validate reconstructed MS tracks reconstructed at $|\eta| > 2.5$. This is done after the first combination pass described above and using the MS Tracks not associated yet.

3.2.1 Energy Loss correction and *Staco* Muon Combined Reconstruction

The *Staco* algorithm deals with sets of Tracks expressed in the same Track Representation, the Perigee Representation with respect to the Oz axis. For the Tracks reconstructed in the Muon Spectrometer, this means that they should have been corrected for the Energy lost in the Calorimeters. When they have been reconstructed by *Muonboy*, we have seen in sections 3.1.4 and 3.1.5, how this is done and, in particular, that no measurement of energy deposited in the Calorimeters is being used. However the signal from an isolated muon is clearly visible in the Calorimeters as illustrated by figure 3.5. Although first, the actual resolution of the measurement of the few GeV deposited by a muon, for a large part in the Hadronic Calorimeter, is not high and second, in real conditions, isolation of a candidate Track should be examined cautiously before attributing a Calorimeter signal to it, it is nevertheless worth to have an option allowing to take into account Calorimeters measurements.

Ideas for such algorithms are numerous [60]. An elegant one [61], developed for *Staco*, consists in evaluating the likelihood of a candidate Energy Loss, E_{Loss}, by the product of two distributions: a Landau parametrization of E_{Loss} scaled from the measured muon track momentum and a Gaussian centered on the measured Energy Loss in the Calorimeters, E_{Loss}^{meas}, with a width representing the resolution of the Calorimeters Energy measurement. *Staco* is equipped with an optional stage preceding those described above, allowing to backtrack Muon Spectrometer Tracks measured at the Entrance of the Muon Spectrometer correcting it using this method. It was shown that the Standalone performance are indeed somewhat improved by such a method. However after combination with ID tracks, the gain in the resolution is much smaller, of the order of 4% in relative terms.

One issue with such approach is that, in real conditions, isolation criteria have to be designed carefully for the method to be applied. A worrisome consequence is that this makes the actual performance dependent on the pile-up level and in general of the environment of the muon, for instance making moot transposition of performance observed on the Z decay mass peak to other physical final states. Given these concerns, the default option of the *Staco* algorithm was to not allow this backtracking, waiting that more experience is gained on the working conditions of the experiment, providing meanwhile reliable performance robust against pileup and in general busy muon environments.

3.3 Muon Tagging in ATLAS: *MuTag*

As we have seen in section 1.4, it could happen that the reconstruction of a Track within the Muon Spectrometer is not possible because of imperfect acceptance coverage or because at low p_T no enough energy is available to reach the outer or even the medium Stations. This leads to spots of inefficiencies in the (η, ϕ) space and to a drop in Track reconstruction at low momentum. The last issue was pointed very early in the ATLAS performance studies [62]. It was found then that the identification efficiency could be extended to low momenta provided that the Track Segments in the Inner most Stations could be used.

The *MuTag* algorithm was developed first to recover the loss of identification at low p_T and latter to recover those due to poor coverage. Its principle is trivial and illustrated in figure 3.6: ID tracks are extrapolated up to the level of Muon Spectrometer Stations and tentatively matched with Tracks segments.

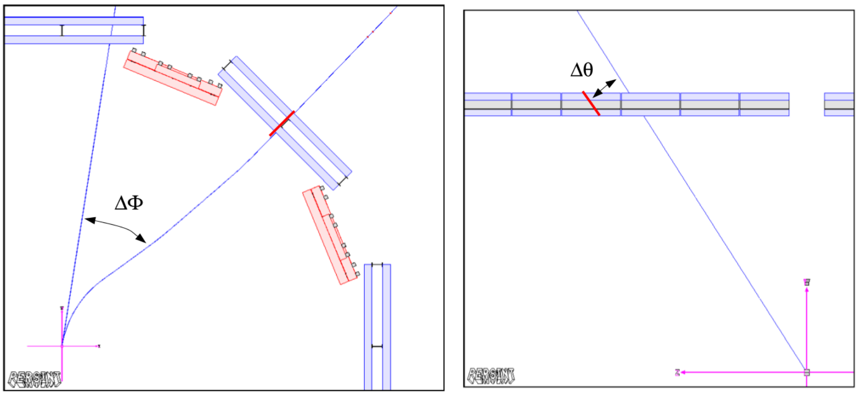

Figure 3.6: *MuTag* algorithm matching Track Segments and ID Tracks extrapolated up to Muon Spectrometer Stations (left) in ϕ and (right) in η

The early version was simply a matching between the ϕ and η of the Track at Interaction Point and ϕ and η coordinates of the Track Segment in the Inner Stations. Although this is an outdated stage of the algorithm history, it is interesting to note that due to the simplicity of solenoidal Field, the extrapolation of ID Tracks up to the Inner Stations is extremely simple. Indeed as illustrated by the figure 3.7(a), the difference between the ϕ of the ID Track at the Interaction Point and the ϕ coordinate of the point where this Track crosses the Inner Stations is to a very good approximation simply inversely proportional to p_T, the proportionality factor being a simple function of η independent on p_T. The case of the η matching is even simpler: in first approximation, the η of the ID Track at the Interaction Point and the η coordinate of the point where this Track crosses the Inner Stations coincide. This extremely simple relations, in flabbergasting contrast with what happens in the Muon Spectrometer [2], allowed immediately, with some educated guesses on the widths of the distributions of differences ϕ and η, to solve the problem of the low reconstruction efficiency at low p_T, as illustrated by the figure 3.7(b).

Later, the ATHENA Tracking software machinery was used to perform the propagation of the ID Track. The code, therefore immediately more cryptic, becomes however much more powerful since not only the concomitant propagation of the errors of the ID track measurement allows more solid matching criteria, but the idea could be extended to address also the issue of imperfect acceptance coverage of the Muon Spectrometer layout.

---

[2] For Track Segments from other Stations than the Inner Stations of the Muon Spectrometer, the complexity of the trajectories in the magnetic field of the toroids prevents any simple analytical parametrization of the connection between them and an ID Track.

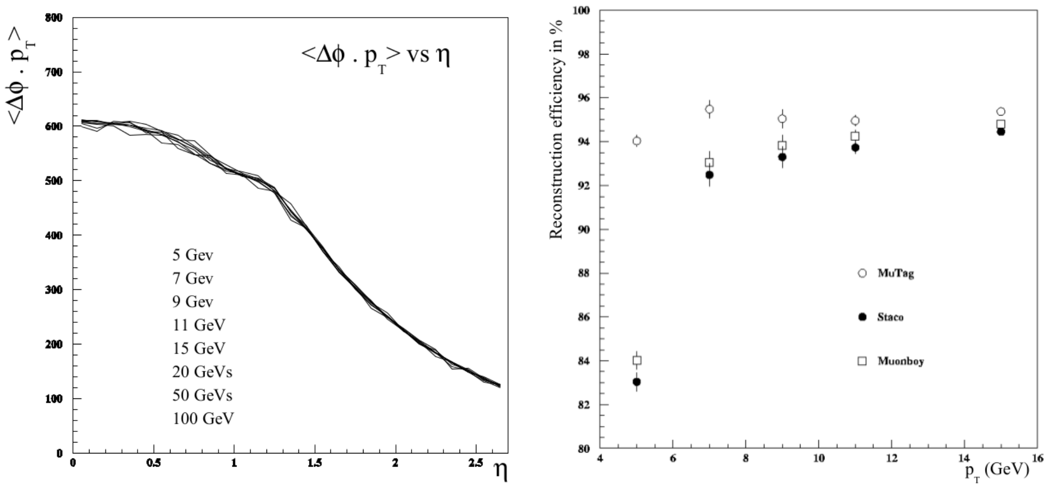

(a) (b)

Figure 3.7: Early version of *MuTag*: (a) Mean value of the product of transverse momentum of an ID Track by the difference between the angular ϕ of this Track at the beam axis and the ϕ of the point where the ID Tracks trajectory crosses the MS entrance against the η of the Track, for various single muon samples at fixed transverse momentum; (b) First *MuTag* performance; the points marked "*MuTag*" are obtained adding to the *Staco* reconstructed muons, the muons tagged by *MuTag*;

It is important to be conscious of the dangers of an algorithm such as *MuTag*. Its intrinsic efficiency is really very high and it is easy to forget how much it is prone to build fake muons. To require a highly consistent object such as MS track as *Staco* does is incomparably more demanding than to base an identification on a matching with a Track segment. Therefore the role of a algorithm such as *MuTag* should be strictly confined, a last resort when everything else has failed so to say

All over its evolution, the strategy of the algorithm remained the same: *MuTag* runs after *Staco* on its leftovers, i.e it works on the ID Tracks that have not been combined by *Staco* and on Tracks Segments that where not used in Muon Spectrometer Tracks that have been successfully combined by *Staco*. This allows to get a clean and simple picture with no overlap between Candidates categories and clear precedence of Combined Candidates over Tagged Candidates. Furthermore strict cuts are applied on the quality of the ID tracks and MS segments considered and on their matchings, themselves only allowed in some corners of the MS. Finally the *MuTag* muon are sorted post-reconstruction in "Tight", "Medium" or "Loose" candidates categories (*Staco* muon are themselves "Tight" candidates) according to such criteria as the number of segments tagging a given ID tracks or the number of second coordinate hits of the tagging segments.

The strict policy against the fake muons which is followed in all the stages of the *Staco* chain does not result in a loss of reconstruction efficiency and at the start of the LHC, the *Staco* chain was ready to provide the best performance to the Run 1 analyses.

Chapter 4

Performance of Muon Reconstruction in ATLAS

In this chapter I review the performance of the *STACO* chain of reconstruction of muons in ATLAS.

The driving principles of the development of this chain was to get the highest efficiency for the lowest rate of fake candidates. It is quite easy to get a very high reconstruction efficiency spoiled by a huge contamination of fake candidates, by permissively tagging Inner Detector track on the basis of some matching activity in the other sub-detectors. On the contrary and as easily, one can get a very high purity sacrificing reconstruction efficiency at low momentum and in the weaker spots of the Muon Spectrometer acceptance. It is much difficult to get both high efficiency and purity.

As discussed earlier, the strategy of the *STACO* chain, is built chiefly on a efficient and robust Standalone reconstruction (*Muonboy Stage*) introducing fake rejection early in the process, followed by a combination with tracks for the Inner Detector (*Staco* stage). The tagging of an Inner Detector track with a Track segment in the Muon Spectrometer (*MuTag* stage) which comes next is intrinsically more prone to form fake candidates. It is therefore strictly conditioned to the previous stages and under severe control. This highly prioritized hierarchy of a few algorithms insures high efficiency of reconstruction of true muons and high rejection of fake candidates. Very importantly in practice, the simplicity of this scheme is a help for the understanding of the reconstruction software, i.e its debugging.

The development of the *STACO* chain software had always included the routine validation of the performance of the reconstruction on simulations of more or less complex events from single muons to full physical events with pile up. This effort which can be tracked back to the “Physics TDR” [62, 63], culminated with the studies for the Computing System Commissioning (CSC) books [64]. Some of the CSC books results are presented in the section 4.1.

Tests on real data were also very important for the development of the *STACO* chain. The earliest were on a setup at CERN combining some elements of all the ATLAS sub-detectors. Besides enforcement of the integration of the reconstruction software within the general ATLAS software framework, it has been the opportunity to test alignment software and the proper use of its output in the reconstruction. Some of the results obtained then are presented in the section 4.2.

The extended commissioning period which followed the incident at the LHC start was also important. The main legacy of this period is a set of special software modules developed to deal with the specific topology of cosmics muons. They latter provide a proper reconstruction for the alignment of Muon Spectrometer stations with cosmics data. The section 4.3 presents some of the results that were obtained during this period.

Finally the long awaited collision data came. Extensive studies of the resonances were done to establish the actual performance of the *STACO* chain. Some of the excellent results that were obtained are presented in the last section 4.4.

4.1 Performance on simulated samples

Since 1999, ATLAS has regularly evaluated the performance of its evolving design, on benchmark physical processes using large simulated samples [62]. It embarked in increasing larger simulation and reconstruction efforts, the Data Challenges, using ever improving realistic Detector description, simulation and reconstruction softwares, making intensive use of tools such as the GRID. These efforts culminated in the performance reported in the ATLAS Detector paper [10] and the Computing System Commissioning (CSC) books [64]. For both reports the *STACO* chain, comprising the stand-alone (i.e. using only muon Spectrometer measurements) reconstruction *Muonboy* (cf section 3.1), the combined reconstruction *Staco* (cf section 3.2), and the Track Segment based identification algorithm *MuTag* (cf section 3.3) was the default chain for all the analyses presented, owing for its highest efficiency, purity, and robustness. Some of the results concerning Muon Performance [65] are reported here.

The efficiency of the reconstruction of a muon is shown in figure 4.1(a) as a function of $|\eta|$ for muons with p_T =100 GeV and in figure 4.1(b) as a function of p_T. The reconstruction efficiencies are shown for the *Muonboy* stand-alone muon reconstruction, the *Staco* combined reconstruction and the combination of *Staco* and the *MuTag* Track Segment based identification,

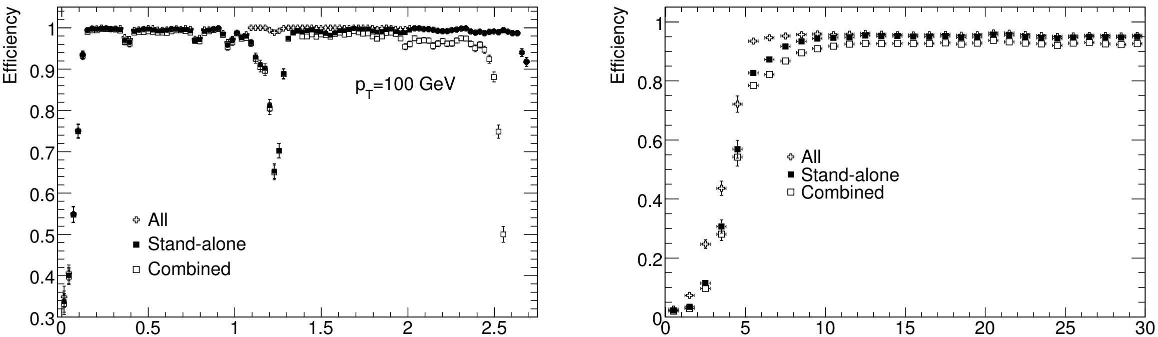

(a) (b)

Figure 4.1: Reconstruction efficiency (a) as a function of $|\eta|$ for p_T=100GeV and (b) as a function of p_T, of the *Muonboy* stand-alone reconstruction, of the *Staco* combined reconstruction and of *Staco* followed by the *MuTag* segment based identification.

The effect of the central large allowance space appears as a drop of efficiency at η ∼0 in figure 4.1(a). The EE Stations missing in the initial Data-taking Layout are the main explanation of the efficiency drop of the stand-alone and combined reconstruction efficiencies around $|\eta|$ ∼1.2. The combined reconstruction efficiency drops down sharply at $|\eta|$ ∼2.5 owing to the ID acceptance which stops there.

As explained in the section 3.3, *MuTag* allows to recover efficiency lost due to the missing EE Stations in the range $1.0 < |\eta| < 1.3$. Above this range, up to $|\eta|$ ∼2, it recovers some efficiency lost at the combination stage [1]. As shown in figure 4.1(b), *MuTag* allows to flatten the efficiency down to p_T ∼6 GeV , which would otherwise significantly decreases already at p_T ∼10 GeV . At lower p_T, it adds almost 20% to the overall efficiency down to p_T ∼3 GeV . Below this momentum the efficiency drops down to ∼0 due to the threshold effect of the energy deposited in the calorimeters which requires a minimal energy to be able to cross them.

---

[1] The performance of *MuTag* displayed in figure 4.1(a) for $|\eta|$ >2 are somewhat old. As explained in section 3.3, dedicated tagger for the End Cap area have been implemented in the version used for the analyses of collision Data, which brings the *Staco*+*MuTag* efficiency almost at the level of the stand-alone reconstruction efficiency for all the range $|\eta|$ >2 [66].

Figure 4.2 shows the various contributions to the transverse momentum relative resolution of the stand-alone reconstruction as a function of p_T. At low momentum, up to 20 GeV , the resolution is dominated by the fluctuations of the Energy lost in the calorimeters. At high momentum, above 200 GeV , the contributions, linear in the momentum (cf appendix D.3), from tube resolution and alignment dominate. In the intermediate momentum range the dominating resolution is coming from the multiple scattering effect in the Muon Spectrometer and is almost independent of the momentum (cf appendix D.4).

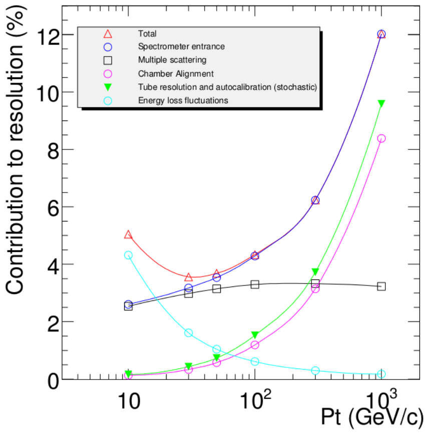

Figure 4.2: Contributions to the Transverse momentum resolution for muons from stand-alone reconstruction as a function of p_T for $|\eta| < 1.5$.

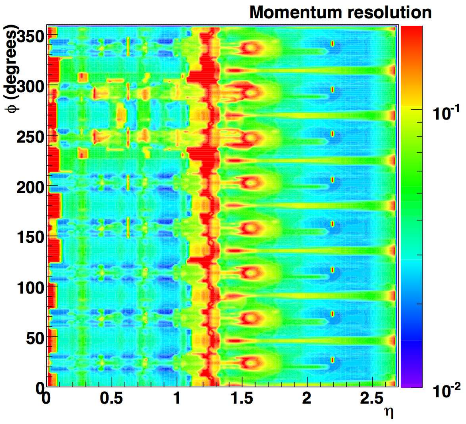

Figure 4.3: Transverse momentum resolution of the stand-alone reconstruction as a function of ϕ and $|\eta|$ for p_T=100GeV .

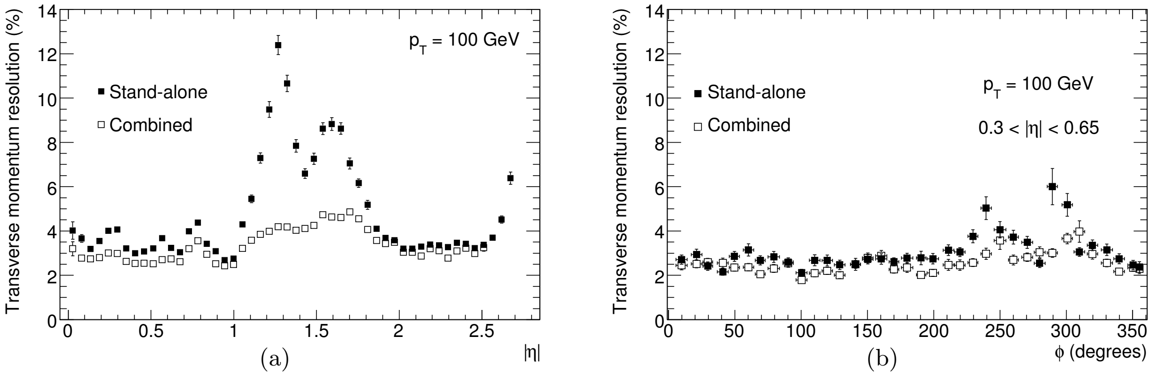

(a) (b)

Figure 4.4: Transverse momentum resolution in % for muons with p_T=100GeV as a function (a) of $|\eta|$ and (b) of ϕ, for the *Muonboy* stand-alone reconstruction, and the *Staco* combined reconstruction.

The figure 4.3 shows in the $\eta - \phi$ plane, the estimate of the resolution at p_T =100 GeV obtained from the Marc Virchaux algorithm, `Resomu`, part of *Muonboy*, which used the ATLAS Magnetic field map and the detailed *AMDB/AGDD* description of active and passive material in the Muon Spectrometer (cf chapter 2). The figure 4.3 illustrated the very non uniform nature of the momentum resolution. One can identify the "shadows" of the various features, dead matter spots and acceptance issues, that have been described in sections 1.3.2 and 1.3.3. This is illustrated further in figures 4.4 showing the momentum resolutions obtained with full simulation for the stand-alone and combined reconstructions, as functions of η and ϕ: the poor resolution in the η range of the missing EE Stations appears clearly in figure 4.4(a), as does, in the figure 4.4(b), the resolution degradation in the feet area.

The momentum resolutions for the stand-alone and combined reconstructions obtained with full simulation are again shown in figures 4.5, this time as a function of p_T for Barrel and End Cap areas. One finds back the stand-alone resolution behavior of figure 4.2 . At high momentum the combined resolution is dominated by the measurement in the Muon Spectrometer while the combined resolution is, at low momentum, the Inner Detector resolution, which is itself dominated by the multiple scattering effect within the ID.

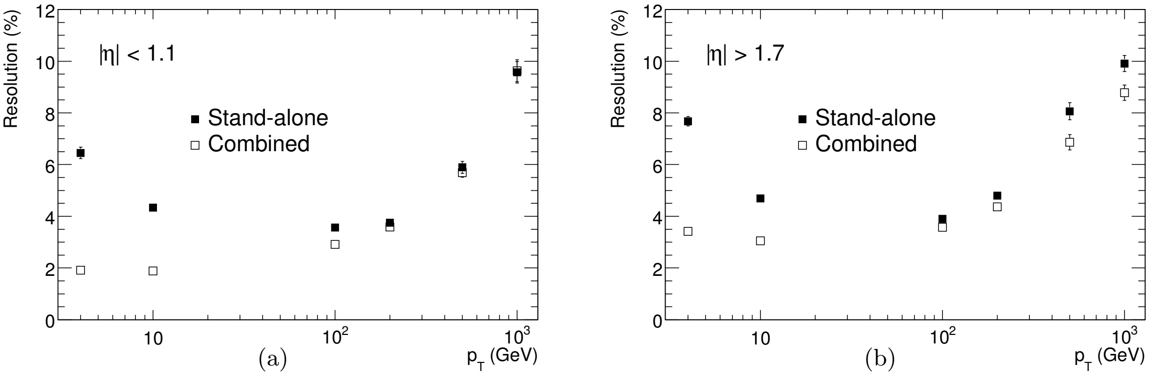

(a) (b)

Figure 4.5: Transverse momentum resolution in % of the *Muonboy* stand-alone reconstruction, and the *Staco* combined reconstruction, as a function of p_T in (a) Barrel and (b) End Cap regions.

Finally the figures 4.6(a) and 4.6(b) gives estimates of the fake muon rate of stand-alone and combined reconstructions as a function of η. The sample used was a collection of $t\bar{t}$ events containing at least one lepton, overlaid with pile-up interactions for a reference luminosity of 10^{33} cm^{-2} s^{-1}and neutron-photon background within the Muon Spectrometer twice the nominal value. As shown in figure 4.6(a), the stand-alone fake muons rate is, in these conditions, everywhere below 2% at low momentum and is reduced by about one order of magnitude in combined reconstruction as shown in figure 4.6(b).

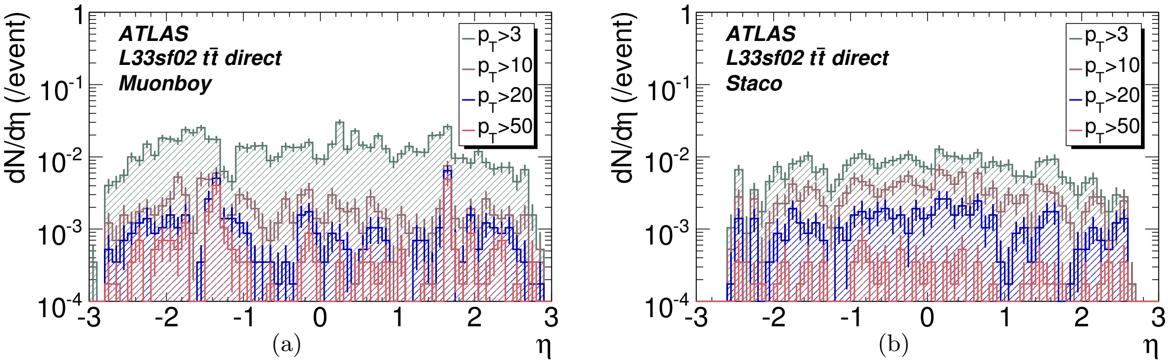

(a) (b)

Figure 4.6: Fake rates for (a) *Muonboy* stand-alone reconstruction and (b) *Staco* combined reconstruction as functions of η in $t\bar{t}$ sample at high luminosity. Fake rates are shown for a variety of p_T thresholds.

Owing for its superior performance in terms of efficiency, resolution and purity, the *STACO* chain was selected by the ATLAS collaboration as the reference software to be used in the Physical analyses presented in as the CSC books [64].

4.2 Performance on test-beam tests on the ATLAS H8 setup

From 2000 to 2004, a series of test beam campaigns involving various elements of the ATLAS Detector was set up in the CERN North Area on the H8 beam line. It culminates in 2004, with a large scale set up combining elements of all the sub-detectors as illustrated in figure 4.7 [67].

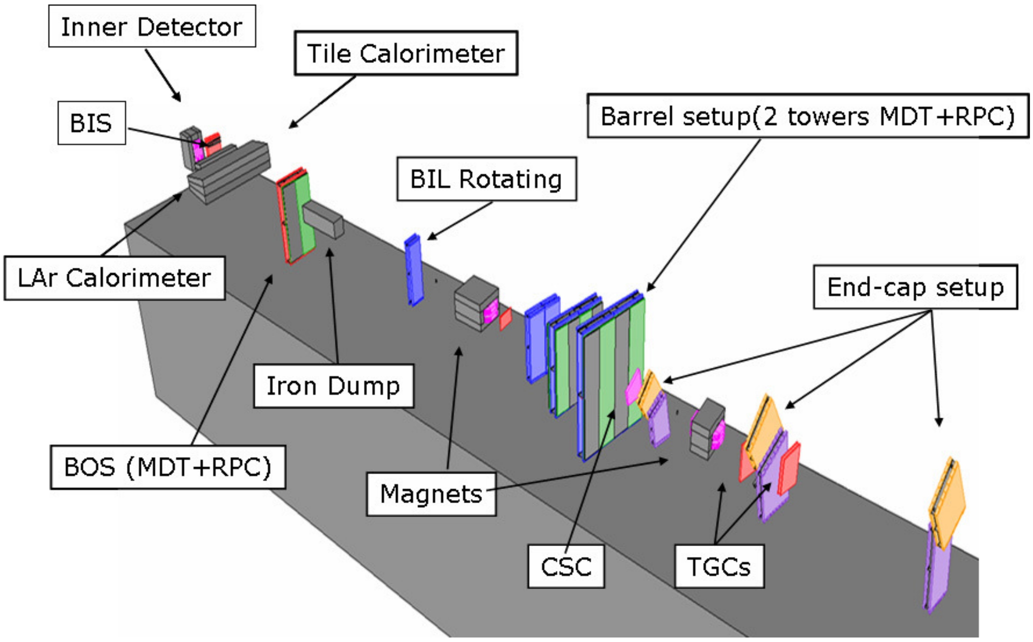

Figure 4.7: Sketch of the ATLAS combined test-beam set-up in 2004

The H8 muon stand consisted in a Barrel and an End Cap section each reproducing sectors of the ATLAS Muon Spectrometer. In the Barrel section, two Inner, two Medium and two Outer Large Stations (BIL/BML/BOL), with complete MDT (tubes axis oriented vertically) and RPC units, were installed fully equipped with the optical alignment system. In the End Cap section, Large and Small Inner, Medium and Outer Stations (EI/EM/EO), also fully equipped with optical alignment system, were installed as well as TGC units.

A bending magnet in front of the Barrel Stations allowed to deflect muons horizontally, i.e in a plane perpendicular to the Tube Layers. An other bending magnet placed in between the EI and EM Stations allowed to emulate the magnetic deflection of the End Cap part of the ATLAS Muon Spectrometer. It was possible to move the different Barrel Stations in a controlled way, by translating them by few millimeters in the z-direction, i.e perpendicularly to the tube axis and within the Tube Layer plane, or by rotating them by few mrad around the y-direction, i.e around the axis perpendicular to the Tube Layer plane. The various results of the 2004 Combined Test beam were reported in [68–73].

From Software development point of view, the 2004 Combined Test beam was an opportunity to test a prototype of the full chain of reconstruction within the ATHENA framework. A key element of this chain is the Conditions Database which provides various informations of the actual Data-Taking conditions. In this campaign, only the Alignment constants could be retrieved in this way. The “R-T” MDT Calibration constants, which allow to convert drift time from MDT tubes in drift radii, were produced for the different H8 test beam configurations, written in flat files and retrieved by a dedicated ad hoc ATHENA `Service` within ATHENA, prior to the reconstruction stage, here *Muonboy*.

To allow monitoring of the optical sensors, a large amount of data were taken under stable conditions without any forced displacement of the chambers.

Under the influence of the daily variations of the temperature, the chambers positions and shapes change.

These changes impact directly the sagitta as it can be computed using a constant Geometry.

This is illustrated in the left part of the figure 4.8 where the mean of the sagitta measurements shows a clear correlation with the temperature.

These changes are faithfully recorded by the Alignment system software which provides relative alignment corrections.

As illustrated in the right part of the figure 4.8, these corrections do cancel the sagitta dependence on temperature.

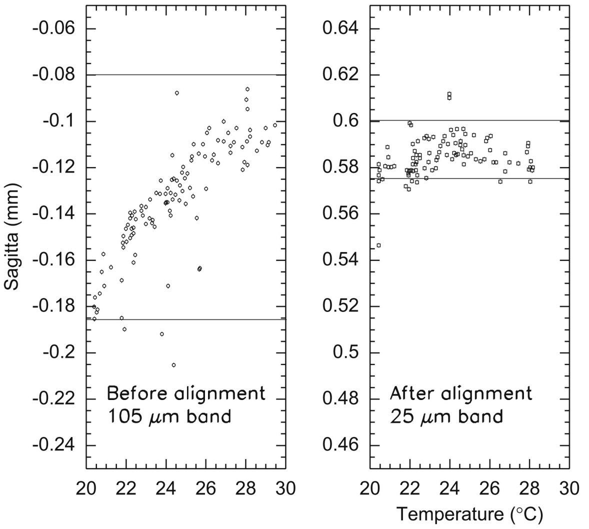

Figure 4.8: Sagitta variations as a function of temperature in the Barrel stand before (left) and after (right) applying the relative alignment corrections.

The figures 4.9 show the sagitta, before and after corrections, obtained in several runs where, by various amounts, the BOL Stations were translated in the z-direction and the BIL and BML rotated around the y-direction. As shown the several millimeters shifts observed before corrections vanish when the corrections from the absolute and relative alignment are applied.

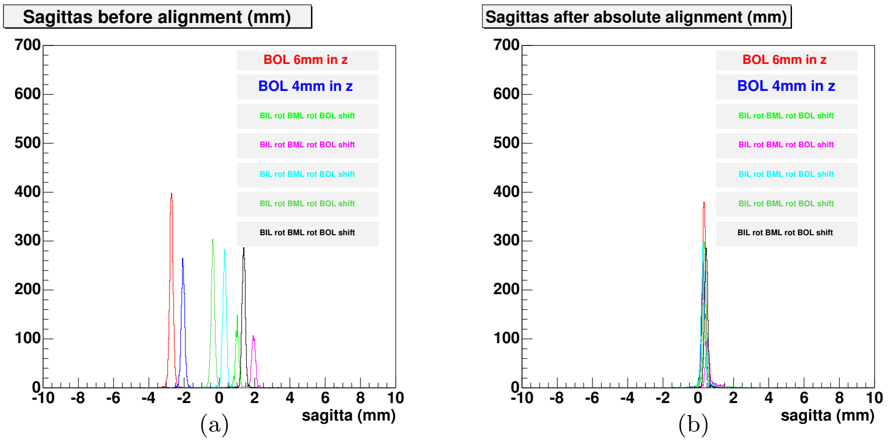

(a) (b)

Figure 4.9: Sagitta distributions for several runs in which different controlled movements on MDT chambers were performed. (a) before and (b) after alignment corrections were applied

Both the right part of the figure 4.8 and the figure 4.9(b) show that the relative alignment corrections, correcting from the relative displacement of the Stations with time, does not correct for the absolute misalignment of these Stations.

The H8 test beam of 2004 was also the occasion to test on real data the concept of alignment with tracks which allows the absolute alignment of the Barrel Stations of the Muon Spectrometer. In H8 test beam conditions, the illuminated surface was not large enough to constrain all the Chambers position parameters. Still the results of figures 4.10 show that the overall sagitta shift before corrections can be canceled within 5μm while reducing significantly the width of the sagitta distribution. More spectacularly, the figures 4.11 show that systematics shifts with strong dependence on the position of the track within the Station can be corrected for. In particular, the figure 4.11(b) shows that, the very strong dependence on the second coordinate (along tube axis) of the sagitta before corrections that one obtains rotating the BIL Station around the y-direction, is totally corrected by the track based alignment.

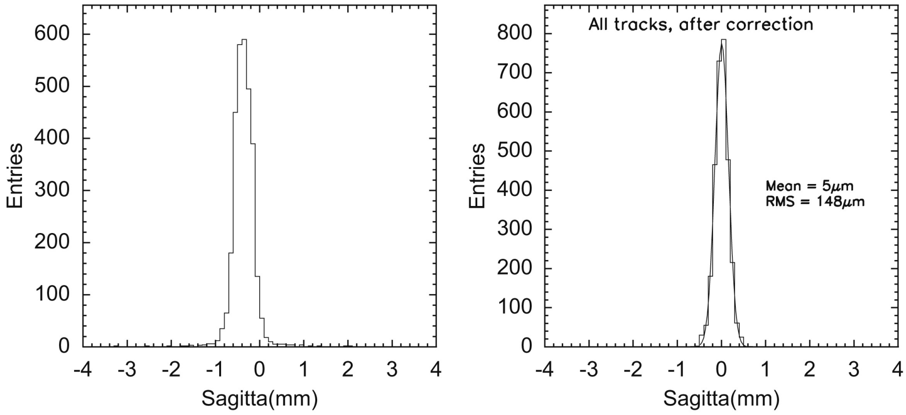

Figure 4.10: Sagitta distribution of selected tracks before and after the alignment fit. Since there was no field within the volume of the Stations, a null mean value of the sagitta is expected. Left: Distribution of sagitta of selected tracks with the chambers at the survey position. The muon sagitta is centered at $-351\mu m$ and the distribution width is $209\mu m$. Right: Distribution of sagitta after alignment fit. The mean value of sagitta is now $5\mu m$ and the distribution width is $148\mu m$.

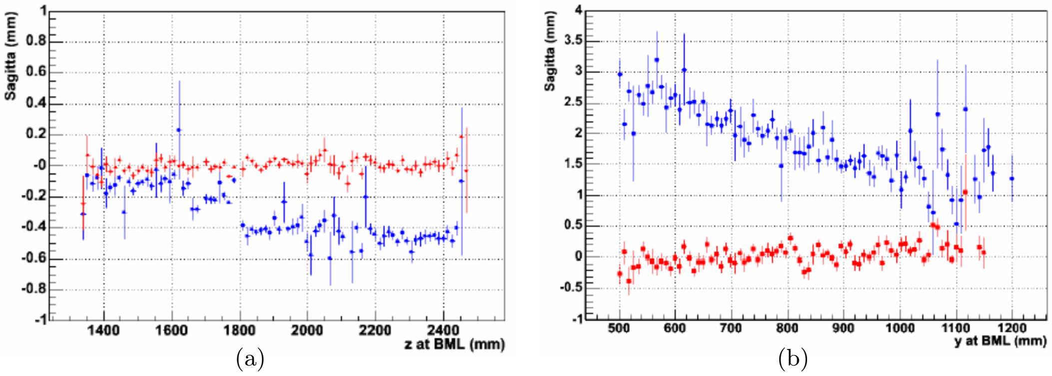

(a) (b)

Figure 4.11: Mean value of the sagitta as a function of the Track segment coordinate in the BML chamber before (blue/dark) and after (red/light) corrections form track based alignment; (a) sagitta as a function of the z-coordinate; z=1800 mm is the location of the transition between the two BML Stations; (b) sagitta as a function of the y-coordinate for a run with large rotation of the BIL Station.

A study was performed of the Track segment efficiency and hit efficiency. The Track segment efficiency in a tested Station was estimated selecting events such that, in each of the two other Stations taken as references, one Track Segment was reconstructed. Then one checked for the presence of a Track Segment in the tested Station along the path defined by the Track Segments of the reference Stations. The resulting efficiency of the Stations was found to be independent of the beam Energy as illustrated in the figure 4.12(a). The sensitivity to the threshold level of the signal discriminator of the MDT electronics was also found small as shown in the figure 4.12(b), as long as the threshold is not too low, i.e electronics noise not too high. The hit efficiency can be derived from the Track Segment efficiency. A hit efficiency of the order of 95-96% was found in line with the simulations which showed that the walls of the tubes and δ-ray electrons induce an inefficiency of the order of ~5% .

Finally a study of the muon catastrophic energy losses within the calorimeters was done using a 350GeV muon beam [72, 73]. By cutting on energy depositions in the different calorimeters com-

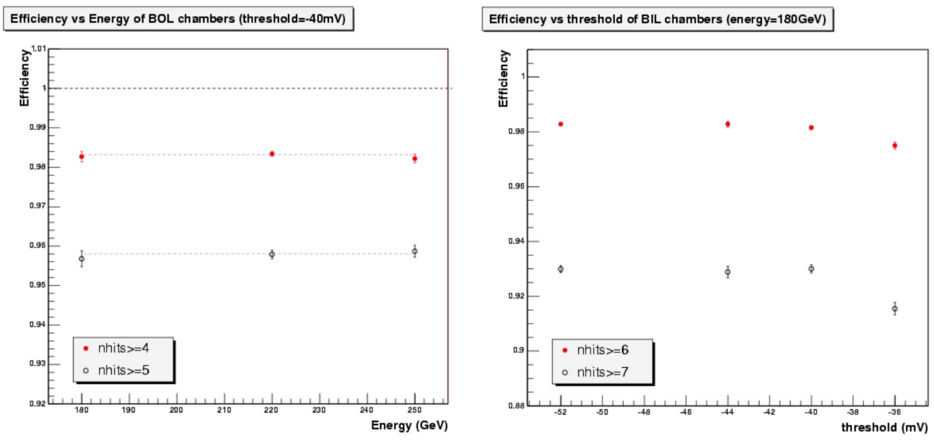

(a) (b)

Figure 4.12: (a) Track segment efficiency in the BOL chamber versus the beam energy (b) Track segment efficiency versus MDT threshold of the BIL chamber, for two cases: 1/ when the most stringent requirement to validate a track segment (nhits=ntotal) and 2/ when (nhits=ntotal-1)are used. The beam momentum is $180 GeV/c$.

partments and requiring a track reconstructed in the Muon Spectrometer section, a pion-free sample of muons was selected and the distribution of the energy seen in the calorimeters studied. The figure 4.13(a) show the spectra of these energies and the figure 4.13(b), the probability for a muon to lose more than a certain energy. Simulation results are presented along read data. As it can be seen there is a very good agreement between the H8 data and the Monte Carlo simulation.

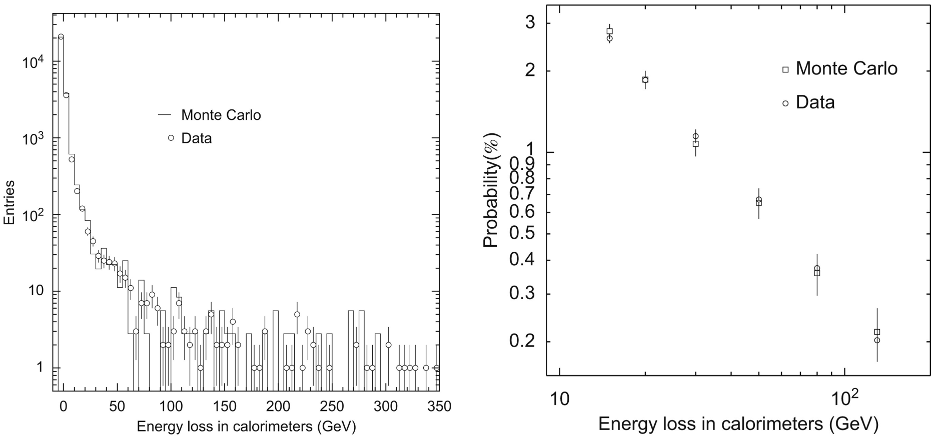

(a) (b)

Figure 4.13: (a) Energy deposited in the calorimeters by particles tagged as muons. (b) Probability in % for catastrophic energy loss as a function of the energy lost in the calorimeters

The data samples collected at the ATLAS H8 setup were actually the first large size ones from the real devices that we could used. These tests allowed to check many basics aspects of the detector functioning and simulation as well as an opportunity to test successfully in real conditions, the software integration of the reconstruction program in the larger framework designed to feed it with devices signal and condition data such as informations from the stations alignment algorithms which were themselves brilliantly validated.

4.3 Performance from Cosmics Rays Commissioning

In 2008 and 2009, ATLAS recorded hundreds million of cosmic ray events. This extended period allowed to perform the commissioning of the different sub-detectors and of the software [74]. The cosmics rays reach the ATLAS detectors mainly via the two access shafts used for the detector installation shown in figure 4.14(a), producing spots of downward tracks as shown on figures 4.14(b) and 4.14(c). The characteristics of these events led to important changes in the muon reconstruction algorithm.

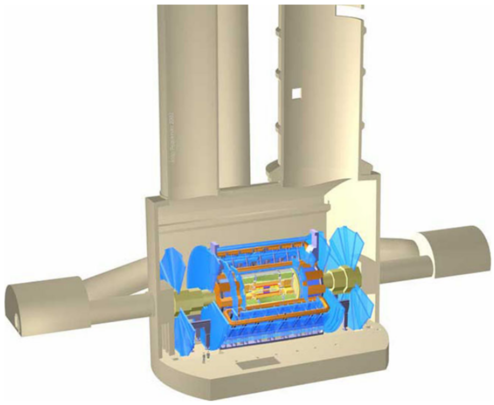

(a) The ATLAS detector in the experimental cavern. Above the cavern are the two access shafts used for the detector installation

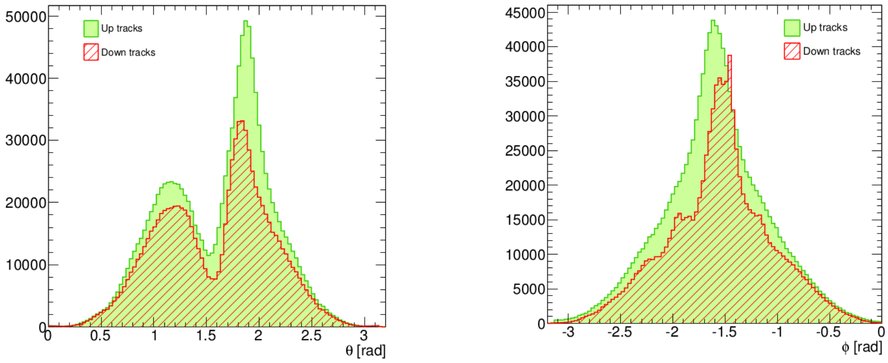

(b) Distribution of the polar angle of cosmics ray tracks; the peaks corresponds to the access shafts

(c) Distribution of the azimuthal angle of cosmics ray tracks;

Figure 4.14: Cosmics rays in ATLAS (from [66])

The most important feature of these muons is that they are not at all pointing to the Interaction point, not at all projective. All the criteria requiring such a projectivity had to be relaxed both for Track Segment and Tracks reconstructions. In addition, the presence of second coordinate hits in Track segment seeding Track reconstruction, was relaxed owing both for the topology and the triggering conditions on cosmic rays.

The second important feature of the cosmics muons is their complete asynchronism with respect to the 40 MHz ATLAS readout clock synchronized on the LHC clock during normal operation. This is a major difficulty for the MDT drift time conversion in radius since the starting time, the t_0, with respect to which the arrival time is to be counted, is unknown. For *Muonboy*, this led to develop a stage, preceding the actual reconstruction, in which for each Station containing a Track Segment, a scan on t_0 was done to find the value giving the best penalty factor for this segment (cf section 3.1.2).

This stage sets a table associating to each Station the best value found, which, in a second stage, is handed over to the ATHENA "R-T" `Service` prior the full reconstruction stage. These conditions led also to use in the reconstruction a reference resolution of 500μm instead of the 100μm used in standard settings.

The last of the peculiarities of the cosmics muons having a major impact, is the direction of their propagation. Although the situation for a track in the bottom part is "standard", changes had to be made in *Muonboy*, especially for the back tracking stage, for the tracks in the upper part.

Many studies were done on the cosmic ray event samples and reported in [74, 75] and especially in [66]. Some of them are presented bellow.

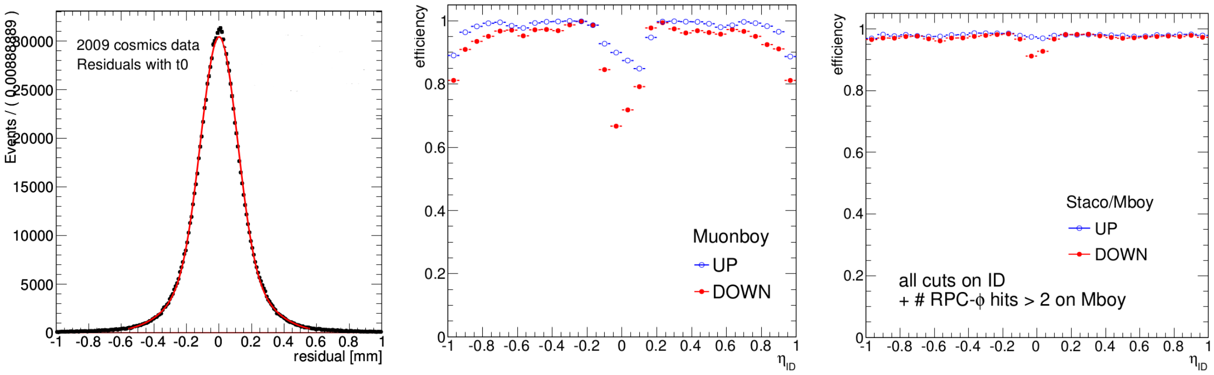

(a) MDT hits residuals (b) *Muonboy* Efficiency (c) *Staco* Efficiency conditioned to successful stand-alone reconstruction.

Figure 4.15: Examples of studies on the cosmic rays (from [66])

The figure 4.15(a) shows the distribution of the residuals of MDT hits belonging to a reconstructed track, i.e the difference in impact parameter between the value predicted by the reconstructed track trajectory and the actually measured impact parameter. From the residual studies a MDT impact parameter resolution of ~150μm was derived.

The figure 4.15(b) displays the reconstruction efficiency of the stand-alone reconstruction. The non projective nature of the tracks is responsible of the enlarged and complex structure of the η ~0 gap.

The efficiency of the combined reconstruction relatively to the stand-alone reconstruction is shown in figure 4.15(c) for a special selection, requiring at least three ϕ RPC-hits, picking up track topologies closer to the collision topology. By conditioning to the stand-alone successful reconstruction, one sees that most of the peculiarities of dealing with cosmic rays cancel out, but a small drop of the efficiency at η ~0 for the tracks reconstructed in the lower part of the detector.

The figure 4.16 shows the distributions of the difference $\Delta p = p_{MS} - p_{ID}$, of the momenta of the Muon Spectrometer and ID tracks. The left part of the figure is obtained taking the Muon Spectrometer tracks measured at the entrance of the Muon Spectrometer. One clearly sees the effect of the energy lost in the calorimeters in the difference between the upper and lower tracks samples. The right part of the figure is obtained taking the Muon Spectrometer tracks backtracked down to the beam line, nicely illustrating the correction of energy in the back tracking stage.

Very nice studies of the tracks parameters resolutions were done by comparing the two pieces of the same cosmic ray reconstructed in the upper and lower parts of the detectors. For instance the width of the distribution of the ratio $\frac{\Delta p_T}{p_T} = 2\frac{p_T^{up}-p_T^{down}}{p_T^{up}+p_T^{down}}$ computed for the transverse momenta of the upper and

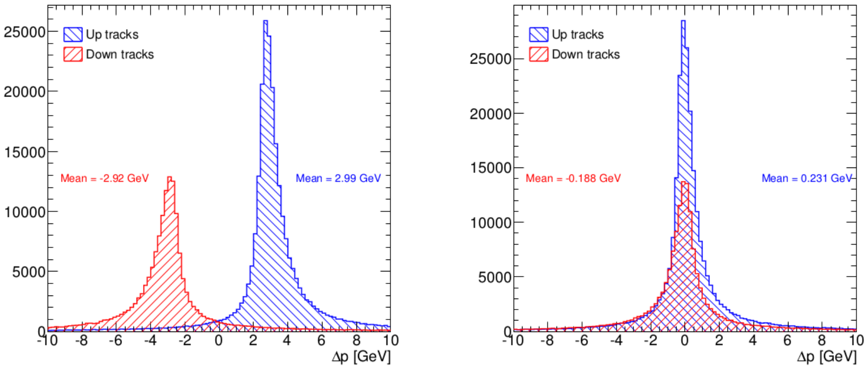

Figure 4.16: Difference of momentum Δp between Muon Spectrometer and ID tracks; Left: Muon Spectrometer tracks at the entrance of the Spectrometer Right: Muon Spectrometer tracks back tracked to beam line (from [66])

lower tracks back tracked to beam line is expected to be $\sqrt{2}$ times the momentum resolution. Actually because of the Landau tails, the resolution is extracted by fitting a Landau distribution convoluted with a Gaussian. This leads to the result shown in figure 4.17 in which one recognizes the characteristic shape of the momentum resolution already discussed about the simulation figures 4.2, 4.6(a) and 4.6(b).

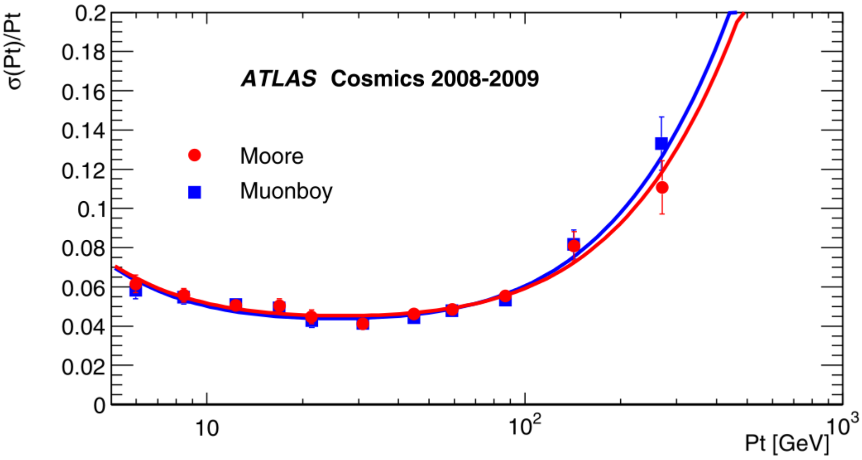

Figure 4.17: Transverse momentum resolution for the barrel region only, $|\eta| < 1.1$. (from [75])

The commissioning data were the first test of the reconstruction software performed at the scale of the full apparatus. The integration of the software was complete and tested in real conditions.

Although with limitations imposed by the particularities of the cosmics rays, many important aspects were studied, checked and understood such as tube resolution and energy losses corrections. These particularities forced to develop specific algorithms which although they were not to be used later in collisions data, remained crucial for such specific and important tasks as the alignment with cosmics data.

4.4 Performance on Collisions Data

The most recent evaluation of the Muon reconstruction performance on collision data has been published in [76] (older studies can be found in [77] and [78]) . The Muon reconstruction used in this paper is the *STACO* chain, since most of the ATLAS analyses and in particular the Higgs analyses [79, 80] used it.

As we have seen the *STACO* chain comprised the standalone reconstruction *Muonboy*, the combined (CB) reconstruction *Staco*, and the Track Segment Tagging (ST) identification *MuTag*. An other identification algorithm *CaloTag* was considered which associates an ID track to deposits in the calorimeters compatible with a minimum ionizing particle. The sample of the *CaloTag* candidates has the lowest purity and *CaloTag* is used for $|\eta|$ <0.1 only, in the central part where the Muon Spectrometer instrumentation is very poor. Some of the results of the analyses of [76] are described here.

The muon reconstruction performance are estimated from decays of Z, J/ψ and Υ in pairs of muons. The data samples used in these analyses, were mostly collected in the $\sqrt{s}$ = 8 TeV run of 2012 and correspond to an integrated luminosity of 20.3pb^{-1} . The studies are based on about 9M of $Z \rightarrow \mu\mu$ events, 2 to 17M (depending on the analysis performed) $J/\psi \rightarrow \mu\mu$ events, and about 5M of $\Upsilon \rightarrow \mu\mu$ events. The background processes considered are $Z \rightarrow \tau\tau$, $W \rightarrow \mu\nu$, $W \rightarrow \tau\nu$, diboson (WW, WZ and WW) productions, $t\bar{t}$, $b\bar{b}$, $c\bar{c}$, QCD multijet and W+jets. The reconstruction efficiencies on $Z \rightarrow \mu\mu$ are shown in figure 4.18.

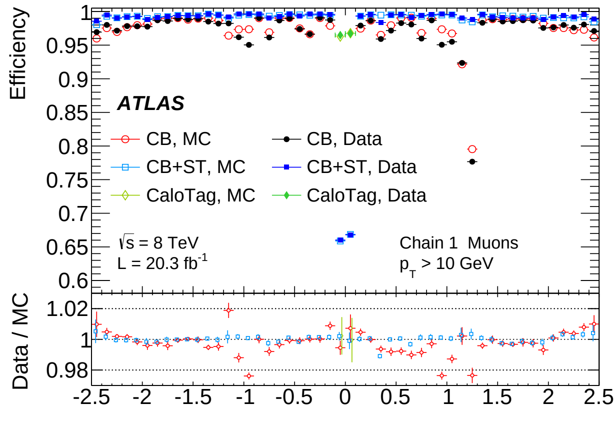

Figure 4.18: Muon reconstruction efficiencies as a function of η measured in $Z \rightarrow \mu\mu$ for muons with $p_T > 10$ GeV .

The combination of *Staco*+*MuTag* (CB+ST) gives an uniform muon reconstruction efficiency of about 99 % over most the detector regions. The drop of the *Staco*+*MuTag* efficiency in the $|\eta|$ <0.1 region is compensated by *CaloTag*. The drops of the *Staco* efficiency in the regions, 1.1< η <1.3, due to the missing EE Stations, and $|\eta| > 2$ are recovered by *MuTag* as expected (cf section 3.3) and anticipated from simulation studies (cf section 4.1). The figure 4.18 shows a good agreement between Monte Carlo and Data. This good agreement is illustrated by the figures 4.19 which show the ratio between data and Monte Carlo efficiencies over the (Φ, η) space.

All the discrepancies between Data and simulation can be tracked down to issues in the simulation or to detector conditions not included in the simulation. For instance the drop of ~0.1% of the *Staco* at η ~0.5 is due non simulated RPC detector conditions.

Owing to the less demanding criteria of *MuTag*, the Data/Monte Carlo agreement for the *Staco*+*MuTag* efficiency is in general better, as shown in the figure 4.19(b) but on a very localized spot which has been understood as originating from a partially inactive MDT chamber which has not been simulated accordingly.

The study of the momentum scale and resolution of a reconstructed muon has be done using $Z \rightarrow \mu\mu$ and $J/\psi \rightarrow \mu\mu$ events by rescaling and smearing the momenta reconstructed in Monte Carlo

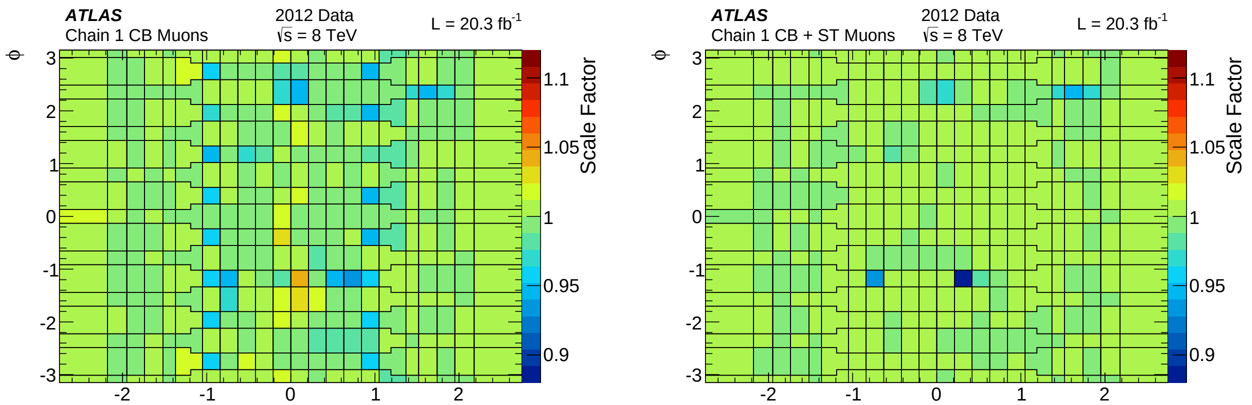

(a) (b)

Figure 4.19: Data/MC efficiency scale factor (a) for CB and (b) for CB+ST muons as a function of η and ϕ for muons with p_T >10 GeV .

events. It was found that the resolution of the stand-alone reconstructed muon has to be corrected by at most 15%. In addition to an absolute correction of ∼30 MeV at low momenta, a relative correction of few per mill was found necessary: less than 0.1% for large MS sectors, ∼0.3% for small MS sectors and up to ∼0.4% in some corners.

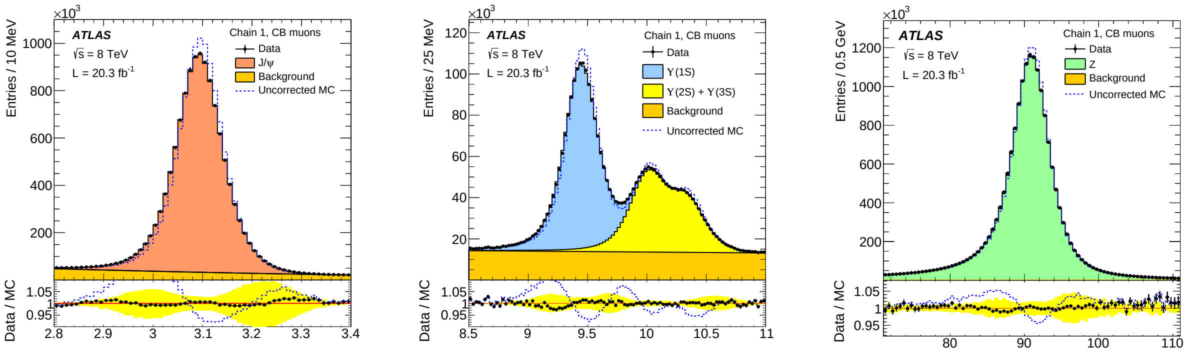

(a) (b) (c)

Figure 4.20: Dimuon invariant mass distribution of $J/\psi \rightarrow \mu\mu$ (a), $\Upsilon \rightarrow \mu\mu$ (b) and $Z \rightarrow \mu\mu$ (c) candidate events reconstructed with CB muons.

Finally the mass scale and resolution of dimuon system for the combined reconstruction was studied on $Z \rightarrow \mu\mu$, $J/\psi \rightarrow \mu\mu$ and $\Upsilon \rightarrow \mu\mu$ events by fitting the mean and width of the distributions of the mass of the di-muon system for Monte Carlo samples adjusted to the same distributions on data, as shown in the figures 4.20. The mean mass results of these fits are shown as a function of η in figures 4.21 for the Z, J/ψ and Υ samples.

As shown by these figures, the mass scale at the Z mass is appropriately described by the uncorrected Monte Carlo at a level better than 0.1%. For lower masses and high η, a correction up to 0.5% becomes necessary. This is understood as the effect of imperfections of the energy losses simulation, the relative effect of which is higher at lower p_T and when the weight in the combination of Muon Spectrometer measurement is greater as in the high η region. The dimuon mass widths were also studied and it was found that the uncorrected Monte-Carlo widths are lower by 5 to 10 % than those observed in the data.

To summarize, the *STACO* chain was shown to perform extremely well on the data from collisions data, necessitating efficiencies and energy scale corrections at the few per mill level only.

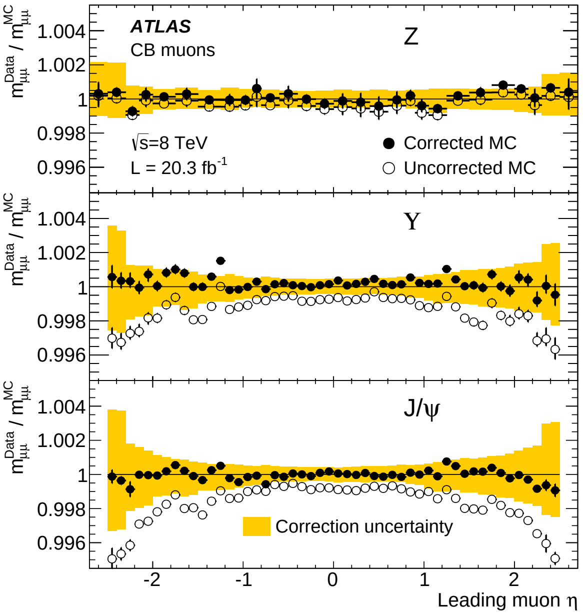

Figure 4.21: Ratio of the fitted mean mass, $m_{\mu\mu}$, for data and corrected MC from Z (top), Υ (middle), and J/ψ(bottom) events as functions of the pseudo-rapidity of the highest-p_T muon.

4.5 Conclusions

The performance on simulated sample were established routinely during the entire period of the development of the *STACO* chain. Actually this development has been always driven by the need to maintain the highest efficiencies for the lowest possible rate of fake muons.

Equally important has been the imperative of deliver a software that could make the best use of the informations on the data taking conditions among which, the most important ones, the alignment data. Hence the importance of the investment in the description of the geometry of the detector in close connection with our colleagues in charge of the alignment of the stations of the Muon Spectrometer. All this was tested with success in realistic conditions as soon as it became possible with the H8 test-beam setup.

At the end of years of development and testing, the *STACO* chain was fully operational for the start of the LHC foreseen at the end of 2008. The LHC incident and the resulting delay opened a extended commissioning period. This allowed to check various basic aspects of the detector and of the software, within however the limitations imposed by the specificities of the cosmics muons.

But the last words of all this story has been for the real data when the LHC started at last. For the greatest satisfaction of all those who have been involved in the long development of the *STACO* chain, tests on resonances have confirm its quality beyond expectations in terms of efficiencies, resolution, energy scale biases and purity. From the start, the *STACO* chain was ready to serve the physics analyses.

Chapter 5

Two Bosons production: Measurements of cross sections and anomalous Triple Gauge couplings

In this chapter, I describe the studies performed on the data of the Run 1 period of LHC data taking, of the production of two vector bosons, W, Z or γ, with the W and Z decaying leptonically, in electrons or in muons. These final states fitted well with the expertise on leptons reconstruction available in the ATLAS group of my institute at the start of the LHC, in particular on the reconstruction of the muons which for all the analyses presented in this chapter was performed with the *STACO* chain.

These studies cover all the diboson final states, ZZ, WZ, WW, $W\gamma$ and $Z\gamma$. They were performed with many ATLAS colleagues. In my institute, they resulted from an exalting collaboration which, beside my Saclay colleagues Samira Hassani and Ahmimed Ouraou, has involved a group of young and talented colleagues physicists: João Firmino da Costa, Eve Le Menedeu, Camilla Maiani, Joany Manjarrés Ramos, Sofia Protopapadaki, and Dimitra Tsionou. Thanks to them I could contribute to these measurements in particular on their Statistical aspects developping a Software package `FLIT` [81] which has been used to extract the diboson production cross sections and the limits on anomalous Triple Gauge couplings. I had similar contributions to the measurement of the production cross sections of $W\gamma\gamma$ three bosons final state [82] and of the 4-leptons final states [83], two analyses that are not reported here.

Hereafter I first review the diboson productions. Their cross sections at the LHC are discussed in section 5.2.1. The anomalous couplings between three vector bosons that the study of the diboson production allows to probe, are discussed in section 5.2.2. The topic of the anomalous couplings, theory and available measurements, is developed in some details in a review proposed in the appendix A. In this chapter I will refer often to this review.

Then from section 5.3 to section 5.7, I report the measurements, cross sections and anomalous couplings, of the production of ZZ pairs [84, 85], of WZ pairs [86–89], of WW pairs [90, 91], of $W\gamma$ pairs [92], and of $W\gamma$ pairs [92]. The statistical aspects of these measurements are developed in some details in the section dedicated to the ZZ pair production.

Finally I conclude this chapter in section 5.8 with a summary and a discussion of the cross sections measurements and of the limits on anomalous couplings that are presented in the previous sections.

5.1 Introduction

The Standard Model (SM) gauge symmetry $SU(3)_c \times SU(2)_L \times U(1)_Y$ imposes interactions between Gauge bosons. For instance the gluons, gauge fields of the $SU(3)_c$ symmetry, engage in three and four gluons interactions as a consequence of the non-abelian nature of $SU(3)_c$. Similarly the non-abelian nature of the $SU(2)_L$ symmetry leads to Triple and Quartic Gauge bosons Couplings (TGC and QGC) of the electroweak vector bosons W, Z and γ.

However these fields are not the gauge fields of the $SU(2)_L \times U(1)_Y$ symmetry but mixtures of them. The W, Z and γ are promoted to the status of the relevant physical fields after the Spontaneous Electroweak Symmetry Breaking. In the course of this breaking, the W and Z bosons acquire masses and couplings to the Higgs boson.

The precise values prescribed by the SM for the Triple and Quartic Gauge bosons Couplings and for the Higgs boson couplings, are crucial for the SM renormalizability. Any departure has major consequences on the tree-level unitarity of electroweak processes such as the scattering of two W-bosons [1]: the Triple and Quartic Gauge couplings are exactly so that the leading divergences of the cross section with the energy do cancel while the Higgs boson couplings do insure the cancellation of the sub-leading divergences.

Therefore the experimental investigation of TGCs offers an opportunity not only to explore the gauge symmetry of the SM but also to catch manifestations of new physics in a particularly sensitive area. Indeed anomalous TGCs and Higgs boson couplings are among the low-energy effects through which such a new physics could reveal itself well before the energy scale of the associated new degrees of freedom is reached. To study these low-energy effects in a model independent way is the purpose of the currently very active field of the Effective Field Theory (EFT) analyses.

A review of the physics of the interactions between electroweak bosons is proposed in the appendix A. Hereafter I will remind few points, will refer to this appendix for details.

5.2 Two Bosons production at LHC

5.2.1 Cross sections and strong and electroweak corrections

The factorization theorem backs the QCD-improved parton model which describes high energy proton-proton interactions in terms of scattering of the partons which composed the protons. The cross section of the proton-proton interaction is the convolution of the parton-parton scattering cross section weighted by the probabilities of the partons to carry some fraction of the protons momenta. The cross section of the $pp \to V_1 V_2 X$ process with two bosons W, Z or γ in the final state can be written as

$$\sigma_{pp} = \iint \mathrm{d}x_a \mathrm{d}x_b \;\; f_a(x_a, \mu_f) f_b(x_b, \mu_f) \;\; \sigma_{ab}(x_a, x_b, \mu_f, \mu_r) \tag{5.1}$$

where $f_{a,b}(x_{a,b}, \mu_f)$ are the parton distribution functions (PDFs) for partons in proton and σ_{ab} is the cross section of the hard interaction $ab \to V_1 V_2$. The scales μ_f and μ_r are the factorization and renormalization scales resulting from the treatment of the divergences occurring in long-distance/low-energy and short-distance/high-energy physics respectively.

These factorization and renormalization scales would be irrelevant if the contributions at all orders were collected in equation (5.1). For finite order approximation, it is advised to set $\mu_f = \mu_r = Q$ where Q is a “natural” hard scale of the process, say the mass of the two bosons system. The impact of missing higher orders uses to be estimated from the changes of the cross section computed varying a

---

[1] A reconstruction of the SM Lagrangian can even be attempted from the sole perspective of the reining in of the divergences of these processes [93]

parameter ξ from 2 to 1/2 while setting $\mu_f/\xi = \mu_r/\xi = Q$ or sometimes $\mu_f\xi = \mu_r/\xi = Q$. As expected the relative change uses to decrease when the order of the pertubative expansion increases. However the arbitrariness of the procedure has been often underlined as has been the risk of underestimating of the true uncertainties.

The accepted wisdom is that Next-to-Leading-Order QCD (NLO QCD) corrections are needed to get a reliable prediction of the cross section and Next-to-NLO QCD (NNLO QCD) corrections to get a first meaningful estimate of the theoretical errors [94]. Things can get complicated by the opening of processes with new initial states in higher Orders.

The Leading-Order (LO) diagrams for the two bosons production, $qq' \to V_1V_2$, are shown in figures 5.1. The two bosons final state V_1V_2 can be WW, WZ, $W\gamma$, ZZ and $Z\gamma$.

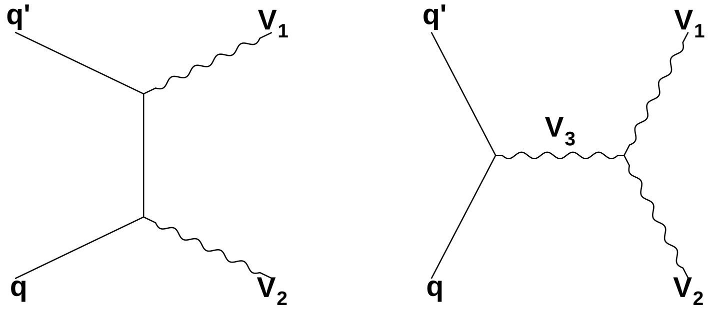

Figure 5.1: LO diagrams for two Bosons production at LHC

The NLO QCD corrections arise from virtual loop diagrams and the real emission diagrams as those shown in figures 5.2, $qq' \to V_1V_2g$ as well as $qg \to V_1V_2q'$, a qg initial state process opening at NLO. These corrections are very large and non-uniform over the phase space. The computations of the NLO QCD corrections started in the early 90's and were available for all channels at the start of the Tevatron Run 2 [95–108]. They have been assessed for LHC Run 1 with the parton-level Monte-Carlo program `MCFM` in [109]. The NLO QCD corrections amount for several tens of % for integrated cross sections and up to few hundreds of % in places for some differential cross sections.

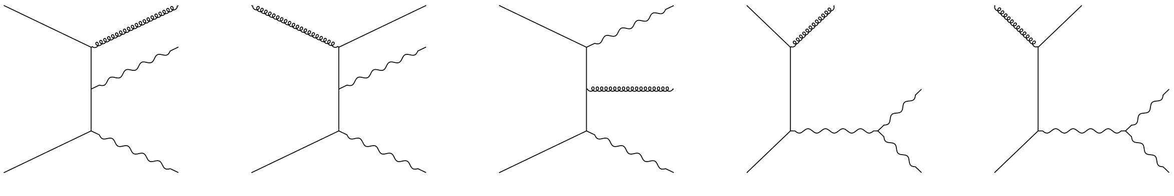

(a) (b) (c) (d) (e)

Figure 5.2: Some real emission NLO diagrams for two Bosons production at LHC

An early known contribution of a different kind comes from the Higgs boson production diagram shown in figure 5.3(a) followed by the Higgs boson decay in two electroweak bosons. This particular process contributes for less than about 5% to the WW and ZZ channels. Because of its importance for the Higgs searches, it has received a lot of attention. It has been known for some time up to the NNLO QCD level and up to the NLO for the electroweak corrections [110]. The NNNLO QCD corrections have been obtained recently [111].

The size of the NLO QCD corrections of two bosons production motivated assessment of the NNLO QCD corrections less specific than the Higgs production one. For a long time, the only available of these contributions was the one arising from gluon-gluon fusion diagram shown in figure 5.3(b) [112–120]. This gg initial state process opens at NNLO. The suppression of its contribution by an extra α_S factor with respect to NLO corrections is compensated by the large gluon PDF. It was assumed that this NNLO QCD gg correction, of the order of 10%, was providing the bulk of the full NNLO QCD correction.

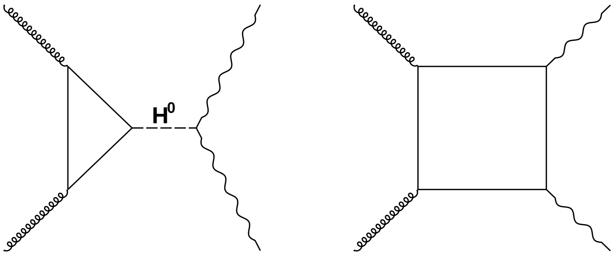

(a) (b)

Figure 5.3: Some NNLO diagrams for two Bosons production at LHC

Beyond NLO QCD corrections

With the advent of the LHC Run 1 analyses, some tensions between the measurements and the predictions have sparked a surge of theoretical computations of the complete NNLO QCD corrections. They are now available for all channels but the WZ one [121–125]. They are much smaller than the NLO QCD corrections, usually of the order of a couple of tens of %.

In [125], the NNLO QCD corrections for the integrated cross sections of $Z(\to \ell^+\ell^-)\gamma$ and $W(\to \ell\nu)\gamma$, were found to amount for about 8% and 19% respectively at $\sqrt{s} = 7$ TeV. They decrease down to 3% and 7% respectively when it is required that the number of jets is 0 [2]. Interestingly the relative contribution of the gluon-gluon fusion was found quite small, about 6% of the NNLO QCD correction for $Z(\to \ell^+\ell^-)\gamma$. On the contrary the gluon-gluon fusion contribution to the NNLO QCD corrections was found large for the ZZ and WW [121, 124] channels: the NNLO QCD corrections were found to increase cross sections by about 10% and more than a half of this increase is due to the gluon-gluon fusion.

It should be noted that in all cases, the impact of the missing higher orders on the NLO order cross section estimated in the usual way, was found to largely underestimate the actual difference between the NLO and NNLO QCD cross sections. For instance a factor 3 difference was found in the case of the WW final state [124]. The uncertainties of the order of few % estimated in the same way but for the NNLO QCD cross sections are believed to be more reliable. However it is already known that they are too underestimations for the case of the ZZ final state as discussed below.

For the WZ final state, only the so-called “approximate” NNLO ($\tilde{n}$NLO) QCD estimation seems to be available [126–128]. This particular theoretical approach has been validated against the full NNLO QCD computation for the WW channel [127]. In [126], the integrated WZ cross section was found to be increased by about 5% by the NNLO QCD corrections. The impact on some differential distributions was found however significantly larger reaching in places few tens of %. Interestingly some observables are much less affected than others. In particular the NNLO QCD corrections of the distribution of the transverse mass of the WZ system are much smaller than the corrections of the

---

[2] The reference [125] gives also the NNLO QCD corrections $Z(\to \nu\nu)\gamma$, 12% decreasing down to −2% if one requires 0 jet

distribution of the missing transverse energy or of the transverse momentum of the hardest of the decay leptons.

Further QCD corrections beyond the NNLO QCD order have been investigated. For instance the NNNLO QCD contribution of the gluon-gluon fusion in the ZZ channel was studied in [129]. It was found to reach from 50% to 100% of the NNLO QCD gg contribution which, as mentioned above, accounts for more than a half of the full NNLO QCD correction. Actually this increase exceeds the uncertainty from missing higher orders estimated in the NNLO QCD ZZ study of [121]. These NNNLO QCD gg contributions provide for now the proper estimate of the uncertainties from missing higher orders for the NNLO QCD estimations.

Other QCD theoretical developments have been triggered by the ATLAS and CMS measurements of the WW cross sections $\sim 2\sigma$ above predictions [90, 130–132]. In order to circumvent a large $t\bar{t}$ background, these cross sections were obtained from counts of events without jet above a certain p_T threshold. This dependence on transverse momentum motivated to resort to techniques of resummation of Leading Logarithms (LL) contributions on top of the fixed order NNLO QCD corrections. These techniques sum up to all orders contributions of the form $\alpha_S^n L^m$ where L are large logarithms of the ratio of the transverse momentum to the WW system mass. These corrections, known now up to NNLL+NNLO QCD order, have alleviated the discrepancy between measurements and predictions [133–136].

NLO EW corrections

With the level of precision reached for the QCD corrections, it is necessary now to know the electroweak corrections at the Next-to-Leading-Order (NLO EW). Indeed since $\alpha_{EW} \sim \alpha_S^2$, the NLO EW and NNLO QCD corrections can be guessed to be of the same order of magnitude. The NLO EW corrections are now known for all channels [137–143]. For the integrated cross sections, they are typically small, of the order of few percent, e.g. $\sim +2\%$ for the WW channel and $\sim -3\%$ for the ZZ and $W\gamma$ channels, and even negligible for the WZ channel [139, 143]. However they can reach few tens of % in places for differential cross sections. An interesting feature is that these corrections receive contributions from photon induced processes such as for instance $\gamma q \to WZq'$. These contributions are negligible for ZZ but can be significant when a W-boson is in the final state. Therefore they depend on the photon PDF in the proton which is not well known [144]. Assessment of the uncertainties of the electroweak correction will become an acute issue for the higher statistics at higher energies available for the Run 2.

Monte Carlo Programs

The comparison of the theory and experiments rests on the availability of Monte-Carlo programs which, incorporating the most up-to-date theoretical predictions, produce samples of realistic physical events. These events can be propagated in the detailed simulation of the detectors, and then analyzed like the real data.

Key components of the General purpose Monte-Carlo programs, such as `PYTHIA` [145], `SHERPA` [146], or `HERWIG` [147] are their Parton Shower (PS) algorithms which relate a hard process defined at parton level to a final state of hadrons and other particles that can feed detectors simulation. From a configuration of initial and final state partons, a PS algorithm generates a cascade of successive branchings of a mother parton to two daughter partons down to a certain stage at which partons form hadrons. PS algorithms sum up soft and collinear contributions but are inaccurate for large angle hard emission. On the contrary, matrix elements calculations describe well processes with largely separated energetic partons but are not convenient for a realistic final state description.

During the last decade, tremendous progress have been made combining the two approaches by matching PS and matrix elements calculations avoiding double-counting in kinematic regions where they overlap and by consistently merging samples of different parton multiplicities. These efforts lead to modern Monte-Carlo programs producing physical events samples with corrections up to NLO QCD such as `MC@LNO` [148] and `POWHEG` [149].

As we have seen, the present focus is on NNLO QCD and NLO EW corrections. Quite recently, implementations of corrections at NLO for both QCD and EW have been presented in the `POWHEG` and `HERWIG` contexts in [150, 151] and methods and implementation prototypes for the combination of NNLO QCD and PS have been proposed in [152, 153].

5.2.2 Anomalous couplings

As shown in figure 5.1, the Two Boson production involves a vertex with three Gauge bosons. These Triple Gauge Bosons Coupling (TGC) vertices can be the "charged" $WW\gamma$ and WWZ vertices, involved in the WW, WZ and $W\gamma$ productions, or the "neutral" ZZZ, $ZZ\gamma$ and $Z\gamma\gamma$ vertices, involved in the ZZ and $Z\gamma$ productions. As discussed in the section A.1, the Standard Model does fix precisely the forms of the charged TGCs and does forbid any neutral TGCs. These prescriptions are indissociable from the SM renormalizability.

A fairly general description of interactions departing from those prescribed by the SM is provided by the framework of the Effective Lagrangians discussed in sections A.2.1 and A.3.1. These Lagrangians describe interactions between the W-boson, Z-boson and photons fields that are allowed under minimalist conditions such as Lorentz invariance and Bose symmetry. The departures from the SM are parametrized by coupling constants, null in the SM, called anomalous Triple Gauge bosons Couplings (aTGCs) which appear in the Effective Lagrangians (A.13) and (A.29) given in appendix. These aTGCs are shown in tables 5.1 along with the vertices and the two Boson productions that they affect, and the behaviors under C and P of the interactions they account for.

(a) Charged TGCs

<table>
<tr><td>Vertex</td><td colspan="2">WWZ</td><td colspan="2">$WW\gamma$</td></tr>
<tr><td>Two boson production</td><td>WZ</td><td colspan="2">WW</td><td>$W\gamma$</td></tr>
<tr><td>C and P
$\not{C}$ and/or $\not{P}$</td><td colspan="2">Δg_1^Z, $\Delta\kappa_Z$, λ_Z
g_4^Z, g_5^Z, $\widetilde{\kappa}_Z$, $\widetilde{\lambda}_Z$</td><td colspan="2">Δg_1^γ, $\Delta\kappa_\gamma$, λ_γ
g_4^γ, g_5^γ, $\widetilde{\kappa}_\gamma$, $\widetilde{\lambda}_\gamma$</td></tr>
</table>

(b) Neutral TGCs

<table>
<tr><td>Vertex</td><td>ZZZ</td><td colspan="2">$ZZ\gamma$</td><td>$Z\gamma\gamma$</td></tr>
<tr><td>Two boson production</td><td colspan="2">ZZ</td><td colspan="2">$Z\gamma$</td></tr>
<tr><td>CP
$\not{C}\not{P}$</td><td>f_5^Z
f_4^Z</td><td>f_5^γ
f_4^γ</td><td>$h_{3,4}^Z$
$h_{1,2}^Z$</td><td>$h_{3,4}^\gamma$
$h_{1,2}^\gamma$</td></tr>
</table>

Table 5.1: Anomalous Triple Gauge Couplings in Two Bosons production processes

The effect of the presence of an aTGC is a modification of the cross section at high energy. This is illustrated in figure 5.4 showing for the WZ production, the distribution of the transverse momentum of the Z for Data and simulations of SM processes and the contribution of non null aTGCs [86]. Clearly the evidence for aTGCs is to be looked for in an excess at high energies.

This aTGC characteristic leads to violation of the unitarity of the Two boson production cross section at some energy in the center of mass, $\sqrt{\hat{s}}$. Traditionally, this violation is cured by transforming the aTGCs into Form Factors depending on the energy using the ansatz

$$\zeta(\hat{s}) = \frac{\zeta_0}{(1+\hat{s}/\Lambda_{FF}^2)^n} \tag{5.2}$$

As discussed in sections A.2.2 and A.3.2, a dependence with energy is possible in the framework of the sightly distinct approach of the Vertex Functions. However the arbitrariness of the ansatz (5.2) has been criticized many times (cf introduction of the section A.2.3). The limits that are reported in this chapter have been obtained without Form Factors.

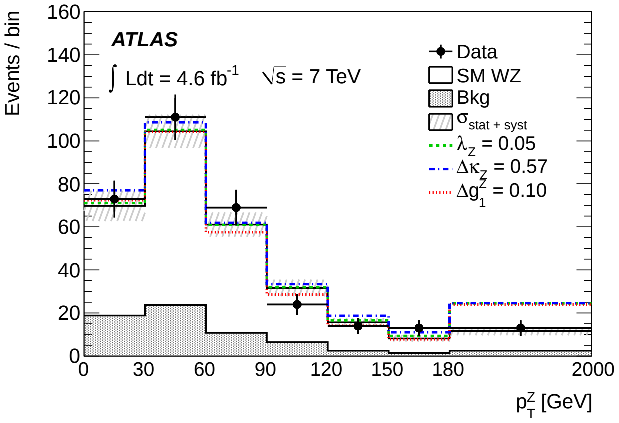

Figure 5.4: Distribution of p_T^Z of WZ candidate events of the 7 TeV WZ ATLAS analysis [86]; Data are shown together with expected background and signal events, assuming the Standard Model; Expected events in the case of anomalous TGCs are also shown.

An very practical issue is that there is a lot of aTGCs, viz 14 charged and 12 neutral aTGCs. There is not too much to expect from the combination of the measurements of the different Two Bosons productions. For instance, one sees in tables 5.1 that the ZZ and the $Z\gamma$ productions depend on two distinct sets of parameters. Therefore the combination of the measurements of these two processes does not bring any further constrain on the neutral aTGCs. This holds true also for the WZ and $W\gamma$ productions. However since the WW production does depends on all the charged parameters, the limits on the charged TGCs limits are improved by combining the measurements of the three WZ, $W\gamma$ and WW processes. But with 14 parameters to deal with, this is a very small consolation.

The number of parameters can be reduced by imposing $U(1)_{em}$ on the charged Effective Lagrangian (A.29) [3]. But this has the very limited effect of removing just three aTGCs, namely Δg_1^γ, g_4^γ and g_5^γ. Much more effective is the traditional choice to exclude in addition the charged aTGCs violating C and/or P and the CP violating neutral aTGCs (the second rows in tables 5.1): it remains only 5 charged and 6 neutral aTGCs. This is still a large number of parameters and, specifically for the charged aTGCs which received a lot of attention, some "scenarios" were developed which bluntly impose certain relations between the parameters. Among them, the “LEP scenario” imposes the relations

$$\lambda_\gamma = \lambda_Z \quad \text{and} \quad \Delta g_1^Z = \Delta\kappa_Z + \tan^2\theta_W \Delta\kappa_\gamma \tag{5.3}$$

reducing to 3 the number of independent charged aTGCs respecting C and P. Clearly in the context of the Effective Lagrangian approach such relations come out from nowhere. Their origin is to be found in an other much more consistent and actually as old approach, the Effective Field Theory approach.

This approach is discussed in some details in the sections A.2.3, A.3.3, and A.5. The Effective

---

[3] The neutral Effective Lagrangian (A.13) is already $U(1)_{em}$ invariant

Field Theory (EFT) is concerned with low-energy manifestations of a Physics Beyond the Standard Model "living" at a high energy scale, Λ. However, the EFT remains agnostic on the details of this new Physics and retains only that it can allow interactions between the "low-energy" SM fields beyond those of the SM Lagrangian [4].

The EFT Lagrangian is the infinite sum of all fields couplings invariant under $SU(3)_c \times SU(2)_L \times U(1)_y$. Each of these couplings is an operator O_i^d of mass-dimension d in the SM fields "before" the Spontaneous Symmetry Breaking, i.e the Gauge Fields of $SU(3)_c \times SU(2)_L \times U(1)_Y$, the Higgs doublet and the quarks and leptons fields.

Remarkably, the SM Lagrangian collects already all these couplings up to mass-dimension 4. Therefore the EFT Lagrangian takes the form

$$L_{EFT} = L_{SM} + \sum_{d \geqslant 5} L_{EFT}^d \text{ with } L_{EFT}^d = \sum_i \frac{C_i^d}{\Lambda^{d-4}} O_i^d \tag{5.4}$$

in which the constants C_i^d are dimensionless and the effects accounted for by the term L_{EFT}^d are the smaller as d is larger. Re-expressed in term of the fields "after" the Spontaneous Symmetry Breaking, i.e. the W, Z, γ and Higgs boson fields, the EFT operators of mass-dimension $d \geqslant 5$, give birth to new couplings between them, i.e to new and therefore anomalous Triple Gauge Bosons couplings as well as new Higgs boson couplings.

From here, an EFT analysis proceeds by truncating the above expansion at some rank d_c, neglecting higher orders effects. Then because of this truncation, relations are predicted between the various anomalous Triple Gauge Bosons couplings and Higgs boson couplings which are valid however only up to the $\frac{1}{\Lambda^{d_c-4}}$ order. The operators O_i^d are known wholly up to the dimension 7 and for specific applications up to dimension 8. Since the odd dimension operators violate the conservations of baryon and lepton numbers, the first dimension considered is 6.

Due to the opportunities offered by the LEP2 measurements, the EFT description up to dimension 6 for the charged aTGCs have been established a long time ago [154]. Up to the $\frac{1}{\Lambda^2}$ order, the predictions are

$$\Delta g_1^\gamma = g_{4,5}^{\gamma,Z} = 0 \tag{5.5}$$

$$\lambda_\gamma = \lambda_Z \quad \text{and} \quad \Delta g_1^Z = \Delta\kappa_Z + \tan^2\theta_W \Delta\kappa_\gamma \tag{5.6}$$

$$\widetilde{\lambda}_\gamma = \widetilde{\lambda}_Z \quad \text{and} \quad \widetilde{\kappa}_Z + \tan^2\theta_W \widetilde{\kappa}_\gamma = 0 \tag{5.7}$$

reducing the 14 charged aTGCs of tables 5.1 to just 5 independent parameters that one can choose to be Δg_1^Z, $\Delta\kappa_\gamma$, λ_γ , $\widetilde{\kappa}_\gamma$ and $\widetilde{\lambda}_\gamma$. These 5 independent parameters are related to the constant couplings of the dimension-6 EFT operators by the relations (A.35), (A.37), (A.39) and (A.43) given in appendix. One should note that these latter relations do depend on the Basis of the dimension-6 EFT operators that was chosen while the relations (5.5), (5.6) and (5.7) are valid in any Basis (cf A.5 for more details on Bases issue).

The neutral aTGCs do not receive contributions from the dimension-6 EFT operators. So the EFT expansion should be pushed up to dimension 8. The predictions, which were derived more recently [155], are up to the $\frac{1}{\Lambda^4}$ order

$$h_{2,4}^{\gamma,Z} = h_3^\gamma = f_5^Z = 0 \quad , \quad f_5^\gamma = h_3^Z \quad \text{and} \quad h_1^Z = -f_4^\gamma \tag{5.8}$$

---

[4] The classical example of such mechanism is the 4-point interaction of the Fermi Theory of the β-decay which is ultimately explained in terms of exchange of the heavy W-boson.

reducing the 12 neutral aTGCs of tables 5.1 to just 4 independent parameters that one can choose to be f_5^γ, f_4^γ, f_4^Z and h_1^γ. These 4 independent parameters are related to the constant couplings of dimension-8 EFT operators by the relations (A.24), (A.26), (A.27) and (A.28) given in appendix.

The tables 5.2 show how the Two Boson production processes depend on the independent aTGC parameters in the EFT framework.

(a) Charged TGCs

	Δg_1^Z	$\Delta\kappa_\gamma$, λ_γ	$\widetilde{\kappa}_\gamma$, $\widetilde{\lambda}_\gamma$
WZ , WW	✓	✓	✓
$W\gamma$		✓	✓

(b) Neutral TGCs

	f_5^γ	f_4^γ	f_4^Z	h_1^γ
ZZ	✓	✓	✓	
$Z\gamma$	✓	✓		✓

Table 5.2: EFT aTGCs in Two Bosons production processes; the rows show the Two Bosons production channels; the columns show the aTGCs separated according to their behaviors under C and P; the mark "✓" indicates a dependence of the Two Bosons production on the particular aTGC.

The EFT approach is not just the Effective Lagrangian approach supplemented with opportune relations between the aTGCs.

It is an effective theory only valid at energies lower than Λ. Therefore such traditional devices as the Form Factors are to be excluded since the unitary violation issues that they cure, are explicitly outside the domain of validity of the theory. Beyond the banishment of the Form Factors, it is not yet totaly clear how this restriction is to be taken into account in the experimental analyses.

Moreover the EFT approach is limited to the effects of lowest order in Λ and neglects explicitly the higher orders. A consistent use of the EFT approach imposes some changes in the way limits on anomalous couplings are traditionally derived. For instance, the amplitude of the two bosons production process is the sum of the SM amplitude plus a non-SM amplitude proportional to the anomalous coupling ζ, schematically $|SM\rangle + \zeta \times |TGC\rangle$. Therefore the cross section, proportional to the square of the process amplitude is "naturally" a quadratic function of the anomalous couplings. The EFT approach consistency imposes to neglect the quadratic terms because they are of an order explicitly neglected, e.g. for the charged aTGCs case, since $\zeta \propto \frac{1}{\Lambda^2}$, the ζ^2 terms are of the order of $\frac{1}{\Lambda^4}$, i.e the same order of the contributions of the neglected dimension-8 operators. This has drastic consequences on the experimental aTGC limits that we will explore latter in this chapter.

5.3 Study of the ZZ Production

Hereafter I present the analysis of the production of two Z-bosons of the sample of the ATLAS data at 8 TeV .

The ZZ production can be studied in two channels for the decays of the two bosons system, $ZZ \rightarrow \ell\bar{\ell}\ell'\bar{\ell}'$ or $ZZ \rightarrow \ell\bar{\ell}\nu\bar{\nu}$, where l and l' are electrons or muons. Both channels were studied in the analysis of the ATLAS data at 7 TeV [156]. However only the measurements of the channel $ZZ \rightarrow \ell\bar{\ell}\ell'\bar{\ell}'$ has been published for the 8 TeV sample. Cross sections measurements were first presented in [84]. The analysis was completed and extended to measurements of aTGCs in the work of my PhD student Sofia Protopapadaki [85].

5.3.1 Selection and backgrounds

The final states of interest are those of the fully leptonic decays $ZZ \rightarrow \ell\bar{\ell}\ell'\bar{\ell}'$, with ℓ and ℓ' muons or electrons. They contain 4 muons, 2 muons and 2 electrons, or 4 electrons. Hereafter they will be named $\mu\mu\mu\mu$, $ee\mu\mu$, and $eeee$. The signature is very simple and clean: 4 leptons of high transverse momenta, well separated and isolated, that can be paired in two same flavor opposite sign couples forming Z-like systems. Among all the channels of two bosons productions, the $ZZ \rightarrow \ell\bar{\ell}\ell'\bar{\ell}'$ channel is the one with the lowest background.

The base event selection consists in selecting the appropriate charge and flavor mixes of four isolated "central" leptons, muons (Combined and Segment-Tagged muons) and electrons in the main acceptance of the sub-detectors, i.e $|\eta| < 2.5$, with $p_T > 7$ GeV. Since the ZZ production cross section is among the smallest, the selection is extended to "forward" leptons in the regions beyond the η coverage of the Inner Detector, viz up to $|\eta_\mu| < 2.7$ for muons and $|\eta_\mu| < 4.9$ for electrons. Higher p_T are required for these leptons: more than 10 GeV for muons and 20 GeV for electrons. The selection is also extended to CaloTag muons but only if $|\eta| < 0.1$ and $p_T > 20$ GeV. In the details, the selection gets complicated by requirements limiting the number of the "extended" leptons in the selected events. At the end, the total yield of selected events increases by $\sim 17\%$ with respect to the base selection.

The figures 5.5 compare the data and simulations of Standard Model Signal with estimates of the backgrounds for the leptons pair forming the Z of highest transverse momentum. The total number of selected events is 321 among which 171 are $ee\mu\mu$ events, 86 $\mu\mu\mu\mu$ events and 64 $eeee$ events. One sees that data and predictions agree quite well. One sees also that the backgrounds contribution is very small, $\sim 6\%$ of the total number of events.

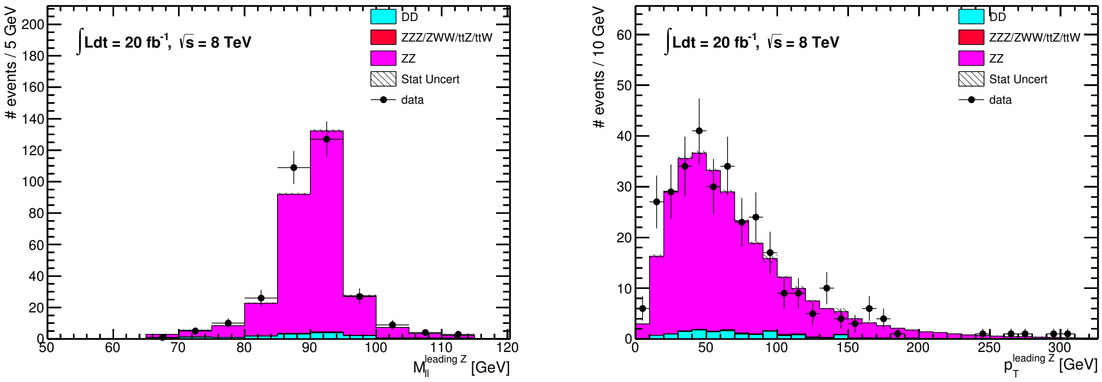

Figure 5.5: Distributions of the mass (left) and of the transverse momentum (right) of the 2 leptons forming the Z of highest transverse momentum, the leading Z.

The background processes are classified as irreducible or reducible, according to whether the selected leptons are genuine prompt high energy leptons or one or more of them are actually “fake” leptons.

The irreducible background processes are triboson (ZZZ and ZWW final states) and $t\bar{t}(Z/W)$ productions as well as Double Parton Interactions resulting in the separated production of two Z-bosons. They are estimated from MC simulations and are severely sub-leading as illustrated by figures 5.5.

In the final states of the reducible background processes, prompt leptons from Z, W or t decays are accompanied by “fake” leptons from jets and photons. These “fakes” leptons are leptons from in-flight decays of light mesons or heavy flavor hadrons or results from the misidentification of jets or photons as electrons. Cuts on Isolation and impact parameters reject efficiently these “fake” leptons. However, owing for the large cross sections of the reducible background processes, a significant number of events survive the cuts. Furthermore they tend to populate the tails of the jets distributions which are not accurately described by Monte Carlo simulations. Therefore the contribution of the reducible background processes is better estimated from data themselves using the so-called Data-driven (DD) methods. Generically these methods consists in reversing few cuts of the events selection, typically isolation, impact parameters and electron identification criteria. From the events counts then dominated by backgrounds sources one extrapolates their contributions into the signal region.

In the case of the ZZ analysis, one uses an auxiliary sample dominated by $Z+jets$ events to determine the fake-factor, i.e the probability of a “fake” lepton to be selected as a genuine lepton. Then one counts the number of events containing one or two objects passing the reversed cuts. Assuming that these failing objects are “fake” leptons and using the probability estimated on the $Z+jets$ sample, one then estimates how many “fake” leptons have successfully passed the selection. MC-based corrections are done to correct the “pure-background” assumption for the samples obtained reversing the cuts and for the auxiliary $Z+jets$ sample. The DD background so estimated is shown on figures 5.5. The shapes of the DD background distributions are taken from MC simulations. The uncertainties on the DD background estimates are on one hand, statistical errors from the sizes of the samples used in the DD procedure, and on the other hand, systematics errors derived comparing results obtained using a global or a differential fake-factor, i.e constant or varying with the lepton p_T and η.

As mentioned above the total background is quite low: the ratio of the SM signal over the background contribution is 17 summing all channels, 33 for the $\mu\mu\mu\mu$ channel and ~ 13 for the $ee\mu\mu$ and $eeee$ channels.

5.3.2 Cross sections definitions and measurements

The aim is to measure the cross section of the ZZ production with two Zs on mass-shell. Precisely one defines the total cross section, σ_{tot}, requiring that both Zs have masses between 66 GeV and 116 GeV. The data for this measurement are the numbers of events selected in each of the 3 final states channels.

5.3.2.1 Data Modelization

The number of events n^b selected in the final states indexed here by b, is understood as the outcome of a random draw from a Poisson distribution of mean ν^b. This mean is the sum of a irreducible and reducible background components ν^b_{IrB} and ν^b_{ReB}, and a signal component ν^b_S proportional to σ_{tot}, the integrated luminosity $\mathscr{L}$, and the branching ratio into the final states of interest Br^b

$$\nu^b = \nu^b_S + \nu^b_{IrB} + \nu^b_{ReB} = \mathcal{F}^b Br^b \mathscr{L} \sigma_{tot} + \nu^b_{IrB} + \nu^b_{ReB} \tag{5.9}$$

The factor $\mathcal{F}^b$ accounts for the loss of signal events which either did not fall in the phase space acceptance defined by the kinematical cuts of the selection or, if they did, have not been retained due to inefficiencies of the trigger, the reconstruction or the identification. It is usual to factorize the two effects writing

$$\nu^b = A^b C^b Br^b \mathscr{L} \sigma_{tot} + \nu^b_{IrB} + \nu^b_{ReB} \tag{5.10}$$

where the factor A^b accounts for phase space acceptance and the factor C^b accounts for inefficiencies.

More precisely one defines a fiducial phase space volume close to, but simpler than, the phase space volume carved by the kinematical cuts of the selection: one requires the masses of the Zs to be between 66 GeV and 116 GeV, $p_T > 7$ GeV for all final state leptons, $|\eta| < 2.7$ for all muons, and $|\eta| < 2.5$ for all electrons but possibly one which is required to have $|\eta| < 4.9$. Because of the muons and electrons are not treated equally, this does not defined a fiducial phase space common to all three final states but actually three fiducial volumes, one for each of them. The fiducial cross sections, σ^b_{fid} are defined as the integrals of the cross section over the fiducial volumes. The acceptance factor A^b is the ratio of the fiducial and total cross sections, $\sigma^b_{fid}/\sigma_{tot}$.

The factor A^b is computed at truth level from the Monte-Carlo generators `POWHEG` and `gg2VV`, the latter for the gluon-gluon fusion contribution [157]. The factor C^b is calculated as the ratio of the number of selected events over the number of generated events in the fiducial volume using fully simulated and reconstructed samples [5]. The selected MC events should be weighted to correct differences observed between Data and simulations for the trigger, the reconstruction and the identification efficiencies.

At this stage the expectation value ν^b appears as a function of the sole cross section σ_{tot} with all the other factors in (5.10) computable. However these factors are derived from quantities inaccurately known, which induce systematic errors on the cross section determination. Therefore ν^b should be considered as a function of the actual although uncertain values of these quantities as well.

For each source of systematic error, one introduces a pulled nuisance parameter η such that the central value and the uncertainty range are mapped for η on 0 and on the interval $[-1;+1]$. For instance if the luminosity is measured as $\mathscr{L}_o \pm \delta\mathscr{L}$, one builds the nuisance parameter $\eta_{\mathscr{L}} = \frac{\mathscr{L}-\mathscr{L}_o}{\delta\mathscr{L}}$. For small uncertainties, one writes

$$\nu^b(\sigma_{tot}, \boldsymbol{\eta}) = A^b_o C^b_o Br^b \mathscr{L}_o \sigma_{tot} \times (1+\sum_s \alpha^b_s \eta_s) + \nu^b_{IrB,o} \times (1+\sum_s \beta^b_s \eta_s) + \nu^b_{ReB,o} \times (1+\sum_s \gamma^b_s \eta_s) \tag{5.11}$$

where the α^b_s, β^b_s and γ^b_s are the differential sensitivities of the corresponding components to the systematic source indexed by s. A single source can act on several components of several bin expectations.

If one aims to the fiducial cross section, the modelization becomes

$$\nu^b(\sigma^b_{fid}, \boldsymbol{\eta}) = C^b_o Br^b \mathscr{L}_o \sigma^b_{fid} \times (1+\sum_s \alpha^b_s \eta_s) + \nu^b_{IrB,o} \times (1+\sum_s \beta^b_s \eta_s) + \nu^b_{ReB,o} \times (1+\sum_s \gamma^b_s \eta_s) \tag{5.12}$$

where the α^b_s could be different than those appearing in (5.11). Indeed some systematics source can affect more specifically the extrapolation from the fiducial phase space volume to the total phase space volume which is irrelevant for the fiducial cross section determination.

---

[5] By construction, the factor C^b accounts for inefficiencies, as well as for the small extrapolation from the effective selection phase space to the simpler fiducial phase space. It corrects also for the small contamination of ZZ events decaying in pairs of τ which subsequently decay in electrons or muons.

5.3.2.2 Likelihood

At this point the modelization of the data consists in saying that the observed event count is drawn from a Poisson distribution the mean of which is given by (5.11) or (5.12) as a function of the parameter of interest σ_{tot} or σ^b_{fid}, and of the nuisance parameters $\boldsymbol{\eta}$, with the additional knowledge that the latter are somehow 0 with an uncertainty of 1.

Under very general conditions the best estimates of the parameters are given by the estimators obtained maximizing the Likelihood, the probability of the observation. For a set of observed events counts $\boldsymbol{\eta}$ in independent bins and noting σ the total or fiducial cross section aimed for, the normalized Likelihood used here is:

$$L(\sigma, \boldsymbol{\eta}) = \frac{\prod_b \mathscr{P}(n^b; \nu^b) \prod_s \mathscr{G}_s(\eta_s; 0, 1)}{\prod_b \mathscr{P}(n^b; n^b) \prod_s \mathscr{G}_s(0; 0, 1)} \tag{5.13}$$

$$L(\sigma, \boldsymbol{\eta}) = \frac{\prod_i \mathscr{P}(n^i; \nu^i) \prod_s \mathscr{G}_s(\eta_s; 0, 1)}{\prod_i \mathscr{P}(n^i; n^i) \prod_s \mathscr{G}_s(0; 0, 1)} \tag{5.14}$$

where $\mathscr{P}(n; \nu)$ is the Poisson distribution of mean ν and $\mathscr{G}_s(\eta_s; 0, 1)$ is the Gaussian distribution of mean 0 and width 1.

Strictly speaking the Likelihood is rather the numerator of (5.13). The denominator is actually the absolute upper bound of the numerator so that one has $L(\sigma, \boldsymbol{\eta}) \leq 1$. This normalization is advised in [158, 159] as the appropriate mean to assess the quality of a fit. Since the Likelihood is a measure of the compatibility between the data and a certain theory of the data, the ratio (5.13) can be seen as a comparison between, at the numerator, the theory defined by the parameters σ and $\boldsymbol{\eta}$ and, at the denominator, the best ever, although unknown, theory: the one which predicts exactly the observed events counts.

It should be noted that the denominator in (5.13) does not depend on σ and $\boldsymbol{\eta}$. As we will see the determination of the point estimates of these parameters involves to maximize $L(\sigma, \boldsymbol{\eta})$ and the determination of the Confidence domains involves ratio of the values of $L(\sigma, \boldsymbol{\eta})$ at different points. Therefore for both of these issues the normalization of $L(\sigma, \boldsymbol{\eta})$ is irrelevant. However there is an other issue: the assessment of the quality of the fit. The normalization in (5.13) makes $L(\sigma, \boldsymbol{\eta})$ the proper quantity to address this third issue.

In (5.13) the term $\prod_s \mathscr{G}_s(\eta_s; 0, 1)$ constrains the nuisance parameters $\boldsymbol{\eta}$ within their uncertainties. Ideally a Likelihood should contain only probabilities of data. The constrain term can be seen as a tentative to reconstruct the various Likelihoods built on the data which were used to measure the nuisance parameters [6]. This is a decent approximation for many systematics, such as uncertainties from reconstruction efficiencies or from Luminosity. For other systematics this is a fiction, a Frequentist fairy tale. For instance for QCD scales or generators uncertainties, one takes bluntly extreme cases felt as reasonable and do with the differences. But the determined Frequentist is not stopped by this: he confesses his sins lucidly, controls the damages to the best, and carries on.

In practice the working Likelihood quantity is the opposite of the logarithm of (5.13)

$$nLL(\sigma, \boldsymbol{\eta}) = -\ln\left(L(\sigma, \boldsymbol{\eta})\right) = \sum_b [\nu^b - n^b + n^b \ln(n^b/\nu^b)] + \sum_s \frac{\eta_s^2}{2} \tag{5.15}$$

$nLL(\sigma, \boldsymbol{\eta})$ is always positive. As $n^b \to \infty$, the product $2 \times nLL$ approaches the usual Pearson's and Neyman's Chi-square functions $\chi^2 = \sum_b \frac{(n^b - \nu^b)^2}{D^b} + \sum_s \eta_s^2$ with respectively $D^b = \nu^b$ and $D^b = n^b$. For

---

[6] If motivated, other functions than the Gaussian distribution can be used for this approximation.

finite n^b, it is known that both Chi-square functions are biased.

5.3.2.3 Method for the extraction of Cross sections and errors

The central values of the measurements, $(\hat{\sigma}, \hat{\boldsymbol{\eta}})$, are obtained by minimizing $nLL(\sigma, \boldsymbol{\eta})$

$$\forall\, \sigma \text{ and } \boldsymbol{\eta}, \text{ one has } nLL(\sigma, \boldsymbol{\eta}) \geq nLL(\hat{\sigma}, \hat{\boldsymbol{\eta}}) \tag{5.16}$$

If one has a single event count n^b, the condition (5.16) leads to a perfect match between the data and the prediction, $n^b = \nu^b$ so that $nLL(\hat{\sigma}, \hat{\boldsymbol{\eta}}) = 0$. Indeed one obtains $\hat{\boldsymbol{\eta}} = 0$ and, according to whether one wants to measure the total or the fiducial cross sections,

$$\hat{\sigma}_{tot} = \frac{n^b - \nu^b_{B,o}}{A^b_o\, C^b_o\, Br^b\, \mathscr{L}_o} \text{ or } \hat{\sigma}^b_{fid} = \frac{n^b - \nu^b_{B,o}}{C^b_o\, Br^b\, \mathscr{L}_o} \tag{5.17}$$

If there are more than one counts, a perfect match is less likely and the value of $nLL(\hat{\sigma}, \hat{\boldsymbol{\eta}}) > 0$ can be used to assess the quality of the fit.

Once the estimates $\hat{\sigma}$ and $\hat{\boldsymbol{\eta}}$ are obtained, one wants error intervals on them. A basic method to set a “68.3% Confidence Level interval” for σ is to take the end points of the interval as the solutions of [7]

$$\Delta nLL(\sigma) = 1/2 \tag{5.18}$$

where $\Delta nLL(\sigma)$ is the Profile Likelihood defined as

$$\Delta nLL(\sigma) = -ln\left[\frac{L(\sigma, \hat{\hat{\boldsymbol{\eta}}})}{L(\hat{\sigma}, \hat{\boldsymbol{\eta}})}\right] \text{ with } \forall\, \boldsymbol{\eta},\ nLL(\sigma, \boldsymbol{\eta}) \geq nLL(\sigma, \hat{\hat{\boldsymbol{\eta}}}) \tag{5.19}$$

which by construction is always greater or equal to 0.

The Confidence interval for any nuisance parameter is obtained reformulating the prescription (5.18) by “profiling” the cross section and all other nuisance parameters [8].

What is the rationale behind the condition (5.18)? It is that $\Delta nLL(\sigma)$ offers a measure of the “acceptability” of a given value σ given the data. The cross section value the most compatible with the data is $\hat{\sigma}$. Its “performance” is quantified by the value of $L(\hat{\sigma}, \hat{\boldsymbol{\eta}})$. If now we consider an alternative value of the cross section σ different from $\hat{\sigma}$, one only has to compute the corresponding Likelihood and compare it to $L(\hat{\sigma}, \hat{\boldsymbol{\eta}})$. But for which value of $\boldsymbol{\eta}$? The best that we can do is to take the value which makes σ the best looking possible, i.e $\hat{\hat{\boldsymbol{\eta}}}$, and compare $L(\sigma, \hat{\hat{\boldsymbol{\eta}}})$ to $L(\hat{\sigma}, \hat{\boldsymbol{\eta}})$. This is what $\Delta nLL(\sigma)$ does. By construction $\Delta nLL(\hat{\sigma}) = 0$ and the worst σ performs with the data, the larger $\Delta nLL(\sigma)$ is. It is therefore natural to set a threshold on the value of $\Delta nLL(\sigma)$ to separate the “acceptable” values of σ such that $\Delta nLL(\sigma) < K$ from the “unacceptable” values such that $\Delta nLL(\sigma) > K$.

Now for the value of the threshold K, one has to turn towards some probabilist reasonings. The frequentist posture is that whatever the procedure to build an error interval is, an objective Level of Confidence in this procedure is assessed by imagining multiple repetitions of the whole experiment and measuring the coverage, i.e the frequency with which the procedure gives an error interval which indeed contains the value of the true cross section. A “68.3% Confidence Level interval” is supposed

---

[7] This is the analogue of the familiar $\Delta\chi^2 = 1$ prescription.

[8] The central values of the nuisance parameters are expected to remain close to 0. Their errors can be less than 1 although a sizable reduction is an indication that the data of the current analysis do constrain significantly the systematic error source and should be investigated. Nuisance parameters errors greater than 1 means that there is a bug somewhere. For the ZZ analysis, the nuisance parameters central values are never bigger than a couple of tens of % and their errors lower than 1 by never more than a couple of %.

to result from a procedure such that whatever is the true value of the cross section, the coverage is greater than 68.3%.

To do a cut on $\Delta nLL(\sigma)$ is a procedure that does not guarantee the frequentist coverage. There are other methods to be discussed later which do guarantee the frequentist coverage but they are very expensive in terms of CPU processing time.

However asymptotically, if the number of events is high enough, then a simple cut on $\Delta nLL(\sigma)$ turns out to be a good enough approximation of the true thing: if one cuts at $K = 1/2$ as in (5.19), then the coverage is greater than 68.3% in the regions of interest. However since this is only an approximate method, checks and validations are de rigueur

The most natural way to check the sanity of the whole procedure is to verify that it behaves as expected on controlled conditions, e.g resorting to pseudo-experiments.

The figure 5.6 has been obtained choosing 20 values of σ_{tot} over a range encompassing the actual measurement. For each σ_{tot}, 10^5 pseudo-experiments were produced and each pseudo experiment was analyzed in the same way as the true data are.

This figure shows the fraction of the 10^5 pseudo-experiments for which it turned out that the σ_{tot} of their generation was indeed in the error interval. This is an estimation of the coverage of the Interval procedure. Since the error intervals are announced to be 68.3% Confidence Level intervals, the coverage should be 68.3%. As we can see in figure 5.6, this is obtained within the statistics fluctuations.

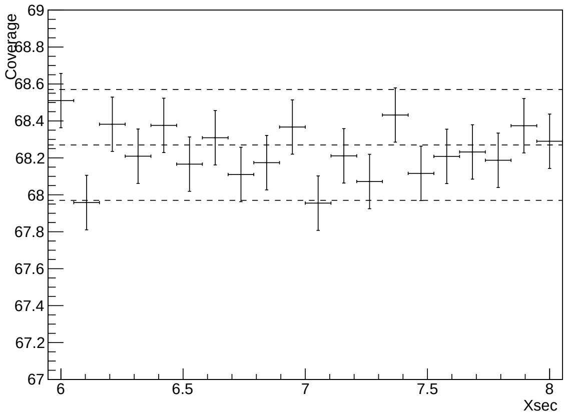

Figure 5.6: Estimation of the coverage of the Confidence Interval procedure as a function of the total cross section

These simulations can be used also to study biases of the cross section estimates. For the ZZ analysis they amounts for less than one per-mill of the cross section.

5.3.2.4 Results

The table 5.3 shows the total cross section obtained combining the three ZZ final states.

The total error on the cross section measurement amounts for about 8% of the total cross section. Its receives contributions from the various sources, statistical and systematics and it is desirable to assess them numerically. However this assessment is not unambiguous and definitions are needed.

As we saw in 5.3.2.3, the statistical procedure delivers central values and errors for the cross section as well as for the nuisance parameters. These central values and errors are refereed hereafter as from the main fit.

The statistical errors on the cross section are defined as the total errors on the cross section obtained by redoing a fit while fixing the nuisance parameters at their central values in the main fit.

The error from a given systematic source is defined by performing two fits with all nuisance parameters free but the nuisance parameter corresponding to this source which is kept fixed at its main fit central value plus or minus its main fit errors. The variations of the central value of cross section in these two fits with respect to its value in the main fit is taken as the errors on the cross section from the source.

σ_{tot} [pb]	Measurement	$6.98\ ^{+0.42}_{-0.40}(stat.)\ ^{+0.38}_{-0.33}(syst.)\ ^{+0.20}_{-0.19}(lumi.)$
	Theory	$7.06\ \pm 0.25$

Table 5.3: Total ZZ cross section: measurement combining all channels and theoretical prediction. The theoretical prediction is computed with `MCFM` with error from QCD scales and PDFs.

The table 5.3 gives the statistical errors, the Luminosity errors and, indicated by "(syst.)", the errors from other sources computed subtracting quadratically the statistical and Luminosity errors from the total errors. One sees that the statistical error amounts for about 6% of the total cross section.

The table 5.4 shows in % of the total cross section measurement, the contributions from all the systematic sources. Its shows that the main systematics, each amounting for about 3% of the cross section, are the uncertainties from Luminosity, from the Data Driven background and from the Monte Carlo generators. The reconstruction and selection effects are sub-leading. The main ones are the cuts on isolation and impact parameter for the muons and on electron identification for the electrons. The errors from uncertainties on PDFs and QCD scales are low. They affect mainly the extrapolation for the fiducial to the total phase space volume.

Source	Error (%)
Luminosity	$^{+2.87}_{-2.76}$
e-Identification efficiency	$^{+1.63}_{-1.61}$
μ-Isolation and impact parameter	$^{+1.92}_{-1.89}$
MC generators	$^{+2.97}_{-2.88}$
QCD scales and PDFs	$^{+0.79}_{-0.78}$
Data Driven Background	$^{+2.99}_{-3.00}$

Table 5.4: Main systematic uncertainties on the combined total ZZ cross section in % of the measured cross section.

The table 5.3 gives also the theoretical prediction for the total cross-section computed with `MCFM` with error from QCD scales and PDFs. In the figure 5.7, this prediction is compared graphically to the measurement combining all channels. Also shown are the measurements from each channel separately. The prediction and measurement agree very well.

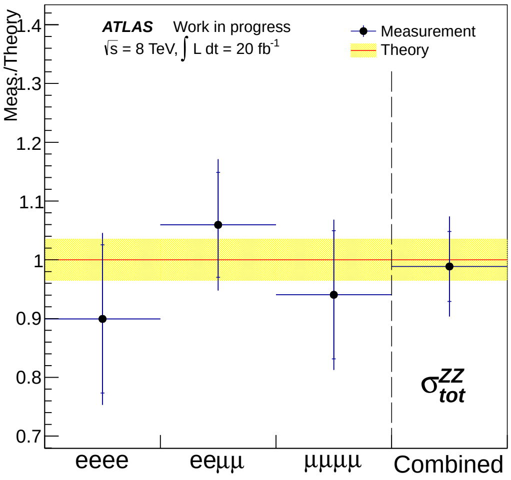

Figure 5.7: Measured total ZZ cross section, per channel and combining all of them, normalized to the theoretical predictions computed with `MCFM`.

As we saw, `MCFM` computations are at the NLO level and contains the NNLO gluon-gluon fusion contribution. Using the software implementation described in [160], the NLO EW corrections were found to reduce the cross section by about 4.4%. On the other hand, the NNLO QCD corrections were estimated in [121] to amount for about 11% among which 60% are due to gluon-gluon fusion. Therefore the NNLO QCD and NLO EW corrections of the `MCFM` estimate nearly cancel.

5.3.2.4.1 Fit Quality

In 5.3.2.3, we saw that the error interval is determined by comparing the performance of a test cross section σ to the performance of the cross section the most compatible with data $\hat{\sigma}$. This is what the ratio in the definition of $\Delta nLL(\sigma)$ (5.19) does. Therefore because it serves as a reference point, the performance of $\hat{\sigma}$ itself is not examined in the determination of the errors. How much this performance is good is the specific issue of the quality of the fit.

In the same way that the performance of $\hat{\sigma}$ serves as a reference in the determination of the errors, one needs a reference against which the performance of $\hat{\sigma}$ can be compared to assess the quality of the fit. Actually the definition of the normalized Likelihood in (5.13) does already incorporate such a reference point. Indeed due the ratio in (5.13), the minimal value of the normalized likelihood, $L(\hat{\sigma}, \hat{\boldsymbol{\eta}})$, does compare the performance of $\hat{\sigma}$ at the numerator to the best one can ever do at the denominator.

The idea is therefore to build on the minimal value of the normalized Likelihood [9]. More precisely, one evaluates how much likely would it be to find the value $L(\hat{\sigma}, \hat{\boldsymbol{\eta}})$ that has been found with the actual data, if the true value of the cross section was indeed $\hat{\sigma}$. To determine this, one uses pseudo-experiments generated under the assumption that the true value of the cross section is $\hat{\sigma}$ and one builds the distribution of the minimal value of the normalized Likelihood found in each pseudo-experiment.

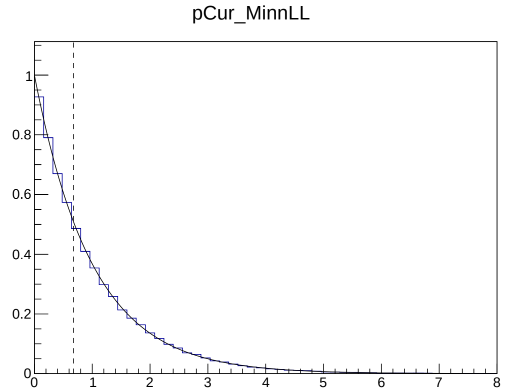

Figure 5.8: Normalized distribution of $-ln(L(\hat{\sigma}, \hat{\boldsymbol{\eta}}))$ obtained with 10^5 pseudo experiments. The dashed vertical line shows the value obtained with actual data.

The figure 5.8 shows the distribution of $-ln(L(\hat{\sigma}, \hat{\boldsymbol{\eta}}))$ obtained for 10^5 pseudo experiments. The value of $L(\hat{\sigma}, \hat{\boldsymbol{\eta}})$ found with the true data is shown by the dashed vertical line.

To assess how much this value is “typical”, one computes the fraction of pseudo experiments for which a minimal value of the normalized Likelihood worst than the actual value has been found, i.e one integrates the distribution of figure 5.8 to the right of the dashed line. This is the p-value of the quality of the fit. The bigger the fit quality p-value is, the better the fit is. For the ZZ analysis, one finds a very good fit p-value of $50.8 \pm 0.2\%$.

One can show that under asymptotic conditions of large statistics the distribution of the figure 5.8 should tend to a χ^2 law of 2 degrees of freedom for 3 bins minus one unconstrained parameter. This law is shown by the solid blue line on the figure. One sees that indeed this is an excellent approximation of the distribution built with the pseudo experiments. This is usually the case of all measures of the diboson productions cross sections till the moment the integrated luminosity has been high enough to allow few hundreds events to be selected. However this nice feature is specific to cross section measurements. For anomalous couplings, the asymptotic conditions do not hold and one has to resort to pseudo experiments.

---

[9] One should note that the minimal value of the exact “unnormalized” Likelihood, the numerator of (5.13) is inappropriate for this investigation. See [161] for related issues.

5.3.2.4.2 P-values of the edges of the Confidence Interval

Let's consider the edges of the error interval of the measurement in table 5.3, say the upper edge, $\sigma^+_{tot} = 6.98 + 0.60$ pb. Let's assume that this is the true value of the cross section.

That the data fluctuations have been such that the true value ends up to be at the extreme edge of the error interval is somehow a "disappointing" performance. With the actual data, one got $\Delta nLL(\sigma^+_{tot}) = 1/2$. But surely if σ^+_{tot} is the true value, one can hope that in many repetitions of whole experiment, σ^+_{tot} would perform, in terms of $\Delta nLL(\sigma^+_{tot})$, often better than this.

This leads to investigate how much 1/2 is a likely value for $\Delta nLL(\sigma^+_{tot})$ if σ^+_{tot} is indeed the true value.

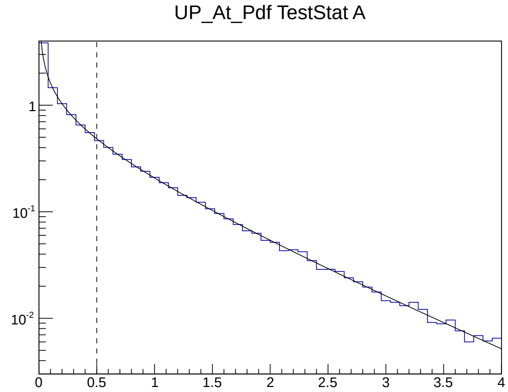

Figure 5.9: Normalized distribution of $\Delta nLL(\sigma^+_{tot})$ obtained with 10^5 pseudo experiments.

To do this, one resorts to pseudo experiments generated assuming that σ^+_{tot} is the true value and one builds the distribution of the $\Delta nLL(\sigma^+_{tot})_{pExp}$ found for each pseudo experiment. The figure 5.9 shows this distribution obtained for 10^5 pseudo experiments. The fraction above 1/2 is by definition the p-value of σ^+_{tot}.

For any other value of the cross section σ, one would have proceed the same way: one would have first compute $\Delta nLL(\sigma)_{Data}$ with the actual data, then produce pseudo experiments assuming that σ is the true value, then build the normalized distribution of the $\Delta nLL(\sigma^+_{tot})_{pExp}$ found for each pseudo experiment, and finally integrate the distribution on the right of $\Delta nLL(\sigma)_{Data}$ to obtain the p-value of σ. Since a priori, the distributions for different values of the cross section assumed to be the true one are different, this is to be done for each value of the cross section, a very time consuming procedure.

For the ZZ analysis, one estimates the p-value of σ^+_{tot} to be $31.9 \pm 0.1\%$. This value is very close to $100 - 68.3 = 31.7\%$.

Actually, the proper frequentist procedure works the other way around: the edges of a $x\%$ Confidence Level Interval are found by requiring that they have p-values equal to $(100 - x)\%$. This guarantees that the coverage is then greater than $x\%$.

The prescription (5.18) is far simpler and faster and since the p-value of σ^+_{tot} is found close to the target, it seems to be a good substitute for the proper procedure. The explanation for this good performance is that when the number of events is large, the distribution of $\Delta nLL(\sigma^+_{tot})$ follows asymptotically a simple χ^2 law with 1 degree of freedom for the sole unconstrained parameter σ^+_{tot}. This laws is the blue solid line in the figure 5.9 and one sees that this is indeed an excellent approximation of the distribution.

But here also, this nice feature is specific to cross section measurements. For anomalous couplings, the asymptotic conditions do not hold and one has to resort to pseudo experiments.

5.3.3 Anomalous Triple Gauge Couplings measurements

The production of ZZ pairs allows to probe the ZZZ and $ZZ\gamma$ vertices. As shown by the tables 5.1, it is sensitive to 4 anomalous Couplings, viz the 2 CP respecting f_5^Z and f_5^γ and the 2 CP violating f_4^Z and f_4^γ. For convenience, one will note them ζ_i in the following.

The amplitude of the ZZ production process receives components proportional to the anomalous couplings. Schematically one has

$$|.\rangle = |SM\rangle + \sum \zeta_i \, |i\rangle \tag{5.20}$$

It follows that the cross section and so also the signal expectation of the events count in a bin are bilinear functions of the ζ_is

$$\nu_S^b(\boldsymbol{\zeta}) = Y_{00}^b + \sum_{i=1}^{4} Y_{0i}^b \zeta_i + \sum_{i=1}^{4} Y_{ii}^b \zeta_i^2 + \sum_{i,j=1;j>i}^{4} Y_{ij}^b \zeta_i \zeta_j \tag{5.21}$$

where the first term is proportional to the square of the SM amplitude, the second term to the interferences of the SM amplitude with the aTGC amplitudes, the third term to the squares of the aTGC amplitudes, and the fourth term to the interferences between the aTGC amplitudes.

The polynomial coefficients Y_{ij}^b are determined using `SHERPA` and `POWHEG+gg2VV` fully simulated samples and reweighing techniques using the BHO program [162] which for a given event and a choice of anomalous couplings values returns a weight proportional to the cross section. These coefficients are also corrected for difference in efficiencies between data and Monte Carlo as this was done for the coefficients of the data modelization for the cross section measurement (5.11) or (5.12).

The determination of the systematics errors follows a similar path. However the sensitivity to some sources such as the PDFs and QCD scales uncertainties is different. Indeed in the cross section determination, the sensitivity to these sources enters through ratios of cross sections such as the factor A^b. A change of the cross section is irrelevant if the numerator and the denominator move in concert. For the aTGC case, this increase has a full effect as it becomes clear acknowledging for instance that the Y_{00}^b is the number of events predicted by the SM.

Contrary to the cross section measurement case, the aTGC measurement is dominated by statistics fluctuations from low event counts as illustrated by the figure 5.10.

It shows, merging all the 4 leptons final states, the distribution of the transverse momentum distribution of the 2 leptons system forming the Z of the highest p_T for data and simulations comprising SM and Background contributions as well as the effect of setting all anomalous couplings at $f_{4,5}^{Z,\gamma} = 0.005$.

As it clear from this figure, the sensitivity to the anomalous couplings is coming from weakly populated kinematics regions and no asymptotic large statistics regime can settle.

The reference [85] presents a systematic study looking for the kinematic variables the most sensitive to aTGC, alone or by pair, and for optimal binning. It turns out that the distribution of the p_T of the leading Z offers the best sensitivity with the binning shown in figure 5.11.

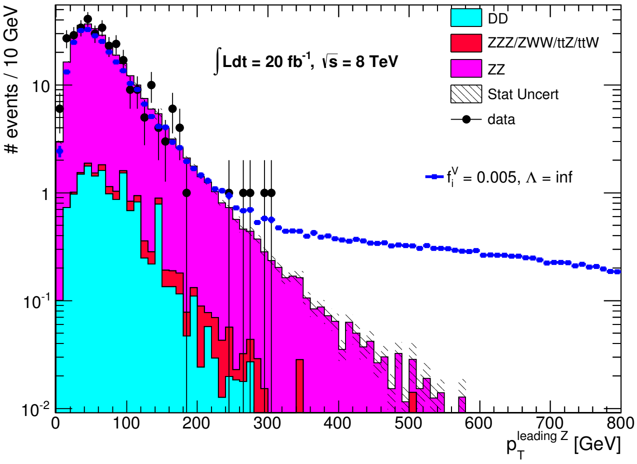

Figure 5.10: Distribution of the transverse momentum distribution of the 2 leptons system forming the Z of the highest p_T.

5.3.3.1 Statistical Analysis

The statistical treatment for the aTGCs measurements is similar to, although slightly more sophisticated than, what has been done for the cross section.

The Likelihood $L(\boldsymbol{\zeta}, \boldsymbol{\eta})$ is still given by the equation (5.13). It is now a function of a set parameters of interest $\boldsymbol{\zeta}$, not just of a single one as before. The bin content expectation ν^b is

$$\nu^b(\boldsymbol{\zeta}, \boldsymbol{\eta}) = \nu^b_S(\boldsymbol{\zeta}) \times (1 + \sum_s \alpha^b_s \eta_s) + \nu^b_{IrB,o} \times (1 + \sum_s \beta^b_s \eta_s) + \nu^b_{ReB,o} \times (1 + \sum_s \gamma^b_s \eta_s) \tag{5.22}$$

where the signal component ν^b_S is now a function bilinear in the parameters of interest given by (5.21). It is important to note that due to this dependence, the bin content is bound from below. In a very simple case, the consequences of this bound are discussed in detail in the appendix C [10].

The best estimates of the parameters, $\hat{\boldsymbol{\zeta}}$ and and $\hat{\boldsymbol{\eta}}$, are given by the Maximum Likelihood Estimators as before

$$\forall\, \boldsymbol{\zeta} \text{ and } \boldsymbol{\eta},\; nLL(\boldsymbol{\zeta}, \boldsymbol{\eta}) \geq nLL(\hat{\boldsymbol{\zeta}}, \hat{\boldsymbol{\eta}}) \tag{5.23}$$

Since one can want to determine more than 1 parameter at once, the statement on the errors is not always a Confidence Interval, but in general a piece of the multi-dimensional parameter space, a Confidence Domain. In addition the Confidence Level for the anomalous Couplings is traditionally taken to be 95% rather than 68.3% as for the cross section.

The Confidence Domain is no more obtained from a the simple prescription similar to (5.18) but it has to be based on the p-values. Precisely a given hypothesis $\boldsymbol{\zeta}$ is still scored on the basis of its Profile Likelihood value $\Delta nLL(\boldsymbol{\zeta})$ defined as in (5.19) by

$$\Delta nLL(\boldsymbol{\zeta}) = -ln[L(\boldsymbol{\zeta}, \hat{\hat{\boldsymbol{\eta}}})/L(\hat{\boldsymbol{\zeta}}, \hat{\boldsymbol{\eta}})] \text{ with } \forall\, \boldsymbol{\eta},\; nLL(\boldsymbol{\zeta}, \boldsymbol{\eta}) \geq nLL(\boldsymbol{\zeta}, \hat{\hat{\boldsymbol{\eta}}}) \tag{5.24}$$

$$ProfL(\lambda) = \frac{L(\lambda, \hat{\hat{\boldsymbol{\eta}}})}{L(\hat{\lambda}, \hat{\boldsymbol{\eta}})} \tag{5.25}$$

but instead to cut on $\Delta nLL(\boldsymbol{\zeta})$ as in (5.18) one now computes the probability to get a as bad or worse than $\Delta nLL(\boldsymbol{\zeta})$ if the true value is indeed $\boldsymbol{\zeta}$. This probability is the p-value of the hypothesis $\boldsymbol{\zeta}$.

The 95% Confidence Level Domain is defined as the most compact volume of the parameter space such that outside it any point has a p-value lower than 5%. Such a definition ensures that the coverage of the procedure, the cornerstone of the Frequentist approach, is indeed 95% .

Deliberately the Frequentist approach has no inference rule to go from the actual data to the theory contrary to the Bayesian approach with its priors on the parameters updated by the Bayes rule. The frequentist statements are not on the actual Confidence Domain obtained from data but on the procedure which produces it. Confronted to such a procedure, the Frequentist approach is to consider it as a “machine making domains” and to act as a tester of this machine. The Frequentist practitioner repeatedly injects simulated data in the machine and looks at the outputs. She determines how many times the output domains do contain, do “cover”, the true value that she used in her simulation, and very reasonably, she assesses her confidence in the procedure from the fraction of successes, the coverage. A Frequentist “machine making x% Confidence Level Domains” is built such that the coverage is, by contract, at least x% whatever the true parameters are.

---

[10] Briefly while the likelihood is approximatively a gentle 2nd order polynomial in the parameter of interest ζ when the expectation is linear in ζ, it is a fourth-order polynomial with typically two minimas and a maximum in between when the expectation depends quadratically on ζ.

From the publication of the paper from G.J. Feldman and R.D. Cousins [163], it has become clear in the HEP community that such a procedure is to build domains such that the p-value function is lower than $(100 - x)\%$ outside the domain.

In practice to work with p-values means that one has to do a lot of pseudo experiments. They should be done cleanly notably for what concerns systematic sources fluctuations and they should be done very fast which involved various technical tricks and a lot of code optimization. Then one can reasonably explore the p-value function over the space of the parameters of interest. This function is high, close to 100%, in the immediate vicinity of $\hat{\boldsymbol{\zeta}}$ and decreases further away from the best estimate. It remains to catch the contour on which the p-value function crosses the 5% level.

Despite all optimization, the computation of a single p-value is still time consuming and one can not afford to compute the p-value function for too many points. For instance, one can compute the p-value function only at the nodes of a rectangular grid. Instead here the p-values are computed only along a set of few rays passing by the origin $\boldsymbol{\zeta} = 0$ and spanning the $[0; 2\pi]$ angle range. This is convenient for typically oval-shaped contours. About ten of rays are enough to get a decent sampling. Then starting from educated guesses, one runs a dichotomous iterative procedure along each ray. Generally about ten of trials are enough to catch the transition point where the p-value function crosses the 5% level.

5.3.3.2 Results

The data used to extract Confidence Intervals on the anomalous Couplings are shown in the figure 5.11.

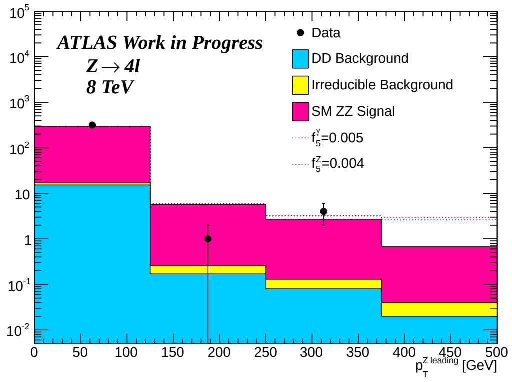

Figure 5.11: Numbers of events in p_T^Z bins for data, predicted by SM and for two non null aTGCs scenarios. *(ZZ analysis)*

They are the numbers of events in 4 bins in transverse momentum of the 2 leptons system forming the Z of the highest p_T. The Upper edge of the last bin goes to infinity.

Are shown the numbers of events found in the 8 TeV data sample as well as those predicted in a simulation comprising the SM ZZ production and the irreducible and Data-Driven estimates of the backgrounds. These numbers are reported in the table 5.5. As it can be seen there are tensions between the SM predictions and data mainly in the two first bins.

	[0-200]	[200-260]	[260-380]	[380-∞]
Observed ZZ	316	1	4	0
SM Expected	296.06 ±4.64	5.69 ± 0.20	2.71 ± 0.11	0.67 ± 0.04
$f_5^\gamma = 0.005$	296.25 ±4.64	5.88 ± 0.20	3.23 ± 0.11	2.96 ± 0.04
$f_5^Z = 0.004$	296.24 ±4.64	5.87 ± 0.20	3.18 ± 0.11	2.61 ± 0.04

Table 5.5: Numbers of events in p_T^Z bins for data, predicted by SM and for two non null aTGCs scenarios. *(ZZ analysis)*

Also shown in the figure 5.11 are the predictions for two non null aTGCs scenarios: $f_5^Z = 0.004$ and $f_5^\gamma = 0.005$. They correspond approximatively to the size of the one-dimension Confidence Domains for these couplings discussed below. As shown in the table 5.5, both predict about 3 events in the highest p_T^Z bin.

One considers first the four one-dimension fits of the anomalous Couplings, i.e the fits where all couplings but one are fixed to 0.

The quality of these fits can be evaluated by the same method described in the section 5.3.2.4. The p-value of the four fits are found to be of the order of 6%. A p-value of 6% is not excessively good although not redhibitory. This poor performance reflects mostly the compatibility of the SM with the actual data and results from the tensions between the SM events counts predictions and data discussed above.

The table 5.6 shows the Confidence Intervals for each of the one-dimension fits in the column "Observed". The Lower and Upper ends of the Confidence Interval for the anomalous Coupling f_5^Z are shown in the figures 5.12 by the solid red vertical line.

Parameter	Observed	Expected
f_4^γ	[-0.0046, 0.0046]	[-0.0056($^{+0.0013}_{-0.0017}$), 0.0056($^{+0.0017}_{-0.0013}$)]
f_4^Z	[-0.0041, 0.0040]	[-0.0049($^{+0.0011}_{-0.0014}$), 0.0049($^{+0.0014}_{-0.0011}$)]
f_5^γ	[-0.0046, 0.0047]	[-0.0056($^{+0.0013}_{-0.0017}$), 0.0056($^{+0.0017}_{-0.0013}$)]
f_5^Z	[-0.0040, 0.0040]	[-0.0048($^{+0.0011}_{-0.0015}$), 0.0048($^{+0.0015}_{-0.0011}$)]

Table 5.6: Observed and Expected one-dimension 95% Confidence Level Intervals of the anomalous Couplings; the figures reported between parentheses are not errors but distributions widths (cf text) *(ZZ analysis)*

The figures 5.12 show also intervals ends named "Asimov". They correspond to aTGCs analyses in which the actual data are replaced by the SM expectations. The name "Asimov" is borrowed from the Asimov dataset concept developed in [164] which, very roughly, corresponds to the idea that injecting in input the mean of the inputs, one gets in output the mean of the outputs. These Asimov limits allow to guess if there is any anomaly in the results that one obtains with the actual data. In figures 5.12, one sees that the "Asimov" limits are quite compatible with the Observed limits although the latter are somewhat more stringent owing to the downward fluctuation of the data with respect to SM expectations in the most sensitive bin.

The Asimov limits are very fast to obtain and this is very much appreciated in these studies which are usually very CPU time consuming. However they do not provide a "width" scale that would allow to evaluate the likelihood of the difference between them and the Observed limits [11]. The solution is to use pseudo experiments that one generates from the SM expectations. The figures 5.12 show the distributions of the Lower and Upper ends of Confidence Intervals for these pseudo experiments. The means of these distributions are indicated in the figures as "Expected". As it can be seen they are nicely close to the Asimov limits. The figures 5.12 show also the 1 and 2-σ widths containing 68.3% and 95.4% of the distributions respectively. The means and 1-σ widths are reported in table 5.6 in the column "Expected". One notes that the low statistics in the most sensitive bins results in a marked asymmetry of the distributions [12].

Both the table 5.6 and the figures 5.12 show that the actual Observed limits are in the expected range of fluctuations from SM expectations.

---

[11] The reference [164] gives results on this resolution aspect but they are not easily transposable here.

[12] It interesting to note that for the most part, the one-dimension Confidence Domains are statistical in origin. If all systematics uncertainties are zeroed, the Asimov Intervals for f_5^Z and f_5^γ for instance go from $[-0.0051, +0.0051]$ and $[-0.0059, +0.0060]$ to $[-0.0050, +0.0050]$ and $[-0.0058, +0.0057]$ respectively.

One considers now the six two-dimensions fits, i.e fits in which all but two of the anomalous couplings are fixed to 0. As for the one-dimension fits, one can compute Observed, Asimov and Expected limits but now in a two dimensions space. The results are shown on the figures 5.13. The yellow and green bands are the analogues of the 1 and 2-σ 1D-widths of the distributions of the figures 5.12. The figures 5.13 show that the observed 2-dimension 95% Confidence level Domains are within the expected fluctuations around the SM expectations.

The one-dimension Confidence Domains from table 5.6 are reported on the anomalous Couplings axes in figures 5.13. A feature which is worth to comment is that these one-dimension limits "touch" the two-dimensions Confidence Domains when the latter cross the aTGC axes. In other words, the one-dimension limits are only marginally stronger than the two-dimensions limits.

This is a feature which is not seen on the CMS similar plots. CMS does not derive its two-dimensions Confidence Domains from a p-value analysis. Instead the frontiers of these Domains are obtained solving the condition $\Delta nLL(\boldsymbol{\zeta}) = 2.45^2/2$. The value "2.45" is the radius on which a two dimensional Normal Gaussian should be integrated to get 0.95 as a result. The CMS method amounts for assuming not only that an asymptotic regime settled but that it is described by a χ^2 law with 2 degrees of freedom because one has 2 parameters.

Actually the second point does not hold due to degeneracy which arises in anomalous couplings analyses [13]. This degeneracy arises because only one of the data bins is effectively constraining anomalous couplings, and it arises in a particular manner because the events count expectation is a bilinear function of these couplings.

When the problem is linear in the parameters a degeneracy uses to translate into a huge correlation between the parameters along a "blind" axis corresponding to the parameters combination which lets the expectation unchanged. In the case of anomalous couplings, the "blind" direction is orthoradial so to say. Indeed by linear combination of the parameters and shift of the origin, such a bilinear expectation can be put in the form $\nu^b = \nu_0^b + \rho^2$ with $\rho = \sqrt{\zeta_1^2 + \zeta_2^2}$ where the $\zeta_{1,2}$ are the linearly combined and shifted parameters. Effectively only ρ is measured and the blind direction corresponds to change in the polar angle which is not measured at all. This degeneracy is hidden in figure such as the figures 5.13 and, de facto, the problem is essentially with one degree of freedom only.

The concept of degree of freedom it is irrelevant for the proper frequentist method based on p-values. Despite its heaviness, this method protects against this sort of pitfalls.

---

[13] To my best knowledge, this was shown first by our ATLAS colleague Masahiro Mori.

5.3.3.3 EFT Results

As discussed before, the EFT operators analysis leads to significant reduction of the number of parameters for the description of the neutral anomalous Triple Gauge Couplings [155]. Instead of the 12 neutral anomalous Couplings given in table 5.1, the EFT analysis ends up on just 4 parameters, all but one violating CP. The relations between the EFT parameters and the anomalous couplings to which the ZZ production is sensitive are (cf equations (A.24), (A.26) and (A.27)):

$$f_5^Z = 0 \tag{5.26}$$

$$f_5^\gamma = \frac{v^2 m_Z^2}{4c_w s_w}\frac{C_{\tilde{B}W}}{\Lambda^4} \tag{5.27}$$

$$f_4^\gamma = -\frac{v^2 m_Z^2}{4c_w s_w}\Big(-c_w s_w \frac{C_{BB}}{\Lambda^4} + (c_w^2 - s_w^2)\frac{C_{BW}}{\Lambda^4} + 4 s_w c_w \frac{C_{WW}}{\Lambda^4}\Big) \tag{5.28}$$

$$f_4^Z = \frac{v^2 m_Z^2}{2c_w s_w}\Big(c_w^2 \frac{C_{BB}}{\Lambda^4} + 2c_w s_w \frac{C_{BW}}{\Lambda^4} + 4 s_w^2 \frac{C_{WW}}{\Lambda^4}\Big) \tag{5.29}$$

Since in the EFT framework $f_5^Z = 0$, the ZZ production does depend only on 3 anomalous couplings. Since there are 4 EFT parameters, there is a degeneracy between these parameters: a combination of them, actually a combination of C_{BB}, C_{BW} and C_{WW}, can not be measured in ZZ production.

Nevertheless, the whole problem can be parametrized in terms of the 4 EFT parameters and limits can be extracted on them following the procedure described in section 5.3.3.1. To the best of my knowledge, the one-dimension limits on the neutral EFT parameters at LHC were derived for the first time in the ZZ analysis described here [85]. They are shown in table 5.7.

One can convert the limits shown in this table into limits on the scale Λ by assuming $C_{xyz} \sim 1$. This is by no means justified theoretically but this gives a taste of the scales with which we are dealing. In this way one gets lower limits for Λ in the range 0.5 to 0.6 TeV.

EFT Parameter	Observed [TeV^{-4}]	Expected [TeV^{-4}]
$C_{\tilde{B}W}/\Lambda^4$	[-15.53 , 15.65]	[$-18.86(^{+4.48}_{-5.53})$, $18.87(^{+5.55}_{-4.47})$]
C_{BB}/Λ^4	[-7.98 , 7.83]	[$-9.53(^{+2.24}_{-2.72})$, $9.52(^{+2.71}_{-2.24})$]
C_{BW}/Λ^4	[-8.43 , 8.56]	[$-10.34(^{+2.45}_{-3.12})$, $10.35(^{+3.12}_{-2.43})$]
C_{WW}/Λ^4	[-7.07 , 7.17]	[$-8.57(^{+1.95}_{-2.73})$, $8.60(^{+2.71}_{-1.95})$]

Table 5.7: Observed and Expected one-dimension 95% Confidence Level Intervals of the neutral EFT parameters; the figures reported between parentheses are not errors but distributions widths (cf text) *(ZZ analysis)*

5.3.3.3.1 Consistency requirement As already discussed, a consistent application of the EFT analysis requires to drop the two last terms in the parametrization of the signal expectation (5.21). Indeed in the EFT analysis the neutral anomalous coupling ζ_i are of the order of $1/\Lambda^4$ and one neglects explicitly contributions to ζ_i of higher orders. One should not allow a form such as (5.21) to introduce back terms inconsistent with this approximation. This requirement emerged clearly recently only and it has not been integrated in the experiments analyses yet. The following discussion is thus exploratory at best.

Let's say that (5.21), takes the form $\nu_S^b = a\zeta^2 + b\zeta + c$ and that $\zeta = \alpha/\Lambda^4 + \beta/\Lambda^6 + ...$ where the term β/Λ^6 is the first term of higher order that we are neglecting. Then $\nu_S^b = c + b\alpha/\Lambda^4 + b\beta/\Lambda^6 + a\alpha^2/\Lambda^8 + ...$

If $b \neq 0$ then if we neglect β/Λ^6, $b\beta/\Lambda^6$ goes away. Thus $a\alpha^2/\Lambda^8$ which is of higher order should goes away too. Therefore one should drop the quadratic term $a\zeta^2$ in ν_S^b. However if $b = 0$, there is no reason to do so.

So the precise EFT consistency prescription is that one should drop in the parametrization of the signal expectation (5.21) any bilinear term which involves a coupling the amplitude of which does interfere with the SM amplitude.

The anomalous coupling f_4^γ and f_4^Z correspond to interactions which violate CP. So their associated amplitudes do not interfere with the SM. Therefore the EFT consistency prescription does affect neither their one-dimension limits in table 5.6 nor their paired two-dimensions limits in figures 5.13. The EFT parameters C_{BB}/Λ^4, C_{BW}/Λ^4, and C_{WW}/Λ^4 correspond also to interactions which violate CP. So their one-dimension limits in table 5.7 are unaffected.

It remains the anomalous coupling f_5^γ and the EFT parameter $C_{\widetilde{B}W}$ which are related by (5.27). Their situation is puzzling. They correspond to interaction which do not violate CP and their associated amplitude is not prevented to interfere with the SM amplitude. So their are not “protected” against the EFT consistency prescription. Still it is a fact of experience that the term of interference with the SM is excessively small. So small actually that if one drops the bilinear terms in (5.21), the sensitivity to f_5^γ and $C_{\widetilde{B}W}$ vanishes totally. I was unable to found an explanation of this state of affairs. If there is a reason which would explain the observed vanishing interference with the SM and therefore protect against the EFT consistency prescription, then the limits on f_5^γ and $C_{\widetilde{B}W}$ will be those presented above. If there is no such reason, then the ZZ production leads to no limits on these parameters.

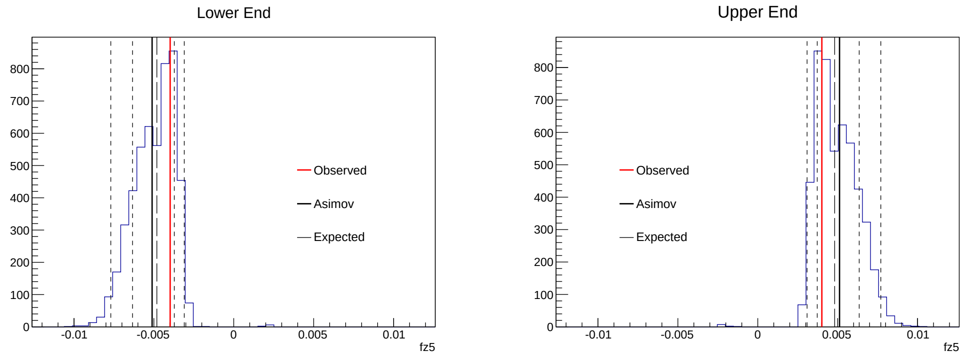

Figure 5.12: Lower and Upper Ends of the 95% Confidence Level Intervals for one-dimension fits. The red lines show the Observed limits, the black solid lines the Asimov limits, the thin long dashed black lines the Expected limits and the dashed lines the 1 and 2 σ-bands. *(ZZ analysis)*

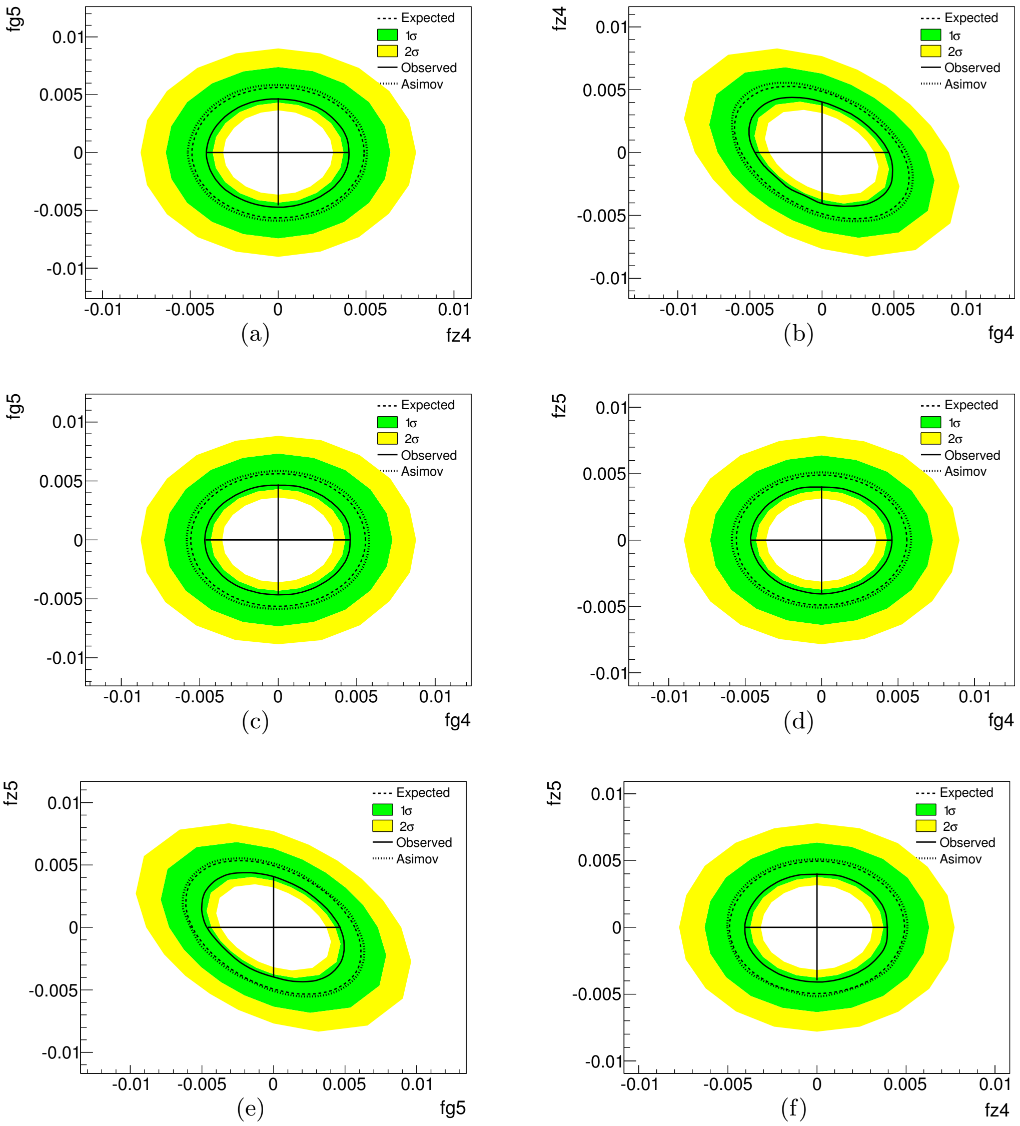

(a) (b)

(c) (d)

(e) (f)

Figure 5.13: Observed, Asimov and Expected two-dimension 95% Confidence Level Domains. The black solid lines show the Observed limits, the dotted lines the Asimov limits, the dashed lines the Expected limits, the green and yellow bands correspond to the 1 and 2 σ-bands. The one-dimension 95% Confidence Level Domains for the Observed limits are reported on the anomalous Couplings axes. *(ZZ analysis)*

5.4 Study of the WZ Production

Hereafter I present the analysis of the production of a pair of WZ-bosons of the sample of the ATLAS data at 8 TeV .

The first ATLAS measurement of this production was done for the 7 TeV data sample in [86]. The cross section measurement on the first part sample of the 8 TeV data (13fb^{-1}) was published in [87, 165]. The analysis was extented to the full data sample in the reference [89] and completed with the measurements of aTGCs in [88].

5.4.1 Selection and backgrounds

The final states of interest are those of the fully leptonic decays $WZ \rightarrow \ell' \nu \ell \bar{\ell}$, with ℓ' and ℓ muons or electrons. They contain 3 electrons, 2 electrons and 1 muon, 1 electron and 2 muons, or 3 muons. Hereafter they will be named eee, $ee\mu$, $e\mu\mu$ and $\mu\mu\mu$. Two of the leptons of the same flavor and opposite charges are associated to the Z-boson and the remaining lepton to the W-boson. On the basis of the sign of the charge of this last lepton, the 4 above event categories can be further split in decay from a W^+ or a W^- boson.

The signature is simple: missing transverse energy (E_T^{miss}) from the escaping ν and 3 leptons of high transverse momenta, well separated and isolated, among which 2 can be paired in a Z-like system.

Selected muons are isolated Combined or Segment-Tagged candidates in the main acceptance of the MS and ID detectors, i.e $|\eta| < 2.5$. Electrons should be isolated and within the calorimeter acceptance $|\eta| < 2.47$ but not in the weak area $1.37 < |\eta| < 1.52$. For both muons and electrons, $p_T > 15$ GeV is required. Events with more than 3 leptons with $p_T > 7$ GeV are rejected in order to reduce the contamination from ZZ production. In addition one of the lepton is required to have $p_T > 25$ GeV and to have triggered the event recording.

Two leptons of the same flavor and opposite charges are required to form a system of mass within 10 GeV of the Z-boson mass. The third lepton is attributed to the W-boson and its identification is reinforced by requiring $p_T > 20$ GeV and by imposing tighter isolation criteria and electron identification criteria.

To tag large missing energy in the event, a cut is done, not on the E_T^{miss} but on the transverse mass of the W-boson computed from the vectorial missing transverse energy attributed to the escaping ν and the transverse momentum of the lepton attributed to the W as

$$m_T^W = \sqrt{2 E_T^{\ell} E_T^{miss} - 2 \vec{p}_T^{\,\ell} \vec{E}_T^{miss}} \tag{5.30}$$

It is required that $m_T^W > 30$ GeV.

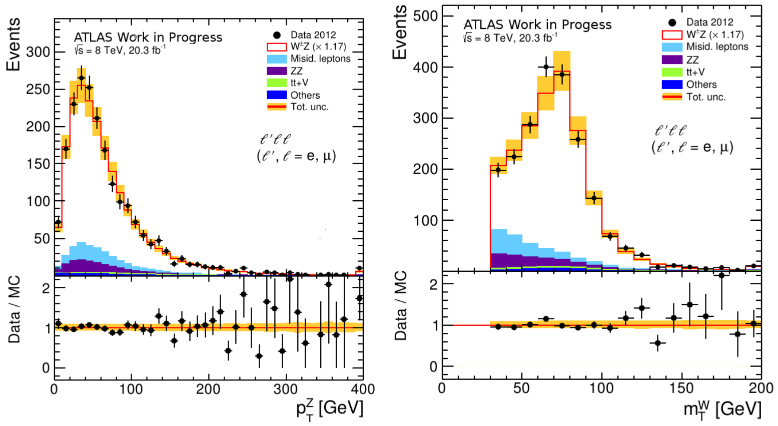

Figure 5.14: Distributions for the selected events of the transverse momentum of the 2 leptons forming the Z-boson like system (left) and of the transverse mass of the W-boson candidate (right).

The figures 5.14 compare the data and simulations of Standard Model Signal with estimates of the backgrounds for the distributions of the transverse momentum of the 2 leptons forming the Z-boson like system and of the transverse mass of the W-boson candidate.

One sees that the backgrounds contamination is larger for the WZ production than for the ZZ production: it amounts for about 20% of the selected events.

The irreducible backgrounds, those producing the right amount of genuine prompt high energy leptons, are the productions of ZZ, $t\bar{t}+V$ (with V being a Z or a W boson), $t+Z$, and VV' (mainly $W(Z/\gamma*)$) from Double Parton scattering. Their contributions are estimated by MC means and amount together for about a half of the background contribution. For 70%, the irreducible backgrounds contribution is due to ZZ production.

The other half of background contribution is from reducible backgrounds, for which one or more of the selected leptons are actually "fake". They originate from the productions of $Z+j$, $Z\gamma$, $t\bar{t}$, and WW. This contribution is estimated with a Data-driven method quite similar but more sophisticated than the one used for ZZ production. One counts the events in which one or two leptons pass all the selection criteria but the isolation cut. The counts of these events inform on the proportion of the selected events which are actually backgrounds events for which one or two fake leptons have been identified as genuine leptons. This requires one has an estimate of the probability f of a fake lepton to be identified as a genuine prompt lepton.

The analysis keeps track of the lepton being associated to the W or being the leading or trailing lepton associated to the Z boson. The probability f is estimated on $Z+j$ and $W+j$ data samples. Systematics uncertainties on the DD background include statistical uncertainties of the f determination on the $Z/W+j$ data samples, biases from the transverse missing energy cuts, and taking or not account of the difference in the composition of the fake lepton kinds (heavy flavor decays leptons, photon conversion, light flavor jet) in the Signal and $Z/W+j$ data samples.

The ratio of the SM signal over the background contribution is about 4 summing all channels, and ranges from about 4.5 for $\mu\mu\mu$ to about 3 for eee

5.4.2 Cross sections definitions and measurements

The aim is to measure the total cross section of the WZ production with the W and Z on mass-shell. The total Phase Space is defined by requiring the Z mass to be between 66 GeV and 116 GeV. One can ignore the sign of the W boson in the final state and this defines the "unsigned" cross section σ_{tot}^{WZ}, or one can track this sign and defines the two "signed" cross sections $\sigma_{tot}^{W^+Z}$ and $\sigma_{tot}^{W^-Z}$.

One aims also for fiducial cross sections. Contrary to the ZZ analysis one defines a fiducial Phase Space common to all the various channels. This allows to derive a fiducial cross section combining all channels. The fiducial phase space is defined by: the leptons are required to have $|\eta| < 2.5$, $p_T > 15$ GeV for the Z leptons and $p_T > 20$ GeV for the W lepton; the Z-leptons are required to form a system of mass within 10 GeV from the nominal Z mass and the transverse mass of the W to be greater than 30 GeV. As the total cross sections, one has "unsigned" and "signed" fiducial cross sections.

The derivations of the cross sections is similar to what is done for the ZZ analysis with the same kind of Data Modelization, Likelihood building and extraction method that are described in sections 5.3.2.1, 5.3.2.2 and 5.3.2.3.

The data are the numbers of events in the final states channels of interest. They are the 4 "unsigned" events counts n^b with $b = eee$, $ee\mu$, $ee\mu$ and $\mu\mu\mu$ if one ignores the sign of the W boson or the 8 "signed" events counts $n^{\pm,b}$ if one keeps track of it [14].

---

[14] The "unsigned" events counts range from ~ 600 events to ~ 400 events from $\mu\mu\mu$ to eee channels.

5.4.2.1 Results on "unsigned" cross sections

One starts by the measurements of the total and fiducial cross sections of WZ production ignoring the sign of the final state W boson. One uses the 4 "unsigned" events counts n^b as data inputs.

The tables 5.8 show the fiducial and total cross sections obtained combining the 4 channels. The quoted errors have been computed as described in section 5.3.2.3. The quality of the combined fit is evaluated with the means described in section 5.3.2.4. The p-value of the fit is found to be quite good: $48.2 \pm 0.2\%$.

σ_{fid}^{WZ} [fb]	Measurement	$35.1^{+0.9}_{-0.9}$ (stat) $^{+0.9}_{-0.8}$ (syst) $^{+1.1}_{-1.1}$ (lumi)
	Theory	30.0 ± 2.1

σ_{tot}^{WZ} [pb]	Measurement	$24.4^{+0.7}_{-0.6}$ (stat) $^{+0.6}_{-0.6}$ (syst) $^{+0.8}_{-0.7}$ (lumi)
	Theory	21.0 ± 1.6

Table 5.8: "Unsigned" Fiducial and total cross section: measurement combining all channels and theoretical prediction. The theoretical prediction is computed with `POWHEG` and `PYTHIA` with error from QCD scales and PDFs.

The Table 5.9 shows the systematics errors on the combined measurement of the fiducial cross section. Beside the luminosity contribution, the main contributions are from on one hand, the uncertainties on the Identification and reconstruction efficiencies of electron and muons, and on the other hand, the uncertainties on the backgrounds contributions.

The tables 5.8 give also the theoretical cross sections. In the figure 5.15, the prediction for the fiducial cross section is compared graphically to the measurement combining all channels. Also shown are the measurements from each channel separately.

Clearly the measurements are above the predictions. These theoretical cross sections are at the NLO QCD level.

As discussed in section 5.2, the NLO EW corrections have been found negligible [139, 143] and no NNLO QCD calculations are available for WZ.

However a NNLO QCD correction of the order of 5% can be expected on the basis of the corrections found in the framework of the so-called "approximate" NNLO ($\tilde{n}$NLO) QCD [126]. Such a correction would bring the difference between the measurement and the prediction from the actual 2-σ level to below the 1.5-σ level.

Source	Errors (%)
Luminosity	$^{+3.2}_{-3.0}$
e - Id. Efficiency	$^{+1.0}_{-1.0}$
μ - Rec.Efficiency	$^{+1.4}_{-1.4}$
MC Backgrounds	$^{+0.9}_{-0.8}$
Data Driven Background	$^{+1.4}_{-1.3}$

Table 5.9: Main systematic uncertainties on the combined fiducial WZ cross section in % of the measured cross sec-

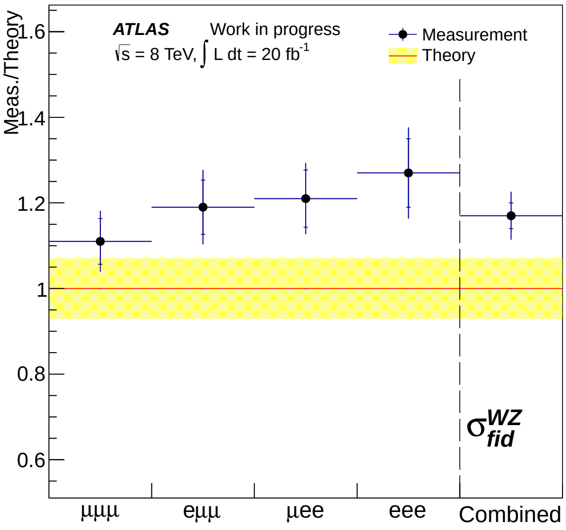

Figure 5.15: Measured fiducial cross sections, per channel and combining all them, normalized to the theoretical predictions

5.4.2.2 Results on "signed" cross sections

One considers now the cross sections of WZ production discerning the sign of the charge of the final state W boson. One uses the 8 "signed" events counts $n^{\pm,b}$ as data inputs.

The fiducial cross sections, $\sigma_{fid}^{W^+Z}$ and $\sigma_{fid}^{W^-Z}$, are derived building a single Likelihood function

$$nLL(\sigma_{fid}^{W^+Z}, \sigma_{fid}^{W^-Z}, \boldsymbol{\eta}) \tag{5.31}$$

running on the all the $n^{\pm,b}$ events counts and depending on the two cross sections simultaneously. Although the two cross sections parametrize separately the signal components of the expectations of the positive and negative events counts, the nuisance parameters are possibly acting on all event counts expectations. So to treat all the bins together allows to get the most stringent effects on the nuisance parameters.

$\sigma_{fid}^{W^+Z}$ [fb]	Measurement	$21.1^{+0.7}_{-0.7}$(stat) $^{+0.5}_{-0.4}$(syst) $^{+0.7}_{-0.6}$(lumi)
	Theory	18.8 ± 1.3
$\sigma_{fid}^{W^-Z}$ [fb]	Measurement	$14.0^{+0.6}_{-0.6}$(stat) $^{+0.4}_{-0.4}$(syst) $^{+0.5}_{-0.4}$(lumi)
	Theory	11.1 ± 1.0

Table 5.10: "Signed" fiducial cross-sections: measurements combining all channels and theoretical predictions. The theoretical predictions are computed with `POWHEG` and `PYTHIA` with errors from QCD scales and PDFs.

The tables 5.10 show the fiducial cross sections obtained combining all channels. The p-value of the combined fit is found to be quite decent: 14.5%. The measurements are quite correlated: the parametrization of the vicinity of minimum of (5.31) by the HESSE algorithm from the Minuit suite [166] gives a correlation factor of 51%.

The tables 5.10 give also the theoretical cross sections. In the figures 5.16 the predictions is compared graphically to the measurement combining all channels. Also shown are the measurements from each channel separately.

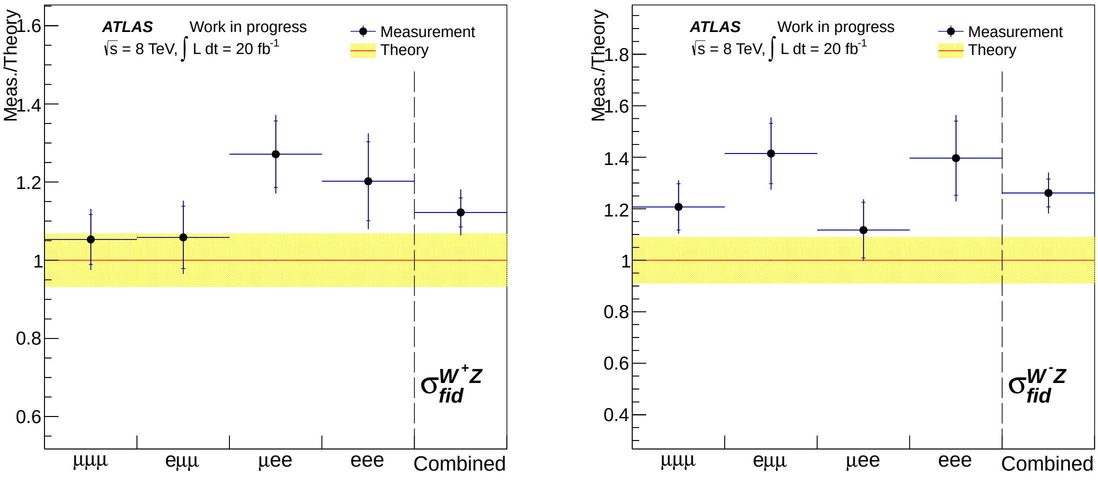

Figure 5.16: "Signed" Measured fiducial cross sections, per channel and combining all of them, normalized to the theoretical predictions.

A measurement of the ratio of the fiducial cross section

$$\rho = \sigma_{fid}^{W^+Z} / \sigma_{fid}^{W^-Z} \tag{5.32}$$

is desirable since the systematics are expected to cancel for a good part. To perform this measurement, one only has to use the Likelihood function (5.31) and performs a change of variables which makes it a function of ρ. In the process one can also use as the new variable

$$\sigma_{fid}^{\Sigma} = \sigma_{fid}^{W^+Z} + \sigma_{fid}^{W^-Z} \tag{5.33}$$

so that one gets at the same time a new measurement of the "unsigned" fiducial cross section, already measured in section 5.4.2.1 but by significantly different means. Therefore we work with the Likelihood function

$$nLL(\rho, \sigma_{fid}^{\Sigma}, \boldsymbol{\eta}) = nLL\left(\sigma_{fid}^{W^+Z} = \frac{\rho\sigma_{fid}^{\Sigma}}{1+\rho}, \sigma_{fid}^{W^-Z} = \frac{\sigma_{fid}^{\Sigma}}{1+\rho}, \boldsymbol{\eta}\right) \tag{5.34}$$

$\rho = \sigma_{W^+Z}^{fid} / \sigma_{W^-Z}^{fid}$	Measurement	$1.51^{+0.09}_{-0.08}(\text{stat})\ ^{+0.01}_{-0.02}(\text{syst})$
	Theory	1.69 ± 0.07
$\sigma_{\Sigma}^{fid} = \sigma_{W^+Z}^{fid} + \sigma_{W^-Z}^{fid}$ [fb]	Measurement	$35.1^{+0.9}_{-0.9}(\text{stat})\ ^{+0.9}_{-0.8}(\text{syst})\ ^{+1.1}_{-1.1}(\text{lumi})$
	Theory	30.0 ± 2.1

Table 5.11: Ratio and sum of the fiducial cross-sections: measurements combining all channels and theoretical predictions. The theoretical predictions are computed with `POWHEG` and `PYTHIA` with errors from QCD scales and PDFs.

The tables 5.11 show the measurements of ρ and σ_{Σ}^{fid} obtained combining all channels together. The two measurements are found to be weakly correlated: the correlation factor is -6%.

Consistently one finds back in the measurement of σ_{Σ}^{fid} the measurement of the "unsigned" fiducial cross section from the tables 5.8.

The tables 5.11 give the prediction for ρ. This prediction is compared graphically with the measurement obtained combining all the channels together. Also shown are the ρ measurements from each channel separately.

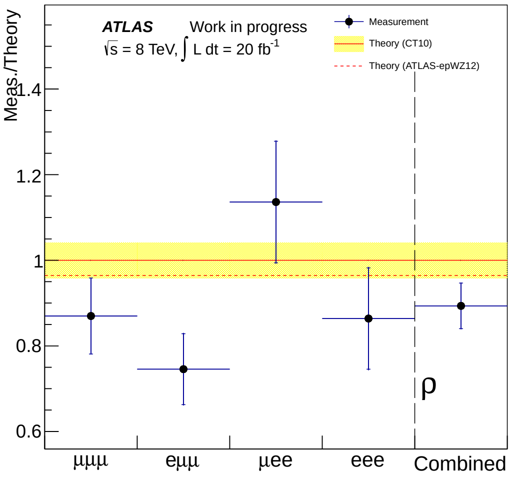

Figure 5.17: Measured ratio of fiducial cross sections, per channel and combining all of them, normalized to the theoretical predictions.

The combined measurement has a precision of about 6% not excessively larger than the theoretical error. The difference between prediction and measurement is at the 1-σ level.

5.4.3 Anomalous Triple Gauge Couplings measurements

The production of WZ pairs allows to probe the WWZ vertex. As shown by the tables 5.1, it is sensitive to 7 anomalous Triple Gauge Couplings, viz the 3 C and P respecting parameters Δg_1^Z, $\Delta\kappa_Z$, and λ_Z, and the 4 C or P violating parameters g_4^Z, g_5^Z, $\widetilde{\kappa}_Z$, and $\widetilde{\lambda}_Z$. Traditionally the C or P violating parameters are ignored and only limits on Δg_1^Z, $\Delta\kappa_Z$ and λ_Z are derived. As for the ZZ analysis, the expectation of the event counts in a given bin is a bilinear function of the anomalous couplings noted generically ζ_i

$$\nu_S^b(\boldsymbol{\zeta}) = Y_{00}^b + \sum_{i=1}^{3} Y_{0i}^b \zeta_i + \sum_{i=1}^{3} Y_{ii}^b \zeta_i^2 + \sum_{i,j=1;j>i}^{3} Y_{ij}^b \zeta_i \zeta_j \tag{5.35}$$

Various kinematical quantities can be used to derived limits on anomalous couplings. In the analysis of 7 TeV data sample, ATLAS chose to use the transverse momentum of the Z boson, p_T^Z [86]. However as discussed in section 5.2, it has been found that the NNLO QCD corrections, estimated in the so-called "approximate" NNLO ($\tilde{n}$NLO) framework [126], would affect more significantly some distributions than others. Notably the distribution of the transverse mass of the WZ system, m_T^{WZ}, is little affected. Therefore it has been decided to derive limits on anomalous couplings using this quantity. It is defined as

$$m_T^{WZ} = \sqrt{(E_T^{miss} + \Sigma E_T^{\ell_i})^2 - (\vec{E}_T^{miss} + \Sigma \vec{p}_T^{\,\ell_i})^2} \tag{5.36}$$

where the sum runs on the 3 decays leptons.

Precisely the data that are used are the bin contents of the distribution of m_T^{WZ} merging all the channels shown on the figure 5.18. The Upper edge of the last bin goes to infinity. The figure shows the data and the expected SM yields, signal and backgrounds.

Also shown are the contributions from non null anomalous couplings of the order of the limits derived bellow. They amount for a approximate doubling of the predicted number of events in the last bin and for an increase by about 1/3 in the next to last bin.

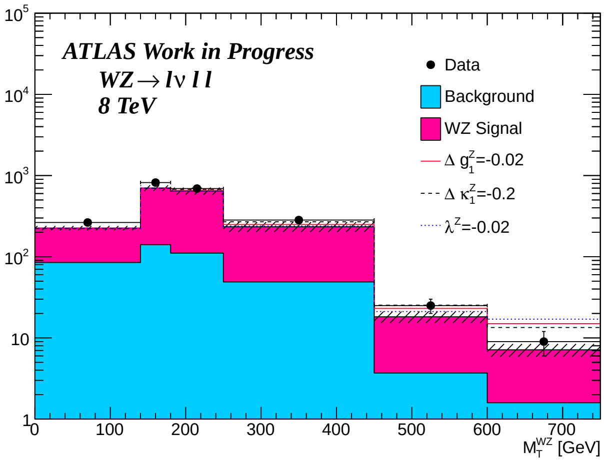

Figure 5.18: WZ Transverse Mass distribution.

The statistical treatment is similar to what has been done for the ZZ analysis: the systematics sources modify the signal and backgrounds as in (5.22) and the compatibility with the data of a given hypothesis on the values of the anomalous couplings $\boldsymbol{\zeta}$ and of the nuisance parameters $\boldsymbol{\eta}$ is assessed with a Likelihood function $nLL(\boldsymbol{\zeta}, \boldsymbol{\eta})$ analogue to (5.15).

In particular, the compatibility of the data and the SM predictions at the exclusion of any anomalous couplings contributions, can be appreciated by minimizing $nLL(\boldsymbol{\zeta} = 0, \boldsymbol{\eta})$ as a function of the nuisance parameters $\boldsymbol{\eta}$ only. Then the quantity $nLL(\boldsymbol{\zeta} = 0, \hat{\boldsymbol{\eta}})$ where $\hat{\boldsymbol{\eta}}$ is the solution of this minimization, can be used to assess the compatibility of the data and the SM predictions. Indeed $nLL(\boldsymbol{\zeta} = 0, \hat{\boldsymbol{\eta}})$ is the appropriate Statistics to use since, as already discussed in sections 5.3.2.2 and 5.3.2.4, it is comparing the best that one can do under the constrain $\boldsymbol{\zeta} = 0$ and the best ever, although unknown, theory of the data. One finds a p-value of $33 \pm 0.1\%$ which is quite good.

5.4.3.1 Results

One now considers the three one-dimension fits, i.e fits in which all but one of the parameters Δg_1^Z, $\Delta\kappa_Z$ and λ_Z are fixed at 0. The qualities of these fits are estimated by computing p-values as described in section 5.3.3.2. These p-values are good and range from 26% to 28%. That they are somewhat lower than the value found testing the pure SM case indicates that the data do not show departure from the SM prediction which would call for anomalous Couplings contributions.

Parameter	Observed	Expected
Δg_1^Z	[-0.019; 0.029]	[-0.016 $(^{+0.007}_{-0.007})$; 0.032$(^{+0.007}_{-0.009})$]
$\Delta\kappa_Z$	[-0.19 ; 0.30]	[-0.17 $(^{+0.06}_{-0.05})$; 0.25 $(^{+0.06}_{-0.07})$]
λ_Z	[-0.016; 0.016]	[-0.016 $(^{+0.004}_{-0.004})$; 0.016$(^{+0.004}_{-0.004})$]

Table 5.12: Observed and Expected one-dimension 95% Confidence Level Intervals of the anomalous Couplings; the figures reported between parentheses are not errors but distributions widths (cf text). *(WZ analysis)*

The table 5.12 shows the Confidence Intervals for each of the one-dimension fits in the column “Observed”. The Lower and Upper ends of the Confidence Interval for the anomalous Couplings are shown in the figures 5.19.

One notes that the limit on $\Delta\kappa_Z$ is by an order of magnitude less stringent than those on the two other anomalous couplings. This difference originates from the dependence on the energy in the center of mass of the process, $\sqrt{\hat{s}}$, of the contributions to the cross section of the different anomalous couplings: while the contributions of Δg_1^Z and λ_Z grow as $\hat{s}$, the $\Delta\kappa_Z$ one grows as $\sqrt{\hat{s}}$ only.

The figures 5.19 show also the Asimov intervals ends. As for the ZZ analysis they are obtained replacing the actual data by the SM expectations. They are quite close to the Observed limits. As much as reassuring this is, this does not tell if the differences between the Observed and Asimov limits are exceptional or “natural”. This is better assessed, but at a much higher cost in CPU time, by generating pseudo experiments around the SM expectations. This allows to build the “natural” distribution of the intervals ends shown in figures 5.19 with their means indicated as “Expected” as well as their 1 and 2-σ widths. The means and 1-σ widths are reported in table 5.12 in the column “Expected”.

Both the table 5.12 and the figures 5.19 show that the actual Observed limits are in the expected range of fluctuations around SM expectations [15].

Next one considers the 3 two-dimension fits, i.e fits in which all but two of the anomalous couplings are fixed to 0. The Observed and Expected limits as well as the 1 and 2-σ bands are shown in figures 5.20. These figures show that the observed 2-dimension 95% Confidence Level Domains are within the expected fluctuations around the SM expectations.

One notes that the two-dimension contours depart from the one-dimension intervals more than they did in the ZZ analysis (see figures 5.13). This indicates that the constrains on anomalous couplings arise less exclusively from a single bin. This has the effect to lift, although very partially, the particular degeneracy of the parameters of interest in the case of anomalous couplings that was discussed in section 5.3.3.2.

---

[15] As the ZZ anomalous couplings limits, the WZ limits are dominated by statistical errors. The sensitivity to systematic errors is however slightly larger in particular concerning the theoretical uncertainties: if the uncertainties from QCD scales and PDFs are switched off, the sizes of the Confidence Intervals decrease by about 10% for Δg_1^Z and λ_Z and about 20% for $\Delta\kappa_Z$.

5.4.3.2 EFT Results

As discussed before, the EFT operators analysis leads to significant reduction of the number of charged anomalous Couplings [167]. Instead of the 14 charged anomalous Couplings given in table 5.1, the EFT analysis ends up on just 5 parameters, 3 respecting C and P and 2 violating C and/or P. Putting the later aside, the relations between the EFT parameters and the anomalous couplings to which the WZ production is sensitive are (cf equations (A.34), (A.35) and (A.39)):

$$\begin{aligned}\Delta g_1^Z &= \frac{m_Z^2}{2}\frac{C_W}{\Lambda^2}\\ \Delta\kappa_Z &= \frac{m_W^2}{2}\Big(\frac{C_W}{\Lambda^2} - \tan^2\theta_W\frac{C_B}{\Lambda^2}\Big)\\ \lambda_Z &= \frac{3g^2 m_W^2}{2}\frac{C_{WWW}}{\Lambda^2}\end{aligned} \tag{5.37}$$

Contrary to the ZZ case, there is no degeneracy for the measurements of the EFT parameters. The whole problem can be parametrized in terms of the EFT parameters and limits can be extracted on them following the same procedure than for the anomalous couplings. The one-dimension 95% Confidence Level Intervals are given in the table 5.13.

One notes that the limits on C_B/Λ^2 are much less stringent than those on the other EFT parameters. From the one-dimension limits on the anomalous couplings of the table 5.12 and the relations (5.37), one sees that the poor sensitivity to $\Delta\kappa_Z$ is reported exclusively on the measurement of the C_B/Λ^2 EFT parameter.

One can convert the limits of the table 5.12 into limits on the scale Λ by assuming $C_{xyz} \sim 1$. This is by no means justified theoretically but this gives a taste of the scales with which we are dealing. The limits on C_W/Λ^2 and C_{WWW}/Λ^2 translate into lower limits for Λ in the range 0.3 to 0.5 TeV. The limits on C_B/Λ^2 point to a limit of the order of $\sim$ 50 GeV which once again underlines the limitation of the measurement of this parameter.

EFT parameter	Observed [TeV $^{-2}$]	Expected [TeV $^{-2}$]
C_W/Λ^2	[-4.3 ; 6.8]	[-3.7 ; 7.6]
C_B/Λ^2	[-320 ; 210]	[-270 ; 180]
C_{WWW}/Λ^2	[-3.9 ; 4.0]	[-3.9 ; 3.8]

Table 5.13: Observed and Expected one-dimension 95% Confidence Level Intervals on the EFT parameters. *(WZ analysis)*

5.4.3.2.1 Consistency requirement As already discussed, a consistent application of the EFT analysis requires to drop the two last terms in the parametrization of the signal expectation (5.35). Indeed since in the EFT analysis the charged anomalous coupling ζ_i are of the order of $1/\Lambda^2$, these bilinear terms $\zeta_i\zeta_j$ are of the order of $1/\Lambda^4$ which is beyond the retained order. This requirement emerged clearly recently only and it has not been integrated in the experiments analyses yet and results which follows are given for illustrative and exploratory purposes only. If one drops the terms bilinear in the anomalous parameter, one gets the results shown in the tables 5.14.

The dynamic of the fit is deeply modified by the removal of the bilinear terms, it is non trivial to explain how one goes from the results of the tables 5.12 and 5.13 to those of the tables 5.14.

Parameter	With bilinear terms	Without bilinear terms
Δg_1^Z	[-0.019; 0.029]	[-0.021; 0.021]
$\Delta\kappa_Z$	[-0.19 ; 0.30]	[-0.20 ; 0.36]
λ_Z	[-0.016; 0.016]	[-0.10 ; 0.39]

Table 5.14: Observed one-dimension 95% Confidence Level Intervals of the anomalous Couplings obtained with and without bilinear terms in the Signal expectations *(WZ analysis)*

Nevertheless, one can get an idea of the gross features by examining the coefficients of the bilinear expression (5.35). Let's say that this expression takes the form $a\zeta^2+b\zeta+c$ for one anomalous coupling ζ. One can guess that the ratio, $a\zeta_o/b$ where ζ_o is a typical value of the ends of the Confidence Interval on ζ, is an appropriate figure of merit of the importance of the quadratic terms in the expression (5.35) and therefore, of the amplitude of the expected changes of the Confidence Intervals when one drops these terms. Typically this ratio is ~ 0.5 for Δg_1^Z, ~ 1.5 for $\Delta\kappa_Z$, and ~ 20 for λ_Z.

The large ratio for λ_Z means that the anomalous amplitude associated to this coupling interferes quite little with the SM amplitude. In consequence the square of this amplitude has an overwhelming relative contribution in the signal parametrization. When one removes it the sensitivity to λ_Z drops significantly up to the point that the limits on this parameter become almost as poor as those on $\Delta\kappa_Z$ as it can be read in table 5.14.

One concludes that within the framework of a consistent application of the EFT approach, the WZ production study brings constrains only on the anomalous coupling Δg_1^Z and on the EFT parameter C_W/Λ^2.

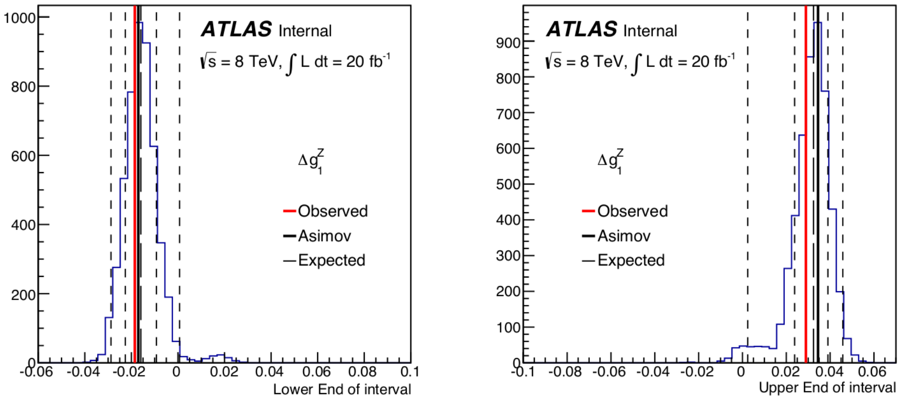

Figure 5.19: Lower and Upper Ends of the 95% Confidence Level Intervals for one-dimension fits. The red lines show the Observed limits, the black solid lines the Asimov limits, the thin long dashed black lines the Expected limits and the dashed lines the 1 and 2 σ-bands. *(WZ analysis)*

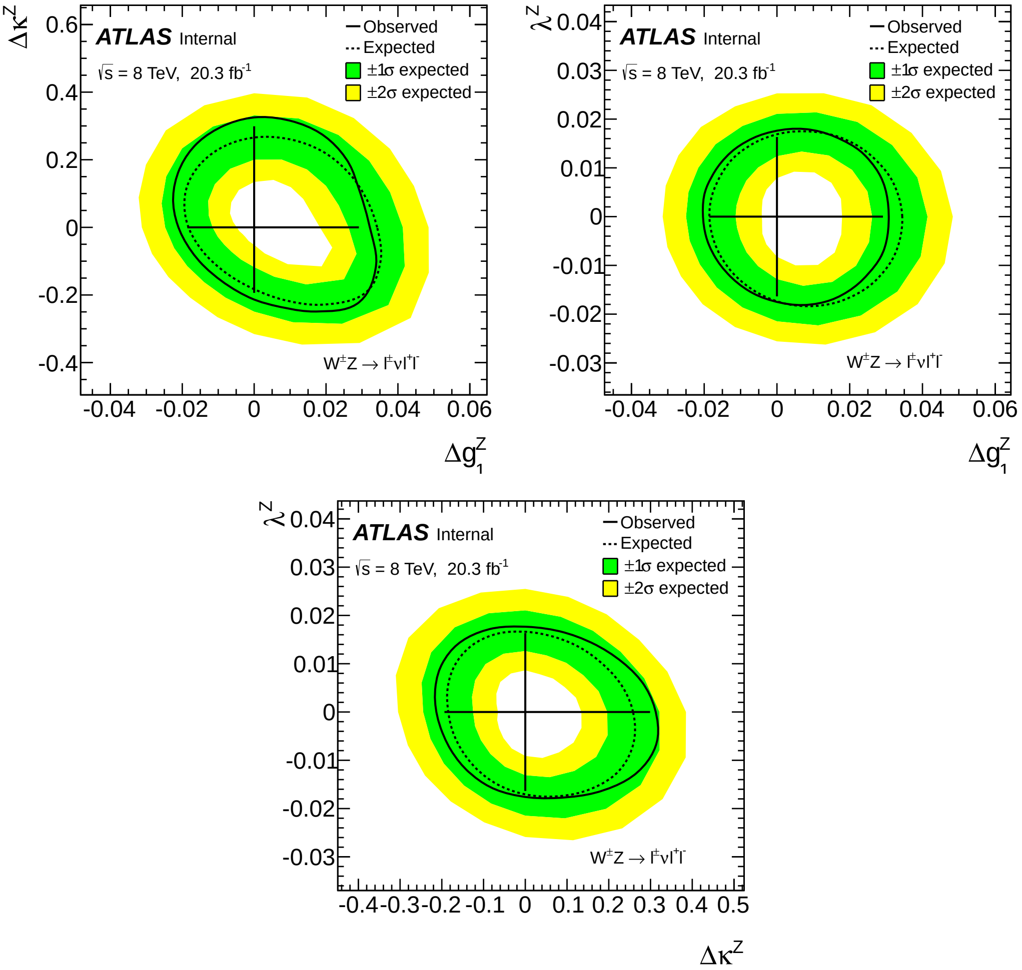

Figure 5.20: Observed, Asimov and Expected two-dimension 95% Confidence Level Domains. The black solid lines show the Observed limits, the dashed lines the Expected limits, the green and yellow bands correspond to the 1 and 2 σ-bands. The one-dimension 95% Confidence Level Domains for the Observed limits are reported on the anomalous Couplings axes. *(WZ analysis)*

5.5 Study of the WW Production

Hereafter I present the analysis of the production of WW bosons pairs in the sample collected by ATLAS for p-p collisions at $\sqrt{s} = 8$ TeV in 2012, corresponding to to 20.3 fb^{-1} of integrated luminosity [90, 91].

5.5.1 Selection and backgrounds

The final states of interest are the fully leptonic decays $WW \to \ell'\nu\ell\nu$ where ℓ and ℓ' are electrons or muons. They contains 2 electrons, 1 electron and a muon, or 2 muons. Hereafter they will be named ee, $e\mu$, and $\mu\mu$. As the 2 produced W bosons, the 2 final state leptons are necessarily of opposite charge.

The signature is simple: missing transverse energy (E_T^{miss}) from the escaping νs and 2 leptons of high transverse momenta, well separated and isolated, and opposite in charge.

Selected muons are isolated Combined candidates in the main acceptance of the MS and ID detectors, i.e $|\eta| < 2.4$. Electrons should be isolated and within the calorimeter acceptance $|\eta| < 2.47$ but not in the weak area $1.37 < |\eta| < 1.52$. Two leptons of opposite charge are required. The lepton of highest p_T should have $p_T > 25$ GeV while the other one should have $p_T > 20$ GeV. Events with more than 2 leptons with $p_T > 7$ GeV are rejected to reduce the contamination from other diboson productions.

In order to reduce backgrounds from low mass resonances, multijets and Drell-Yan events, cuts are made on the mass of the 2 leptons system, $m_{\ell\ell'}$. It is required to be greater than 15 GeV for $ee/\mu\mu$ channels and 10 GeV for $e\mu$ channel. In addition $m_{\ell\ell'}$ is required to be at least 15 GeV away from the Z boson mass for $ee/\mu\mu$.

After these cuts, the Drell-Yan contamination is still significant specially for the $ee/\mu\mu$ channels. Further reduction is obtained by requirements on the missing energy. The missing energy computed with tracks p_T^{miss}, is required to be greater than 20 GeV for $e\mu$ and 45 GeV for $ee/\mu\mu$. In addition a cut is applied on the relative scalar $E_{T,Rel}^{miss}$, equal to the norm of the usual $\vec{E}_T^{miss}$ or its projection on the closest jet or lepton if the latter points in the same direction ($E_{T,Rel}^{miss}$ is found more robust than E_T^{miss} against mis-measurement of a jet and a lepton). It is required that $E_{T,Rel}^{miss}$ is greater than 15 GeV for $e\mu$ and 45 GeV for $ee/\mu\mu$.

At this stage the selected events are overwhelmingly from top-quark production ($t\bar{t}$ or single t). This contamination is severely reduced with marginal loss on signal by a jet veto cut which rejects events with any jet above $p_T > 25$ GeV within $|\eta| < 4.5$.

The figures 5.21 show the distributions of the transverse momentum of the lepton of highest p_T. There is a large difference in the number of events selected in the different channels: 5067 events are selected in the $e\mu$ channel against 594 and 975 in the ee and $\mu\mu$ channels respectively.

The background contamination is similar in all channels $\sim 30\%$. The main source of the backgrounds contamination is the top-production at the level of $50 - 60\%$. The other background sources are the $W + jets$, the Drell-Yan and the other diboson productions which vary in importance according to the channel considered. All backgrounds are estimated with Data-Driven (DD) background methods but the diboson background which is estimated from Monte Carlo.

For the top background, one counts the number of events in a top background dominated Control Region defined as the normal events selection without the jet veto cut to which one adds that H_T the scalar sum of transverse momentum of leptons and jets should be greater than 300 GeV. This events number is extrapolated to the signal region using factors essentially estimated from Monte Carlo. The systematic errors on the top production contributions at the level of $\sim 10\%$ result among other sources from the uncertainties on the correction of non-top contribution in the Control region and

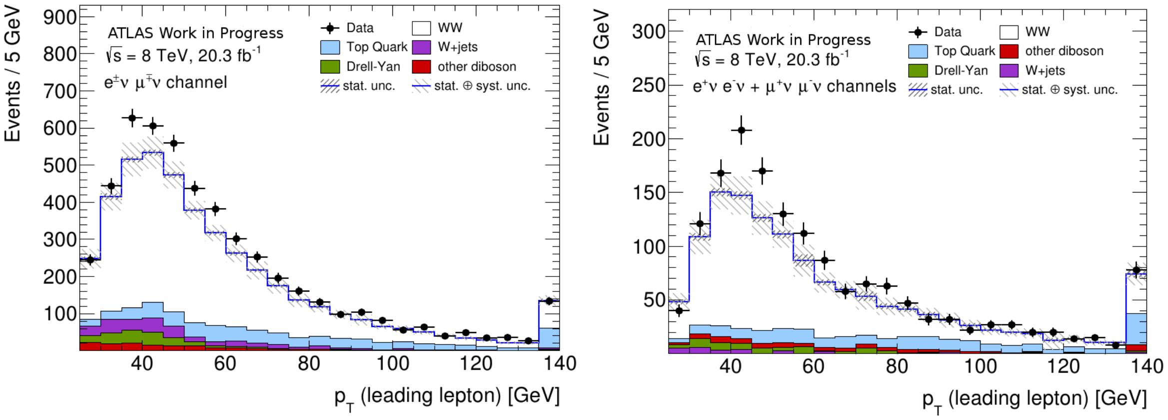

Figure 5.21: Distributions of the transverse momentum of the lepton of highest p_T for the $e\mu$ channel (left) and merging the ee and $\mu\mu$ channels (right).

from uncertainties on the extrapolation factors used (jet energy scale and resolution, Parton shower and harmonization modeling).

The $W + jets$ contribution is estimated with a DD method similar to those used for the $Z + jets$ estimates in the ZZ and WZ methods. It is based on on one hand, the probabilities, ϵ_{real} and ϵ_{fake}, for true prompt leptons and fake leptons from backgrounds to be selected as genuine prompt leptons estimated on dedicated samples enriched in fake leptons, and on the other hand, the events counts in Control Regions defined relaxing some identification and isolation criteria in the nominal selection. Using ϵ_{real} and ϵ_{fake} these counts are used to estimate the contamination in the Signal Region. The systematics errors on the $W + jets$ contribution result among other sources from uncertainties from possible differences in the mixes of the types of fake leptons (heavy flavor decays leptons, conversion, light flavor jet) in the samples used to extract ϵ_{real} and ϵ_{fake} and in the Control Regions. These systematic errors amount for $\sim 50\%$ in the most contaminated $e\mu$ channel and for more than 100% in the two other channels.

The Drell-Yan contribution is estimated from event counts in Control regions defined by inverting the cut on p_T^{miss}. The main uncertainty on this contribution comes from uncertainties on jets and E_T^{miss} energy scale. The systematic errors on the Drell-Yan production contribution are $\sim 10\%$ for $e\mu$ and reach $\sim 50\%$ for $ee/\mu\mu$.

5.5.2 Cross sections definitions and measurements

Both total and fiducial cross-section are derived. The fiducial volume is defined for each channel by the selection discussed in preceding sections. The data are the 3 numbers of events selected in each of the $e\mu$, ee, and $e\mu$ channels.

5.5.2.1 Results

The table 5.15 shows the total WW production cross sections obtained combining all channels. The p-values of the combined fit is quite good, $72.0 \pm 0.1\%$.

σ_{tot}^{WW} [pb]	Measurement	$71.0\ ^{+1.1}_{-1.1}$ (stat) $^{+5.7}_{-5.0}$ (syst) $^{+2.1}_{-2.0}$ (lumi)
	Theory	$63.2\ ^{+1.6}_{-1.4}$ (scale) ± 1.2 (PDF)

Table 5.15: Total WW production cross sections: measurements combining all channels and theoretical predictions. The prediction is at the NNLO QCD order [124].

The total errors amount for about 8% of the measured cross sections. As shown by the table 5.15, the measurements is dominated by systematics errors.

The table 5.16 shows the main systematics errors on the total WW production cross section obtained combining all channels. The main contributions are on the experimental side, from the uncertainties on jets and E_T^{miss} and on the DD background estimates, and on the theoretical side, from the uncertainties on generators (Parton Shower, hadronization, underlying event) and on the jet veto cut. This last uncertainty is obtained summing up the scale uncertainties, on the $N_{jets} \geq 0$ and $N_{jets} \geq 1$ inclusive jets cross-sections considered as uncorrelated.

Source	Errors (%)
Luminosity	$^{+3.0}_{-2.8}$
Pileup	$^{+1.5}_{-1.4}$
E_T^{miss} and jets	$^{+4.6}_{-4.4}$
QCD scales and PDFs	$^{+1.1}_{-1.1}$
Jet Veto uncertainty	$^{+3.5}_{-3.3}$
Generators	$^{+2.7}_{-2.5}$
Data Driven Backgrounds	$^{+3.2}_{-3.2}$

Table 5.16: Main systematic uncertainties on the combined total WW production cross section in % of the measured cross section.

The table 5.15 gives also the theoretical cross sections computed at the NNLO QCD order [124].

In the figures 5.22, the predictions for the total WW production cross sections are compared graphically to the measurement combining all channels. Also shown are the measurements from each channel separately.

The agreement between prediction and measurement is at the 1-σ level.

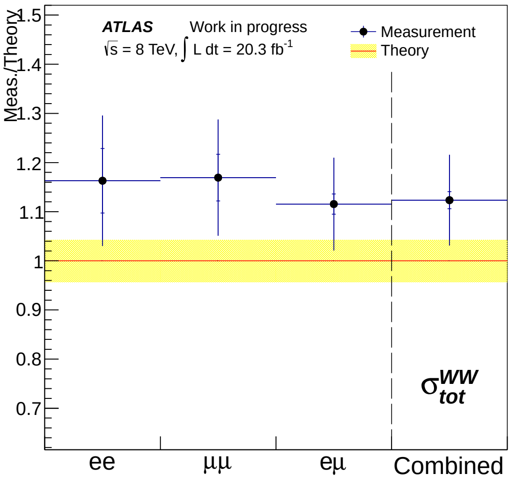

Figure 5.22: Measured total WW production cross sections, per channel and combining all of them, normalized to the theoretical predictions.

5.5.3 Anomalous Triple Gauge Couplings measurements

The production of WW pairs allows to probe the $WW\gamma$ and WWZ vertices. As shown by the tables 5.1, it is sensitive to 14 anomalous Triple Gauge Couplings, viz the 6 CP respecting parameters Δg_1^Z, $\Delta\kappa_Z$, λ_Z, Δg_1^γ, $\Delta\kappa_\gamma$, and λ_γ, and the 8 CP violating parameters g_4^Z, g_5^Z, $\widetilde{\kappa}_Z$, $\widetilde{\lambda}_Z$, g_4^γ, g_5^γ, $\widetilde{\kappa}_\gamma$, and $\widetilde{\lambda}_\gamma$. Traditionally the CP violating parameters are ignored. Furthermore one imposes $U(1)_{em}$ invariance which leads to $\Delta g_1^\gamma = 0$. Therefore only limits on Δg_1^Z, $\Delta\kappa_Z$, λ_Z, $\Delta\kappa_\gamma$, and λ_γ are derived.

One can study anomalous couplings in WW production considering these 5 parameters as independent or one can work with only a subset of them adopting a particular scenario, i.e assuming some relations between these parameters. Both approaches have been followed in [91]. Here I consider one example of the second option. I adopt the so-called LEP scenario which reduces the number of independent parameters from 5 to 3 by imposing

$$\lambda_\gamma = \lambda_Z \quad \text{and} \quad \Delta g_1^Z = \Delta\kappa_Z + \tan^2\theta_W \Delta\kappa_\gamma \tag{5.38}$$

As already discussed the motivation for these relations is that they are predicted by the EFT approach. The 3 independent anomalous couplings retained are Δg_1^Z, $\Delta\kappa_Z$, and λ_Z.

As for the other diboson analyses, the expectation of the event counts in a given bin is parametrized as a bilinear function of the anomalous couplings noted generically ζ_i

$$\nu_S^b(\boldsymbol{\zeta}) = Y_{00}^b + \sum_{i=1}^{3} Y_{0i}^b\zeta_i + \sum_{i=1}^{3} Y_{ii}^b\zeta_i^2 + \sum_{i,j=1;j>i}^{3} Y_{ij}^b\zeta_i\zeta_j \tag{5.39}$$

The kinematical variable used to derive limits on the anomalous couplings is $p_T^{Lead.}$ the transverse momentum of the lepton of highest p_T. Only the events from the $e\mu$ channel selection are used.

Precisely the data that are used are the contents of the 3 last bins of the distribution of $p_T^{Lead.}$ shown on the figure 5.23 [16]. The figure shows the data and the expected SM yields, signal and backgrounds.

The SM prediction has been computed with `MC@NLO` [148] with NLO EW corrections. Systematics has been added to cover the differences of the p_T distributions between `MC@NLO` and `POWHEG+PYTHIA 8`.

Also shown in the figure 5.23 are the contributions from non null anomalous couplings of the order of the limits derived bellow. They amount for an increase by a factor from 3 to 4 of the predicted number of events in the last bin and by about 10 to 20% in the next to last bin.

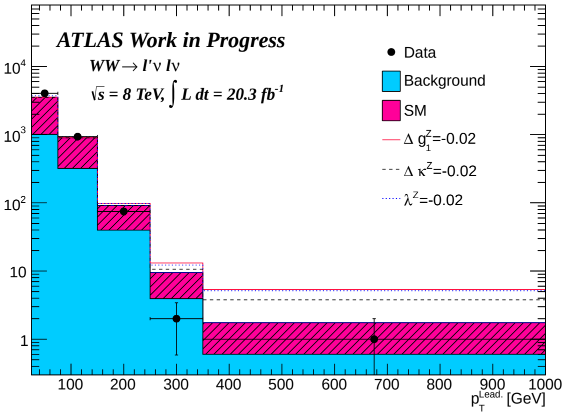

Figure 5.23: Distribution of the transverse momentum of the lepton of highest p_T.

---

[16] 75 events in the 150 GeV $< p_T^{Lead.} <$ 250 GeV range, 2 events in the 250 GeV $< p_T^{Lead.} <$ 350 GeV range, and 1 event in the 350 GeV $< p_T^{Lead.} <$ 1000 GeV range

5.5.3.1 Results

One considers first the 3 one-dimension fits, i.e fits in which all but one of the anomalous couplings are fixed at 0. The qualities of these fits are estimated by computing p-values as described in section 5.3.3.2. These p-values are of the order of 6% which is not great but not redhibitory.

Parameter	Observed	Expected
Δg_1^Z	[-0.014 ; 0.026]	[-0.022 $(^{+0.007}_{-0.009})$; 0.028 $(^{+0.008}_{-0.008})$]
$\Delta\kappa_Z$	[-0.024 ; 0.019]	[-0.028 $(^{+0.007}_{-0.009})$; 0.025 $(^{+0.010}_{-0.008})$]
λ_Z	[-0.019 ; 0.019]	[-0.024 $(^{+0.007}_{-0.009})$; 0.023 $(^{+0.009}_{-0.007})$]

Table 5.17: Observed and Expected one-dimension 95% Confidence Level Intervals of the anomalous Couplings; the figures reported between parentheses are not errors but distributions widths (cf text). *(WW analysis)*

The table 5.17 shows the Confidence Intervals for each of the one-dimension fits in the column “Observed”. The Lower and Upper ends of the Confidence Interval for the anomalous Couplings λ_Z are shown in the figures 5.24.

These figures show also the Asimov intervals ends obtained replacing the actual data by the SM expectations. A proper assessment of the “naturality” of the observed limits is obtained generating pseudo experiments around the SM expectations to build the “natural” distributions of the intervals ends. They are shown in figures 5.24 with their means indicated as “Expected” as well as their 1 and 2-σ widths. The means and 1-σ widths are reported in table 5.17 in the column “Expected”.

Both the table 5.17 and the figures 5.24 show that the actual Observed limits are in the expected range of fluctuations around SM expectations [17].

Next one considers the 3 two-dimension fits for which all but two of the anomalous couplings are fixed at 0. The Observed and Expected limits as well as the 1 and 2-σ bands are shown in figures 5.25. These figures show that the observed 2-dimension 95% Confidence Level Domains are within the expected fluctuations around the SM expectations.

5.5.3.2 EFT Results

We have already seen that the EFT operators analysis reduces the number of the parameters from the 14 charged anomalous Couplings given in table 5.1 to just 5 parameters of which 3 are respecting C and P. The relations between the EFT parameters and the anomalous couplings to which the WW production is sensitive are the same than for the WZ analysis case (cf equations (5.37) and equations (A.34), (A.35) and (A.39)):

$$\begin{aligned}\Delta g_1^Z &= \frac{m_Z^2}{2}\frac{C_W}{\Lambda^2}\\ \Delta\kappa_Z &= \frac{m_W^2}{2}\Big(\frac{C_W}{\Lambda^2} - \tan^2\theta_W \frac{C_B}{\Lambda^2}\Big)\\ \lambda_Z &= \frac{3g^2 m_W^2}{2}\frac{C_{WWW}}{\Lambda^2}\end{aligned} \tag{5.40}$$

The problem is re-parametrized in terms of the EFT parameters and one obtains the one-dimension

---

[17] The WW limits are dominated by statistical errors. If the systematics uncertainties are switched off, the size of the Asimov intervals decrease by about $\sim 10\%$.

95% Confidence Level Intervals given in the table 5.18.

As discussed early, one can convert the limits of the table 5.17 into limits on the scale Λ by assuming for a moment $C_{xyz} \sim 1$. The limits on C_W/Λ^2 and C_{WWW}/Λ^2 translate into lower limits for Λ in the range 0.3 to 0.5 TeV. The limits on C_B/Λ^2 point to a limit of the order of $\sim$ 0.200 GeV.

EFT parameter	Observed [TeV $^{-2}$]	Expected [TeV $^{-2}$]
C_W/Λ^2	[-5.2 ; 10.1]	[-8.6 $\left(^{+2.9}_{-4.0}\right)$; 11.5 $\left(^{+3.5}_{-2.9}\right)$]
C_B/Λ^2	[-20 ; 26.]	[-27. $\left(^{+8.}_{-11.}\right)$; 30. $\left(^{+10.}_{-8.}\right)$]
C_{WWW}/Λ^2	[-4.5 ; 4.5]	[-5.7 $\left(^{+1.7}_{-2.2}\right)$; 5.7 $\left(^{+2.1}_{-1.6}\right)$]

Table 5.18: Observed and Expected one-dimension 95% Confidence Level Intervals on the EFT parameters; the figures between parentheses are not errors but distribution widths. *(WW analysis)*

5.5.3.2.1 Consistency requirement As already discussed, a consistent application of the EFT analysis requires to drop the two last terms in the parametrization of the signal expectation (5.39). Doing so one gets the results shown in the tables 5.19.

Parameter	With bilinear terms	Without bilinear terms
Δg_1^Z	[-0.014 ; 0.026]	[-0.02 ; 0.11]
$\Delta\kappa_Z$	[-0.024 ; 0.019]	[-0.20 ; 0.05]
λ_Z	[-0.019 ; 0.019]	[-2.0 ; 2.0]

Table 5.19: Observed one-dimension 95% Confidence Level Intervals of the anomalous Couplings obtained with and without bilinear terms in the Signal expectations *(WW analysis)*

Judged from the size of the intervals one can quantify the degradation of the limits by a factor 3, 6 and 400 for Δg_1^Z, $\Delta\kappa_Z$, and λ_Z respectively. As in the similar situation for the WZ analysis it is not trivial to track how one goes from the results of the tables 5.17 and 5.18 to those of the tables 5.19. However one can capture the gross features by considering that the parametrization of the expectation of the content of the last bin is of the form $a\zeta^2 + b\zeta + c$ for one anomalous coupling ζ, and by taking the ratio $a\zeta_o/b$, where ζ_o is the value of the interval ends, as a measure of the importance of the quadratic terms. Typically this ratio is $\sim$ 0.5 for Δg_1^Z, $\sim$ 2 for $\Delta\kappa_Z$, and $\sim$ 120 for λ_Z. Therefore the massive degradation of the limits on λ_Z is explained by the smallness of the interference of the anomalous amplitude with the SM amplitude of the process with respect to the square of the anomalous amplitude. When the quadratic term is removed the sensitivity to λ_Z drops dramatically.

Therefore as in the case of the WZ analysis, one concludes that within the framework of a consistent application of the EFT approach, the WW production study brings constrains only on the anomalous coupling Δg_1^Z and on the EFT parameter C_W/Λ^2.

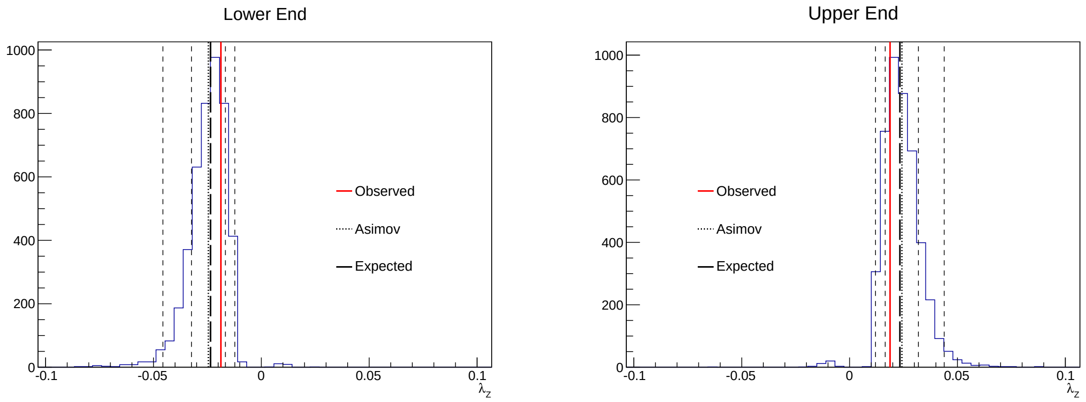

Figure 5.24: Lower and Upper Ends of the 95% Confidence Level Intervals for one-dimension fits. The red lines show the Observed limits, the black solid lines the Asimov limits, the thin long dashed black lines the Expected limits and the dashed lines the 1 and 2 σ-bands. *(WW analysis)*

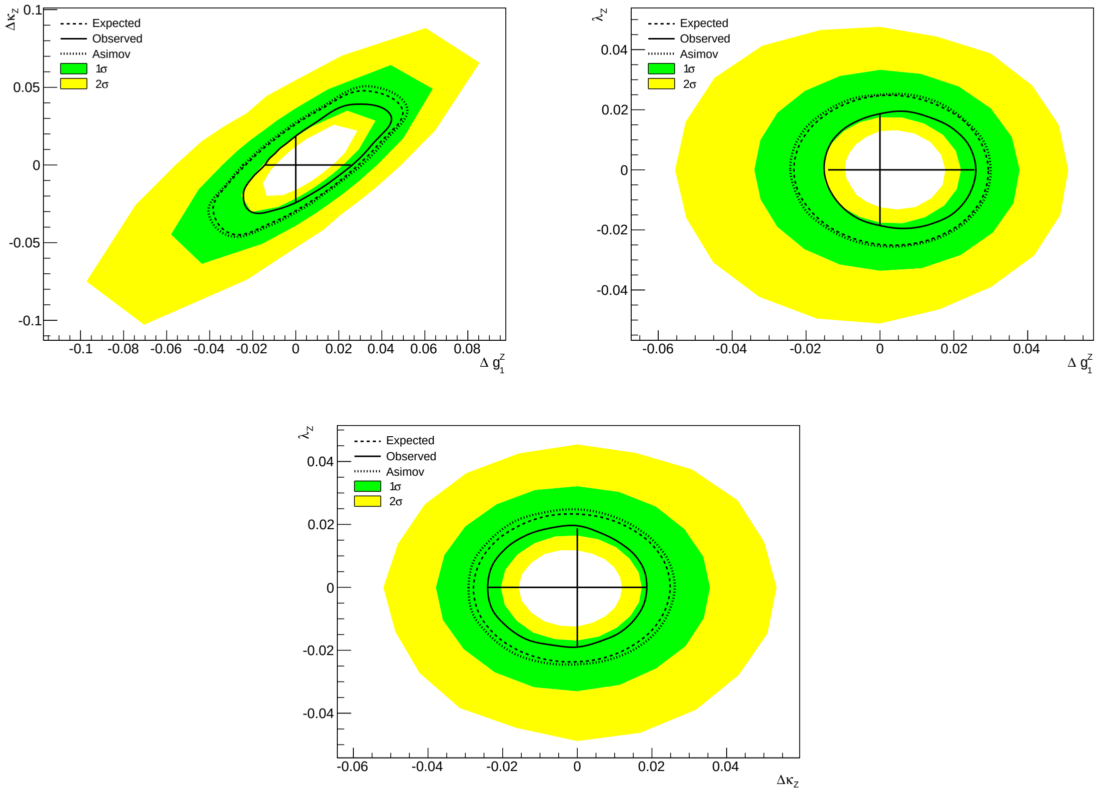

Figure 5.25: Observed, Asimov and Expected two-dimension 95% Confidence Level Domains. The black solid lines show the Observed limits, the dotted lines the Asimov limits, the dashed lines the Expected limits, the green and yellow bands correspond to the 1 and 2 σ-bands. The one-dimension 95% Confidence Level Domains for the Observed limits are reported on the anomalous Couplings axes. *(WW analysis)*

5.6 Study of the $W\gamma$ Production

Hereafter I present the analysis of the production of a pair of $W\gamma$ bosons of the sample of the ATLAS data at 7 TeV [92].

5.6.1 Selection and backgrounds

The final states of interest are those of the fully leptonic decays $W\gamma \to \ell\nu\gamma$, where ℓ is a muon or an electron. Hereafter they will be named $e\nu\gamma$ and $\mu\nu\gamma$. The signature is simple: missing transverse energy (E_T^{miss}) from the escaping ν, a pair of a lepton and a γ with high transverse momenta, well separated and isolated.

Selected muons are isolated Combined candidates with $|\eta| < 2.4$. Electrons should be isolated and have $|\eta| < 2.47$ excluding the weak area $1.37 < |\eta| < 1.52$. For both muons and electrons, $p_T > 25$ GeV is required. Events are selected requiring exactly one of such lepton. Photon should be isolated and have $|\eta| < 2.37$ excluding $1.37 < |\eta| < 1.52$ also. They are required to have $p_T > 15$ GeV. Large missing energy is required $E_T^{miss} > 35$ GeV. In addition a cut is applied on the transverse mass of the lepton-E_T^{miss} system, $m_T = \sqrt{2E_T^{\ell}E_T^{miss} - 2\vec{p}_T^{\,\ell}\vec{E}_T^{miss}} > 40$ GeV. For the $e\nu\gamma$ channel it is required that the mass of the $e\gamma$ system is not within 15 GeV of the Z-mass in order to reduce contamination from Z-boson decaying in e^-e^+ with one of the electrons is misidentified as a γ. Finally a large angular separation $\Delta R(\ell,\gamma) > 0.7$ is required between the lepton and the photon, in order to avoid the Final State Radiation (FSR) kinematical region where the γ is radiated at low angle from the lepton.

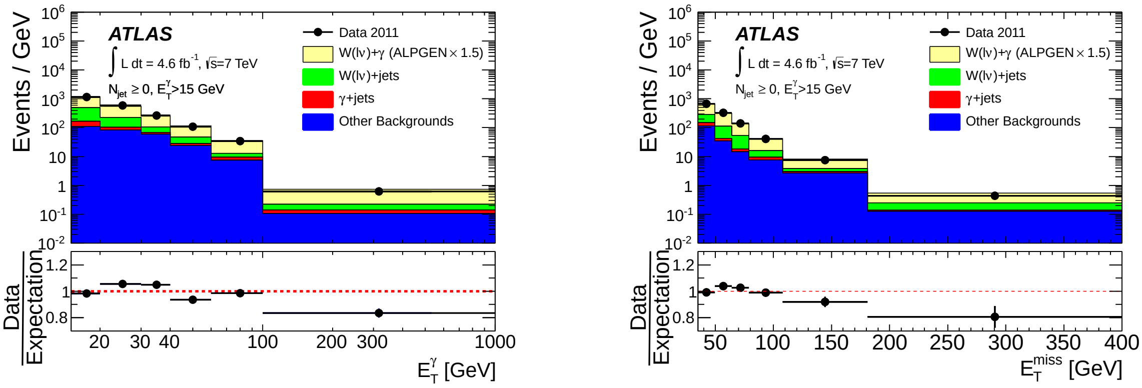

Figure 5.26: Combined distributions for $\ell\nu\gamma$ candidate events in the electron and muon channels of the photon transverse energy (left) and the missing transverse energy (right); the expected signal is taken from an `ALPGEN` (LO) simulation scaled by about 50% so that the predicted signal and backgrounds estimates match the observed yields.

The figures 5.26 compare combining all channels, the data and simulations of Standard Model Signal with estimates of the backgrounds for the distributions of the γ transverse energy and of the missing transverse energy.

One sees that the backgrounds contamination is large, about 40% of the selected events. For a half this contamination comes from $W + jets$ events when mesons produced in jet fragmentation produce a γ. Events from production of $Z + X$, where a Z-decay lepton is misidentified as a γ or a γ results from radiation from initial-state quark or charged lepton, contribute to background for about 20%. For about 10%, $\gamma + jets$ events can mimic $W\gamma$ events with lepton from heavy quark decays. The remaining 20% come from production of $t\bar{t}$, of single top, of WW and of W and Z bosons decaying in τ.

The $W + jets$ and $\gamma + jets$ backgrounds are estimated using Data Driven (DD) methods. All the others background sources are estimated by MC simulations.

The Data Driven method is a two-dimensional sideband method, the so-called ABCD method: 2 selection criteria are chosen and reversed in turn; this defines 4 regions, the A signal region with the 2 criteria applied and 3 control regions, B and C with only one of the selection criteria reversed and D with both criteria reversed. Assuming the control regions to be dominated by backgrounds, the ratio of the number of event in the region D and for instance in region B, tells how to estimate the number of background events in the signal region from the number of events in the region C. For $W + jets$, the two quantities on which the selection criteria are built, are the Photon isolation and identification. For $\gamma + jets$, they are the lepton isolation and E_T^{miss}.

The uncertainties on the DD background estimates are due to the limited sizes of data samples and to systematic errors, mainly on the photon isolation. In total the DD background uncertainties amount for 20-30%. The errors on the backgrounds estimated from MC are from theoretical uncertainties as well as from uncertainties from energy scale and resolution of the reconstructed objects. They amount for 10-20%.

5.6.2 Cross sections definitions and measurements

For the $W\gamma$ analysis, it has been decided to measure the cross sections only in a "extended" fiducial phase space common to the electron and muon channels. It is defined by: a charged lepton with $p_T > 25$ GeV and $|\eta| < 2.47$, a neutrino with $p_T > 35$ GeV, and a photon $p_T > 15$ GeV well separated from the charged lepton by requiring $\Delta R(\ell, \gamma) > 0.7$.

Two types of cross sections are defined: for the inclusive cross section no further criteria are added, for the exclusive cross section, one rejects events with any jet such that $E_T > 30$ GeV and $|\eta| < 4.4$.

The derivation of the cross sections is similar to what is done for the ZZ and WZ analyses described in 5.3.2.1, 5.3.2.2 and 5.3.2.3. The data are the numbers of selected events in the two electron and muon final states [18].

5.6.2.1 Results

The tables 5.20 show the inclusive and exclusive cross sections obtained combining the electron and muon channels. The p-value of the combined fit for the inclusive cross section is found to be very good, 79.6 ± 0.1%. The combined fit for the exclusive cross section is even better with a p-value, 85.0 ± 0.1%.

The total errors amount for about 13% of the measured cross sections. As shown by the tables 5.20, the measurements are totally dominated by systematics errors. The table 5.21 shows the main systematics errors on the combined measurement of the inclusive cross section. The main contributions are from Photon identification and isolation and from DD backgrounds estimates.

The tables 5.20 give also the theoretical cross sections computed with `MCFM`. In the figures 5.27, the predictions for the inclusive and exclusive cross sections are compared graphically to the measurement combining all channels. Also shown are the measurements from each channel separately.

The measurements are above the predictions. These theoretical cross sections are at the NLO QCD level. For the inclusive cross section, the discrepancy between data and NLO prediction is quite significant, at the level of 2-σ or so. As discussed in section 5.2, the NNLO QCD order corrections have been found to be 19% in [125] and the NLO EW order corrections at the level of -3%. A correction of +15% brings the discrepancy at the 1-σ level.

---

[18] respectively 7399 and 10914 events (4449 and 6578 events for the exclusive selection)

For the exclusive cross section, the discrepancy between data and theory is smaller, at the 1-σ level. This is expected since the requirement of no jet in the final state is expected to reduce QCD corrections in particular those not already included in the NLO QCD predictions of MCFM. The reduced NNLO QCD correction found to be of the order of 7% further reduces further the Data-prediction discrepancy.

$\sigma_{fid}^{W\gamma}$ $N_{jet} \geq 0$ [pb]	Measurement	$2.77\ ^{+0.03}_{-0.03}$ (stat) $^{+0.35}_{-0.30}$ (syst) $^{+0.14}_{-0.13}$ (lumi)
	Theory	1.96 ± 0.17

$\sigma_{fid}^{W\gamma}$ $N_{jet} = 0$ [pb]	Measurement	$1.76^{+0.03}_{-0.03}$ (stat) $^{+0.22}_{-0.19}$ (syst) $^{+0.08}_{-0.08}$ (lumi)
	Theory	1.39 ± 0.13

Table 5.20: Inclusive and exclusive $W\gamma \to \ell\nu\gamma$ cross sections: measurements combining all channels and theoretical predictions. The theoretical predictions are computed with `MCFM`.

Source	Errors (%)
Luminosity	$^{+5.2}_{-4.8}$
jet and E_T^{miss}	$^{+1.2}_{-1.3}$
Photon Id and Isolation	$^{+8.1}_{-7.3}$
Electromagnetic Scale	$^{+2.1}_{-2.0}$
QCD scales and PDFs	$^{+4.6}_{-4.4}$
Data Driven Backgrounds	$^{+8.2}_{-7.8}$

Table 5.21: Main systematic uncertainties on the combined inclusive $W\gamma \to \ell\nu\gamma$ cross section in % of the measured cross section.

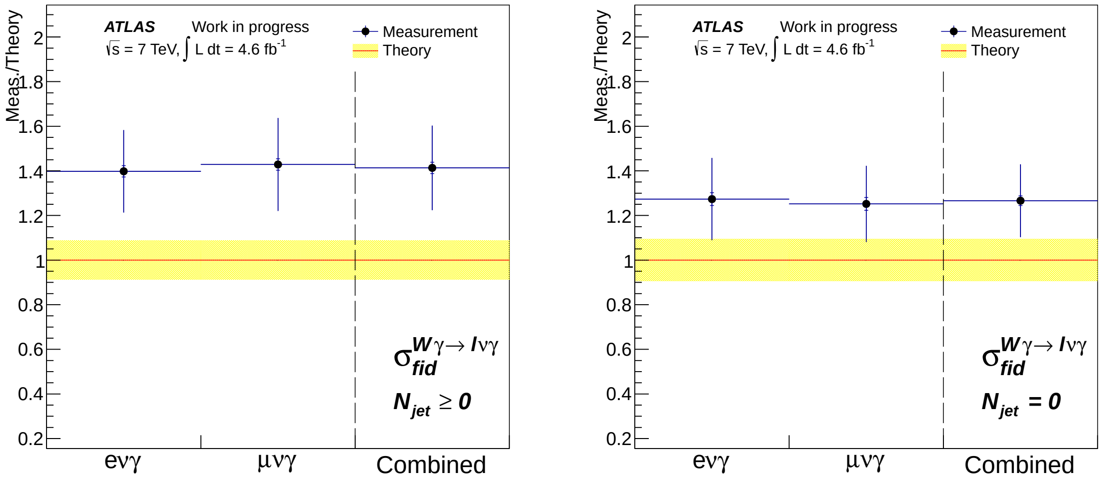

Figure 5.27: Measured $W\gamma \to \ell\nu\gamma$ cross sections, per channel and combining all of them, normalized to the theoretical predictions; Inclusive cross section on the left, exclusive cross section on the right.

5.6.3 Anomalous Triple Gauge Couplings measurements

The production of $W\gamma$ pairs allows to probe the $WW\gamma$ vertex. As shown by the tables 5.1, it is sensitive to 7 anomalous Triple Gauge Couplings, viz the 3 C and P respecting parameters Δg_1^γ, $\Delta\kappa_\gamma$, and λ_γ, and the 4 C or P violating parameters g_4^γ, g_5^γ, $\widetilde{\kappa}_\gamma$, and $\widetilde{\lambda}_\gamma$. Traditionally the C or P violating parameters are ignored. Furthermore one imposes $U(1)_{em}$ invariance which leads to $\Delta g_1^\gamma = 0$. Therefore only limits on $\Delta\kappa_\gamma$ and λ_γ are derived. As for the other diboson analyses, the expectation of the event counts in a given bin is a bilinear function of the anomalous couplings noted generically ζ_i

$$\nu_S^b(\boldsymbol{\zeta}) = Y_{00}^b + \sum_{i=1}^{2} Y_{0i}^b \zeta_i + \sum_{i=1}^{2} Y_{ii}^b \zeta_i^2 + \sum_{i,j=1;j>i}^{2} Y_{ij}^b \zeta_i \zeta_j \tag{5.41}$$

Contrary to the ZZ, WZ and WW analyses, the data used for the derivation of limits on anomalous couplings are not bin contents of some spectra histograms but simply counts of events such that $E_\gamma^T > 100$ GeV. They are 2 events counts: the numbers of events in the electron and muons channels separately [19]. Only events selected by the exclusive selection are counted.

5.6.3.1 Results

One first considers the 2 one-dimension fits, i.e fits in which all but one of the parameters $\Delta\kappa_\gamma$ and λ_γ are fixed at 0.

Parameter	Observed	Expected
$\Delta\kappa_\gamma$	[-0.41; 0.46]	[-0.38 $\left(^{+0.12}_{-0.18}\right)$; 0.43$\left(^{+0.18}_{-0.12}\right)$]
λ_γ	[-0.065; 0.061]	[-0.060 $\left(^{+0.018}_{-0.028}\right)$; 0.056$\left(^{+0.028}_{-0.018}\right)$]

Table 5.22: Observed and Expected one-dimension 95% Confidence Level Intervals of the anomalous Couplings; the figures reported between parentheses are not errors but distributions widths (cf text). *($W\gamma$ analysis)*

The table 5.22 shows the Confidence Intervals for each of the one-dimension fits in the column "Observed". The Lower and Upper ends of the Confidence Interval for the anomalous Couplings are shown in the figures 5.28.

The figures 5.28 show also the Asimov intervals ends, as before obtained replacing the actual data by the SM expectations. A proper assessment of the "naturality" of the observed limits is obtained generating pseudo experiments around the SM expectations. This allows to build the "natural" distribution of the intervals ends shown in figures 5.28 with their means indicated as "Expected" as well as their 1 and 2-σ widths. The means and 1-σ widths are reported in table 5.22 in the column "Expected".

Both the table 5.22 and the figures 5.28 show that the actual Observed limits are in the expected range of fluctuations around SM expectations [20].

Next one considers the two-dimension fit for which both $\Delta\kappa_\gamma$ and λ_γ are adjusted. The Observed and Expected limits as well as the 1 and 2-σ bands are shown in figures 5.29. This figure shows that the observed 2-dimension 95% Confidence Level Domain is within the expected fluctuations around the SM expectations.

---

[19] 82 and 86 events respectively

[20] Much more than in the ZZ and WZ cases, the $W\gamma$ anomalous couplings limits are dependent on the systematic errors: if the systematics uncertainties are switched off, the sizes of the Confidence Intervals decrease by about 50%.

5.6.3.2 EFT Results

At the time of the publication of the ATLAS $W\gamma$ analysis [92], no EFT analysis was performed. The results shown in this section have been derived for this memoir.

As discussed before, the EFT operators analysis reduce the number of parameters from the 14 charged anomalous Couplings given in table 5.1 to just 5 parameters, among which 3 are respecting C and P. The relations between the EFT parameters and the anomalous couplings to which the $W\gamma$ production is sensitive are (cf equations (A.35) and (A.39)):

$$\Delta\kappa_\gamma = \frac{m_W^2}{2}\left(\frac{C_W}{\Lambda^2} + \frac{C_B}{\Lambda^2}\right) \text{ and } \lambda_\gamma = \frac{3g^2 m_W^2}{2}\frac{C_{WWW}}{\Lambda^2} \tag{5.42}$$

Clearly there is a total degeneracy between the EFT parameters C_W and C_B in the $W\gamma$ measurements, only the sum being constrained. The one-dimension fit on these parameters are identical and will be noted hereafter as limit on $C_{W,B}$. As clearly shown by equations (5.42), we are dealing here with a simple rescaling of the anomalous couplings $\Delta\kappa_\gamma$ and λ_γ. The one-dimension 95% Confidence Level Intervals are given in the table 5.23.

Compared to the limits on the same parameters from the WZ analysis listed in table 5.13, it appears clearly that the $W\gamma$ analysis is much less constraining but on the EFT parameter C_B/Λ^2 for which one gains a factor 2 to 3. If for a moment ones takes $C_{xyz} \sim 1$, one sees that the lower limits on Λ are around ~ 0.1 TeV from $C_{W,B}/\Lambda^2$ limits and around ~ 0.25 TeV from C_{WWW}/Λ^2 limits.

EFT parameter	Observed [TeV $^{-2}$]	Expected [TeV $^{-2}$]
$C_{W,B}/\Lambda^2$	[-99 ; 111]	[-92 ; 104]
C_{WWW}/Λ^2	[-15.7 ; 14.8]	[-14.6 ; 13.6]

Table 5.23: Observed and Expected one-dimension 95% Confidence Level Intervals on the EFT parameters. *($W\gamma$ analysis)*

5.6.3.2.1 Consistency requirement As already discussed, a consistent application of the EFT analysis requires to drop the two last terms in the parametrization of the signal expectation (5.41). Doing so one gets the results shown in the tables 5.24.

Parameter	With bilinear terms	Without bilinear terms
$\Delta\kappa_\gamma$	[-0.41; 0.46]	[-0.45 ; 1.21]
λ_γ	[-0.065; 0.061]	[-6.4 ; 1.6]

Table 5.24: Observed one-dimension 95% Confidence Level Intervals of the anomalous Couplings obtained with and without bilinear terms in the Signal expectations *($W\gamma$ analysis)*

Following a mechanism already discussed in the section 5.4.3.2 for the WZ analysis, the massive degradation of the limits on λ_γ and therefore on C_{WWW}/Λ^2 results from a quite small interference between the SM amplitude and the amplitude associated to this anomalous coupling.

So it looks that within the framework of a consistent application of the EFT approach, the study of the $W\gamma$ production brings very weak if any constrains. However the analysis described here was based only on the event counting above $E_\gamma^T > 100$ GeV. This makes the fit results particularly sensitive to the bounding from below that is built by the bilinear terms in (5.41). More bins would bring more stability and alleviate partially the degradation of the limits when the bilinear terms are turned over.

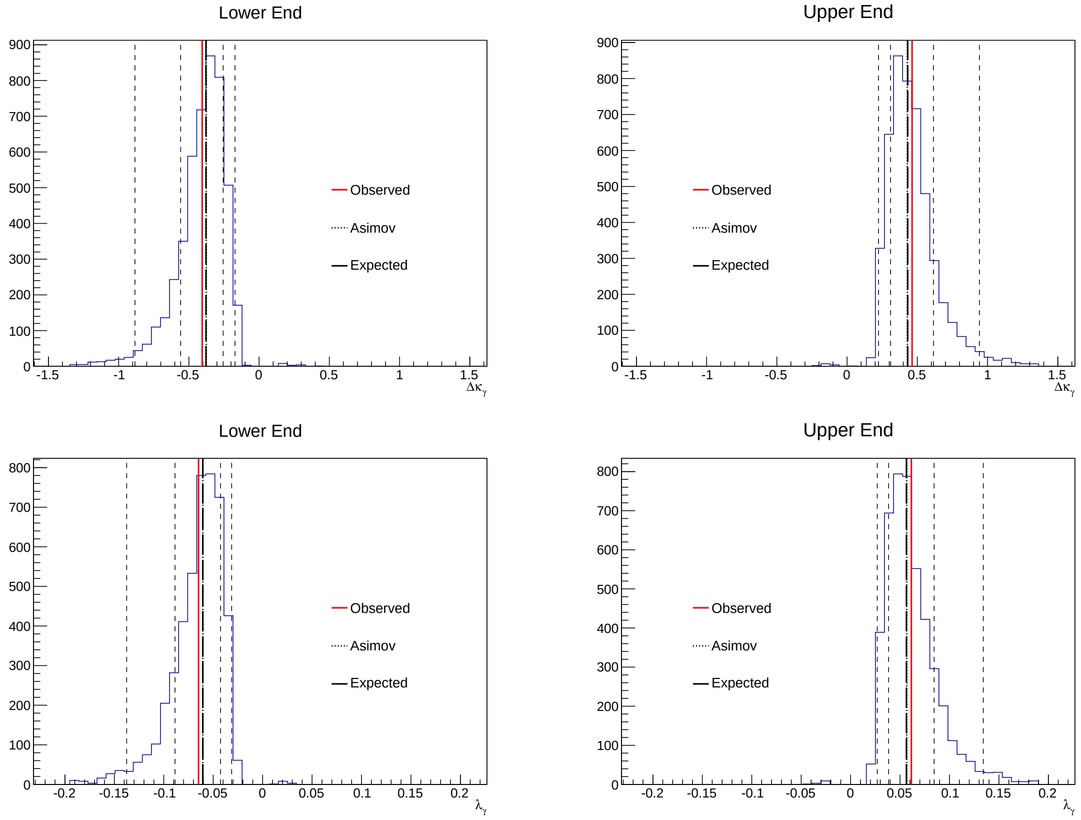

Figure 5.28: Lower and Upper Ends of the 95% Confidence Level Intervals for one-dimension fits. The red lines show the Observed limits, the black solid lines the Asimov limits, the thin long dashed black lines the Expected limits and the dashed lines the 1 and 2 σ-bands. *(Wγ analysis)*

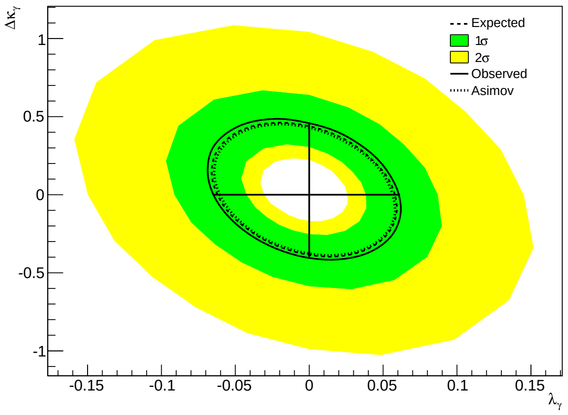

Figure 5.29: Observed, Asimov and Expected two-dimension 95% Confidence Level Domains. The black solid lines show the Observed limits, the dotted lines the Asimov limits, the dashed lines the Expected limits, the green and yellow bands correspond to the 1 and 2 σ-bands. The one-dimension 95% Confidence Level Domains for the Observed limits are reported on the anomalous Couplings axes. *(Wγ analysis)*

5.7 Study of the $Z\gamma$ Production

Hereafter I present the analysis of the production of a pair of $Z\gamma$-bosons on the sample of the ATLAS data at 7 TeV [92].

5.7.1 Selection and backgrounds

Two decay modes have been studied: the $Z\gamma \to \ell\bar{\ell}\gamma$ mode where the Z-boson decays in electrons or muons pair and the $Z\gamma \to \nu\bar{\nu}\gamma$ mode where the Z-boson decays in neutrinos pair

For the $Z\gamma \to \ell\bar{\ell}\gamma$ analysis the decay leptons are identified as in the $W\gamma$ analysis (cf section 5.6.1). It is required that there exists exactly one pair of leptons of same flavor and opposite charge that forms a system with invariant mass $m_{\ell\ell} > 40$ GeV and that there is one isolated photon with $E_T^{\gamma} > 15$ GeV.

For the $Z\gamma \to \nu\bar{\nu}\gamma$ analysis, one requires a photon with $E_T^{\gamma} > 100$ GeV and $E_T^{miss} > 90$ GeV. The photon, missing energy and jets are required to be well separated in the transverse plane. Events with leptons identified as in the $W\gamma$ analysis are rejected.

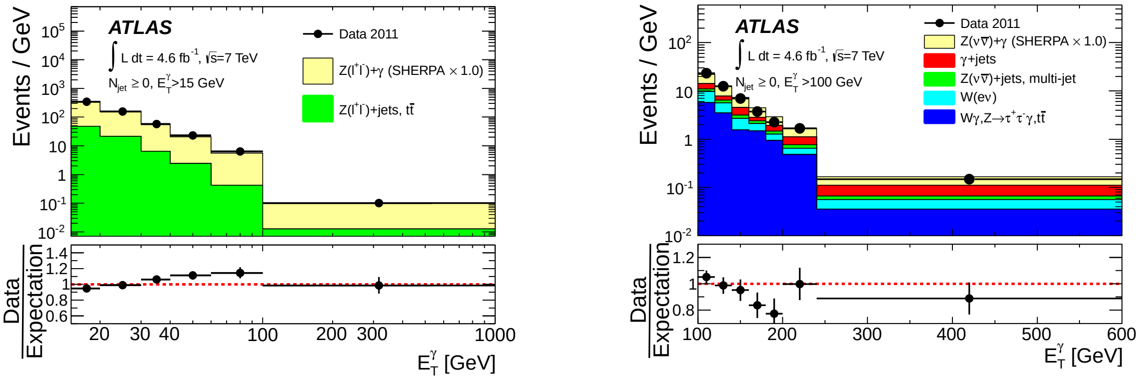

Figure 5.30: Distributions of the transverse energy of the γ for the $Z\gamma \to \ell\bar{\ell}\gamma$ events combining electron and muon decays (left) for the $Z\gamma \to \nu\bar{\nu}\gamma$ events (right); The expected signal is taken from an `SHERPA` (LO) simulation scaled so that the predicted signal and backgrounds estimates match the observed yields.

The figures 5.30 show the distributions of the transverse energy of the γ in $Z\gamma \to \ell\bar{\ell}\gamma$ and $Z\gamma \to \nu\bar{\nu}\gamma$ events. The backgrounds are at the level of $\sim$ 15% for the $Z\gamma \to \ell\bar{\ell}\gamma$ events and of $\sim$ 60% for the $Z\gamma \to \nu\bar{\nu}\gamma$ events.

The main source of the backgrounds in the $Z\gamma \to \ell\bar{\ell}\gamma$ analysis ($>$ 98%) is the $Z + jets$ events production. It is estimated from data in the same way than the $W + jets$ background contribution is in the $W\gamma$ analysis. The systematic errors of $\sim$ 20% result from the uncertainties on photon identification.

The main background sources for the $Z\gamma \to \nu\bar{\nu}\gamma$ analysis are for 35% the production of $W\gamma$ events, and for 25% each, the productions of W-boson and of $\gamma + jets$ events.

The $W\gamma$ events can mimic $\nu\bar{\nu}\gamma$ events when the W-boson decay products are not reconstructed. This contribution is determined from MC simulations with a systematic errors at the level of 15%.

The production of W-boson contributes to background when the W boson decays in a $e\nu$ pair with the electron reconstructed as a γ. The probability of such a misidentification, $f_{e->\gamma}$, is estimated on $e\gamma$ events forming a system with a mass close to the Z boson mass. A control region is defined by substituting to the γ requirement in the $\nu\bar{\nu}\gamma$ selection, a requirement for an electron. Counting events in this control region and using $f_{e->\gamma}$, one computes the number of events in the $\nu\bar{\nu}\gamma$ signal region. The uncertainties on $f_{e->\gamma}$ are dominating the $\sim$ 10% systematic error on this contribution.

The $\gamma + jets$ events contribute to background when missing energy builds up from decays of heavy quark in neutrinos and energy mis-measurements. In the $\nu\bar{\nu}\gamma$ selection, E_T^{miss} and the photon are required to be well separated. The contribution from this background is estimated from data by inversing this separation. The selected events are then dominated by $\gamma+jets$ events. From the number of events so selected, one extrapolates the contamination in the signal region by using a extrapolation factor determined in MC simulations. A systematic error on this contribution at the level of $\sim 20\%$, is obtained by varying the thresholds on E_T^{miss} and jet multiplicity.

5.7.2 Cross sections definitions and measurements

As in the $W\gamma$ analysis, it has been decided to measure the cross sections only in a "extended" fiducial phase space. For the $Z\gamma \to \ell\bar{\ell}\gamma$ analysis it is defined by 2 same flavor opposite charge leptons with $p_T > 25$ GeV and $|\eta| < 2.47$ forming a system of mass $m_{\ell\ell} > 40$ GeV and a photon $p_T > 15$ GeV well separated from the charged lepton by requiring $\Delta R(\ell, \gamma) > 0.7$. For the $Z\gamma \to \nu\bar{\nu}\gamma$ analysis it is defined by the transverse momentum of the two neutrinos system $p_T^{\nu\nu} > 90$ GeV and and a photon $p_T > 100$ GeV.

As for the $W\gamma$ analysis two types of cross sections are defined: for the inclusive cross section no further criteria are added, for the exclusive cross section, one rejects events with any jet such that $E_T > 30$ GeV and $|\eta| < 4.4$.

The derivation of the cross sections is similar to what is done for the other diboson analyses. The data for the $Z\gamma \to \ell\bar{\ell}\gamma$ analysis are the two events counts in the electron and muon channels [21]. For the $Z\gamma \to \nu\bar{\nu}\gamma$ analysis, the data are the single events count of selected events[22].

5.7.2.1 Results

5.7.2.1.1 $Z\gamma \to \ell\bar{\ell}\gamma$ analysis

The tables 5.25 show the inclusive and exclusive cross sections for $Z\gamma \to \ell\bar{\ell}\gamma$ obtained combining the electron and muon channels. The p-values of the combined fit for the inclusive and exclusive cross sections are found to be very good, $86.9 \pm 0.1\%$ and $84.2 \pm 0.1\%$, respectively.

The total errors amount for about 10% of the measured cross sections. As shown by the tables 5.25, the measurement is dominated by systematics errors. The table 5.26 shows the main systematics errors on the combined measurement of the inclusive cross section. The main contribution is from Photon identification and isolation followed by the contributions from DD backgrounds estimates and from the QCD Scales and PDFs.

The tables 5.25 give also the theoretical cross sections computed with `MCFM`. In the figures 5.31, the predictions for the inclusive and exclusive cross sections are compared graphically to the measurement combining all channels. Also shown are the measurements from each channel separately.

The agreement between prediction and measurement is good for both inclusive and exclusive cross sections. As discussed in section 5.2, in [125] the NNLO QCD order corrections for the inclusive and exclusive cross sections have been found to be 8% and 3% respectively. These corrections improve the comparison between prediction and measurement for the inclusive cross sections and slightly deteriorate for the exclusive cross sections. However, even taking into account, the additional NLO EW corrections of the order of -5% discussed in [142], the agreement between prediction and measurement remains excellent, of the order of 1-σ or less.

---

[21] respectively 1908 and 2756 events (1417 and 2032 events for the exclusive selection)

[22] 1094 and 662 events for the inclusive and exclusive selections respectively

$\sigma_{fid}^{Z\gamma\to\ell\bar{\ell}\gamma}$ $N_{jet} \geq 0$ [pb]	Measurement	$1.31^{+0.02}_{-0.02}$ (stat) $^{+0.11}_{-0.10}$ (syst) $^{+0.05}_{-0.05}$ (lumi)
	Theory	1.18 ± 0.05

$\sigma_{fid}^{Z\gamma\to\ell\bar{\ell}\gamma}$ $N_{jet} = 0$ [pb]	Measurement	$1.05^{+0.02}_{-0.02}$ (stat) $^{+0.10}_{-0.09}$ (syst) $^{+0.04}_{-0.04}$ (lumi)
	Theory	1.06 ± 0.05

Table 5.25: Inclusive and exclusive $Z\gamma \to \ell\bar{\ell}\gamma$ cross sections: measurements combining all channels and theoretical predictions. The theoretical predictions are computed with `MCFM`.

Source	Errors (%)
Luminosity	$^{+4.1}_{-3.7}$
Photon Id and Isolation	$^{+6.2}_{-5.6}$
Electromagnetic Scale	$^{+1.5}_{-1.5}$
QCD scales and PDFs	$^{+3.5}_{-3.4}$
Data Driven Backgrounds	$^{+3.7}_{-3.4}$

Table 5.26: Main systematic uncertainties on the combined inclusive $Z\gamma \to \ell\bar{\ell}\gamma$ cross section in % of the measured cross section.

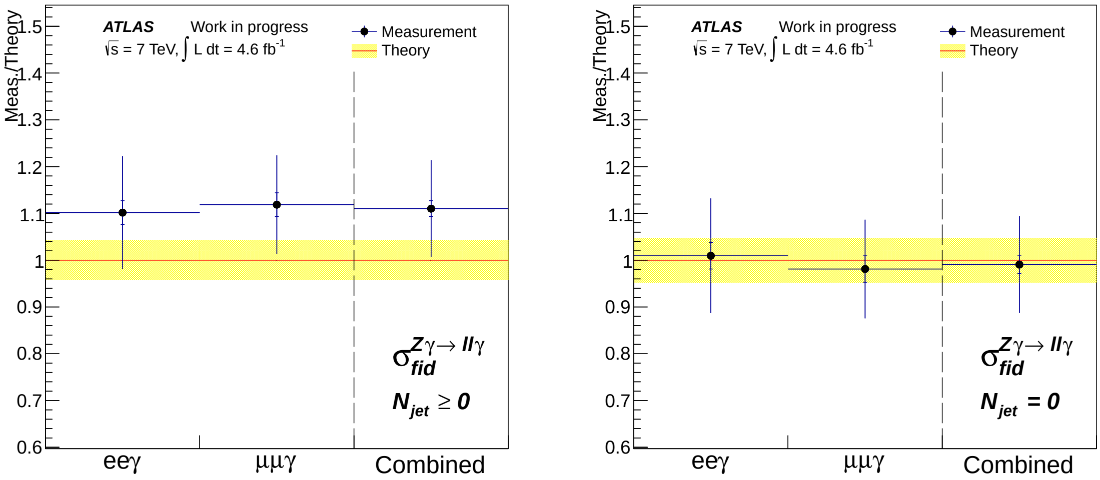

Figure 5.31: Measured $Z\gamma \to \ell\bar{\ell}\gamma$ cross sections, per channel and combining all of them, normalized to the theoretical predictions; Inclusive cross sections on the left, exclusive cross sections on the right.

5.7.2.1.2 $Z\gamma \to \nu\bar{\nu}\gamma$ analysis

The tables 5.27 show the inclusive and exclusive cross sections for $Z\gamma \to \nu\bar{\nu}\gamma$. Since the fit data is a single events count there is no possible assessment of the quality of the fit.

$\sigma_{fid}^{Z\gamma\to\nu\bar{\nu}\gamma}$ $N_{jet} \geq 0$ [pb]	Measurement	0.133±0.013 (stat) ±0.020 (syst) ±0.005 (lumi)
	Theory	0.156 ± 0.012

$\sigma_{fid}^{Z\gamma\to\nu\bar{\nu}\gamma}$ $N_{jet} = 0$ [pb]	Measurement	0.116 ±0.010 (stat) ±0.013 (syst) ±0.004 (lumi)
	Theory	0.115 ± 0.009

Table 5.27: Inclusive and exclusive $Z\gamma \to \nu\bar{\nu}\gamma$ cross sections: measurements and theoretical predictions. The theoretical predictions are computed with `MCFM`.

The total errors amount for about 20% of the measured cross sections.

As shown by the tables 5.27, the measurements is not totally dominated by systematics errors with statistical errors amounting for a third to a half of the total errors.

The table 5.28 shows the main systematics errors on the measurement of the inclusive cross section. The main contribution is from Photon identification and isolation followed by the contribution from the Electromagnetic scale.

Source	Errors (%)
Luminosity	$^{+4.4}_{-4.1}$
Photon Id and Isolation	$^{+13.9}_{-12.4}$
Electromagnetic Scale	$^{+5.9}_{-5.5}$
QCD scales and PDFs	$^{+3.4}_{-3.2}$
Data Driven Backgrounds	$^{+3.8}_{-3.8}$

Table 5.28: Main systematic uncertainties on the inclusive $Z\gamma \to \nu\bar{\nu}\gamma$ cross section in % of the measured cross section.

The tables 5.27 give also the theoretical cross sections computed with `MCFM`. In the figure 5.32, the predictions for the inclusive and exclusive cross sections are compared graphically to the measurements.

The agreement between prediction and measurement is good for both inclusive and exclusive cross sections.

As discussed in section 5.2, in [125] the NNLO QCD order corrections for the inclusive and exclusive cross sections have been found to be 12% and -2% respectively.

These corrections slightly deteriorate the the agreement between prediction and measurements. However, even taking into account, the additional NLO EW corrections of the order of -5% discussed in [142], the agreement between prediction and measurement remains excellent, of the order of 1-σ or less.

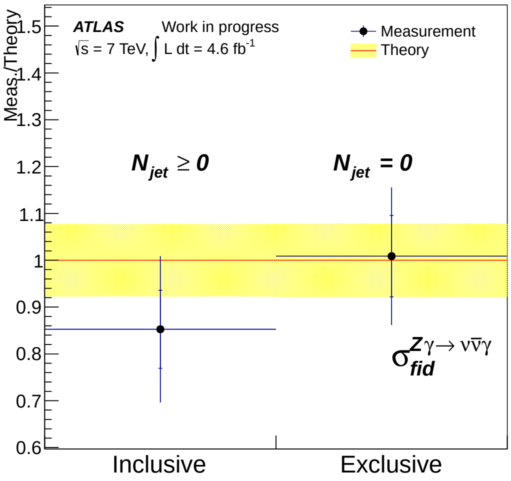

Figure 5.32: Measured $Z\gamma \to \nu\bar{\nu}\gamma$ cross sections normalized to the theoretical predictions.

5.7.3 Anomalous Triple Gauge Couplings measurements

The production of $Z\gamma$ pairs allows to probe the $ZZ\gamma$ and $Z\gamma\gamma$ vertices. As shown by the tables 5.1, it is sensitive to 8 anomalous Triple Gauge Couplings, viz the 4 CP respecting parameters h_3^γ, h_4^γ, h_3^Z, and h_4^Z, and the 4 CP violating parameters h_1^γ, h_2^γ, h_1^Z, and h_2^Z. Traditionally the CP violating parameters are ignored and only limits on h_3^γ, h_4^γ, h_3^Z, and h_4^Z are derived. As usual the expectation of the event counts in a given bin is a bilinear function of the anomalous couplings noted generically ζ_i

$$\nu_S^b(\boldsymbol{\zeta}) = Y_{00}^b + \sum_{i=1}^{4} Y_{0i}^b\zeta_i + \sum_{i=1}^{4} Y_{ii}^b\zeta_i^2 + \sum_{i,j=1;j>i}^{4} Y_{ij}^b\zeta_i\zeta_j \tag{5.43}$$

As for the $W\gamma$ analysis, the data used for the derivation of limits on anomalous couplings are not bin contents of some spectra histograms but simply counts of events such that $E_\gamma^T > 100$ GeV. They are 3 events counts: the numbers of the $Z\gamma \to \ell\bar{\ell}\gamma$ events in the electron and muons channels separately and the number of the $Z\gamma \to \nu\bar{\nu}\gamma$ events [23]. In all cases, the exclusive selection is applied.

5.7.3.1 Results

One considers first the 4 one-dimension fits, i.e fits in which all but one of the anomalous couplings are fixed at 0.

Parameter	Observed	Expected
h_3^Z	[-1.3 ; 1.4] $\times 10^{-2}$	[-1.5 $(^{+0.5}_{-0.7})$; 1.6 $(^{+0.7}_{-0.5})$] $\times 10^{-2}$
h_4^Z	[-8.7 ; 8.7] $\times 10^{-5}$	[-9.7 $(^{+3.1}_{-4.6})$; 9.7 $(^{+4.6}_{-3.1})$] $\times 10^{-5}$
h_3^γ	[-1.5 ; 1.6] $\times 10^{-2}$	[-1.7 $(^{+0.5}_{-0.8})$; 1.8 $(^{+0.8}_{-0.5})$] $\times 10^{-2}$
h_4^γ	[-9.4 ; 9.2] $\times 10^{-5}$	[-10.0 $(^{+3.3}_{-5.0})$; 10.0 $(^{+4.9}_{-3.3})$] $\times 10^{-5}$

Table 5.29: Observed and Expected one-dimension 95% Confidence Level Intervals of the anomalous Couplings; the figures reported between parentheses are not errors but distributions widths (cf text). *($Z\gamma$ analysis)*

The table 5.29 shows the Confidence Intervals for each of the one-dimension fits in the column “Observed”. The Lower and Upper ends of the Confidence Interval for the anomalous Couplings h_3^Z and h_4^Z are shown in the figures 5.33.

The figures 5.33 show also the Asimov intervals ends obtained replacing the actual data by the SM expectations. A proper assessment of the “naturality” of the observed limits is obtained generating pseudo experiments around the SM expectations to build the “natural” distributions of the intervals ends. They are shown in figures 5.33 with their means indicated as “Expected” as well as their 1 and 2-σ widths. The means and 1-σ widths are reported in table 5.29 in the column “Expected”.

Both the table 5.29 and the figures 5.33 show that the actual Observed limits are in the expected range of fluctuations around SM expectations [24].

Next one considers the two-dimension fits for which all but two of the anomalous couplings are fixed at 0. The ATLAS $Z\gamma$ analysis chose to fit separately the pairs of the anomalous couplings corresponding to each of the $ZZ\gamma$ and $Z\gamma\gamma$ vertices. Therefore the figures 5.34 show only the two

---

[23] 15, 19 and 662 events respectively

[24] As for the limits obtained in the $W\gamma$ analysis, the systematic errors contribute significantly to the $Z\gamma$ anomalous couplings limits: if the systematics uncertainties are switched off, the sizes of the Confidence Intervals decrease by 50 to 60%.

two-dimension fits for, on one hand h_3^γ and h_4^γ, and on the other hand, h_3^Z and h_4^Z. Are shown the Observed and Expected limits as well as the 1 and 2-σ bands.

These figures show that the observed 2-dimension 95% Confidence Level Domains are within the expected fluctuations around the SM expectations.

5.7.3.2 EFT Results

At the time of the publication of the ATLAS $Z\gamma$ analysis [92], no EFT analysis was performed. The results shown in this section have been derived for this memoir.

As discussed before, the EFT operators analysis reduces the number of parameters for the neutral aTGCs, from the 12 neutral anomalous Couplings given in table 5.1 to just 4 parameters all violating but one. The relations between the EFT parameters and the anomalous couplings to which the $Z\gamma$ production is sensitive are (cf equations (A.20), (A.22), (A.23) and (A.24)):

$$h_3^\gamma = h_4^\gamma = h_4^Z = 0 \tag{5.44}$$

$$h_3^Z = \frac{v^2 m_Z^2}{4 c_w s_w} \frac{C_{\widetilde{B}W}}{\Lambda^4} \tag{5.45}$$

So the derivation of the limit on the single EFT parameter accessible is particularly simple since one only has to rescale the one-dimension fit limits on h_3^Z to obtain those on $\frac{C_{\widetilde{B}W}}{\Lambda^4}$. The results are given in the table 5.30.

Compared to the limits on $\frac{C_{\widetilde{B}W}}{\Lambda^4}$ from the ZZ analysis listed in table 5.7, it appears that the $Z\gamma$ analysis is much less constraining by a factor ~ 3. If for a moment ones takes $C_{\widetilde{B}W} \sim 1$, one finds that the limits from table 5.30 point to lower limits on Λ of ~ 0.4 TeV .

EFT parameter	Observed [TeV $^{-4}$]	Expected [TeV $^{-4}$]
$C_{\widetilde{B}W}/\Lambda^4$	[-43. ; 47.]	[-50. ; 54.]

Table 5.30: Observed and Expected one-dimension 95% Confidence Level Intervals on the EFT parameters. *($Z\gamma$ analysis)*

5.7.3.2.1 Consistency requirement

As already discussed, a consistent application of the EFT analysis requires to drop the two last terms in the parametrization of the signal expectation (5.43). Doing so the fit of h_3^Z gets highly unstable with many local minima which break the usual procedure. The table 5.31 gives an approximate error interval determined by visual inspection of the Profile Likelihood curve which, as bad as it is, is enough to illustrate the main feature of what is going on. The interference term of the h_3^Z amplitude with the SM amplitude is so small that, as it already happened for some parameters in the other diboson analyses, we loose effectively any sensitivity to the anomalous coupling.

Parameter	With bilinear terms	Without bilinear terms
h_3^Z	[-1.3 ; 1.4] $\times 10^{-2}$	[-11 ; 3]

Table 5.31: Observed error Intervals of the anomalous Couplings obtained with and without bilinear terms in the Signal expectations *($Z\gamma$ analysis)*

One concludes that within the framework of a consistent application of the EFT approach, the study of the $Z\gamma$ production brings no constrain on the EFT parameters. However as for the $W\gamma$

analysis, the situation would be highly improved by using spectra of the transverse energy of the photon E_γ^T, rather than simple counts of events above a high E_γ^T threshold.

5.7.3.3 Comments

The first ATLAS and CMS publications on $Z\gamma$ production [92, 168] reached approximately the same sensitivity to anomalous couplings. The limits obtained improved significantly to the LEP and Fermilab results (cf table A.8). Both analyses are based on the transverse energy of the photon and in effect count events above a threshold of the order of 100 GeV.

This is reasonable for the $Z\gamma \to \ell\bar{\ell}\gamma$ channel given its statistics. However the higher statistics available in the $Z\gamma \to \nu\bar{\nu}\gamma$ channel, which at the time was used by ATLAS but not by CMS, allows to reach higher energies and therefore to improve limits.

This was demonstrated by CMS in [169] where using the $Z\gamma \to \nu\bar{\nu}\gamma$ channel and bins at higher E_γ^T, a gain of 5 or so on the ATLAS aTGCs limits from table 5.29 was achieved. Going to the $\sqrt{s} = 8$ TeV sample, CMS got a gain of about 3 using the $Z\gamma \to \ell\bar{\ell}\gamma$ channel [170] and a gain of about 10 using the $Z\gamma \to \nu\bar{\nu}\gamma$ channel [171] (cf table A.8). From table 5.30, one sees that this, translated in the EFT framework, places a lower limit on Λ around ~ 0.7 TeV.

At the time of writing, an ATLAS analysis of the $\sqrt{s} = 8$ TeV sample is on the point to be published which drastically improves the ATLAS aTGCs limits from $Z\gamma$ production [172].

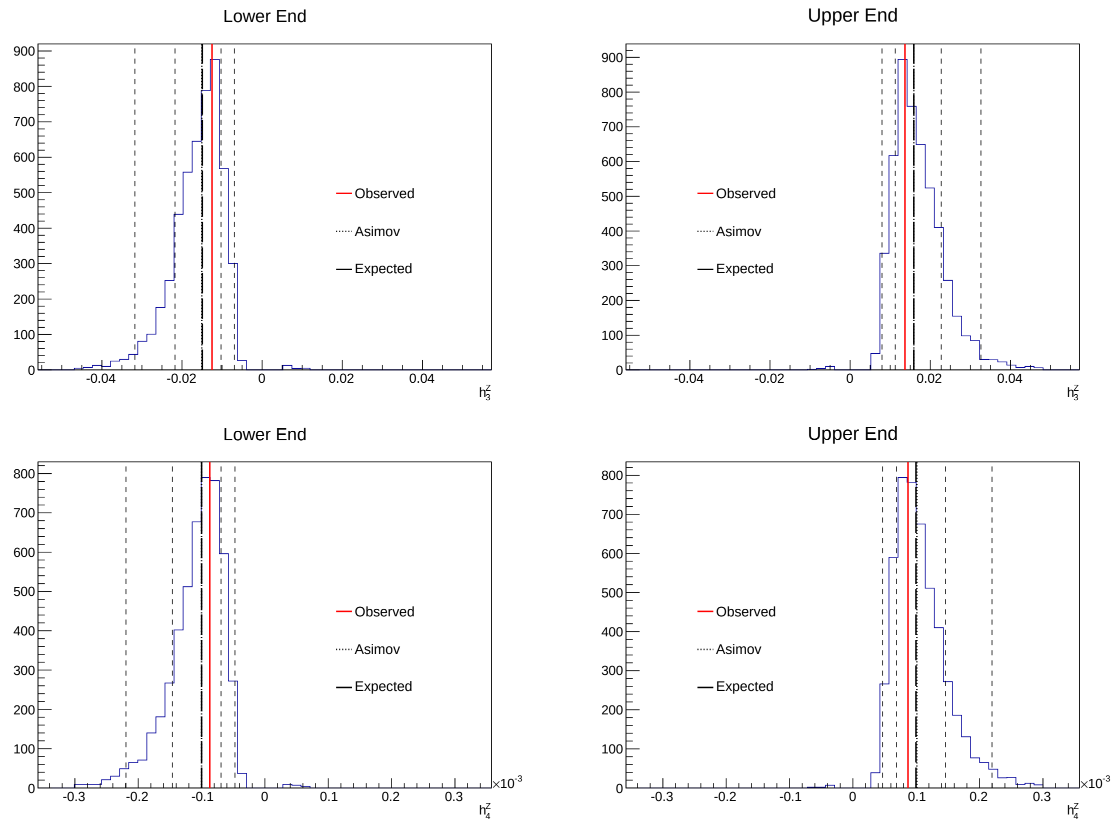

Figure 5.33: Lower and Upper Ends of the 95% Confidence Level Intervals for one-dimension fits. The red lines show the Observed limits, the black solid lines the Asimov limits, the thin long dashed black lines the Expected limits and the dashed lines the 1 and 2 σ-bands. *($Z\gamma$ analysis)*

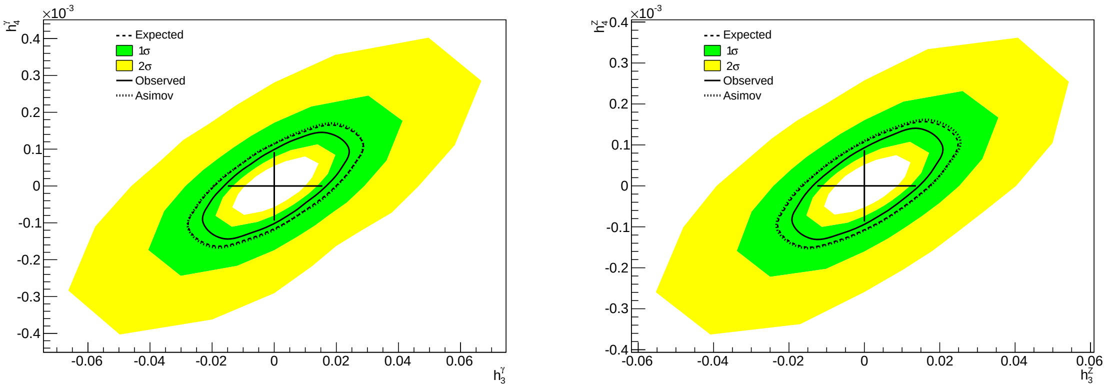

Figure 5.34: Observed, Asimov and Expected two-dimension 95% Confidence Level Domains. The black solid lines show the Observed limits, the dotted lines the Asimov limits, the dashed lines the Expected limits, the green and yellow bands correspond to the 1 and 2 σ-bands. The one-dimension 95% Confidence Level Domains for the Observed limits are reported on the anomalous Couplings axes. *($Z\gamma$ analysis)*

5.8 Summary and conclusions

Hereafter I summarize and comment the results that have been presented in the previous sections.

5.8.1 Cross sections measurements

The figure 5.35 shows the measurements of the cross sections normalized to the theoretical predictions the ZZ production (section 5.3.2, [85]), the WZ production (section 5.4.2, [88]), the WW production (section 5.5.2, [90, 91]), the $W\gamma$ production (section 5.6.2, [92]), and the $Z\gamma$ production (section 5.7.2, [92]).

The ZZ production measurement presented in figure 5.35 should be somewhat improved by a on going analysis of the ZZ production in the 8 TeV sample which should include the $ZZ \to \ell\bar{\ell}\nu\bar{\nu}$ channel [173] in addition to the $ZZ \to \ell\bar{\ell}\ell'\bar{\ell}'$ channel. The errors on the $Z\gamma \to \ell\bar{\ell}\gamma$ cross section measurement are expected to improve by a factor ∼ 2 from an ongoing analysis of the 8 TeV sample [172].

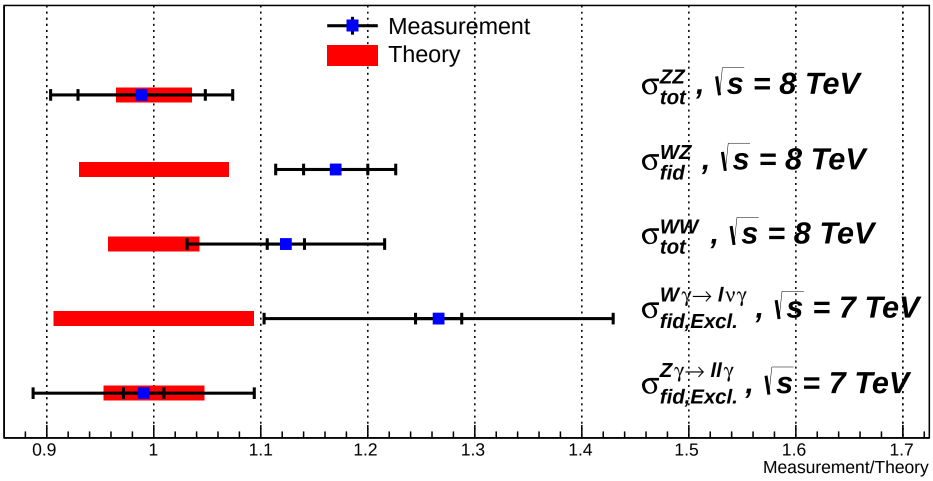

Figure 5.35: Summary of measurements of the cross sections of diboson production normalized to predictions.

The measurements in figure 5.35 are normalized to the theoretical predictions which are all at the NLO QCD level but the prediction for the WW production which is at the NNLO QCD level. As discussed in the previous sections, the agreement between measurements and predictions once the NNLO QCD corrections are taken into account is good, below the 1.5-σ level.

5.8.2 Anomalous Triple Gauge Couplings measurements

The limits on neutral and charged measurements of the Anomalous Triple Gauge Couplings from sections from sections 5.3.3, 5.7.3 5.4.3, 5.5.3, and 5.6.3 are gathered together in tables 5.32 and 5.33 respectively.

5.8.2.1 Neutral Anomalous Couplings

The measurements of the $f^{Z,\gamma}_{4,5}$ anomalous parameters parameterizing the anomalous couplings to which the ZZ production is sensitive (cf table 5.1) are compared to the CMS, LEP and TEVATRON results in table 5.34. The ATLAS and CMS $f^{Z,\gamma}_{4,5}$ limits are compared in figure 5.36.

Parameter	ZZ *analysis*
f_4^γ	[-0.0046, 0.0046]
f_4^Z	[-0.0041, 0.0040]
f_5^γ	[-0.0046, 0.0047]
f_5^Z	[-0.0040, 0.0040]

Parameter	$Z\gamma$ *analysis*
h_3^Z	[-1.3 ; 1.4] $\times 10^{-2}$
h_4^Z	[-8.7 ; 8.7] $\times 10^{-5}$
h_3^γ	[-1.5 ; 1.6] $\times 10^{-2}$
h_4^γ	[-9.4 ; 9.2] $\times 10^{-5}$

Table 5.32: Observed one-dimension 95% Confidence Level Intervals of the neutral anomalous Couplings from sections 5.3.3 and 5.7.3.

Parameter	WZ *analysis*
Δg_1^Z	[-0.019; 0.029]
$\Delta\kappa_Z$	[-0.19 ; 0.30]
λ_Z	[-0.016; 0.016]

Parameter	WW *analysis*, LEP scenario
Δg_1^Z	[-0.014 ; 0.026]
$\Delta\kappa_Z$	[-0.024 ; 0.019]
λ_Z	[-0.019 ; 0.019]

Parameter	$W\gamma$ *analysis*
$\Delta\kappa_\gamma$	[-0.41; 0.46]
λ_γ	[-0.065; 0.061]

Table 5.33: Observed one-dimension 95% Confidence Level Intervals of the anomalous Couplings from sections 5.4.3, 5.5.3, and 5.6.3

As shown by the table 5.34, the $f_{4,5}^{Z,\gamma}$ limits has been greatly improved at the LHC with respect the limits established at LEP and TEVATRON. As mentioned earlier, the ATLAS results present here were obtained using the $ZZ \to \ell\bar{\ell}\ell'\bar{\ell}'$ channel only [85]. The gap between these results and the CMS results displayed in figure 5.36 is expected to be filled by an ongoing analysis which should include the $ZZ \to \ell\bar{\ell}\nu\bar{\nu}$ channel as well [173].

The measurements of the $h_{3,4}^{Z,\gamma}$ anomalous parameters parameterizing the anomalous couplings to which the $Z\gamma$ production is sensitive (cf table 5.1) are compared to the CMS, LEP and TEVATRON results in table 5.35.

	f_4^γ	f_4^Z	f_5^γ	f_5^Z
ATLAS 8 TeV ZZ (5.3.3)	$[-4.6; 4.6] \times 10^{-3}$	$[-4.1; 4.0] \times 10^{-3}$	$[-4.6; 4.7] \times 10^{-3}$	$[-4.0; 4.0] \times 10^{-3}$
CMS 7+8 TeV ZZ [174]	$[-3.0; 2.6] \times 10^{-3}$	$[-2.1; 2.6] \times 10^{-3}$	$[-2.6; 2.7] \times 10^{-3}$	$[-2.2; 2.3] \times 10^{-3}$
LEP [175]	$[-0.17; 0.19]$	$[-0.28; 0.32]$	$[-0.35; 0.32]$	$[-0.34; 0.35]$
D0 [176] ; $\Lambda_{FF} = 1.2$ TeV	$[-0.26; 0.26]$	$[-0.28; 0.28]$	$[-0.30; 0.28]$	$[-0.31; 0.29]$
CDF [177] ; $\Lambda_{FF} = 1.2$ TeV	$[-0.10; 0.10]$	$[-0.12; 0.12]$	$[-0.11; 0.11]$	$[-0.13; 0.12]$

Table 5.34: One-dimension 95% Confidence Level Intervals for neutral aTGCs $f_{4,5}^{Z,\gamma}$ from LEP, TEVATRON and LHC

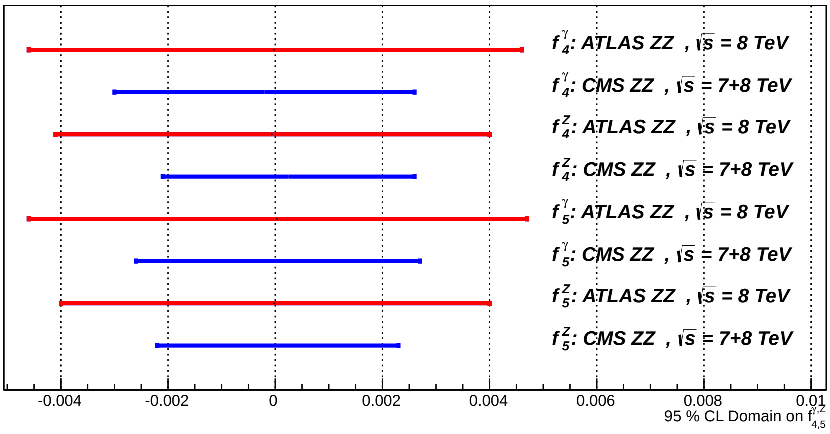

Figure 5.36: ATLAS and CMS Observed one-dimension 95% Confidence Level Intervals of the neutral anomalous Couplings $f_{4,5}^{\gamma,Z}$.

As shown by the table 5.35, the improvement is dramatic at LHC with respect to previous colliders. One notes a huge difference between the ATLAS and CMS results. As discussed in section 5.7.3, this is due to both the use of the 8 TeV sample by CMS and a better use of the highest momenta available in $Z\gamma$ events. An ongoing ATLAS analysis will erase this difference soon [172].

	h_3^γ	h_3^Z	h_4^γ	h_4^Z
ATLAS 7 TeV $Z\gamma$ (5.7.3)	$[-1.5; 1.6] \times 10^{-2}$	$[-1.3; 1.4] \times 10^{-2}$	$[-0.94; 0.92] \times 10^{-4}$	$[-0.87; 0.87] \times 10^{-4}$
CMS 8 TeV $Z\gamma$ [171]	$[-1.12; 0.95] \times 10^{-3}$	$[-1.50; 1.64] \times 10^{-3}$	$[-3.80; 4.35] \times 10^{-6}$	$[-3.96; 4.59] \times 10^{-6}$
LEP [175]	$[-0.05; 0.00]$	$[-0.19; 0.06]$	$[0.01; 0.05]$	$[-0.04; 0.13]$
D0 [178]	$[-0.027; 0.027]$	$[-0.026; 0.026]$	$[-0.0014; 0.0014]$	$[-0.0013; 0.0013]$
CDF [179]	$[-0.022; 0.022]$	$[-0.022; 0.022]$	$[-0.0009; 0.0009]$	$[-0.0009; 0.0009]$

Table 5.35: One-dimension 95% Confidence Level Intervals for neutral aTGCs $h_{3,4}^V$ from LEP, TEVATRON and LHC

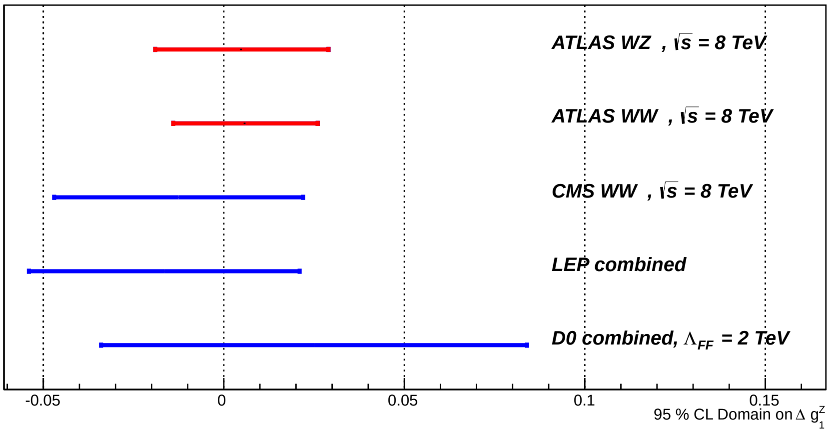

(a) Observed one-dimension 95% Confidence Level Intervals of Δg_1^Z

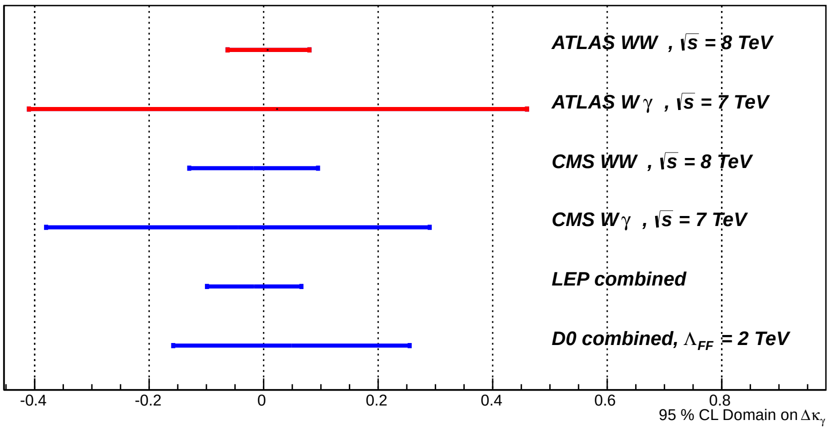

(b) Observed one-dimension 95% Confidence Level Intervals of $\Delta\kappa_\gamma$

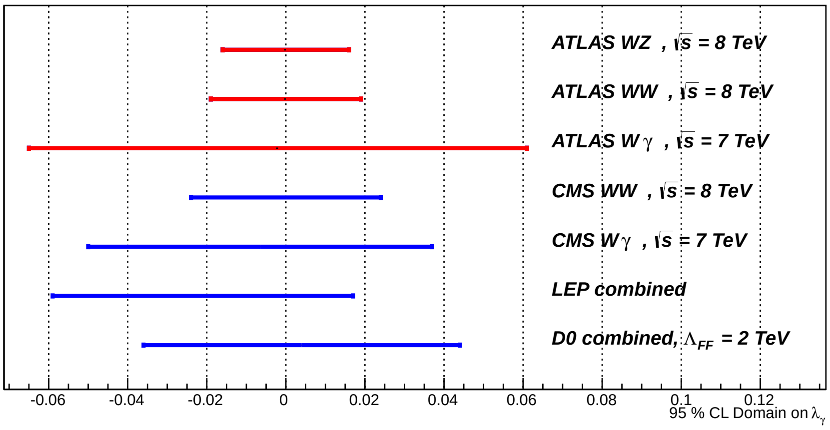

(c) Observed one-dimension 95% Confidence Level Intervals of λ_γ

Figure 5.37: Observed one-dimension 95% Confidence Level Intervals of the charged anomalous Couplings from LEP, TEVATRON and LHC

5.8.2.2 Charged Anomalous Couplings

The table 5.36 show the charged anomalous parameters which parametrize the anomalous couplings to which the WZ, WW and $W\gamma$ productions are sensitive (cf table 5.1). As it was explained in the section 5.5.3, the WW analysis relies on the LEP scenario which corresponds to relations between the anomalous couplings

$$\lambda_\gamma = \lambda_Z \quad \text{and} \quad \Delta g_1^Z = \Delta\kappa_Z + \tan^2\theta_W \Delta\kappa_\gamma \tag{5.46}$$

In table 5.36, the one-dimension intervals for $\Delta\kappa_\gamma$ have been obtained from the $\Delta\kappa_Z$ intervals of the WZ and WW analyses using the relation $\Delta\kappa_\gamma = -\Delta\kappa_Z/\tan^2\theta_W$. On the other hand the limits on Δg_1^Z are directly those obtained in these analyses.

	Δg_1^Z	$\Delta\kappa_\gamma$	λ_γ
ATLAS 8 TeV WZ	[-0.019 ; 0.029]	[-1.00 ; 0.63]	[-0.016 ; 0.016]
ATLAS 8 TeV WW	[-0.014 ; 0.026]	[-0.063 ; 0.080]	[-0.019 ; 0.019]
ATLAS 7 TeV $W\gamma$	*no sensitivity*	[-0.41 ; 0.46]	[-0.065 ; 0.061]
CMS 8 TeV WW [180]	[-0.047 ; 0.022]	[-0.130 ; 0.095]	[-0.024 ; 0.024]
CMS 7 TeV $W\gamma$ [168]	*no sensitivity*	[-0.38 ; 0.29]	[-0.050 ; 0.037]
LEP [175]	[-0.054 ; 0.021]	[-0.099 ; 0.066]	[-0.059 ; 0.017]
D0 [181] $\Lambda_{FF} = 2$ TeV	[-0.034 ; 0.084]	[-0.158 ; 0.255]	[-0.036 ; 0.044]

Table 5.36: Observed one-dimension 95% Confidence Level Intervals of the charged anomalous Couplings(LEP scenario) from LEP, TEVATRON and LHC

The limits on charged anomalous couplings are compared to the CMS, LEP and TEVATRON results in figure 5.37. As one can see the LHC limits at 8 TeV outperform the limits at the previous colliders, although the LEP limit on $\Delta\kappa_\gamma$ is still among the best ones.

5.8.2.3 EFT results

The tables 5.37 and 5.38 collect the limits on the coefficients of EFT operators for neutral and charged anomalous couplings respectively.

As one can see from table 5.37 the most stringent limits for neutral EFT operators are now from the ZZ analysis (see section 5.3.3). As mentioned earlier some improvements are to be expected from ongoing analyses [172, 173], about a factor ~ 2 for the ZZ results and ~ 10 for the $Z\gamma$ results, although no measurement of the CP violating $h_1^{Z,\gamma}$ to which the $Z\gamma$ production is sensitive (cf table 5.1) and which bring constrain on EFT operators (cf equations (A.25), (A.26) and (A.28)) is foreseen. If the C_is are 1, this would translate in limits for Λ at the level of 0.7 TeV.

	EFT Parameter	*ZZ analysis*	*$Z\gamma$ analysis*
CP	$C_{\tilde{B}W}/\Lambda^4$	[-15.53 , 15.65]	[-43. ; 47.]
$\not{C}\not{P}$	C_{BB}/Λ^4	[-7.98 , 7.83]	*not measured*
	C_{BW}/Λ^4	[-8.43 , 8.56]	*not measured*
	C_{WW}/Λ^4	[-7.07 , 7.17]	*not measured*

Table 5.37: Observed one-dimension 95% Confidence Level Intervals of the neutral EFT parameters in TeV $^{-4}$

The table 5.38 shows that the most stringent limits are from the WZ and WW analyses (see sections 5.4.3 and 5.5.3). But for the C_B/Λ^2 parameter for which only the WW limits matters, there is a clear interest in the combination of these two diboson production channels, which optimistically could bring the limit on Λ in the range of 0.6 TeV if for a moment one puts the C_is at 1.

	EFT parameter	*WZ analysis*	*WW analysis*	*$W\gamma$ analysis*
C and P	C_W/Λ^2	[-4.3 ; 6.8]	[-5.2 ; 10.1]	[-99 ; 111]
	C_B/Λ^2	[-320 ; 210]	[-20 ; 26.]	[-99 ; 111]
	C_{WWW}/Λ^2	[-3.9 ; 4.0]	[-4.5 ; 4.5]	[-15.7 ; 14.8]
$\not{C}$ and/or $\not{P}$	$C_{\widetilde{W}WW}/\Lambda^2$, $C_{\widetilde{W}}/\Lambda^2$	*not measured*	*not measured*	*not measured*

Table 5.38: Observed one-dimension 95% Confidence Level Intervals of the charged EFT parameters in TeV $^{-2}$;

Finally, as an exercise I tried in the individual diboson analyses sections presented in this memoir, to apply the EFT consistency requirement consisting in removing quartic dependence on anomalous couplings in the signal expectations (cf sections 5.3.3.3, 5.4.3.2 5.5.3.2, 5.6.3.2, and 5.7.3.2). The conclusions of the exercise look rather distressing since it appears that under this requirement, only the WZ and WW analyses can bring some constrains and only on the sole C_W/Λ^2 parameter. However one should note that none of the analyses presented here were ever optimized in the perspective of this requirement which has drastic consequences. Although it could be that data do not yet allow to be insensitive to the orders that are neglected by the usual EFT expansion, it also true that experimentalists had no chance yet to design strategies to cope with such a radical novelty.

5.8.3 Conclusions

The measurements of the cross sections of diboson productions on data of the Run 1 period have already motivated a surge of theoretical QCD developments. Experimental errors are close and sometimes slightly better than the theoretical errors.

Clearly with an energy as high as 13 TeV and a far larger expected integrated luminosity, the measurements of the cross sections of the Run 2 period will provide some of the most stringent tests of the Standard Model, challenging the QCD and EW predictions of the higher most orders.

The limits on anomalous couplings at LHC have already outperformed the limits from previous colliders. The Limits on neutral anomalous couplings are going to be improved by ongoing analyses of the 8 TeV sample. Time is right to envision combinations of diboson production channels within each of the ATLAS and CMS collaborations and between them.

The currently very popular Effective Field Theory approach for the analyses of the anomalous couplings offers an exciting as well as challenging perspective to test the Standard model at further and further higher scales and to track down indirectly new Physics that could be hiding there.

Concluding remarks

In this memoir, I presented some of my contributions to the preparation of the ATLAS detector and to the study of the two vector bosons production at the LHC.

Having started to work on the Muon Spectrometer project in 1995, I have been able to contribute to the optimization of the design of this detector, to the understanding of its performance, and to its tests and commissioning, all over the years which finally led to its successful inception as soon as the collision of protons started to pour their products in ATLAS.

I contributed chiefly to the reconstruction of the muons both in “Standalone” mode, i.e within the Muon Spectrometer and in “Combination” mode, i.e combining ATLAS sub-detectors. Also I invested heavily in the Description of the Detector, one of the items which, as the description of the magnetic field and the alignment of the detection units of the Muon Spectrometer, are of momentous importance for the reconstruction. Thanks to a thorough work on this items, my colleagues and I forged tools on which, from the earliest days, the ATLAS collaboration could rely to improve and understand the detector.

As explained in this memoir the goal of this work of the reconstruction of the muons has been to provide the best possible performance, in terms of resolution and of efficiency as well as, importantly, of purity of the candidates identified as muons. The two goals of high efficiency and high purity, were the cornerstone principles for the whole of the development period of the $STACO$ chain of reconstruction. As it has been recounted, the performance of this chain has been determined, and its qualities confirmed, in test beams and cosmics data and in innumerable Physics analyses on simulated data prior to the first LHC data. Finally its excellence was demonstrated on the collisions data themselves. The chain was perfectly functional right from the start of proton collisions and ready to serve the analyses of the Physics accessible at the LHC.

I dedicated myself to the studies of the vector bosons interactions in the processes of production of two bosons at the LHC. In this memoir, I have presented the results of these studies, the cross sections which have been measured as well as the limits on the anomalous Triple Gauge Bosons Couplings which have been obtained.

The measurements of the cross sections of the diboson productions on the data of the Run 1 period have already galvanized the realm of the QCD and Electroweak high order corrections, presenting challenging tests of the Standard Model. These tests will be further strengthened with the higher luminosity and energy data to come.

The limits on the anomalous Triple Gauge couplings have been improved, dramatically for most of them, with respect the limits at the previous colliders. I presented the first analyses in the framework of the Effective Field Theory approach. This approach, presently advocated with strength by many theorists, is a exciting framework in which the anomalous couplings of vector bosons and of the Higgs boson join in the quest of a high energy scale physics beyond the Standard Model. The advent of the LHC data triggered new developments in this area too. New challenges for the experimental analyses came out which will have to be taken up with the coming LHC data.

Bibliography

[1] L. Evans and P. Bryant, *LHC Machine*, JINST **3** (2008) S08001.

[2] S. Myers, *The Large Hadron Collider 2008-2013*, Int.J.Mod.Phys. **A28** (2013) 1330035.

[3] D. Denegri, C. Guyot, A. Hoecker, and L. Roos, *L'aventure du Grand Collisionneur LHC : du big bang au boson de higgs.* EDP Sciences, 2014.

[4] ATLAS Collaboration, *Performance of the ATLAS Inner Detector Track and Vertex Reconstruction in the High Pile-Up LHC Environment*, Tech. Rep. ATLAS-CONF-2012-042, CERN, Geneva, Mar, 2012.

[5] ATLAS Collaboration, *Electron efficiency measurements with the ATLAS detector using the 2012 LHC proton-proton collision data*, Tech. Rep. ATLAS-CONF-2014-032, CERN, Geneva, Jun, 2014.

[6] ATLAS Collaboration, T. A. collaboration, *Pile-up Suppression in Missing Transverse Momentum Reconstruction in the ATLAS Experiment in Proton-Proton Collisions at* $\sqrt{s} = 8\ TeV$, Tech. Rep. ATLAS-CONF-2014-019, May, 2014.

[7] ATLAS Collaboration, *Pile-up subtraction and suppression for jets in ATLAS*, Tech. Rep. ATLAS-CONF-2013-083, ATLAS-COM-CONF-2013-097, 2013.

[8] M. Lamont, *LHC, HL-LHC and Beyond*, PoS **EPS-HEP2013** (2014) 149.

[9] ATLAS+CMS Collaboration, *Expected pileup values at the HL-LHC*, Tech. Rep. ATL-UPGRADE-PUB-2013-014, CERN, Geneva, Sep, 2013.

[10] ATLAS Collaboration, G. Aad et al., *The ATLAS Experiment at the CERN Large Hadron Collider*, JINST **3** (2008) S08003.

[11] GEANT4 Collaboration, S. Agostinelli et al., *GEANT4: A Simulation toolkit*, Nucl.Instrum.Meth. **A506** (2003) 250–303.

[12] K. A. Assamagan, K. Bachas, T. Carli, T. Davidek, D. Fassouliotis, L. R. Flores Castillo, N. De Groot, S. Hassani, E. W. Hughes, P. Kluit, I. Korolkov, C. Kourkoumelis, J. F. Laporte, H. Lim, M. Limper, D. Lopez Mateos, B. Mellado Garcia, K. Nikolopoulos, C. Petridou, A. Poppleton, L. Pribyl, G. Ordonez Sanz, A. Ouraou, M. Ridel, A. Ruiz-Martinez, O. Salto, A. Salzburger, G. Schlager, P. Schwemling, G. Usai, and S. L. Wu, *Muons In the ATLAS Calorimeters: Energy Loss Corrections and Muon Tagging*, Tech. Rep. ATL-COM-MUON-2008-009. CERN-ATL-COM-MUON-2008-009, CERN, Geneva, Apr, 2008.

[13] P. R. Norton, *The ASCOT detector at the LHC: Expression of Interest*, . `http://cds.cern.ch/record/1076511`.

[14] J. Chwatowski, A. Dell'Acqua, D. Froidevaux, and M. Nessi, *EAGLE detector layout for simulations towards the L.o.I.*, Tech. Rep. ATL-TECH-92-003. ATC-PN-3, CERN, Geneva, May, 1992.

[15] C. Guyot et al., *A New Fixed Target Experiment For A Precise Test Of Qcd*, Tech. Rep. CERN/SPSC 89-56, SPSC/R 89, CERN, Geneva, 1989.

[16] L. Chevalier, 2016. Habilitation à diriger des recherches.

[17] J. C. Barriere, F. Bauer, M. Fontaine, A. Formica, V. Gautard, P. F. Giraud, H. Graaf, C. Guyot, R. Hart, S. Horvat, O. Kortner, S. Kotov, H. Kroha, F. Linde, I. Ponsot, I. Potrap, and P. Schune, *The alignment system of the barrel part of the ATLAS muon spectrometer*, Tech. Rep. ATL-MUON-PUB-2008-007. ATL-COM-MUON-2008-002, CERN, Geneva, Jan, 2008. backup note for the NIM Atlas detector paper.

[18] S. Aefsky, C. Amelung, J. Bensinger, C. Blocker, A. Dushkin, et al., *The optical alignment system of the ATLAS muon spectrometer endcaps*, JINST **3** (2008) P11005.

[19] F. Bauer, *Alignement du spectrometre à muons d'ATLAS*, 2011. Habilitation à diriger des recherches.

[20] C. Amelung, F. Bauer, , P. F. Giraud, and I. Potrap, *The performance of the ATLAS muon spectrometer alignment*, Tech. Rep. TO BE PUBLISHED, CERN, Geneva.

[21] E. Diehl, *Calibration and Performance of the Precision Chambers of the ATLAS Muon Spectrometer*, Physics Procedia **37** (2012) no. 0, 543 – 548. Proceedings of the 2nd International Conference on Technology and Instrumentation in Particle Physics (TIPP 2011).

[22] N. Amram, C. Bini, T. Dai, A. Salvo, E. Diehl, C. Ferretti, M. Flowerdew, M. Iodice, O. Kortner, D. Levin, S. McKee, F. Petrucci, D. Orestano, F. Rauscher, E. Solfaroli Camillocci, and M. Vanadia, *ATLAS MDT Calibrations for 2011-2012 Collisions*, Tech. Rep. ATL-COM-MUON-2013-030, CERN, Geneva, Nov, 2013.

[23] W. Blum, *High precision drift tubes*, Tech. Rep. MPI-PHE-93-12, 1993.

[24] W. Riegler, M. Aleksa, M. Deile, J. Dubbert, C. Fabjan, et al., *Resolution limits of drift tubes*, Nucl.Instrum.Meth. **A443** (2000) 156–163.

[25] J. Dubbert, S. Horvat, D. Kharchenko, O. Kortner, S. Kotov, et al., *Modelling of the space-to-drift-time relationship of the ATLAS monitored drift-tube chambers in the presence of magnetic fields*, Nucl.Instrum.Meth. **A572** (2007) 50–52.

[26] S. Horvat, D. Kharchenko, O. Kortner, S. Kotov, H. Kroha, et al., *Operation of the ATLAS muon drift-tube chambers at high background rates and in magnetic fields*, IEEE Trans.Nucl.Sci. **53** (2006) 562–566.

[27] F. Bauer, U. Bratzler, H. Dietl, H. Kroha, T. Lagouri, et al., *Construction and test of MDT chambers for the ATLAS muon spectrometer*, Nucl.Instrum.Meth. **A461** (2001) 17–20.

[28] F. Bauer, S. Horvat, O. Kortner, H. Kroha, A. Manz, et al., *Large scale production of monitored drift tube chambers for the ATLAS muon spectrometer*, Nucl.Instrum.Meth. **A518** (2004) 69–72.

[29] A. Nisati, *An Integrated RPC and TGC Detector for the ATLAS Muon Trigger*, Tech. Rep. ATL-MUON-94-042. ATL-M-PN-42, CERN, Geneva, Jun, 1994.

[30] B. Aubert, G. Battistoni, B. A. Dolgoshein, C. Guyot, and W. Witzeling, *Recommendation on the trigger scheme from the Muon Review Panel*, Tech. Rep. ATL-GEN-94-008. ATL-GE-PG-8, CERN, Geneva, Aug, 1994.

[31] A. Aloisio, M. Alviggi, M. Biglietti, V. Canale, M. Caprio, et al., *The trigger chambers of the ATLAS muon spectrometer: Production and tests*, Nucl.Instrum.Meth. **A535** (2004) 265–271.

[32] C. Daum, F. Dydak, C. W. Fabjan, P. Jenni, W. Kozanecki, L. Leistam, L. Mandelli, P. Norton, and K. Pretzl, *Recommendations of the ATLAS Magnet Panel*, Tech. Rep. ATL-GEN-93-002. ATL-GE-PG-2, CERN, Geneva, Mar, 1993.

[33] L. Chevalier, M. Virchaux, J.-F. Laporte, P.-F. Giraud, F. Bauer, A. Ouraou, and D. Pomarède, *AMDBSIMREC: A Structured data base for the ATLAS Spectrometer Simulation Program*, Tech. Rep. ATL-MUON-97-148. ATL-M-PN-148, CERN, Geneva, 1997. `https://cds.cern.ch/record/684070`.

[34] L. Chevalier, J. Ernwein, A. Formica, P.-F. Giraud, J.-F. Laporte, A. Ouraou, P. Sizun, and M. Virchaux, *PERSINT Event Display for ATLAS*, Tech. Rep. ATL-SOFT-PUB-2012-001, CERN, Geneva, Dec, 2012.

[35] K. A. Assamagan, A. Di Ciaccio, S. Goldfarb, J. F. Laporte, D. Lellouch, A. Rimoldi, and M. Virchaux, *A Hierarchical Software Identifier Scheme for the ATLAS Muon Spectrometer; rev. version*, Tech. Rep. ATL-MUON-2004-003. CERN-ATL-MUON-2004-003, CERN, Geneva, Aug, 2002.

[36] J. F. Laporte, L. Chevalier, C. Guyot, and M. Virchaux, *On the Number of Layers per Multilayer in MDT chambers Part I*, Tech. Rep. ATL-MUON-96-126. ATL-M-PN-126, CERN, Geneva, Aug, 1996.

[37] D. Pomarède, J. F. Laporte, and A. Nisati, *Impact of Service and Access Holes on the ATLAS Muon Spectrometer Performances*, Tech. Rep. ATL-MUON-2000-023, CERN, Geneva, Nov, 2000.

[38] J. F. Laporte, A. Ouraou, L. Chevalier, C. Guyot, S. Hassani, E. Lancon, R. Nicolaidou, F. Bauer, A. Formica, P. F. Giraud, D. Pomarède, and P. Schune, *Impact of the initial Layout on the ATLAS Muon Spectrometer Performance, ATL-COM-MUON-2005-007*, Tech. Rep. ATL-MUON-INT-2005-001. ATL-COM-MUON-2005-007. CERN-ATL-MUON-INT-2005-001, CERN, Geneva, 2005.

[39] C. Helsens, H. Bachacou, C. Guyot, J. F. Laporte, and A. Ouraou, *Effect of the muon spectrometer internal alignment on* $Z' \to \mu^+\mu^-$ *reconstruction and discovery sensitivity*, Tech. Rep. ATL-PHYS-INT-2008-044. ATL-COM-PHYS-2008-053, CERN, Geneva, Apr, 2008.

[40] C. Helsens, H. Bachacou, C. Guyot, S. Hassani, J. Laporte, and A. Ouraou, *ATLFAST I parametrisation of the Muon Spectrometer alignment contribution to the momentum resolution including charge mis-identification, and AOD to AOD corrections for ATLFAST-II in MS standalone configuration.*, Tech. Rep. ATL-SOFT-INT-2008-005. ATL-COM-SOFT-2008-021, CERN, Geneva, Nov, 2008.

[41] M. Schott, N. Benekos, J. F. Laporte, and L. Chevalier, *Impacts of misalignment effects on the Muon Spectrometer Performance*, Tech. Rep. ATL-MUON-PUB-2007-006. ATL-COM-MUON-2007-007, CERN, Geneva, Jun, 2007.

[42] D. Drakoulakos, E. Gschwendtner, J. Maugain, F. Rohrbach, and Y. Sedykh, *The high precision X-ray tomograph for quality control of the ATLAS MDT muon spectrometer*, Nucl. Instrum. Methods (1997) .

[43] M. Xiao, *Search for the Higgs boson decaying to four leptons in the ATLAS detector at LHC leading to the observation of a new particle compatible with the Higgs boson.* PhD thesis, Diderot U., Paris, Jun, 2013. Presented 24 May 2013.

[44] *C. Arnault, AGDD: The Detector Description Framework for ATLAS*, `https://indico.cern.ch/event/a00137/session/0/contribution/s3t9/material/1/1.pdf`.

[45] R. Chytracek, J. McCormick, W. Pokorski, and G. Santin, *Geometry description markup language for physics simulation and analysis applications.*, IEEE Trans.Nucl.Sci. **53** (2006) 2892.

[46] D. Benchekroun and J. Collot, *AGDD-Geant4 description of the EM Barrel Presampler*, Tech. Rep. ATL-LARG-2001-015, CERN, Geneva, Jun, 2001.

[47] D. Calvet, A. Fornaini, and S. Gadomski, *The Silicon Trackers transient detector description*, Tech. Rep. ATL-SOFT-2002-002, ATL-COM-SOFT-2002-003, CERN-ATL-SOFT-2002-002, CERN, Geneva, 2002.

[48] G. Karapetian, *Description of the ATLAS Hadronic End-Cap Calorimeter in XML*, Tech. Rep. ATL-LARG-2001-005, ATL-COM-LARG-2001-001, CERN-ATL-LARG-2001-005, CERN, Geneva, 2000.

[49] S. Gadomski, *Model of the SCT detectors and electronics for the ATLAS simulation using Geant4*, Tech. Rep. ATL-SOFT-2001-005, ATL-COM-SOFT-2001-005, CERN-ATL-SOFT-2001-005, CERN, Geneva, 2001.

[50] J. Hrivnac, *GraXML: Modular geometric modeler*, eConf **C0303241** (2003) THJT009, `arXiv:cs/0306012 [cs-gr]`.

[51] J. F. Laporte, L. Chevalier, C. Guyot, and M. Virchaux, *G4AGDD an AGDD based G4 application*, Tech. Rep. ATL-SOFT-2001-002, CERN, Geneva, Mar, 2001.

[52] R. Brun and F. Rademakers, *ROOT - An Object Oriented Data Analysis Framework*, Proceedings AIHENP'96 Workshop, Lausanne, Sep. 1996, Nucl. Inst. Meth. in Phys. Res. A 389 (1997) 81-86 (2010) .

[53] A. Rimoldi, A. DellâAcqua, M. Gallas, A. Nairz, J. Boudreau, V. Tsulaia, and D. Costanzo, *The Simulation of the ATLAS Experiment: Present Status and Outlook*, Tech. Rep. ATL-SOFT-2004-004. ATL-COM-SOFT-2004-006. CERN-ATL-COM-SOFT-2004-006, CERN, Geneva, 2004.

[54] J. Boudreau and V. Tsulaia, *The GeoModel toolkit for detector description*, Proceedings of the CHEP 2004 conference (2005) 353–356.

[55] J. F. Laporte, A. Dell'Acqua, A. Rimoldi, L. Chevalier, and M. Virchaux, *The Atlas Muon Spectrometer Simulation using Geant4*, Tech. Rep. ATL-MUON-2000-020, CERN, Geneva, May, 2000.

[56] J. Meyer, *Muon performance aspects and measurement of the inclusive ZZ production cross section through the four lepton final state with the ATLAS experiment at the LHC.* PhD thesis, Wurzburg U., Wurzburg, Germany, Jul, 2013. Presented 17 Apr 2013.

[57] L. Chevalier, A. Dell'Acqua, and J. Meyer, *An XML generic detector description system and geometry editor for the ATLAS detector at the LHC*, Tech. Rep. ATL-SOFT-PROC-2012-053, ATL-COM-SOFT-2012-075, 2012.

[58] K. Olive and P. D. Group, *Review of Particle Physics*, Chinese Physics C **38** (2014) no. 9, 090001.

[59] W. Lohmann, R. Kopp, and R. Voss, *Energy Loss of Muons in the Energy Range 1-GeV to 10000-GeV*, Tech. Rep. CERN-85-03, CERN-YELLOW-85-03, 1985.

[60] K. Nikolopoulos, D. Fassouliotis, C. Kourkoumelis, and A. Poppleton, *Muon Energy Loss Upsteam of the Muon Spectrometer*, Tech. Rep. ATL-MUON-PUB-2007-002. ATL-COM-MUON-2006-019, CERN, Geneva, Sep, 2006.

[61] D. Lopez Mateos, S. Hassani, E. W. Hughes, J. F. Laporte, and A. Ouraou, *A Bayesian Method for Estimating the Energy Loss of Muons in Calorimeters*, Tech. Rep. ATL-MUON-INT-2009-001. ATL-COM-MUON-2008-007, CERN, Geneva, Mar, 2008.

[62] *ATLAS: Detector and physics performance technical design report.*, vol. 1. CERN-LHCC-99-14, 1999.

[63] *ATLAS detector and physics performance. Technical design report.*, vol. 2. CERN-LHCC-99-15, 1999.

[64] ATLAS Collaboration, G. Aad et al., *Expected Performance of the ATLAS Experiment - Detector, Trigger and Physics*, `arXiv:0901.0512 [hep-ex]`.

[65] D. Adams, K. Assamagan, H. Bachacou, S. Behar, K. Black, et al., *Muon reconstruction and identification: Studies with simulated Monte Carlo samples*, Tech. Rep. ATL-PHYS-PUB-2009-008, ATL-COM-PHYS-2009-151, 2009.

[66] E. Le Menedeu, *Étude des performances du spectromètre à muons du détecteur Atlas au LHC, des cosmiques aux collisions. Mesure de la section efficace de production des dibosons WZ.* PhD thesis, Paris, Université Pierre et Marie Curie, Paris 6, Saclay, 2011. Presented 23 Sep 2011.

[67] B. Di Girolamo, A. Dotti, V. Giangiobbe, P. Johansson, L. Pribyl, and M. Volpi, *Beamline instrumentation in the 2004 combined ATLAS testbeam*, Tech. Rep. ATL-TECH-PUB-2005-001. ATL-COM-TECH-2005-001, CERN, Geneva, 2005.

[68] C. Adorisio, G. Aielli, T. Alexopoulos, M. Alviggi, C. Amelung, et al., *Study of the ATLAS MDT spectrometer using high energy CERN combined test beam data*, Nucl.Instrum.Meth. **A598** (2009) 400–415.

[69] F. Bauer, L. Chevalier, J. Ernwein, A. Formica, P.-F. Giraud, C. Guyot, S. Hassani, A. Krepouri, E. Lancon, J. F. Laporte, R. Nicolaidou, A. Ouraou, P. Ponsot, and P. Schune, *ATLAS 2004 Combined Test Beam results: Muon Chamber Alignment and Muon Reconstruction*, Tech. Rep. ATL-MUON-PUB-2007-003. ATL-COM-MUON-2006-012, CERN, Geneva, Apr, 2006.

[70] F. Bauer, L. Chevalier, J. Ernwein, A. Formica, P.-F. Giraud, C. Guyot, S. Hassani, A. Krepouri, E. Lancon, J.-F. Laporte, R. Nicolaidou, A. Ouraou, P. Ponsot, and P. Schune, *Combined test beam results on the alignment of Muon chambers and Muon reconstruction in the 2004 ATLAS H8 setup*, Nuclear Instruments and Methods in Physics Research Section A: Accelerators, Spectrometers, Detectors and Associated Equipment **572** (2007) no. 1, 98 – 101.

[71] P. F. Giraud, F. Bauer, L. Chevalier, J. Ernwein, A. Formica, C. Guyot, S. Hassani, E. Lancon, J. F. Laporte, R. Nicolaidou, A. Ouraou, and P. Schune, *Track-based absolute alignment in the Atlas muon spectrometer and in the H8 test beam*, Tech. Rep. ATL-MUON-PUB-2006-012. ATL-COM-MUON-2005-019, CERN, Geneva, Oct, 2005.

[72] K. Bachas and C. Petridou, *Studies of the ATLAS Muon Spectrometer with Test Beam and Simulated Physics Data.* PhD thesis, Aristotle University of Thessaloniki, 2008.

[73] K. Bachas, S. Hassani, J.-F. Laporte, R. Nicolaidou, C. Petridou, and D. Sampsonidis, *Studies of catastrophic muon energy losses in ATLAS H8 combined Testbeam data*, Nuclear Physics B - Proceedings Supplements **177-178** (2008) no. 0, 320 – 321.

[74] Atlas, *Studies of the performance of the ATLAS detector using cosmic-ray muons*, The European Physical Journal C **71** (2011) no. 3, 22.

[75] ATLAS Collaboration, *Commissioning of the ATLAS Muon Spectrometer with Cosmic Rays*, The European Physical Journal C **70** (2010) no. 3, 875–916.

[76] ATLAS Collaboration, G. Aad et al., *Measurement of the muon reconstruction performance of the ATLAS detector using 2011 and 2012 LHC proton-proton collision data*, Eur.Phys.J. **C74** (2014) no. 11, 3130, `arXiv:1407.3935 [hep-ex]`.

[77] ATLAS Collaboration, G. Aad et al., *Muon reconstruction efficiency and momentum resolution of the ATLAS experiment in proton-proton collisions at* $\sqrt{s} = 7$ *TeV in 2010*, Eur.Phys.J. **C74** (2014) no. 9, 3034, `arXiv:1404.4562 [hep-ex]`.

[78] ATLAS Collaboration, G. Aad et al., *Performance of the ATLAS Detector using First Collision Data*, JHEP **1009** (2010) 056, `arXiv:1005.5254 [hep-ex]`.

[79] ATLAS Collaboration, G. Aad et al., *Observation of a new particle in the search for the Standard Model Higgs boson with the ATLAS detector at the LHC*, Phys.Lett. **B716** (2012) 1–29, `arXiv:1207.7214 [hep-ex]`.

[80] ATLAS Collaboration, G. Aad et al., *Measurement of the Higgs boson mass from the* $H \to \gamma\gamma$ *and* $H \to ZZ^* \to 4\ell$ *channels with the ATLAS detector using 25* fb^{-1} *of pp collision data*, Phys.Rev. **D90** (2014) no. 5, 052004, `arXiv:1406.3827 [hep-ex]`.

[81] J.-F. Laporte, *FLIT manual*, `https://laportej.web.cern.ch/laportej/Flit/doc/html/index.html`, 2013.

[82] ATLAS Collaboration, G. Aad et al., *Evidence of $W\gamma\gamma$ production in pp collisions at $\sqrt{s} = 8$ TeV and limits on anomalous quartic gauge couplings with the ATLAS detector*, Phys. Rev. Lett. **115** (2015) no. 3, 031802, `arXiv:1503.03243 [hep-ex]`.

[83] G. Aad et al., *Measurements of four-lepton production in pp collisions at $\sqrt{s} =$ 8 TeV with the {ATLAS} detector*, Physics Letters B **753** (2016) 552 – 572, `arXiv:1509.07844 [hep-ex]`.

[84] ATLAS Collaboration, *Measurement of the total ZZ production cross section in proton-proton collisions at $\sqrt{s} = 8$ TeV in 20 fb^{-1} with the ATLAS detector*, Tech. Rep. ATLAS-CONF-2013-020, 2013.

[85] E. S. Protopapadaki, *ZZ diboson measurements with the ATLAS detector at the LHC and study of the toroidal magnetic field sensors.* PhD thesis, Saclay, 2014. `http://inspirehep.net/record/1339812/files/CERN-THESIS-2014-155.pdf`.

[86] ATLAS Collaboration, G. Aad et al., *Measurement of WZ production in proton-proton collisions at $\sqrt{s} = 7$ TeV with the ATLAS detector*, Eur. Phys. J. **C72** (2012) 2173, `arXiv:1208.1390 [hep-ex]`.

[87] ATLAS Collaboration, *A Measurement of WZ Production in Proton-Proton Collisions at $\sqrt{s} = 8$ TeV with the ATLAS Detector*, Tech. Rep. ATLAS-CONF-2013-021, 2013.

[88] ATLAS Collaboration, *Measurements of WZ production cross section and limits on anomalous gauge boson self-couplings in pp collisions at $\sqrt{s} = 8$ TeV with the ATLAS Detector*, To be published .

[89] H. Keoshkerian, *Mesure de la production de di-bosons WZ aupres du LHC avec l'experience ATLAS.* PhD thesis, CERN, 2014. `http://inspirehep.net/record/1339728/files/CERN-THESIS-2014-218.pdf`.

[90] ATLAS Collaboration, T. A. collaboration, *Measurement of the W^+W^- production cross section in proton-proton collisions at $\sqrt{s} = 8$ TeV with the ATLAS detector*, Tech. Rep. ATLAS-CONF-2014-033, 2014.

[91] ATLAS Collaboration, *Measurement of total and differential WW production cross sections in proton-proton collisions at $\sqrt{s} = 8$ TeV with the ATLAS detector and limits on anomalous triple gauge boson couplings*, To be published .

[92] ATLAS Collaboration, G. Aad et al., *Measurements of $W\gamma$ and $Z\gamma$ production in pp collisions at $\sqrt{s}$=7TeV with the ATLAS detector at the LHC*, Phys. Rev. **D87** (2013) no. 11, 112003, `arXiv:1302.1283 [hep-ex]`. [Erratum: Phys. Rev.D91,no.11,119901(2015)].

[93] J. Horejsi, *Introduction to electroweak unification: Standard model from tree unitarity.* World Scientific, 1994.

[94] J. M. Campbell, J. W. Huston, and W. J. Stirling, *Hard Interactions of Quarks and Gluons: A Primer for LHC Physics*, Rept. Prog. Phys. **70** (2007) 89, `arXiv:hep-ph/0611148 [hep-ph]`.

[95] J. M. Campbell and R. K. Ellis, *An Update on vector boson pair production at hadron colliders*, Phys. Rev. **D60** (1999) 113006, `arXiv:hep-ph/9905386 [hep-ph]`.

[96] L. J. Dixon, Z. Kunszt, and A. Signer, *Vector boson pair production in hadronic collisions at order α_s : Lepton correlations and anomalous couplings*, Phys. Rev. **D60** (1999) 114037, `arXiv:hep-ph/9907305 [hep-ph]`.

[97] J. Ohnemus, *Hadronic ZZ, W^-W^+, and $W^\pm Z$ production with QCD corrections and leptonic decays*, Phys. Rev. **D50** (1994) 1931–1945, `arXiv:hep-ph/9403331 [hep-ph]`.

[98] J. Ohnemus, *An Order α_s calculation of hadronic $W^\pm Z$ production*, Phys. Rev. **D44** (1991) 3477–3489.

[99] S. Frixione, P. Nason, and G. Ridolfi, *Strong corrections to $W Z$ production at hadron colliders*, Nucl. Phys. **B383** (1992) 3–44.

[100] U. Baur, T. Han, and J. Ohnemus, *WZ production at hadron colliders: Effects of nonstandard WWZ couplings and QCD corrections*, Phys. Rev. **D51** (1995) 3381–3407, `arXiv:hep-ph/9410266 [hep-ph]`.

[101] J. Ohnemus and J. F. Owens, *An Order α_s calculation of hadronic ZZ production*, Phys. Rev. **D43** (1991) 3626–3639.

[102] J. Ohnemus, *An Order α_s calculation of hadronic W^-W^+ production*, Phys. Rev. **D44** (1991) 1403–1414.

[103] U. Baur, T. Han, and J. Ohnemus, *QCD corrections and nonstandard three vector boson couplings in W^+W^- production at hadron colliders*, Phys. Rev. **D53** (1996) 1098–1123, `arXiv:hep-ph/9507336 [hep-ph]`.

[104] S. Frixione, *A Next-to-leading order calculation of the cross-section for the production of W+ W- pairs in hadronic collisions*, Nucl. Phys. **B410** (1993) 280–324.

[105] J. Ohnemus, *Order α_s calculations of hadronic $W^{\pm}\gamma$ and $Z\gamma$ production*, Phys. Rev. **D47** (1993) 940–955.

[106] U. Baur, T. Han, and J. Ohnemus, *QCD corrections to hadronic $W\gamma$ production with nonstandard $WW\gamma$ couplings*, Phys. Rev. **D48** (1993) 5140–5161, `arXiv:hep-ph/9305314 [hep-ph]`.

[107] U. Baur, T. Han, and J. Ohnemus, *QCD corrections and anomalous couplings in $Z\gamma$ production at hadron colliders*, Phys. Rev. **D57** (1998) 2823–2836, `arXiv:hep-ph/9710416 [hep-ph]`.

[108] D. De Florian and A. Signer, *W gamma and Z gamma production at hadron colliders*, Eur. Phys. J. **C16** (2000) 105–114, `arXiv:hep-ph/0002138 [hep-ph]`.

[109] J. M. Campbell, R. K. Ellis, and C. Williams, *Vector boson pair production at the LHC*, JHEP **07** (2011) 018, `arXiv:1105.0020 [hep-ph]`.

[110] S. Actis, G. Passarino, C. Sturm, and S. Uccirati, *NLO Electroweak Corrections to Higgs Boson Production at Hadron Colliders*, Phys. Lett. **B670** (2008) 12–17, `arXiv:0809.1301 [hep-ph]`.

[111] C. Anastasiou, C. Duhr, F. Dulat, F. Herzog, and B. Mistlberger, *Higgs Boson Gluon-Fusion Production in QCD at Three Loops*, Phys. Rev. Lett. **114** (2015) 212001, `arXiv:1503.06056 [hep-ph]`.

[112] E. W. N. Glover and J. J. van der Bij, *Vector boson pair production via gluon fusion*, Phys. Lett. **B219** (1989) 488.

[113] E. W. N. Glover and J. J. van der Bij, *Z boson pair production via gluon fusion*, Nucl. Phys. **B321** (1989) 561.

[114] T. Binoth, N. Kauer, and P. Mertsch, *Gluon-induced QCD corrections to pp $\rightarrow$ ZZ $\rightarrow$ l anti-l l-prime anti-l-prime*, in *Proceedings, 16th International Workshop on Deep Inelastic Scattering and Related Subjects (DIS 2008)*, p. 142. 2008. `arXiv:0807.0024 [hep-ph]`.

[115] M. Duhrssen, K. Jakobs, J. J. van der Bij, and P. Marquard, *The Process gg $\rightarrow$ WW as a background to the Higgs signal at the LHC*, JHEP **05** (2005) 064, `arXiv:hep-ph/0504006 [hep-ph]`.

[116] J. M. Campbell, R. K. Ellis, and C. Williams, *Gluon-Gluon Contributions to W+ W- Production and Higgs Interference Effects*, JHEP **10** (2011) 005, `arXiv:1107.5569 [hep-ph]`.

[117] T. Binoth, M. Ciccolini, N. Kauer, and M. Kramer, *Gluon-induced W-boson pair production at the LHC*, JHEP **12** (2006) 046, `arXiv:hep-ph/0611170 [hep-ph]`.

[118] K. L. Adamson, D. de Florian, and A. Signer, *Gluon induced contributions to WZ and W gamma production at NNLO*, Phys. Rev. **D65** (2002) 094041, `arXiv:hep-ph/0202132 [hep-ph]`.

[119] K. L. Adamson, D. de Florian, and A. Signer, *Gluon induced contributions to $Z\gamma$ production at hadron colliders*, Phys. Rev. **D67** (2003) 034016, `arXiv:hep-ph/0211295 [hep-ph]`.

[120] J. J. van der Bij and E. W. N. Glover, *Photon Z boson pair production via gluon fusion*, Phys. Lett. **B206** (1988) 701.

[121] F. Cascioli, T. Gehrmann, M. Grazzini, S. Kallweit, P. Maierhofer, A. von Manteuffel, S. Pozzorini, D. Rathlev, L. Tancredi, and E. Weihs, *ZZ production at hadron colliders in NNLO QCD*, Phys. Lett. **B735** (2014) 311–313, `arXiv:1405.2219 [hep-ph]`.

[122] M. Grazzini, S. Kallweit, and D. Rathlev, *ZZ production at the LHC: fiducial cross sections and distributions in NNLO QCD*, Phys. Lett. **B750** (2015) 407–410, `arXiv:1507.06257 [hep-ph]`.

[123] M. Grazzini, S. Kallweit, D. Rathlev, and A. Torre, *$Z\gamma$ production at hadron colliders in NNLO QCD*, Phys. Lett. **B731** (2014) 204–207, `arXiv:1309.7000 [hep-ph]`.

[124] T. Gehrmann, M. Grazzini, S. Kallweit, P. Maierhofer, A. von Manteuffel, S. Pozzorini, D. Rathlev, and L. Tancredi, *W^+W^- Production at Hadron Colliders in Next to Next to Leading Order QCD*, Phys. Rev. Lett. **113** (2014) no. 21, 212001, `arXiv:1408.5243 [hep-ph]`.

[125] M. Grazzini, S. Kallweit, and D. Rathlev, *$W\gamma$ and $Z\gamma$ production at the LHC in NNLO QCD*, JHEP **07** (2015) 085, `arXiv:1504.01330 [hep-ph]`.

[126] F. Campanario and S. Sapeta, *WZ production beyond NLO for high-pT observables*, Phys. Lett. **B718** (2012) 100–104, `arXiv:1209.4595 [hep-ph]`.

[127] F. Campanario, M. Rauch, and S. Sapeta, *W^+W^- production at high transverse momenta beyond NLO*, Nucl. Phys. **B879** (2014) 65–79, `arXiv:1309.7293 [hep-ph]`.

[128] F. Campanario, M. Rauch, and S. Sapeta, *ZZ production at high transverse momenta beyond NLO QCD*, JHEP **08** (2015) 070, `arXiv:1504.05588 [hep-ph]`.

[129] F. Caola, K. Melnikov, R. Rontsch, and L. Tancredi, *QCD corrections to ZZ production in gluon fusion at the LHC*, `arXiv:1509.06734 [hep-ph]`.

[130] ATLAS Collaboration, G. Aad et al., *Measurement of W^+W^- production in pp collisions at $\sqrt{s}$=7ââTeV with the ATLAS detector and limits on anomalous WWZ and $WW\gamma$ couplings*, Phys. Rev. **D87** (2013) no. 11, 112001, `arXiv:1210.2979 [hep-ex]`. [Erratum: Phys. Rev.D88,no.7,079906(2013)].

[131] CMS Collaboration, S. Chatrchyan et al., *Measurement of the W^+W^- Cross section in pp Collisions at $\sqrt{s} = 7$ TeV and Limits on Anomalous $WW\gamma$ and WWZ couplings*, Eur. Phys. J. **C73** (2013) no. 10, 2610, `arXiv:1306.1126 [hep-ex]`.

[132] CMS Collaboration, S. Chatrchyan et al., *Measurement of W+W- and ZZ production cross sections in pp collisions at $\sqrt{s} = 8$ TeV*, Phys. Lett. **B721** (2013) 190–211, `arXiv:1301.4698 [hep-ex]`.

[133] P. Meade, H. Ramani, and M. Zeng, *Transverse momentum resummation effects in W^+W^- measurements*, Phys. Rev. **D90** (2014) no. 11, 114006, `arXiv:1407.4481 [hep-ph]`.

[134] P. Jaiswal and T. Okui, *Explanation of the WW excess at the LHC by jet-veto resummation*, Phys. Rev. **D90** (2014) no. 7, 073009, `arXiv:1407.4537 [hep-ph]`.

[135] P. Jaiswal, P. Meade, and H. Ramani, *Precision diboson measurements and the interplay of pT and jet-veto resummations*, `arXiv:1509.07118 [hep-ph]`.

[136] M. Grazzini, S. Kallweit, D. Rathlev, and M. Wiesemann, *Transverse-momentum resummation for vector-boson pair production at NNLL+NNLO*, JHEP **08** (2015) 154, `arXiv:1507.02565 [hep-ph]`.

[137] M. Billoni, S. Dittmaier, B. Jager, and C. Speckner, *Next-to-leading-order electroweak corrections to $pp \to WW \to 4$ leptons in double-pole approximation at the LHC*, PoS **RADCOR2013** (2013) 018, `arXiv:1311.5491 [hep-ph]`.

[138] A. Bierweiler, T. Kasprzik, J. H. Kuhn, and S. Uccirati, *Electroweak corrections to W-boson pair production at the LHC*, JHEP **11** (2012) 093, `arXiv:1208.3147 [hep-ph]`.

[139] J. Baglio, L. D. Ninh, and M. M. Weber, *Massive gauge boson pair production at the LHC: a next-to-leading order story*, Phys. Rev. **D88** (2013) 113005, `arXiv:1307.4331`.

[140] A. Bierweiler, T. Kasprzik, and J. H. Kuhn, *Vector-boson pair production at the LHC to $\mathcal{O}(\alpha^3)$ accuracy*, JHEP **12** (2013) 071, `arXiv:1305.5402 [hep-ph]`.

[141] W. Hollik and C. Meier, *Electroweak corrections to gamma Z production at hadron colliders*, Phys. Lett. **B590** (2004) 69–75, `arXiv:hep-ph/0402281 [hep-ph]`.

[142] E. Accomando, A. Denner, and C. Meier, *Electroweak corrections to $W\gamma$ and $Z\gamma$ production at the LHC*, Eur. Phys. J. **C47** (2006) 125–146, `arXiv:hep-ph/0509234 [hep-ph]`.

[143] A. Denner, S. Dittmaier, M. Hecht, and C. Pasold, *NLO QCD and electroweak corrections to $W + \gamma$ production with leptonic W-boson decays*, JHEP **04** (2015) 018, `arXiv:1412.7421 [hep-ph]`.

[144] NNPDF Collaboration, R. D. Ball, V. Bertone, S. Carrazza, L. Del Debbio, S. Forte, A. Guffanti, N. P. Hartland, and J. Rojo, *Parton distributions with QED corrections*, Nucl. Phys. **B877** (2013) 290–320, `arXiv:1308.0598 [hep-ph]`.

[145] T. Sjostrand, S. Mrenna, and P. Z. Skands, *A Brief Introduction to PYTHIA 8.1*, Comput. Phys. Commun. **178** (2008) 852–867, `arXiv:0710.3820 [hep-ph]`.

[146] T. Gleisberg, S. Hoeche, F. Krauss, M. Schonherr, S. Schumann, F. Siegert, and J. Winter, *Event generation with SHERPA 1.1*, JHEP **02** (2009) 007, `arXiv:0811.4622 [hep-ph]`.

[147] G. Corcella, I. G. Knowles, G. Marchesini, S. Moretti, K. Odagiri, P. Richardson, M. H. Seymour, and B. R. Webber, *HERWIG 6.5 release note*, `arXiv:hep-ph/0210213 [hep-ph]`.

[148] S. Frixione and B. R. Webber, *Matching NLO QCD computations and parton shower simulations*, JHEP **06** (2002) 029, `arXiv:hep-ph/0204244 [hep-ph]`.

[149] S. Alioli, P. Nason, C. Oleari, and E. Re, *A general framework for implementing NLO calculations in shower Monte Carlo programs: the POWHEG BOX*, JHEP **06** (2010) 043, `arXiv:1002.2581 [hep-ph]`.

[150] L. Barze, G. Montagna, P. Nason, O. Nicrosini, F. Piccinini, and A. Vicini, *Neutral current Drell-Yan with combined QCD and electroweak corrections in the POWHEG BOX*, Eur. Phys. J. **C73** (2013) no. 6, 2474, `arXiv:1302.4606 [hep-ph]`.

[151] S. Gieseke, T. Kasprzik, and J. H. Kuhn, *Vector-boson pair production and electroweak corrections in HERWIG++*, Eur. Phys. J. **C74** (2014) no. 8, 2988, `arXiv:1401.3964 [hep-ph]`.

[152] S. Hoeche, Y. Li, and S. Prestel, *Combining parton showers and NNLO matrix elements*, in *50th Rencontres de Moriond on QCD and High Energy Interactions La Thuile, Italy, March 21-28, 2015.* 2015. `arXiv:1507.05325 [hep-ph]`. `http://inspirehep.net/record/1383897/files/arXiv:1507.05325.pdf`.

[153] S. Alioli, C. W. Bauer, C. Berggren, F. J. Tackmann, J. R. Walsh, and S. Zuberi, *Matching Fully Differential NNLO Calculations and Parton Showers*, JHEP **06** (2014) 089, `arXiv:1311.0286 [hep-ph]`.

[154] K. Hagiwara, S. Ishihara, R. Szalapski, and D. Zeppenfeld, *Low-energy effects of new interactions in the electroweak boson sector*, Phys.Rev. **D48** (1993) 2182–2203.

[155] C. Degrande, *A basis of dimension-eight operators for anomalous neutral triple gauge boson interactions*, JHEP **1402** (2014) 101, `arXiv:1308.6323 [hep-ph]`.

[156] ATLAS Collaboration, G. Aad et al., *Measurement of ZZ production in pp collisions at $\sqrt{s} = 7$ TeV and limits on anomalous ZZZ and ZZγ couplings with the ATLAS detector*, JHEP **03** (2013) 128, `arXiv:1211.6096 [hep-ex]`.

[157] N. Kauer, *Interference effects for $H \to WW/ZZ \to \ell\bar{\nu}_\ell\bar{\ell}\nu_\ell$ searches in gluon fusion at the LHC*, JHEP **12** (2013) 082, `arXiv:1310.7011 [hep-ph]`.

[158] S. Baker and R. D. Cousins, *Clarification of the use of the chi-square and the likelihood functions in fits histograms*, Nuclear Instruments and Methods in Physics Research **221** (1984) 437.

[159] R. D. Cousin, *Generalization of Chisquare Goodness-of-Fit Test for Binned Data using Saturated Models, with Apllication to Histograms*, http://www.physics.ucla.edu/c̃ousins/stats/cousins_saturated.pdf (2013) .

[160] J. Meyer and T. Kasprzik, *Reweighting method to incorporate higher order electroweak corrections into resonant heavy gauge boson pair production predictions*, Tech. Rep. ATL-COM-PHYS-2014-152, CERN, Geneva, Feb, 2014.

[161] J. G. Heinrich, *Can the likelihood function be used to measure goodness of fit?*, CDF/MEMO/BOTTOM/CDFR/5639.

[162] G. Bella, *Weighting Di-Boson Monte Carlo Events in Hadron Colliders*, `arXiv:0803.3307 [hep-ph]`.

[163] G. Feldman and R. Cousins Phys. Rev. **D57** (1998) 3873.

[164] G. Cowan, K. Cranmer, E. Gross, and O. Vitells, *Asymptotic Formulae for Likelihood-Based Tests of New Physics*, Eur. Phys. J. C **71** (2011) 1554, `arXiv:hep-ph/1007.1727v2`.

[165] J. Manjarres Ramos, *WZ Diboson Measurements with the ATLAS experiment at the LHC and Performance of resistive Micromegas in view of HL-LHC applications.* PhD thesis, Saclay. `http://inspirehep.net/record/1296490/files/516495851_CERN-THESIS-2013-199.pdf`.

[166] F. James, *MINUIT - Function Minimization and Error Analysis.* CERN Program Library entry D506, Geneva, 1998.

[167] C. Degrande, N. Greiner, W. Kilian, O. Mattelaer, H. Mebane, et al., *Effective Field Theory: A Modern Approach to Anomalous Couplings*, Annals Phys. **335** (2013) 21–32, `arXiv:1205.4231 [hep-ph]`.

[168] CMS Collaboration, S. Chatrchyan et al., *Measurement of the Wγ and Zγ inclusive cross sections in pp collisions at $\sqrt{s} = 7$âăTeV and limits on anomalous triple gauge boson couplings*, Phys. Rev. **D89** (2014) no. 9, 092005, `arXiv:1308.6832 [hep-ex]`.

[169] CMS Collaboration, S. Chatrchyan et al., *Measurement of the production cross section for $Z\gamma \to \nu\bar{\nu}\gamma$ in pp collisions at $\sqrt{s} = 7$ TeV and limits on $ZZ\gamma$ and $Z\gamma\gamma$ triple gauge boson couplings*, JHEP **10** (2013) 164, `arXiv:1309.1117 [hep-ex]`.

[170] CMS Collaboration, V. Khachatryan et al., *Measurement of the $Z\gamma$ production cross section in pp collisions at 8 TeV and search for anomalous triple gauge boson couplings*, JHEP **04** (2015) 164, `arXiv:1502.05664 [hep-ex]`.

[171] CMS Collaboration, C. Collaboration, *Measurement of the production cross section for Z gamma to nu nu gamma in pp collisions at $\sqrt{s} = 8$ TeV and limits on Z Z gamma and Z gamma gamma triple gauge boson couplings*, Tech. Rep. CMS-PAS-SMP-14-019, 2015.

[172] ATLAS Collaboration, *Measurements of $Z\gamma$ and $Z\gamma\gamma$Production in pp Collisions at $\sqrt{s} = 8$ TeV with the ATLAS Detector*, To be published .

[173] ATLAS Collaboration, *Measurement of the ZZ production cross section in pp collisions at 8 TeV using ZZ-¿2l2nu and ZZ-¿4ldecay channels with the ATLAS detector*, To be published .

[174] CMS Collaboration, V. Khachatryan et al., *Measurements of the ZZ production cross sections in the $2\ell2\nu$ channel in proton-proton collisions at $\sqrt{s} = 7$ and 8 TeV and combined constraints on triple gauge couplings*, `arXiv:1503.05467 [hep-ex]`.

[175] DELPHI, OPAL, LEP Electroweak, ALEPH, L3 Collaboration, S. Schael et al., *Electroweak Measurements in Electron-Positron Collisions at W-Boson-Pair Energies at LEP*, Phys. Rept. **532** (2013) 119–244, `arXiv:1302.3415 [hep-ex]`.

[176] D0 Collaboration, V. M. Abazov et al., *Search for ZZ and $Z\gamma^*$ production in $p\bar{p}$ collisions at $\sqrt{s} = 1.96$ TeV and limits on anomalous ZZZ and $ZZ\gamma^*$ couplings*, Phys. Rev. Lett. **100** (2008) 131801, `arXiv:0712.0599 [hep-ex]`.

[177] CDF, D0 Collaboration, A. Robson, *Diboson Physics at the Tevatron*, EPJ Web Conf. **28** (2012) 06001, `arXiv:1201.4771 [hep-ex]`.

[178] D0 Collaboration, V. M. Abazov et al., *$Z\gamma$ production and limits on anomalous $ZZ\gamma$ and $Z\gamma\gamma$ couplings in $p\bar{p}$ collisions at $\sqrt{s} = 1.96$ TeV*, Phys. Rev. **D85** (2012) 052001, `arXiv:1111.3684 [hep-ex]`.

[179] CDF Collaboration, T. Aaltonen et al., *Limits on Anomalous Trilinear Gauge Couplings in $Z\gamma$ Events from $p\bar{p}$ Collisions at $\sqrt{s} = 1.96$ TeV*, Phys. Rev. Lett. **107** (2011) 051802, `arXiv:1103.2990 [hep-ex]`.

[180] CMS Collaboration, V. Khachatryan et al., *Measurement of the W^+W^- cross section in pp collisions at $\sqrt{s} = 8$ TeV and limits on anomalous gauge couplings*, `arXiv:1507.03268 [hep-ex]`.

[181] D0 Collaboration, V. M. Abazov et al., *Limits on anomalous trilinear gauge boson couplings from WW, WZ and $W\gamma$ production in $p\bar{p}$ collisions at $\sqrt{s} = 1.96$ TeV*, Phys. Lett. **B718** (2012) 451–459, `arXiv:1208.5458 [hep-ex]`.

[182] Q. Ho-Kim and X.-Y. Pham, *Elementary particles and their interactions: concepts and phenomena.* Springer Science & Business Media, 2013.

[183] C. N. Yang and R. L. Mills, *Conservation of Isotopic Spin and Isotopic Gauge Invariance*, Phys. Rev. **96** (Oct, 1954) 191–195.

[184] F. Halzen and A. Martin, *Quarks and Leptons.* John Wiley and Sons, 1984.

[185] G. J. Gounaris, J. Layssac, and F. M. Renard, *Addendum to "Off-shell structure of the anomalous Z and γ self-couplings"*, Phys. Rev. D **65** (Dec, 2001) 017302.

[186] S. Weinberg, *The quantum theory of fields, Chp 12, V1*, vol. 2. Cambridge university press, 1996.

[187] W.-Y. Keung, I. Low, and J. Shu, *Landau-Yang Theorem and Decays of a $Z^{'}$ Boson into Two Z Bosons*, Phys. Rev. Lett. **101** (Aug, 2008) 091802.

[188] G. J. Gounaris, J. Layssac, and F. M. Renard, *Signatures of the anomalous $Z\gamma$ and* ZZ *production at lepton and hadron colliders*, Phys. Rev. D **61** (Mar, 2000) 073013.

[189] G. J. Gounaris, J. Layssac, and F. M. Renard, *Off-shell structure of the anomalous **Z** and γ self-couplings*, Phys. Rev. D **62** (Sep, 2000) 073012.

[190] U. Baur and E. L. Berger, *Probing the weak-boson sector in $Z\gamma$ production at hadron colliders*, Phys. Rev. D **47** (Jun, 1993) 4889–4904.

[191] U. Baur and D. Rainwater, *Probing neutral gauge boson self-interactions in* ZZ *production at hadron colliders*, Phys. Rev. D **62** (Nov, 2000) 113011.

[192] G. J. Gounaris, J. Layssac, and F. M. Renard, *New and standard physics contributions to anomalous Z and γ self-couplings*, Phys. Rev. D **62** (Sep, 2000) 073013.

[193] H. Aihara, T. Barklow, U. Baur, J. Busenitz, S. Errede, et al., *Anomalous gauge boson interactions*, `arXiv:hep-ph/9503425 [hep-ph]`.

[194] A. De Rujula, M. Gavela, P. Hernandez, and E. Masso, *The Selfcouplings of vector bosons: Does LEP-1 obviate LEP-2?*, Nucl.Phys. **B384** (1992) 3–58.

[195] S. Weinberg, *Baryon- and Lepton-Nonconserving Processes*, Phys. Rev. Lett. **43** (Nov, 1979) 1566–1570.

[196] B. Grzadkowski, M. Iskrzynski, M. Misiak, and J. Rosiek, *Dimension-Six Terms in the Standard Model Lagrangian*, JHEP **1010** (2010) 085, `arXiv:1008.4884 [hep-ph]`.

[197] R. Alonso, H.-M. Chang, E. E. Jenkins, A. V. Manohar, and B. Shotwell, *Renormalization group evolution of dimension-six baryon number violating operators*, Physics Letters B **734** (2014) no. 0, 302 – 307.

[198] L. Lehman, *Extending the standard model effective field theory with the complete set of dimension-7 operators*, Phys. Rev. D **90** (Dec, 2014) 125023.

[199] J. Wudka, *Electroweak effective Lagrangians*, Int.J.Mod.Phys. **A9** (1994) 2301–2362, `arXiv:hep-ph/9406205 [hep-ph]`.

[200] S. Willenbrock and C. Zhang, *Effective Field Theory Beyond the Standard Model*, Ann.Rev.Nucl.Part.Sci. **64** (2014) 83–100, `arXiv:1401.0470 [hep-ph]`.

[201] R. Alonso, E. E. Jenkins, A. V. Manohar, and M. Trott, *Renormalization Group Evolution of the Standard Model Dimension Six Operators III: Gauge Coupling Dependence and Phenomenology*, JHEP **1404** (2014) 159, `arXiv:1312.2014 [hep-ph]`.

[202] A. Efrati, A. Falkowski, and Y. Soreq, *Electroweak constraints on flavorful effective theories*, JHEP **07** (2015) 018, `arXiv:1503.07872 [hep-ph]`.

[203] O. Cata, *Revisiting ZZ and γZ production with effective field theories*, `arXiv:1304.1008 [hep-ph]`.

[204] J. Alcaraz, *On the experimental effects of the off-shell structure in anomalous neutral triple gauge vertices*, Phys.Rev. **D65** (2002) 075020, `arXiv:hep-ph/0111283 [hep-ph]`.

[205] K. Hagiwara, R. Peccei, D. Zeppenfeld, and K. Hikasa, *Probing the Weak Boson Sector in e+ e- to W+ W-*, Nucl.Phys. **B282** (1987) 253.

[206] U. Baur and D. Zeppenfeld, *Probing the W W gamma Vertex at Future Hadron Colliders*, Nucl.Phys. **B308** (1988) 127.

[207] G. Brooijmans et al., *Les Houches 2013: Physics at TeV Colliders: New Physics Working Group Report*, `arXiv:1405.1617 [hep-ph]`.

[208] A. Falkowski and F. Riva, *Model-independent precision constraints on dimension-6 operators*, JHEP **02** (2015) 039, `arXiv:1411.0669 [hep-ph]`.

[209] A. Falkowski, M. Gonzalez-Alonso, A. Greljo, and D. Marzocca, *Global constraints on anomalous triple gauge couplings in effective field theory approach*, `arXiv:1508.00581 [hep-ph]`.

[210] A. V. Kotwal, H. Schellman, and J. Sekaric, *Review of Physics Results from the Tevatron: Electroweak Physics*, Int. J. Mod. Phys. **A30** (2015) no. 06, 1541004, `arXiv:1409.5163 [hep-ex]`.

[211] CMS Collaboration, S. Chatrchyan et al., *Measurement of the sum of WW and WZ production with W+dijet events in pp collisions at $\sqrt{s} = 7$ TeV*, Eur. Phys. J. **C73** (2013) no. 2, 2283, `arXiv:1210.7544 [hep-ex]`.

[212] ATLAS Collaboration, G. Aad et al., *Measurement of the $WW + WZ$ cross section and limits on anomalous triple gauge couplings using final states with one lepton, missing transverse momentum, and two jets with the ATLAS detector at $\sqrt{\mathrm{s}} = 7$ TeV*, JHEP **01** (2015) 049, `arXiv:1410.7238 [hep-ex]`.

[213] ATLAS Collaboration, G. Aad et al., *Measurement of the electroweak production of dijets in association with a Z-boson and distributions sensitive to vector boson fusion in proton-proton collisions at $\sqrt{s} = 8$ TeV using the ATLAS detector*, JHEP **04** (2014) 031, `arXiv:1401.7610 [hep-ex]`.

[214] CMS Collaboration, S. Chatrchyan et al., *Measurement of the ZZ production cross section and search for anomalous couplings in 2 l2l ' final states in pp collisions at* $\sqrt{s} = 7$ *TeV*, JHEP **01** (2013) 063, `arXiv:1211.4890 [hep-ex]`.

[215] CMS Collaboration, V. Khachatryan et al., *Measurement of the pp* $\to$ *ZZ production cross section and constraints on anomalous triple gauge couplings in four-lepton final states at* $\sqrt{s}$ *=8 TeV*, Phys. Lett. **B740** (2015) 250–272, `arXiv:1406.0113 [hep-ex]`.

[216] T. Corbett, O. Eboli, and M. Gonzalez-Garcia, *Unitarity Constraints on Dimension-Six Operators*, Phys. Rev. **D91** (2015) no. 3, 035014, `arXiv:1411.5026 [hep-ph]`.

[217] Z. Han and W. Skiba, *Effective theory analysis of precision electroweak data*, Phys. Rev. **D71** (2005) 075009, `arXiv:hep-ph/0412166 [hep-ph]`.

[218] L. Berthier and M. Trott, *Consistent constraints on the Standard Model Effective Field Theory*, `arXiv:1508.05060 [hep-ph]`.

[219] J. Ellis, V. Sanz, and T. You, *The Effective Standard Model after LHC Run I*, JHEP **03** (2015) 157, `arXiv:1410.7703 [hep-ph]`.

[220] A. Falkowski, *Effective field theory approach to LHC Higgs data*, `arXiv:1505.00046 [hep-ph]`.

[221] A. Pomarol and F. Riva, *Towards the Ultimate SM Fit to Close in on Higgs Physics*, JHEP **1401** (2014) 151, `arXiv:1308.2803 [hep-ph]`.

[222] J. Gonzalez-Fraile, *Effective Lagrangian approach to the EWSB sector*, in *International Conference on High Energy Physics 2014 (ICHEP 2014) Valencia, Spain, July 2-9, 2014*. 2014. `arXiv:1411.5364 [hep-ph]`.

[223] T. Corbett, O. Eboli, J. Gonzalez-Fraile, and M. Gonzalez-Garcia, *Robust Determination of the Higgs Couplings: Power to the Data*, Phys.Rev. **D87** (2013) 015022, `arXiv:1211.4580 [hep-ph]`.

[224] T. Corbett, O. J. P. Eboli, D. Goncalves, J. Gonzalez-Fraile, T. Plehn, and M. Rauch, *The Higgs Legacy of the LHC Run I*, `arXiv:1505.05516 [hep-ph]`.

[225] T. Corbett, O. Ãboli, J. Gonzalez-Fraile, and M. Gonzalez-Garcia, *Determining Triple Gauge Boson Couplings from Higgs Data*, Phys.Rev.Lett. **111** (2013) 011801, `arXiv:1304.1151 [hep-ph]`.

[226] A. Biekotter, A. Knochel, M. Kramer, D. Liu, and F. Riva, *Vices and virtues of Higgs effective field theories at large energy*, Phys. Rev. **D91** (2015) 055029, `arXiv:1406.7320 [hep-ph]`.

[227] LHC Higgs Cross Section Working Group 2 Collaboration, *Higgs Basis: Proposal for an EFT basis choice for LHC HXSWG*, Tech. Rep. LHCHXSWG-INT-2015-001, 2015.

[228] W. Buchmuller and D. Wyler, *Effective Lagrangian Analysis of New Interactions and Flavor Conservation*, Nucl. Phys. **B268** (1986) 621–653.

[229] G. F. Giudice, C. Grojean, A. Pomarol, and R. Rattazzi, *The Strongly-Interacting Light Higgs*, JHEP **06** (2007) 045, `arXiv:hep-ph/0703164 [hep-ph]`.

[230] C. Arzt, M. B. Einhorn, and J. Wudka, *Patterns of deviation from the standard model*, Nucl. Phys. **B433** (1995) 41–66, `arXiv:hep-ph/9405214 [hep-ph]`.

[231] J. Wudka, *The Meaning of anomalous couplings*, eConf **C960625** (1996) NEW176, `arXiv:hep-ph/9606478 [hep-ph]`.

[232] A. Pomarol, *Higgs Physics*, in *2014 European School of High-Energy Physics (ESHEP 2014) Garderen, The Netherlands, June 18-July 1, 2014*. 2014. `arXiv:1412.4410 [hep-ph]`.

[233] E. E. Jenkins, A. V. Manohar, and M. Trott, *On Gauge Invariance and Minimal Coupling*, JHEP **09** (2013) 063, `arXiv:1305.0017 [hep-ph]`.

[234] R. S. Gupta, A. Pomarol, and F. Riva, *BSM Primary Effects*, Phys. Rev. **D91** (2015) no. 3, 035001, `arXiv:1405.0181 [hep-ph]`.

[235] E. Masso, *An Effective Guide to Beyond the Standard Model Physics*, JHEP **10** (2014) 128, `arXiv:1406.6376 [hep-ph]`.

[236] M. Gonzalez-Alonso, A. Greljo, G. Isidori, and D. Marzocca, *Electroweak bounds on Higgs pseudo-observables and $h \to 4\ell$ decays*, Eur. Phys. J. **C75** (2015) no. 7, 341, `arXiv:1504.04018 [hep-ph]`.

[237] A. Falkowski, B. Fuks, K. Mawatari, K. Mimasu, F. Riva, and V. sanz, *Rosetta: an operator basis translator for Standard Model effective field theory*, `arXiv:1508.05895 [hep-ph]`.

[238] ATLAS Collaboration, G. Aad et al., *Constraints on non-Standard Model Higgs boson interactions in an effective field theory using differential cross sections measured in the $H \to \gamma\gamma$ decay channel at $\sqrt{s} = 8$ TeV with the ATLAS detector*, `arXiv:1508.02507 [hep-ex]`.

[239] CMS Collaboration, V. Khachatryan et al., *Study of vector boson scattering and search for new physics in events with two same-sign leptons and two jets*, Phys. Rev. Lett. **114** (2015) no. 5, 051801, `arXiv:1410.6315 [hep-ex]`.

[240] J. G. Heinrich, *Coverage of Errors bars for Poisson Data*, CDF/MEMO/STATISTICS/PUBLIC/6438.

[241] U. Baur and D. L. Rainwater, *Probing neutral gauge boson selfinteractions in ZZ production at hadron colliders*, Phys. Rev. **D62** (2000) 113011, `arXiv:hep-ph/0008063`.

[242] R. Brun and F. Rademaker, *ROOT - An Object Oriented Data Analysis Framework*, Nucl.Instrum.Meth. A **389** (1997) 81–86.

[243] R. Barlow, *A note on estimating errors from the likelihood function*, Nucl.Instrum.Meth. A **550** (2005) 392–396.

[244] A. M. L. W. A. Rolke and J. Conrad, *Limits and confidence intervals in the presence of nuisance parameters*, Nucl.Instrum.Meth. A **551** (2005) 493â503.

Appendices

Appendix A

Interactions between Electroweak Gauge Bosons

In this appendix, I review the theory and measurements of the interactions between Electroweak Gauge Bosons, the W, Z and γ bosons.

Within the Standard Model, these interactions are consequences of the non-Abelian nature of the Local Gauge Symmetries under which the Lagrangian of the model is invariant. Crucially the W, Z and γ fields are not the Gauge fields of these Symmetries but the physical fields relevant after the Spontaneous Electroweak Symmetry breaking induced by the Higgs mechanism. The interactions between the W, Z and γ bosons emerge from the interactions between the fundamental Gauge fields which are determined by the $SU(2)_L \times U(1)_Y$ Gauge structure of the Standard Model. Among these interactions are Triple bosons couplings, the forms and number of which are rigidly prescribed. Notably the couplings between three neutral Z and γ bosons are forbidden.

Various frameworks have been proposed to describe possible anomalous couplings different from those prescribed by the Standard Model Lagrangian. The most phenomenological of these frameworks, the Effective Lagrangian and Vertex Function approaches, aim to an effective description of departures from the Standard Model only limited by the most basic prescriptions: Lorentz invariance, Bose symmetry and possibly $U(1)_{em}$ invariance. Instead, the more ambitious approach of the Effective Field Theory describes these departures as the low energy effects of some unspecified high energy physics. This powerful approach can embrace in a consistent framework all the deviations from the Standard Model from anomalous interactions between W, Z and γ bosons to anomalous couplings and decays of the Higgs boson.

In the first section A.1 of this appendix, I review how the interactions between W, Z and γ bosons emerge from the Standard Model Lagrangian insisting of the striking symmetry between γ and Z boson. Modifications of the Lagrangians describing these interactions are briefly discussed as introductions to the Effective Lagrangian and Effective Field theory approaches of the deviations from the Standard Model prescriptions.

The next two sections A.2 and A.3 discuss in details these approaches for the anomalous interactions first between three neutral bosons Z and γ bosons, the so-called Neutral anomalous Triple Gauge Bosons Couplings and then between two W bosons and one neutral boson, the so-called Charged anomalous Triple Gauge Bosons Couplings.

The fourth section A.4 offers a review of the measurements of the anomalous Triple Gauge Bosons Couplings that have been performed at the LEP, TEVATRON and LHC colliders.

The last section A.5 briefly discusses the currently very active field of the Global EFT analyses where the limits on anomalous Triple Gauge Boson Couplings join the Electroweak Precision tests and Higgs boson measurements, in the search of low-energy signs of a Physics Beyond the Standard Model.

A.1 Gauge Bosons interactions in the Standard Model

In this section, we remind how the interactions between the $W^{\pm}$, Z and γ emerge from the Lagrangian of the Standard Model (SM). The symmetry between Z and γ is emphasized. All the interactions terms, but the 4 W-bosons interactions vertex, are shown to follow from a slightly augmented minimal coupling prescription for $U(1)$ Gauge symmetries acting on the "matter" field $W^{\pm}$.

The electroweak sector of the SM is defined by a Lagrangian invariant under the $SU(2)_L \times U(1)_Y$ Gauge symmetry with a specific matter content. The Gauge fields are noted W^i_μ with i running from 1 to 3 for $SU(2)_L$ and B_μ for $U(1)_Y$. The covariant derivative for a $SU(2)_L$ doublet of hypercharge Y is

$$D_\mu = \partial_\mu + ig\frac{\sigma^i}{2}W^i_\mu + ig'\frac{Y}{2}B_\mu \tag{A.1}$$

where the σ^i are the Pauli matrices and g and g' are the coupling constants of $SU(2)_L$ and $U(1)_Y$. The matter content of the theory is defined for each generation in terms of $SU(2)$ representations with hypercharges assigned in order to recover at the end the appropriate electromagnetic charges: a left-handed quark doublet $q_L = \begin{pmatrix} u_L \\ d_L \end{pmatrix}$, a left-handed lepton doublet $l_L = \begin{pmatrix} \nu_L \\ e_L \end{pmatrix}$ and four right-handed singlets u_R, d_R, e_R, and ν_R with hypercharges $Y(l_L) = -1$, $Y(e_R) = -2$, $Y(\nu_R) = 0$, $Y(q_L) = 1/3$, $Y(u_R) = 4/3$ and $Y(d_R) = -2/3$. To this one adds the Higgs complex scalar field doublet H to which the hypercharge $Y = 1$ is assigned.

One defines four new fields, $W^{\pm}_\mu$, Z_μ and A_μ built from the four W^i_μ and B_μ fields as

$$W^{\pm}_\mu = (W^1_\mu \mp W^2_\mu)/\sqrt{2} \tag{A.2}$$

$$Z_\mu = c_r W^3_\mu - s_r B_\mu \quad , \quad A_\mu = s_r W^3_\mu + c_r B_\mu \tag{A.3}$$

where c_r and s_r are the cosine and the sine of θ_r some mixing angle of the W^3_μ and B_μ fields. Couplings between the new fields emerge from the kinetic terms of the W^i_μ and B_μ fields:

$$\mathcal{L}_{kin} = -\frac{1}{4}W^i{}_{\mu\nu}W^{i\mu\nu} - \frac{1}{4}B_{\mu\nu}B^{\mu\nu} \tag{A.4}$$

where $W^i_{\mu\nu} = \partial_\mu W^i_\nu - \partial_\nu W^i_\mu - g\epsilon_{ijk}W^j_\mu W^k_\nu$ and $B_{\mu\nu} = \partial_\mu B_\nu - \partial_\nu B_\mu$. The substitution in (A.4) of the W^i_μ and B_μ fields by the $W^{\pm}_\mu$, Z_μ and A_μ fields, leads to a crowd of terms in which one can identify Triple Gauge bosons Couplings (TGC)

$$\begin{aligned}\mathcal{L}^{SM}_{TGC} = &-igs_r\Big[A^\nu(W^+_{\mu\nu}W^{-\mu} - W^-_{\mu\nu}W^{+\mu}) + A^{\mu\nu}W^+_\mu W^-_\nu\Big] \\ &-igc_r\Big[Z^\nu(W^+_{\mu\nu}W^{-\mu} - W^-_{\mu\nu}W^{+\mu}) + Z^{\mu\nu}W^+_\mu W^-_\nu\Big]\end{aligned} \tag{A.5}$$

and Quartic Gauge bosons Couplings (QGC)

$$\begin{aligned}\mathcal{L}^{SM}_{QGC} = &-g^2 s_r^2(W^-_\mu W^{+\mu}A_\nu A^\nu - W^-_\mu W^+_\nu A^\mu A^\nu) - g^2 c_r^2(W^-_\mu W^{+\mu}Z_\nu Z^\nu - W^-_\mu W^+_\nu Z^\mu Z^\nu) \\ &- g^2 s_r c_r(2W^-_\mu W^{+\mu}A_\nu Z^\nu - W^-_\mu W^+_\nu A^\mu Z^\nu - W^-_\mu W^+_\nu Z^\mu A^\nu) \\ &- \frac{1}{2}g^2(W^{+\mu}W^{+\nu}W^-_\mu W^-_\nu - W^{+\mu}W^+_\mu W^{-\nu}W^-_\nu)\end{aligned} \tag{A.6}$$

where $A_{\mu\nu} = \partial_\mu A_\nu - \partial_\nu A_\mu$ and $Z_{\mu\nu} = \partial_\mu Z_\nu - \partial_\nu Z_\mu$.

This is how the TGCs and QGCs come out in the SM. This dry way to present things provides no insight on what is going on. What follows is an attempt to "naturalize" (A.5) and (A.6).

First one notes a striking symmetry between the A_μ and Z_μ fields in (A.5) and (A.6).

One knows that the A_μ field singles out with the choice $\theta_r = \theta_W$ where θ_W, the Weinberg angle, is defined by $\tan\theta_W = g'/g$. With the above hypercharge assignment of the fermions, A_μ couples identically to the left-handed and right-handed fermions. Most importantly, due to the Higgs doublet hypercharge assignment, A_μ remains massless after the Spontaneous Symmetry Breaking (SSB) when the Higgs doublet is expanded about the minimum dictated by the Higgs potential.

However θ_W has no particular role in $\mathcal{L}_{kin}$ as only g does enter in it. Therefore as far as $\mathcal{L}_{kin}$ is concerned, the A_μ and Z_μ fields should appear very similar. The inverse of (A.3)

$$W^3_\mu = c_r Z_\mu + s_r A_\mu \quad , \quad B_\mu = -s_r Z_\mu + c_r A_\mu \tag{A.7}$$

tells what the symmetry between the A_μ and Z_μ fields is. Clearly the simultaneous crossed substitutions $A \leftrightarrow Z$ and $s_r \leftrightarrow c_r$ let the Lagrangian (A.4) unchanged. And indeed one can check that this formal symmetry hold true in (A.5) and (A.6). Therefore what ever "happens" to a γ in terms of TGC and QGC, "happens" to a Z too and reciprocally. This halves the mnemonic effort to remember the TGCs and QGCs in the SM!

Actually all that "happens" to a γ or a Z can be understood quite simply by considering that two $U(1)$ symmetries, $U(1)_A$ and $U(1)_Z$ associated respectively to the A and Z fields, apply to the Spin-1 W boson field seen as the "matter" field. This makes the vertices that will emerge as "natural" as the vertex of a γ with an electron is a "natural" consequence of requiring $U(1)_{em}$ for the Spin-$\frac{1}{2}$ electron "matter" field. Indeed it can be shown that one can write $\mathcal{L}_{kin}$ in terms of the $W^\pm_\mu$, Z_μ and A_μ fields as [182]

$$\begin{aligned}\mathcal{L}_{kin} = &-\frac{1}{4}A_{\mu\nu}A^{\mu\nu} - \frac{1}{4}Z_{\mu\nu}Z^{\mu\nu} - \frac{1}{2}(\mathcal{D}_\mu W^+_\nu - \mathcal{D}_\nu W^+_\mu)^\dagger(\mathcal{D}^\mu W^{+\nu} - \mathcal{D}^\nu W^{+\mu}) \\ &- ig(s_r A^{\mu\nu} + c_r Z^{\mu\nu})W^+_\mu W^-_\nu - \frac{1}{2}g^2(W^{+\mu}W^{+\nu}W^-_\mu W^-_\nu - W^{+\mu}W^+_\mu W^{-\nu}W^-_\nu)\end{aligned} \tag{A.8}$$

where $\mathcal{D}_\mu = \partial_\mu + ig(s_r A_\mu + c_r Z_\mu)$.

The first three terms of (A.8) are those of a theory with $U(1)_A$ and $U(1)_Z$ acting on the Spin-1 matter field W$^\pm$ [1]. Indeed the first two terms in (A.8) are the standard kinetic terms for the Z_μ and A_μ fields and the third term is the implementation of the minimal prescription for the $U(1)$ couplings to the A and Z fields. This term generates almost all the TGCs and QGCs of the SM

$$\begin{aligned}&-(\mathcal{D}_\mu W^+_\nu - \mathcal{D}_\nu W^+_\mu)^\dagger(\mathcal{D}^\mu W^{+\nu} - \mathcal{D}^\nu W^{+\mu})/2 = \\ &- W^-_{\mu\nu}W^{+\mu\nu}/2 \\ &- igs_r A^\nu(W^+_{\mu\nu}W^{-\mu} - W^-_{\mu\nu}W^{+\mu}) - igc_r Z^\nu(W^+_{\mu\nu}W^{-\mu} - W^-_{\mu\nu}W^{+\mu}) \\ &- g^2 s_r^2(W^-_\mu W^{+\mu}A_\nu A^\nu - W^-_\mu W^+_\nu A^\mu A^\nu) - g^2 c_r^2(W^-_\mu W^{+\mu}Z_\nu Z^\nu - W^-_\mu W^+_\nu Z^\mu Z^\nu) \\ &- g^2 s_r c_r(2W^-_\mu W^{+\mu}A_\nu Z^\nu - W^-_\mu W^+_\nu A^\mu Z^\nu - W^-_\mu W^+_\nu Z^\mu A^\nu)\end{aligned} \tag{A.9}$$

where $W^+_{\mu\nu} = \partial_\mu W^+_\nu - \partial_\nu W^+_\mu$. The first term of (A.9) is the kinetic term for the W$^\pm$ field. The 2^{nd} and 3^{rd} terms describe triple vertices $WW\gamma$ and WWZ. The 4^{th} and 5^{th} terms describe quartic vertices $WW\gamma\gamma$ and $WWZZ$. The last term describes a $WWZ\gamma$ quartic vertex and follows naturally from having simultaneously $U(1)_A$ and $U(1)_Z$.

---

[1] The whole affair in this section is to track and to re-express in terms of A_μ and Z_μ, the couplings between the triplet of non-abelian $SU(2)$ gauge fields W^-_μ, W^+_μ and W^3_μ. Beside a four W interactions terms, they amount for a $U(1)$ symmetry acting on the spin-1 charged field W$^\pm_\mu$ with a Yang-Mills non-minimal coupling to W^3_μ [183].

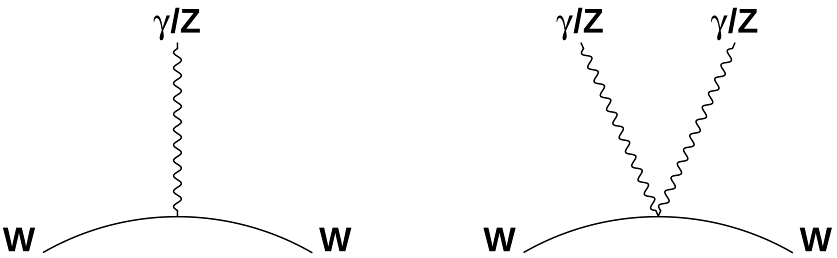

Figure A.1: Standard Model TGC and QGC involving γ or Z

The situation can be graphically represented as in the figures A.1: in a way very similar to the case of QED for a fermion field, to the "matter" line of a W boson, one attaches one or two $U(1)$ Gauge boson lines, i.e or a γ bringing a factor gs_w or a Z-boson bringing a factor gc_w [2]. That one has vertices with 2 Gauge bosons attached is similar to the case of QED for a charged scalar: the gauge invariance requires a quartic vertex with 2 Gauge bosons attached to the matter line in addition to the usual triple vertex with only one Gauge boson [184].

Standing apart, are the 4^{th} (a TGC) and 5^{th} (a QGC) terms of (A.8). There is nothing to do for the 5^{th} term. It describes a 4 W-bosons vertex that is known to be necessary for the cancellation of unitary violation in the scattering of two W-bosons. It is irreducible to this $U(1)_{A,Z}$ approach.

The 4^{th} term is amenable to reason at the price of slight extension. It is a $WW[\gamma/Z]$ TGC term but with a non-minimal coupling to the magnetic moment of the W-boson. It is $U(1)$ invariant since it is built on the field strength tensors $A^{\mu\nu}$ and $Z^{\mu\nu}$ which are invariant on their own. Therefore from the point of view of $U(1)$ invariance, the coupling constant in front of this term is unconstrained. Let's multiply it by an arbitrary constant κ_V with $V = \gamma, Z$. Gathering all the Triple Gauge couplings terms for e.g. the A_μ field, one gets

$$\begin{aligned}\mathcal{L}_{TGC,\gamma} = igs_w(\quad & A^\nu[W^{-\mu}(\partial_\nu W^+_\mu) - (\partial_\nu W^-_\mu)W^{+\mu}] \\ & + W^{-\nu}[\kappa_\gamma W^{+\mu}(\partial_\nu A_\mu) - (\partial_\nu W^+_\mu)A^\mu] \\ & + W^{+\nu}[A^\mu(\partial_\nu W^-_\mu) - \kappa_\gamma(\partial_\nu A_\mu)W^{-\mu}] \quad)\end{aligned} \tag{A.10}$$

One sees that the value $\kappa_\gamma = 1$ is special since it makes the preceding expression invariant under the cyclic permutation of the W^-, W^+ and A fields. This feature is not an accident and does reveal the $SU(2)$ origin of the fourth term of (A.8). It holds between the W^-, W^+ and W^3 fields because they form a triplet of non-abelian Yang-Mills gauge fields. One can include this feature by defining a slightly extended $U(1)$ coupling prescription, the Yang-Mills non-minimal coupling prescription which augments the minimal coupling prescription with a term $-igV^{\mu\nu}W^+_\mu W^-_\nu$. This Yang-Mills non-minimal coupling prescription, is crucial for the cancellation of the unitary violations of tree amplitudes of some electroweak processes [93].

So with the Yang-Mills non-minimal coupling prescription, all the TGCs terms and almost all the QGCs terms of the SM collected in (A.5) and (A.6), result from our $U(1)_A$ and $U(1)_Z$ symmetries, a feature which is graphically captured in figures A.1. The only exception is the 4 W bosons QGC vertex.

---

[2] This shows or at least helps to remember that the SM TGCs and QGCs which involve γs or Zs, involve always a pair of W^+W^- bosons: they are needed to draw the "matter" line.

So the SM Lagrangian generates only $WW[Z/\gamma]$ Triple Gauge Bosons vertices and $WWWW$ and $WW[Z/\gamma][Z/\gamma]$ Quartic Gauge Bosons vertices. There is no coupling involving only neutral Gauge bosons. All the couplings emerge from the transformation of the Gauge invariant terms of (A.8). And all this is completely prescribed by the $SU(2)_L \times U(1)_Y$ Gauge structure of the SM.

How then can we introduce and describe couplings beyond those prescribed by the SM? One can start by modifying the Lagrangians directly. Focusing on the TGC Lagrangian (A.5) and specifically on the A field terms, one can contest the Yang-Mills prescription and introduces back an anomalous coupling to the magnetic moment of the W-boson as we did in (A.10)

$$\mathcal{L}_{aTGC,\gamma} == -igs_r[A^\nu(W^+_{\mu\nu}W^{-\mu} - W^-_{\mu\nu}W^{+\mu}) + (1+\Delta\kappa_\gamma)A^{\mu\nu}W^+_\mu W^-_\nu] \tag{A.11}$$

Since we do want to keep the $U(1)_{em}$ invariance, we do not try to modify the constant in front of the first term above since it gives the electromagnetic charge of the W-boson. But for the Z field terms in (A.5), we do not have such scruples, so that we can propose a new TGC Lagrangian such as

$$\begin{aligned} \mathcal{L}_{aTGC} = -igs_r[A^\nu(W^+_{\mu\nu}W^{-\mu} - W^-_{\mu\nu}W^{+\mu}) + (1+\Delta\kappa_\gamma)A^{\mu\nu}W^+_\mu W^-_\nu] \\ -igc_r[(1+\Delta g_1^Z)Z^\nu(W^+_{\mu\nu}W^{-\mu} - W^-_{\mu\nu}W^{+\mu}) + (1+\Delta\kappa_Z)Z^{\mu\nu}W^+_\mu W^-_\nu] \end{aligned} \tag{A.12}$$

We can continue in this way and introduce new terms, including pure neutral couplings[3], in the Lagrangians. This is the Effective Lagrangian approach that will be detailed in the next sections with the closely related Vertex Function approach.

Alternatively one can generate new couplings reiterating the mechanism that allowed the SM TGCs and QGCs to emerge: one starts from a $SU(2)_L \times U(1)_Y$ invariant term and by substitution of the Before-SSB fields (the W^3_μ, B_μ and Higgs doublet H fields) by the After-SSB fields (the A, Z, $W^\pm$ and Higgs boson fields) one obtains couplings between the later [4]. Such a $SU(2)_L \times U(1)_Y$ invariant term will be an operator, i.e a product of the Before-SSB fields multiplied by a coupling constant. The mass-dimension of this coupling constant should be such that the overall term is of mass-dimension 4 as required for a Lagrangian term. One knows that renormalization would be spoiled if the mass-dimension of this coupling constant is strictly negative [186]. If one restricts the mass-dimension of the coupling constants of these new interactions to be greater than or equal to 0, i.e if one considers operators of dimension four at most, it turns out that the SM Lagrangian contains already all the terms of this kind with couplings fixed by the Gauge invariance. Therefore if $SU(2)_L \times U(1)_Y$ is imposed, novel interactions constructed in this way are necessarily non-renormalizable interactions [5]. This is the realm of the Effective Field Theory approach.

---

[3] For what concerns the couplings of Three Neutral Gauge Bosons, beside $\gamma\gamma\gamma$ coupling which is prevented by the Furry's theorem, the $Z\gamma\gamma$ and $ZZ\gamma$ couplings from dimension-4 operators in A and Z fields can be excluded on the basis of $U(1)_{em}$ alone. Indeed these operators will contain three A and Z fields and a field derivative. For these operators to be $U(1)_{em}$ invariant, the A field should enter via a $A^{\mu\nu}$. The $Z\gamma\gamma$ coupling would have to contain two $A^{\mu\nu}$ which together exhaust the dimension-4 allowed. So $Z\gamma\gamma$ is excluded. Next the $ZZ\gamma$ coupling which is necessarily of the form $A^{\mu\nu}Z^\mu Z^\nu$ is excluded, since $A^{\mu\nu}$ is antisymmetric while $Z^\mu Z^\nu$ is symmetric . And indeed imposing only $U(1)_{em}$, one finds in [185] that there exists only one dimension-4 operator describing a Triple neutral Bosons interaction, a ZZZ vertex: $\tilde{O}_5^{Z*Z*Z*} = Z^\mu Z_\nu(\partial^\sigma Z_\sigma)$. However this interaction has no contribution if the Z-bosons couple to light fermions pairs. Actually in the discussions on the interactions of Gauge bosons, the condition $\partial_\mu V^\mu = 0$ for all massive bosons involved is almost universally used on this basis that the bosons are on-shell or that they are assumed to couple to light fermions pairs.

[4] Examples of this in provided in section B.

[5] Non renormalizable in the sense in which e.g. QED is renormalizable, i.e not only that quantum divergences can be renormalized, i.e absorbed by a redefinition of the parameters of the theory, but also that this involves a finite number of parameters. In non-renormalizable theory divergences can be still absorbed by a redefinition of the parameters but there should be an infinite number of couplings. Now, if the non-renormalizable terms are low-energy effects from high energy interactions at a large scale Λ, one can rank these coupling by their inverse power of Λ, $c \sim 1/\Lambda^{d_i-4}$, i.e in the order of the importance of their low-energy effects. Then it will be appropriate, at the price of a limited precision in the computations, to work with a finite number of couplings retaining them up to some rank. In that way non-renormalizable theory can be made effective and predictive, i.e as good as a renormalizable theory at least at low energy [186].

A.2 Neutral Anomalous Triple Gauge Couplings

In this section, I review the theoretical frameworks that have been designed to describe the interactions of three neutral Gauge bosons, Z-boson or γ, beyond those prescribed by the Standard Model. All these frameworks are phenomenological or effective in the sense that the interactions do not arise from an explicit underlying theory beyond the Standard Model. Instead these frameworks just aim to write down all interactions which are possible under a minimal set of constraints likely to be respected by any of these theories. The vertices of interest are ZZZ, $ZZ\gamma$ and $Z\gamma\gamma$ with the additional condition that two of these bosons are on-shell [6].

A.2.1 Effective Lagrangian approach

The first approach is to write down the most general Lagrangian with all possible Lorentz structures built with the Z-boson and γ fields, but with the fewest number of field derivatives. Under the additional constraint that the Gauge symmetry $U_{em}(1)$ is respected, this effective Lagrangian is [188]

$$\begin{aligned}\mathcal{L}_{NB} = \frac{e}{m_Z^2}\Bigg[&-\Big\{ f_4^\gamma(\partial_\mu F^{\mu\beta}) + f_4^Z(\partial_\mu Z^{\mu\beta})\Big\} Z_\alpha(\partial^\alpha Z_\beta) + \Big\{ f_5^\gamma(\partial^\sigma F_{\sigma\mu}) + f_5^Z(\partial^\sigma Z_{\sigma\mu})\Big\}\widetilde{Z}^{\mu\beta} Z_\beta \\ &-\Big\{ h_1^\gamma(\partial^\sigma F_{\sigma\mu}) + h_1^Z(\partial^\sigma Z_{\sigma\mu})\Big\} Z_\beta F^{\mu\beta} - \Big\{ h_3^\gamma(\partial_\sigma F^{\sigma\rho}) + h_3^Z(\partial_\sigma Z^{\sigma\rho})\Big\} Z^\alpha \widetilde{F}_{\rho\alpha} \\ &-\Big\{ \frac{h_2^\gamma}{m_Z^2}[\partial_\alpha\partial_\beta\partial^\rho F_{\rho\mu}] + \frac{h_2^Z}{m_Z^2}[\partial_\alpha\partial_\beta(\Box + m_Z^2)Z_\mu]\Big\} Z^\alpha F^{\mu\beta} \\ &+\Big\{ \frac{h_4^\gamma}{2m_Z^2}[\Box\partial^\sigma F^{\rho\alpha}] + \frac{h_4^Z}{2m_Z^2}[(\Box + m_Z^2)\partial^\sigma Z^{\rho\alpha}]\Big\} Z_\sigma \widetilde{F}_{\rho\alpha}\Bigg]\end{aligned} \tag{A.13}$$

where m_Z is the mass of the Z-boson, $\widetilde{Z}_{\mu\nu} = 1/2\epsilon_{\mu\nu\rho\sigma}Z^{\rho\sigma}$, $\widetilde{F}_{\mu\nu} = 1/2\epsilon_{\mu\nu\rho\sigma}F^{\rho\sigma}$ and $F^{\mu\nu}$, which was noted $A^{\mu\nu}$ in section A.1, is the electromagnetic strength tensor.

This Lagrangian defines 12 independent dimensionless couplings, f_i^V and h_i^V. None of the field operators of this Lagrangian are in the SM Lagrangian (A.5). Therefore all these couplings, called neutral aTGCs, are null in the SM. The field operators in (A.13) have different mass dimensionalities. The f_i^V and $h_{1,3}^V$ terms are of the form $\frac{C}{m_Z^2}\mathcal{O}_6$ where $\mathcal{O}_6$ is a dimension-6 operator while the $h_{2,4}^V$ terms are of the form $\frac{C}{m_Z^4}\mathcal{O}_8$, where $\mathcal{O}_8$ is a dimension-8 operator.

The meanings of the neutral aTGCs may not be completely clear from the Lagrangian (A.13). The table A.1 sorts out the various couplings, the vertices to which they correspond, the behaviors under CP of their associated field operator [7] and the two bosons production for which they are relevant.

Vertex	ZZZ	$ZZ\gamma$		$Z\gamma\gamma$
Two boson production	ZZ		$Z\gamma$	
CP-even	f_5^Z	f_5^γ	$h_{3,4}^Z$	$h_{3,4}^\gamma$
CP-violating	f_4^Z	f_4^γ	$h_{1,2}^Z$	$h_{1,2}^\gamma$

Table A.1: Neutral aTGCs

There is a particularity indicated in the table A.1 which is worth to discuss. Both the ZZ and the $Z\gamma$ productions allow to probe the $ZZ\gamma$ vertex. However through the study of these productions,

---

[6] One of the two on-shell bosons is necessarily a Z-boson since the Landau-Yang theorem forbids the decay of a spin-1 particle into two γs (see [187], for the extension of this theorem to a spin-1 particle decaying into two Z-bosons).

[7] All terms are C-violating. Hence all CP-even terms are P-violating.

one learns on two distinct "facets", so to say, of the $ZZ\gamma$ vertex: on $f^{\gamma}_{4,5}$ through ZZ and on $h^{Z}_{1,2,3,4}$ through $Z\gamma$. These two sets of couplings are independent as all the couplings in (A.13). They describe two "facets" of the $ZZ\gamma$ vertex differing by the nature of the virtual particle: the γ in the ZZ production and a Z in the $Z\gamma$ production. In [185, 189], the 3 off-shell bosons vertex $Z^{*}Z^{*}\gamma^{*}$ is studied. It is shown how $f^{\gamma}_{4,5}$ and $h^{Z}_{1,2,3,4}$ emerge separately when one pushes 2 of the bosons on-shell. So as perplexing it could be, it should be kept in mind that although the $ZZ\gamma$ vertex contributes to both ZZ and $Z\gamma$ productions, the combination of the constrains obtained from the studies of these two production modes does not put more stringent constrains on the $ZZ\gamma$ vertex.

The CP-parities of the different terms in (A.13) have consequences on the dependence of the cross-section on the couplings [190, 191]. The amplitude of the diboson production is the sum of the SM amplitude plus the anomalous amplitudes each of these proportional to an anomalous coupling. Schematically one has

$$|.\rangle = |SM\rangle + \sum \zeta_i \, |i\rangle \tag{A.14}$$

where the ζ_i are the anomalous couplings. Therefore the production cross section proportional to the square of the process amplitude is a function bilinear in the ζ_i

$$\sigma = Y_{00} + \sum_{i=1} Y_{0i}\zeta_i + \sum_{i=1} Y_{ii}\zeta_i^2 + \sum_{i,j=1;j>i} Y_{ij}\zeta_i\zeta_j \tag{A.15}$$

where the first term is proportional to the square of the SM amplitude, the second term to the interferences of the SM amplitude with the anomalous amplitudes, the third term to the squares of the anomalous amplitudes, and the fourth term to the interferences between the anomalous amplitudes. Since interferences are possible only between components with the same behavior under CP, there is no linear dependence of the cross section on a CP-violating anomalous coupling: the second term in (A.15) runs only on CP-respecting ζ_i. Furthermore the fourth term split in two terms each running on anomalous couplings of same CP-parities. Therefore one has schematically

$$\sigma = \left(Y_{00} + \sum_{i,CP} Y_{0i}\zeta_i + \sum_{i,CP} Y_{ii}\zeta_i^2 + \sum_{i,j,CP} Y_{ij}\zeta_i\zeta_j \right) + \left(\sum_{i,\cancel{CP}} Y_{ii}\zeta_i^2 + \sum_{i,j,\cancel{CP}} Y_{ij}\zeta_i\zeta_j \right) \tag{A.16}$$

Since at it is the most common case the constrain on anomalous couplings will come from a single bin count, i.e on a single integral of the cross section, (A.16) tells us that the correlations will cluster as correlations among couplings of same CP-parities. Furthermore the limits on couplings will be sign symmetric for CP-violating couplings, while it could be not the case for the CP-respecting couplings due to the term linear in these couplings in (A.16).

The anomalous couplings in (A.13) are not form factors depending on the momentum of the off-shell boson since the Lagrangian is a position-space function. However this Lagrangian has been obtained by collecting all terms with the fewest number of derivatives. Other terms, in infinite number, are possible. The infinitely numerous terms that could have been added, would have introduced as many additional constants. They sum up in the Vertex Function approach to form form factors which are functions of the momenta.

A.2.2 Vertex Function approach

The vertex function is the term that comes with a given vertex when one writes down the amplitude for a Feynman diagram. The Vertex Function approach consists in parameterizing the vertex function of the Three Gauge Bosons vertex in figure A.2. The vantage point of this approach is that the vertex function can be written in a fully general and complete way. One forms and sums up all the appropriate tensorial expressions built with the momenta of the vertex bosons. The coefficients of this sum are functions of the norms of these momenta. These functions should verify certain symmetries and conditions.

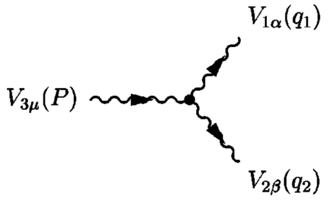

$$= ie\ \Gamma^{\alpha,\beta,\mu}_{V_1V_2V_3}(q_1,q_2,P)$$

Figure A.2: Three bosons vertex and Vertex Function

The reference [189] is an example of such a procedure. It derives the expressions of the vertex functions for three off-shell neutral Gauge Bosons constrained by Bose symmetry on bosons of same type and conservation of vector current on γ legs. Under the same conditions which allowed to derive (A.13), the Vertex Functions for the ZZ and $Z\gamma$ final states are [192]:

$$\Gamma^{\alpha,\beta,\mu}_{ZZV}(q_1,q_2,P) = \frac{i(P^2-m_V^2)}{m_Z^2}\left\{f_4^V\,(P^\alpha g^{\mu\beta}+P^\beta g^{\mu\alpha}) - f_5^V\,\epsilon^{\mu\alpha\beta\rho}(q_1-q_2)_\rho\right\} \tag{A.17}$$

and

$$\begin{aligned}\Gamma^{\alpha,\beta,\mu}_{Z\gamma V}(q_1,q_2,P) = \frac{i(P^2-m_V^2)}{m_Z^2}\Bigg\{ & h_1^V\,(q_2^\mu g^{\alpha\beta}-q_2^\alpha g^{\mu\beta}) + \frac{h_2^V}{m_Z^2}P^\alpha[(Pq_2)g^{\mu\beta}-q_2^\mu P^\beta] \\ & -h_3^V\,\epsilon^{\mu\alpha\beta\rho}q_{2\rho} - \frac{h_4^V}{m_Z^2}P^\alpha\epsilon^{\mu\beta\rho\sigma}P_\rho q_{2\sigma}\Bigg\}\end{aligned} \tag{A.18}$$

where q_1 and q_2 are the momenta of the on-shell bosons and V is the off-shell boson, γ or Z, of momentum P and on-shell mass m_V [8]. The Vertex Functions (A.17) and (A.18) are the momentum-space analogues of (A.13) and the couplings appearing in these formulas are related. They are equal but only at $P^2 = 0$. Indeed unlike those of (A.13), the couplings in (A.17) and (A.18) are form factors depending on P^2. There are actually the sum of the infinitely numerous terms with higher order derivatives that could have been added to (A.13).

Usually the contribution of anomalous TGC to the cross-section leads to a violation of the unitarity at high energies. This is cured by assuming that the form factors decrease rapidly in this regime by parameterizing them with the ansatz $C(P^2) = C_0 \times (1 + P^2/\Lambda_{FF}^2)^{-n}$. Using this parametrization, the constraint from unitarity on anomalous Triple Gauge couplings have been given in [193]. It is conventional to take $n = 3$ for $f_{4,5}^V$ and $h_{1,3}^V$, and $n = 4$ for $h_{2,4}^V$ [190, 193]. The power n and Λ_{FF} are arbitrary as the form of the ansatz itself is. Their only justification is to avoid the unitarity issue. The unitary violation is usually not an issue in machines with fixed energy in the center of mass such as in the e^+e^- colliders that have been built up to now. However the problem, and thus the possible need of parameterizing form factors, is more acute in a *pp* machine such as the LHC where the energy in the center of mass of an actual hard interaction can be very high. On the other hand, to have

---

[8] One can check that $\Gamma^{\alpha,\beta,\mu}_{ZZV}(q_1,q_2,P)$ is invariant under the Bose symmetry $q_1,\alpha \leftrightarrow q_2,\beta$. One can get additional conditions by considering the limit case where the virtuality of V vanishes. When V is a γ "pushed" on-shell, one should have $P_\mu\Gamma^{\alpha,\beta,\mu}_{ZZV}(q_1,q_2,P) = 0$. Since the contraction of P_μ with the term between curly brackets in $\Gamma_{ZZ\gamma}$ is not null, it follows that the multiplicative factor should be 0 when $P^2 = 0$. When V is a Z-boson "pushed" on-shell, since the term between curly brackets in Γ_{ZZZ} is not invariant under the Bose symmetry $q_1,\alpha \leftrightarrow P,\mu$, it follows that the multiplicative factor should be 0 when $P^2 = m_Z^2$. A similar analysis can be done for $\Gamma_{Z\gamma V}$. Consistently with $q_{2\beta}$ being the momentum of the on-shell γ in $Z\gamma V$, one can check that one has $q_{2\beta}\Gamma^{\alpha,\beta,\mu}_{Z\gamma V}(q_1,q_2,P) = 0$. When V is a γ "pushed" on-shell, since the contraction of P_μ with the term between curly brackets in $\Gamma_{Z\gamma\gamma}$ is not null, it follows that the multiplicative factor should be 0 when $P^2 = 0$. Finally, when V is a Z-boson "pushed" on-shell, since the term between curly brackets in $\Gamma_{Z\gamma Z}$ is not invariant under the Bose symmetry $q_1,\alpha \leftrightarrow P,\mu$, it follows that the multiplicative factor should be 0 when $P^2 = m_Z^2$.

to resort to form factor makes difficult the comparison between the results of different experiments. Furthermore the constraints from the unitarity limit using the above form factor parametrization have been designed such that the unitarity limit is never reached however large P^2 is. Such a large scope for the validity of a phenomenological description has been questioned.

A.2.3 Effective Field Theory approach

Both the Effective Lagrangian and Vertex Function approaches have been harshly criticized [167, 194]. They badly behave in loop calculations without providing prescriptions to cure the problems. The cure advocated in [194] is to impose $SU(2)_L \times U(1)_Y$. In reference [167], these approaches are charged to be lacking a proper criteria specifying their range of applicability, i.e an energy scale above which the theory is not to be trusted any more. The mass m_Z in (A.13) is not a scale of the theory but rather a dimensionful parameter allowing to compensate for the dimensionality of the operators. The scale factor Λ_{FF} of the form factor ansatz would be closer to be a scale associated with some new Physics, would it be not impaired with so much arbitrariness.

The reference [167] castigates the anomalous couplings approaches for their obsolescence and the confusion that they bring. It is actually a manifesto for the Effective Field Theory approach which in the context of anomalous Triple Gauge Boson interactions has a long history [154].

A.2.3.1 Effective Field Theory

The EFT approach focuses on the low-energy effects of some new physics characterized by a scale Λ much larger than the energy at hand $\sqrt{s} \ll \Lambda$. The EFT Lagrangian invokes only the low energy fields. It contains the standard low energy interactions plus new interactions terms of mass-dimension ≥ 5 scaled down by some power of Λ. Its does not strive to be valid at arbitrary large energy since anyway above Λ new degrees of freedom will be activated and a new Lagrangian will have to be written down which will involve new fields and new interactions [9].

More precisely, the EFT Lagrangian respects the $SU(2)_L \times U(1)_Y$ Gauge symmetry. It is built using the SM fields only, in particular the bosonic fields are those before-SSB, the W^i_μ, the B_μ and the Higgs doublet fields, and not the after-SSB fields, the W-boson, Z-boson and γ fields. Its contains all the SM terms and an infinite sum of non-SM terms representing all interactions of SM fields respecting $SU(2)_L \times U(1)_Y$. Such an interaction is described by a dimension-d operator scaled by a factor $\frac{C}{\Lambda^{d-4}}$ with C a dimensionless constant. The effective Lagrangian takes the form

$$L_{EFT} = L_{SM} + \sum_{d \geqslant 5} L^d_{EFT} \text{ with } L^d_{EFT} = \sum_i \frac{C^d_i}{\Lambda^{d-4}} O^d_i \tag{A.19}$$

where L^d_{EFT} sums up all the different operators of a given dimension d. As we saw, only the terms that respect $SU(2)_L \times U(1)_Y$ are retained. One can get rid of more operators by imposing other conditions

---

[9] The classic example of EFT is the Fermi Theory of weak interactions. At energies lower than m_W, the effective non-renormalizable term in the Lagrangian is a 4-point vertex with a dimensionful coupling $G_F/\sqrt{2}$. At high energies, the "new" physics manifests itself in the form of the W-boson. The old low-energy Lagrangian is thrown away and a new Lagrangian is formed with interaction vertex involving the new field with a dimensionless coupling g. Since $\frac{G_F}{\sqrt{2}} = \frac{g^2}{8m_W^2}$, the old Lagrangian term appears as an effective term built with an operator of dimension-6 in the fields relevant at low energy, scaled by a factor which encapsulates the underlying high energy interactions, $\frac{C}{\Lambda^2}$, where $\Lambda = m_W$ is the scale of the "new" high energy physics. This analogy shows also that even if there is some evidence for an effective interaction term (e.g. Fermi Theory of β decay), all that can be measured is the factor $\frac{C}{\Lambda^d}$ (e.g. G_F coupling) but not Λ (e.g. the mass of the W-boson) itself. For this, as it was the case for the W-boson, an explicit model of the underlying new physics is needed. The ambition of the EFT, here the Fermi Theory, is just to provide a framework convenient to describe low-energy effects in a model independent way.

such as C and P conservations or, as very often done, the conservations of baryon (B) and lepton (L) numbers [10]. This latter restriction removes all operators of odd dimensions [167] [11].

Then the EFT approach proceeds in retaining only the operators up to a given dimension, d_t thus capturing the leading effects up to order $(\sqrt{s}/\Lambda)^{d_t-4}$, the neglected higher order corrections being suppressed by further powers of $\sqrt{s}/\Lambda$. This is actually the stance of the EFT approach: it offers a effective and consistent treatment of the low-energy effects, including loop computations, up to an accuracy controlled by the order of the truncation of the Lagrangian (A.19). In its full glory the topic is quite technical and complex with possibly tens of operators involved in some analyses [199–201] [12]. Fortunately in the context of the anomalous Triple Gauge bosons interactions, the relevant operators are far fewer.

A.2.3.2 Effective Field Theory approach for Neutral aTGCs

Hereafter, I follow the reference [155] [13]. Requiring conservation of B and L, the first dimension to consider in (A.19) is the dimension 6. It turns out than none of the 59 operators of dimension-6 conserving B and L does induce neutral aTGCs [196]. Therefore one has to look for operators of dimension-8.

This could be worrisome for the fate of the couplings f_i^V and $h_{1,3}^V$ terms since as we saw, they are associated to dimension-6 operators. However these operators are in the after-SSB fields while the EFT operators are in the before-SSB fields. When the EFT operators are rewritten in terms of the after-SSB fields, the Higgs doublet H contributes by its vacuum expectation value, v, a dimension-1 constant, which amounts for a reduction of the dimension of the resulting operator in the after-SSB fields. Thus an operator in the after-SSB fields of a given dimension can actually come from a EFT operator of higher dimension containing H field.

The operator analysis in [155] shows that all the dimension-8 operators that contribute to neutral aTGCs, do contain H fields. This implies that the operators associated to $h_{2,4}^V$ can not be obtained from EFT dimension-8 operators since they are already of dimension-8 in the after-SSB fields. So one has

$$h_2^\gamma = h_2^Z = h_4^\gamma = h_4^Z = 0 \tag{A.20}$$

This lets four CP-even and four CP-violating couplings (cf table A.1).

Next it is shown that only four operators of dimension-8, named O_{BW}, O_{WW}, O_{BB} and $O_{\widetilde{B}W}$, can contribute and that they all, but the last, violate CP. They are

$$\begin{aligned} O_{BW} &= iH^\dagger B_{\mu\nu}\underline{\mathrm{W}}^{\mu\rho}\{D_\rho, D^\nu\}H \quad , \quad O_{WW} = iH^\dagger \underline{\mathrm{W}}_{\mu\nu}\underline{\mathrm{W}}^{\mu\rho}\{D_\rho, D^\nu\}H \\ O_{BB} &= iH^\dagger B_{\mu\nu}B^{\mu\rho}\{D_\rho, D^\nu\}H \quad , \quad O_{\widetilde{B}W} = iH^\dagger \widetilde{B}_{\mu\nu}\underline{\mathrm{W}}^{\mu\rho}\{D_\rho, D^\nu\}H \end{aligned} \tag{A.21}$$

---

[10] However B and L conservations are global symmetries of the SM without being forced upon it. They are "accidental" symmetries in the sense that the operators that enter in the SM Lagrangian just turn out to respect them.

[11] The operators have been systematically classified up to dimension-7. There is only one dimension-5 operator and it violates L [195]. There are 59 B and L conserving dimension-6 operators [196] and 4 B-violating dimension-6 operators [197]. There are 20 dimension-7 operators all violating L, among which 7 violate B too [198].

[12] The counting of 59 dimension-6 operators conserving B and L numbers is for one generation only. When flavor indices for the 3 generations are added, the number of operators reaches 2499 [201]. Various arguments are used to reduce the number of the operators used in an analysis. A most acute point is to adopt a scheme dealing with flavor violation. The coefficient of the operators inducing Flavor Changing Neutral Currents, c_i/Λ^2, should be suppressed in some way since the stringent limits on these processes would translate into an hopeless $\Lambda \sim 1$ PeV if $c_i \sim 1$ [200]. Solutions can be blunt flavor universality assumption or more sophisticated schemes involving Yukawa matrices (cf [202] for review). The number of operators can be further reduced by assuming for instance CP conservation. Also the number of operators used in a particular analysis can be limited simply because this analysis focuses on a particular Physics sector and data set.

[13] A first tentative in [185] was found faulty in [155, 203, 204]. Still it is not clear that there is no tension between the results of these three last references.

where $\underline{\mathrm{W}}_{\mu\nu} = \sigma^i W^i_{\mu\nu}$.

Furthermore it is shown that the CP-even operator, $O_{\widetilde{B}W}$, contributes to the $ZZ\gamma$ vertex only. Hence among the four surviving CP-even couplings, the two concerning the ZZZ and $Z\gamma\gamma$ vertices are null

$$h_3^\gamma = f_5^Z = 0 \tag{A.22}$$

while the two others should be proportional since they both have to be proportional to the same factor $\frac{C_{\widetilde{B}W}}{\Lambda^4}$ which multiplies $O_{\widetilde{B}W}$ in the EFT Lagrangian. These relations turn out to be

$$f_5^\gamma = h_3^Z \tag{A.23}$$

$$f_5^\gamma = \frac{v^2 m_Z^2}{4c_w s_w}\frac{C_{\widetilde{B}W}}{\Lambda^4} \tag{A.24}$$

Finally the three constants C_{BW}, C_{WW} and C_{BB}, which come with the three CP-violating dimension-8 operators, determine the values of the four surviving CP-violating couplings. It is found that

$$h_1^Z = -f_4^\gamma \tag{A.25}$$

$$f_4^\gamma = -\frac{v^2 m_Z^2}{4c_w s_w}\Big(- c_w s_w \frac{C_{BB}}{\Lambda^4} + (c_w^2 - s_w^2)\frac{C_{BW}}{\Lambda^4} + 4s_w c_w \frac{C_{WW}}{\Lambda^4}\Big) \tag{A.26}$$

$$f_4^Z = \frac{v^2 m_Z^2}{2c_w s_w}\Big(c_w^2 \frac{C_{BB}}{\Lambda^4} + 2c_w s_w \frac{C_{BW}}{\Lambda^4} + 4s_w^2 \frac{C_{WW}}{\Lambda^4}\Big) \tag{A.27}$$

$$h_1^\gamma = \frac{v^2 m_Z^2}{4c_w s_w}\Big(- s_w^2 \frac{C_{BB}}{\Lambda^4} + 2c_w s_w \frac{C_{BW}}{\Lambda^4} - 4c_w^2 \frac{C_{WW}}{\Lambda^4}\Big) \tag{A.28}$$

Therefore the EFT analysis of reference [155] concludes that at the order $(\sqrt{s}/\Lambda)^4$ the anomalous neutral boson interactions can be described by just four independent constants, $C_{\widetilde{B}W}$, C_{WW}, C_{BW} and C_{BB} corresponding to one CP-even and three CP-violating interactions.

At this order, these four constants can be taken as well to be f_5^γ, f_4^Z, f_4^γ and h_1^γ. With this choice, one can clearly see on table A.2 how many constants are needed for the description of a given vertex and of a given final state. Both ZZZ and the $Z\gamma\gamma$ vertices are exclusively CP-violating interactions described by two independent constants. The $ZZ\gamma$ vertex corresponds to CP-even and CP-violating interactions and it is described by two independent parameters whatever is the off-shell boson.

<table>
<tr><td>Vertex</td><td>ZZZ</td><td colspan="2">$ZZ\gamma$</td><td>$Z\gamma\gamma$</td></tr>
<tr><td>Two boson production</td><td colspan="2">ZZ</td><td colspan="2">$Z\gamma$</td></tr>
<tr><td>CP-even</td><td></td><td colspan="2">f_5^γ</td><td></td></tr>
<tr><td>CP-violating</td><td>f_4^Z</td><td colspan="2">f_4^γ</td><td>h_1^γ</td></tr>
</table>

Table A.2: EFT description of Neutral aTGCs

The description of the ZZ final state required three independent constants as does the description of the $Z\gamma$ final state. Nicely, two of these constants are common to the two descriptions. This contrasts with the general case shown on table A.1 where not only many more parameters were needed but also where there was no commonality of any sort between the descriptions of the ZZ and $Z\gamma$ final states

The table A.2 illustrated what the EFT approach offers: it does not provide numerical estimates but, thanks to an ordering principle of the effects of the interactions possible under some symmetries constraints, it provides a guidance on what to expect experimentally and how to describe it phenomenologically.

A.3 Charged Anomalous Triple Gauge Couplings

In this section, I review the theoretical frameworks that have been designed to describe the interactions of two W-bosons and one neutral boson, Z-boson or photon, beyond the interactions prescribed by the Standard Model. They are similar to the ones reviewed for the anomalous interactions of Three Neutral Gauge Bosons in section A.2. The vertices of interest are WWZ and $WW\gamma$ and as before two of the bosons are required to be on-shell.

A.3.1 Effective Lagrangian approach

The most general effective Lagrangian containing all the Lorentz structures from W-boson and photon fields with the fewest number of field derivatives without imposing $U_{em}(1)$ is [205]

$$\begin{aligned}\mathcal{L}_{WWV} = ig_{WWV}\Bigg[&(1+\Delta g_1^V)V^\nu(W^+_{\mu\nu}W^{-\mu} - W^-_{\mu\nu}W^{+\mu}) + (1+\Delta\kappa_V)V^{\mu\nu}W^+_\mu W^-_\nu \\ &+\frac{\lambda_V}{m_W^2}W^{+\lambda}_\mu W^{-\mu}_\nu V^\nu_\lambda + ig_4^V W^+_\mu W^-_\nu(\partial^\mu V^\nu + \partial^\nu V^\mu) \\ -ig_5^V\epsilon^{\mu\nu\rho\sigma}(W^-_\mu\partial_\rho W^+_\nu - W^+_\nu\partial_\rho W^-_\mu)V_\sigma &+ \widetilde{\kappa}_V W^+_\mu W^-_\nu \widetilde{V}^{\mu\nu} + \frac{\widetilde{\lambda}_V}{m_W^2}W^{+\lambda}_\mu W^{-\mu}_{\ \nu}\widetilde{V}^\nu_\lambda\Bigg]\end{aligned} \tag{A.29}$$

where m_W is the mass of the W-boson, V^μ is the Z-boson or photon field and the overall coupling g_{WWV} is $g_{WW\gamma} = -gs_w \equiv -e$ and $g_{WWZ} = -gc_w = -e\cot\theta_W$.

This Lagrangian defines 14 independent dimensionless couplings. The operators associated to Δg_1^V and $\Delta\kappa_V$ are already in the SM Lagrangian (A.5) with $\Delta g_1^V = 0$ and $\Delta\kappa_V = 0$ but none of the other operators are. Therefore all these couplings, called charged aTGCs, are null in the SM. All the operators in (A.29) are dimension-4 operators but those associated with λ_V and $\widetilde{\lambda}_V$ which are dimension-6 operators.

The couplings are sorted out in the table A.3 with the corresponding vertices, the behaviors under the C and P symmetries of their operators and the final states in Two Bosons production for which they are relevant.

<table>
<tr><td>Vertex</td><td colspan="2">WWZ</td><td colspan="2">$WW\gamma$</td></tr>
<tr><td>Two boson production</td><td>WZ</td><td colspan="2">WW</td><td>$W\gamma$</td></tr>
<tr><td>C and P-even</td><td colspan="2">Δg_1^Z, $\Delta\kappa_Z$, λ_Z</td><td colspan="2">Δg_1^γ, $\Delta\kappa_\gamma$, λ_γ</td></tr>
<tr><td>C and/or P-violating</td><td colspan="2">g_4^Z, g_5^Z, $\widetilde{\kappa}_Z$, $\widetilde{\lambda}_Z$</td><td colspan="2">g_4^γ, g_5^γ, $\widetilde{\kappa}_\gamma$, $\widetilde{\lambda}_\gamma$</td></tr>
</table>

Table A.3: Charged aTGCs

If $U(1)_{em}$ is imposed some of the couplings in (A.29) are null but not all. First we saw that the term to Δg_1^γ specifies the charge of the W-boson and so that we have $\Delta g_1^\gamma = 0$. We also saw that the operator associated to $\Delta\kappa_\gamma$ is $U(1)_{em}$ invariant on its own and that therefore $\Delta\kappa_\gamma$ can be different from 0.

Similarly each of the operators associated to $\widetilde{\kappa}_\gamma$, λ_V and $\widetilde{\lambda}_V$ are also $U(1)_{em}$ invariant. Therefore $U(1)_{em}$ does not force them to be 0. On the contrary the terms associated to g_4^γ and g_5^γ are not $U(1)_{em}$ invariant and therefore one has $g_4^\gamma = 0$ and $g_5^\gamma = 0$.

To summarize $U(1)_{em}$ reduces the number of independent parameters from 14 to 11, 5 respecting C and P and 6 violating C and/or P, by imposing

$$\Delta g_1^\gamma = g_4^\gamma = g_5^\gamma = 0 \tag{A.30}$$

A.3.2 Vertex Function approach

The Vertex Function for charged aTGCs is [205]

$$\begin{aligned}\Gamma_V^{\alpha,\beta,\mu}(q,\bar{q},P) = f_1^V(q-\bar{q})^\mu g^{\alpha\beta} - \frac{f_2^V}{m_W^2}(q-\bar{q})^\mu P^\alpha P^\beta + f_3^V(P^\alpha g^{\mu\beta} - P^\beta g^{\mu\alpha}) \\ +if_4^V(P^\alpha g^{\mu\beta} + P^\beta g^{\mu\alpha}) + if_5^V\epsilon^{\mu\alpha\beta\rho}(q-\bar{q})_\rho - f_6^V\epsilon^{\mu\alpha\beta\rho}P_\rho - \frac{f_7^V}{m_W^2}(q-\bar{q})^\mu\epsilon^{\alpha\beta\rho\sigma}P_\rho(q-\bar{q})_\sigma\end{aligned} \tag{A.31}$$

where q and $\bar{q}$ are the W$^+$ and W$^-$ bosons momenta and V is the photon or Z-boson field of momentum P. Contrary to the (A.17) and (A.18) cases, the boson V is not necessarily the off-shell boson.

The contributions of the operators of (A.29) to (A.31) are

$$f_1^V = 1 + \Delta g_1^V + \frac{s}{2m_W^2}\lambda_V \quad , \quad f_2^V = \lambda_V \quad , \quad f_3^V = 2 + \Delta g_1^V + \Delta\kappa_V + \lambda_V \quad , \quad f_4^V = g_4^V$$

$$f_5^V = g_5^V \quad , \quad f_6^V = \widetilde{\kappa}_V - \widetilde{\lambda}_V \quad , \quad f_7^V = -\frac{1}{2}\widetilde{\lambda}_V \tag{A.32}$$

The unitary issue arises with Vertex Function (A.31) as it does with (A.17) and (A.18) . Again the form factors are parametrized with the ansatz $C(s) = C_0 \times (1+s/\Lambda_{FF}^2)^{-n}$ where it is conventional to take $n = 2$ [193, 206].

A.3.3 Effective Field Theory approach for Charged aTGCs

Hereafter, I follow the reference [167]. Requiring B and L conservations, the first dimension of operators relevant for aTGCs is the dimension 6.

The operator analysis of [167] found five operators, named O_{WWW}, O_W, O_B, $O_{\widetilde{W}WW}$ and $O_{\widetilde{W}}$. The first three respect both C and P while the last two violate C and/or P. They are

$$O_{WWW} = Tr\Big[\not{W}_{\mu\nu}\not{W}^{\nu\rho}\not{W}^{\mu}_{\rho}\Big] \quad , \quad O_W = (D_\mu H)^\dagger \not{W}^{\mu\nu}(D_\nu H) \quad , \quad O_B = (D_\mu H)^\dagger \not{B}^{\mu\nu}(D_\nu H)$$

$$O_{\widetilde{W}WW} = Tr\Big[\widetilde{\not{W}}_{\mu\nu}\not{W}^{\nu\rho}\not{W}^{\mu}_{\rho}\Big] \quad , \quad O_{\widetilde{W}} = (D_\mu H)^\dagger \widetilde{\not{W}}^{\mu\nu}(D_\nu H) \tag{A.33}$$

where $\not{W}_{\mu\nu} = \frac{i}{2}g\sigma^i W^i_{\mu\nu}$ and $\not{B}_{\mu\nu} = \frac{i}{2}g' B_{\mu\nu}$.

The C and P-even operator O_{WWW} contains no Higgs field. Hence its accompanying constant C_{WWW} determines both λ_γ and λ_Z, since their associated C and P-even operators are already of dimension-6 in the after-SSB fields. It is found

$$\lambda_\gamma = \lambda_Z \tag{A.34}$$

$$\lambda_\gamma = \frac{3g^2 m_W^2}{2}\frac{C_{WWW}}{\Lambda^2} \tag{A.35}$$

In the same way, since the P violating operator $O_{\widetilde{W}WW}$ contains no Higgs field, its accompanying constant $C_{\widetilde{W}WW}$ determines $\widetilde{\lambda}_\gamma$ and $\widetilde{\lambda}_Z$. It is found

$$\widetilde{\lambda}_\gamma = \widetilde{\lambda}_Z \tag{A.36}$$

$$\widetilde{\lambda}_\gamma = \frac{3g^2 m_W^2}{2}\frac{C_{\widetilde{W}WW}}{\Lambda^2} \tag{A.37}$$

Then the two constants C_W and C_B, accompanying the C and P-even operators O_W, O_B should determine the values of the four remaining C and P-even couplings (cf table A.3). It is found

$$\Delta g_1^\gamma = 0 \tag{A.38}$$

$$\Delta g_1^Z = \frac{m_Z^2}{2}\frac{C_W}{\Lambda^2} \quad , \quad \Delta\kappa_\gamma = \frac{m_W^2}{2}\Big(\frac{C_W}{\Lambda^2} + \frac{C_B}{\Lambda^2}\Big) \quad , \quad \Delta\kappa_Z = \frac{m_W^2}{2}\Big(\frac{C_W}{\Lambda^2} - \tan^2\theta_W\frac{C_B}{\Lambda^2}\Big) \tag{A.39}$$

The three last relations impose a relation between the anomalous couplings only

$$\Delta g_1^Z = \Delta\kappa_Z + \tan^2\theta_W \Delta\kappa_\gamma \tag{A.40}$$

Finally the constant $C_{\widetilde{W}}$ accompanying $O_{\widetilde{W}}$ should determine the six remaining C or P-violating couplings. It is found

$$g_4^\gamma = g_5^\gamma = g_4^Z = g_5^Z = 0 \tag{A.41}$$

$$\widetilde{\kappa}_\gamma = \frac{m_W^2}{2}\frac{C_{\widetilde{W}}}{\Lambda^2} \quad , \quad \widetilde{\kappa}_Z = -\tan^2\theta_W \frac{m_W^2}{2}\frac{C_{\widetilde{W}}}{\Lambda^2} \tag{A.42}$$

The two last relations impose a relation between the anomalous couplings only

$$\widetilde{\kappa}_Z + \tan^2\theta_W \widetilde{\kappa}_\gamma = 0 \tag{A.43}$$

The identities (A.34), (A.36), (A.40) and (A.43) are consequences of retaining only the contributions of the operators up to dimension-6, and as such they are not exact. Actually, they are shown to be modified by corrections from dimension-8 operators [154]. However since these corrections are suppressed by a factor $1/\Lambda$ with respect to the dimension-6 contributions, they should be approximately true in the low-energy regime [14].

Vertex	WWZ		$WW\gamma$
Two boson production	WZ	WW	$W\gamma$
C and P-even	Δg_1^Z		
	$\Delta\kappa_\gamma$, λ_γ		
C and/or P-violating	$\widetilde{\kappa}_\gamma$, $\widetilde{\lambda}_\gamma$		

Table A.4: EFT description of Charged aTGCs

So the EFT analysis concludes that at the order $(\sqrt{s}/\Lambda)^2$ the Charged aTGCs WWV can be described by just 5 independent constants, C_{WWW}, C_W, C_B, $C_{\widetilde{W}WW}$ and $C_{\widetilde{W}}$, corresponding to two C and/or P violating and three C and P-even interactions. At this order, these 5 constants can be as well taken to be Δg_1^Z, $\Delta\kappa_\gamma$, λ_γ, $\widetilde{\kappa}_\gamma$ and $\widetilde{\lambda}_\gamma$ [15]. With this choice, the dependence to the constants of the vertices and Two Bosons production reactions can be represented as on the table A.4. One sees that all the vertices and all the Two Bosons production reactions depend on 4 common parameters, $\Delta\kappa_\gamma$, λ_γ, $\widetilde{\kappa}_\gamma$ and $\widetilde{\lambda}_\gamma$, while the WWZ vertex and the WZ and WW productions depend on an additional parameter, Δg_1^Z.

---

[14] The relations (A.34) and (A.40) are defining the so-called "LEP scenario", a parametrization which is largely used to derive experimental limits on charged aTGCs. It has happened that the additional assumption $C_W = C_B$ was done. This adds the relation $\Delta\kappa_\gamma = 2\cos^2\theta_W \Delta g_1^Z$ to (A.34) and (A.40)

[15] One can argue that choosing these 5 couplings, one can take $\Delta\kappa_Z$ instead of $\Delta\kappa_\gamma$. However one notes from table A.3 that the $W\gamma$ production reaction does depend only on 4 parameters while the WW and WZ production reactions do depend on 5 parameters. So it seems appropriate to include the 4 parameters that the $W\gamma$ production constrains in the five parameters that we retain. In this view, the fifth variable could be indifferently Δg_1^Z or $\Delta\kappa_Z$. To retain Δg_1^Z and the 4 "$W\gamma$" parameters, as done here, is the choice that seems to have been made for LEP and TEVATRON combined measurements.

A.4 Measurements of Anomalous Triple Gauge Couplings

In this section I review the anomalous Triple Gauge Couplings measurements which were done at LEP, at TEVATRON and at LHC.

A.4.1 Measurements of Anomalous Triple Gauge Couplings at LEP

The LEP collaborations summarized and combined their aTGC parameters measurements in [175].

The charged aTGC parameters were measured at LEP2 in the two W-bosons production reaction, $e^+e^- \to W^-W^+$, to which TGCs contribute in the s-channel as shown in figure A.3(a). The decay of the two W-bosons final state was studied in the fully leptonic or hadronic modes, as well as in the cleanest semi-leptonic mode.

With a lower sensitivity, charged aTGC parameters were also measured in the single W-boson and single γ production reactions, $e^+e^- \to W^\mp e^\pm \nu(\bar{\nu})$ and $e^+e^- \to \gamma\nu\bar{\nu}$, to which TGCs contribute by Vector Boson Fusion as shown in figures A.3(b) and A.3(c).

Both total production cross-section and angular distributions were used to extract aTGC parameters limits. The combined fit used the “LEP scenario” defined by the equations (A.34) and (A.40) (see footnote 14) and limited itself to the aTGC parameters respecting C and P. The table A.5 gives the 95% Confidence Level Intervals for each aTGC parameter with the other parameters fixed at 0.

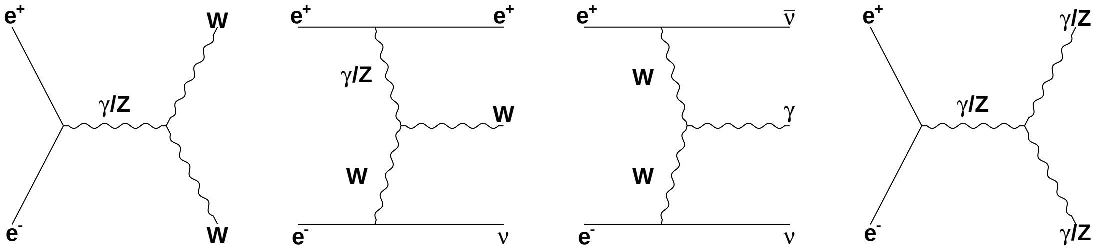

(a) (b) (c) (d)

Figure A.3: TGC diagrams at LEP2

Recently, the LEP2 measurements combination was done at new in [207, 208]. The results of this new analysis are drastically different from those of the former combination. This new combination was done in a consistent EFT perspective in which not only the “LEP scenario” equations were used but also the cross-sections dependence on the aTGC parameters was restricted to the linear terms.

Indeed since the operator expansion is up to the dimension-6 operators, the quadratic terms in aTGC parameters are of the same order than the contributions from the neglected dimension-8 operators (cf end of section A.5 for more details). This consistency condition changes drastically the fit results, with λ_γ and Δg_1^Z errors increased by an order of magnitude. This is due to a poorly constrained direction which appears in the parameters space along the $\lambda_\gamma + \Delta g_1^Z \sim 0$ line.

However it was shown in [209] that the Higgs Data bring constraints on aTGC parameters with a very different correlation pattern, so that the errors on aTGC parameters are drastically reduced when the LEP2 and Higgs Data are combined.

The neutral aTGC were studied in the Two Vector Bosons production processes, $e^+e^- \to ZZ$ and $e^+e^- \to Z\gamma$, to which the TGCs contributes in the s-channel as shown in figure A.3(d). As for the charged aTGC parameters both total production cross-section and angular distributions were used to extract limits on neutral aTGC parameters. The tables A.7, A.8 and A.6 give the 95% Confidence Level Intervals from the combined fit for each aTGC parameter with the other parameters fixed at 0.

A.4.2 Measurements of Anomalous Triple Gauge Couplings at TEVATRON

A review of the measurements of the aTGC parameters performed at TEVATRON can be found in [210].

The charged aTGC parameters were measured in the Two Vector Bosons production processes, $p\bar{p} \to W^-W^+X$, $p\bar{p} \to WZX$ and $p\bar{p} \to W\gamma X$ to which TGCs contribute in the s-channel as shown in figures A.4(a), A.4(b) and A.4(c).

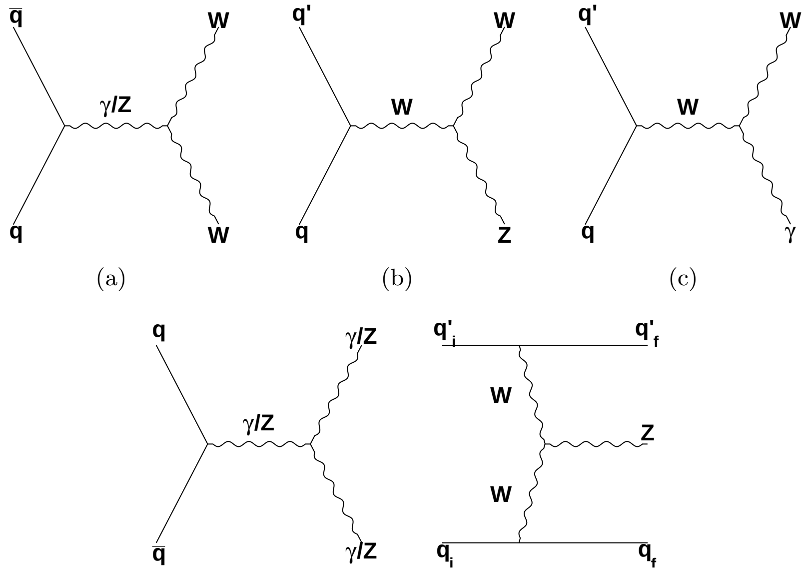

(a) (b) (c)

(d) (e)

Figure A.4: TGC diagrams at TEVATRON and LHC

These reactions have been studied in the cases where all the final state W-bosons decay leptonically. Then the observables sensitive to aTGC parameters are the spectrum of the transverse momentum of the photon in $W\gamma$ production, of the Z-boson in WZ production, and the spectra of both the leading and trailing leptons in WW production.

The WW and WZ production reactions can also be studied by requiring the leptonic decay of one W-boson while the other vector boson is required to decay hadronically. Despite a huge background, the transverse momentum spectrum of the jets system of the $WW + WZ \to l\nu jj$ events so selected turns out to be the observable the most sensitive to the aTGC parameters.

Combining all its measurements of these final states, the D0 collaboration delivered the stronger limits on the aTGC parameters [181]. Using a form factor with $\Lambda = 2$ TeV and the "LEP scenario" equations, the combined fit gave the 95% C.L. intervals reported in the table A.5, for each aTGC parameter when the other parameters are fixed at 0.

The neutral aTGCs were studied in $Z\gamma$ and ZZ production reactions to which TGCs contribute in the s-channel as shown in figure A.4(d). The table A.8 gives the results of the fits performed by D0 and CDF. The 95% C.L. intervals are given for each aTGC parameter with the others parameters fixed at 0. Both analyses used a form factor with $\Lambda = 1.5$ TeV [178, 179].

Apparently, only one TEVATRON ZZ analysis was published. The 95% C.L. intervals on the f_i^V parameters of this D0 analysis are given in table A.6 for each aTGC parameter keeping the other parameters at 0. A form factor with $\Lambda = 1.2$ TeV was used [176]. Sometimes, as in [177] for instance, some limits on the f_i^V parameters (form factor with $\Lambda = 1.2$ TeV) are reported from a CDF analysis of $ZZ \to l^+l^-jj$ which seems however to not have been published. For completeness, these limits are reported in table A.6.

A.4.3 Measurements of Anomalous Triple Gauge Couplings at LHC

Limits on anomalous Triple Gauge Couplings have been obtained using the data collected during the two first periods of data taking at LHC, at energy in the center of mass of the colliding protons of $\sqrt{s} = 7$ TeV and $\sqrt{s} = 8$ TeV. The integrated Luminosities collected per experiment during these periods have been respectively about $5fb^{-1}$ and $20fb^{-1}$ for each experiment, ATLAS and CMS. With the exception of the study of Vector Boson Fusion process, the final states analyzed at LHC have been similar to those analyzed at TEVATRON. The ATLAS and CMS collaborations provided systematically aTGC limits with no form factor. These limits are those that are reported in the aTGC limits tables for LHC. They were derived by fitting one parameter fixing all other parameters at 0.

The charged aTGC parameters were studied in $pp \to W^-W^+X$ (see figure A.4(a)) with the W bosons decaying in leptons. ATLAS published an analysis of its 7 TeV data sample and reported limits for the C and P-even anomalous couplings from a study of the distribution of the transverse momentum of the leading (highest p_T) lepton from W-bosons decays [130]. CMS extracted limits studying the distribution of the mass of the 2 decay leptons in its 8 TeV data sample [180]. Quite remarkably CMS gave limits in terms of EFT parameters only [16].

The $WW + WZ \to l\nu jj$ process was also studied (see figures A.4(a) and A.4(b)) using the 7 TeV data, by CMS in [211] and ATLAS in [212]. Limits on aTGC were extracted from the distribution of the transverse momentum of the di-jets system. The "LEP" scenario was used to derive the aTGC limits reported in the table A.5. The CMS collaboration specifically did not measure the Δg_1^Z coupling.

The charged aTGC parameters of the WWZ vertex were specifically measured in the WZ production reaction (see figure A.4(b)) by ATLAS in [86] using the 7 TeV data. Only leptonic decays of the W and Z bosons were studied. The aTGCs limits were extracted from the distribution of the transverse momentum of the Z and were produced only for anomalous couplings respecting both C and P. The limits are reported in the table A.5.

The WWZ vertex was also specifically accessed studying the process $pp \to X + Z2j$ by ATLAS in [213] using the 7 TeV data. This vertex contributes by Vector Boson Fusion as shown on figure A.4(e). The process was observed for the first time by CMS. The aTGC limits reported in the table A.5 were obtained from the number of events with a mass of the di-jets system above 1 TeV. The sensitivity to the parameter $\Delta\kappa_Z$ did not allow to measure it.

The vertex $WW\gamma$ was specifically studied in the $W\gamma$ production reaction (see figure A.4(c)) using the 7 TeV data, by ATLAS in [92] and by CMS in [168]. In both analyses, the W was required to decay leptonically. To extract aTGC limits, the ATLAS analysis used the number of events with a γ of transverse momentum p_γ^T above 100GeV . Instead, the CMS analysis used the distribution of p_γ^T. The limits were produced assuming $U(1)_{em}$ and only for the parameters which respect both C and P. They are reported in the table A.5.

The neutral aTGC parameters f_i^V were studied in ZZ production (see table A.1 and figure A.4(d)). The selected final states were $ZZ \to (l^+l^-)(l'^+l'^-)$ or $ZZ \to (l^+l^-)(\nu\bar{\nu})$. ATLAS extracted its limits from the distribution of the transverse momentum of the leading Z in $ZZ \to (l^+l^-)(l'^+l'^-)$ and of the l^+l^- system in $ZZ \to (l^+l^-)(\nu\bar{\nu})$. CMS did the same for this last final state but used the mass of the 4 leptons system for the former. ATLAS has published a study of the two final states for the 7 TeV data [156]. In [174] CMS has published an analysis of $ZZ \to (l^+l^-)(\nu\bar{\nu})$ using the 7 TeV and 8 TeV data. These limits were combined with the aTGC limits extracted from the CMS studies of $ZZ \to (l^+l^-)(l'^+l'^-)$ with 7 TeV data [214] and 8 TeV data [215]. This produces the most stringent limits on the f_i^V parameters which are reported in the table A.6. Temporary results from the ATLAS

---

[16] The corresponding CMS limits reported in A.5 are taken from CMS site page https://twiki.cern.ch/twiki/bin/view/CMSPublic/PhysicsResultsSMPaTGC

8 TeV $ZZ \to (l^+l^-)(l'^+l'^-)$ data were obtained in [85]. They are also shown in the table A.6.

The neutral aTGC parameters h_i^V were studied in $Z\gamma$ production (see table A.1 and figure A.4(d)). The aTGC limits were extracted by ATLAS from the number of events with a photon of p_γ^T above 100 GeV , while CMS used the distribution of p_γ^T. The analyses of $Z\gamma \to (l^+l^-)\gamma$ and $Z\gamma \to (\nu\bar{\nu})\gamma$ for the 7 TeV data were published in [92] for ATLAS and in [169] for CMS. In addition CMS published 8 TeV data analyses of $Z\gamma \to (l^+l^-)\gamma$ in [170] and of $Z\gamma \to (\nu\bar{\nu})\gamma$ in [171]. All these limits are reported in the table A.8.

<table>
<tr><th></th><th>Δg_1^Z</th><th>$\Delta\kappa_Z$</th><th>$\Delta\kappa_\gamma$</th><th>λ_Z</th><th>λ_γ</th><th></th></tr>
<tr><td>LEP combined [175]</td><td>$[-0.054; 0.021]$</td><td></td><td>$[-0.099; 0.066]$</td><td colspan="2">$[-0.059; 0.017]$</td><td>LEP Scenario</td></tr>
<tr><td>D0 Combined [181]</td><td>$[-0.034; 0.084]$</td><td></td><td>$[-0.158; 0.255]$</td><td colspan="2">$[-0.036; 0.044]$</td><td>LEP Scenario ; $\Lambda_{FF} = 2$ TeV</td></tr>
<tr><td>ATLAS 7TeV [130]</td><td>$[-0.039; 0.052]$</td><td>$[-0.043; 0.043]$</td><td></td><td colspan="2">$[-0.062; 0.059]$</td><td>WW ; LEP Scenario</td></tr>
<tr><td>CMS 8TeV [180]</td><td>$[-0.047; 0.022]$</td><td></td><td>$[-0.130; 0.095]$</td><td colspan="2">$[-0.024; 0.024]$</td><td>WW ; LEP Scenario</td></tr>
<tr><td>CMS 7TeV [211]</td><td><i>Not measured</i></td><td></td><td>$[-0.11; 0.14]$</td><td colspan="2">$[-0.038; 0.030]$</td><td>$WW + WZ \to (l\nu)(jj)$; LEP Scenario</td></tr>
<tr><td>ATLAS 7TeV [212]</td><td>$[-0.055; 0.071]$</td><td></td><td>$[-0.21; 0.22]$</td><td colspan="2">$[-0.039; 0.040]$</td><td>$WW + WZ \to (l\nu)(jj)$; LEP Scenario</td></tr>
<tr><td>ATLAS 7TeV [86]</td><td>$[-0.057; 0.093]$</td><td>$[-0.37; 0.57]$</td><td></td><td>$[-0.046; 0.047]$</td><td></td><td>WZ</td></tr>
<tr><td>ATLAS 8TeV [213]</td><td>$[-0.50; 0.26]$</td><td><i>Not measured</i></td><td></td><td>$[-0.15; 0.13]$</td><td></td><td>$pp \to X + Z2jVBF$</td></tr>
<tr><td>ATLAS 7TeV [92]</td><td></td><td></td><td>$[-0.41; 0.46]$</td><td></td><td>$[-0.065; 0.061]$</td><td>$W\gamma$</td></tr>
<tr><td>CMS 7TeV [168]</td><td></td><td></td><td>$[-0.38; 0.29]$</td><td></td><td>$[-0.050; 0.037]$</td><td>$W\gamma$</td></tr>
</table>

Table A.5: 95% C.L. Intervals for charged aTGCs from LEP, TEVATRON and LHC

	f_4^γ	f_4^Z	f_5^γ	f_5^Z	
LEP combined [175]	$[-0.17; 0.19]$	$[-0.28; 0.32]$	$[-0.35; 0.32]$	$[-0.34; 0.35]$	
D0 [176]	$[-0.26; 0.26]$	$[-0.28; 0.28]$	$[-0.30; 0.28]$	$[-0.31; 0.29]$	$ZZ \to (l^+l^-)(l'^+l'^-)$; $\Lambda_{FF} = 1.2$ TeV
CDF [177]	$[-0.10; 0.10]$	$[-0.12; 0.12]$	$[-0.11; 0.11]$	$[-0.13; 0.12]$	$ZZ \to (l^+l^-)(jj)$; $\Lambda_{FF} = 1.2$ TeV
ATLAS 7TeV [156]	$[-1.5; 1.5] \times 10^{-2}$	$[-1.3; 1.3] \times 10^{-2}$	$[-1.6; 1.5] \times 10^{-2}$	$[-1.3; 1.3] \times 10^{-2}$	$ZZ \to (l^+l^-)(l'^+l'^-)$, $ZZ \to (l^+l^-)(\nu\bar{\nu})$
ATLAS 8TeV [85]	$[-4.6; 4.6] \times 10^{-3}$	$[-4.1; 4.0] \times 10^{-3}$	$[-4.6; 4.7] \times 10^{-3}$	$[-4.0; 4.0] \times 10^{-3}$	$ZZ \to (l^+l^-)(l'^+l'^-)$
CMS 7+8TeV [174]	$[-3.0; 2.6] \times 10^{-3}$	$[-2.1; 2.6] \times 10^{-3}$	$[-2.6; 2.7] \times 10^{-3}$	$[-2.2; 2.3] \times 10^{-3}$	$ZZ \to (l^+l^-)(l'^+l'^-)$, $ZZ \to (l^+l^-)(\nu\bar{\nu})$

Table A.6: 95% C.L. Intervals for neutral aTGCs f_i^V from LEP, TEVATRON and LHC (CDF [177] is an unpublished result; ATLAS 8TeV [85] is a preliminary result))

Parameters	h_1^γ	h_1^Z	h_2^γ	h_2^Z
LEP combined [175]	$[-0.05; 0.05]$	$[-0.12; 0.11]$	$[-0.04; 0.02]$	$[-0.07; 0.07]$

Table A.7: 95% C.L. Interval for neutral aTGCs $h_{1,2}^V$ from LEP combination [175]

	h_3^γ	h_3^Z	h_4^γ	h_4^Z	
LEP combined [175]	$[-0.05; 0.00]$	$[-0.19; 0.06]$	$[0.01; 0.05]$	$[-0.04; 0.13]$	
D0 [178]	$[-0.027; 0.027]$	$[-0.026; 0.026]$	$[-0.0014; 0.0014]$	$[-0.0013; 0.0013]$	$Z\gamma \to (l^+l^-)\gamma$; $\Lambda_{FF} = 1.5$ TeV
CDF [179]	$[-0.022; 0.022]$	$[-0.022; 0.022]$	$[-0.0009; 0.0009]$	$[-0.0009; 0.0009]$	$Z\gamma \to (l^+l^-)\gamma$, $Z\gamma \to (\nu\bar{\nu})\gamma$; $\Lambda_{FF} = 1.5$ TeV
ATLAS 7TeV [92]	$[-1.5; 1.6] \times 10^{-2}$	$[-1.3; 1.4] \times 10^{-2}$	$[-0.94; 0.92] \times 10^{-4}$	$[-0.87; 0.87] \times 10^{-4}$	$Z\gamma \to (l^+l^-)\gamma$, $Z\gamma \to (\nu\bar{\nu})\gamma$
CMS 7TeV [169]	$[-2.9; 2.9] \times 10^{-3}$	$[-2.7; 2.7] \times 10^{-3}$	$[-1.5; 1.5] \times 10^{-5}$	$[-1.3; 1.3] \times 10^{-5}$	$Z\gamma \to (l^+l^-)\gamma$, $Z\gamma \to (\nu\bar{\nu})\gamma$
CMS 8TeV [170]	$[-4.6; 4.6] \times 10^{-3}$	$[-3.8; 3.7] \times 10^{-3}$	$[-3.6; 3.5] \times 10^{-5}$	$[-3.1; 3.0] \times 10^{-5}$	$Z\gamma \to (l^+l^-)\gamma$
CMS 8TeV [171]	$[-1.12; 0.95] \times 10^{-3}$	$[-1.50; 1.64] \times 10^{-3}$	$[-3.80; 4.35] \times 10^{-6}$	$[-3.96; 4.59] \times 10^{-6}$	$Z\gamma \to (\nu\bar{\nu})\gamma$

Table A.8: 95% C.L. Intervals for neutral aTGCs $h_{3,4}^V$ from LEP, TEVATRON and LHC

A.5 Global Effective Field Theory analyses

As we have seen in the section A.3, there are five dimension-6 EFT operators relevant for the Charged aTGCs. There are listed in (A.33). Three of them contain Higgs doublet field. In the appendix B, it is shown for 2 of these operators how they generate Triple and Quartic Gauge couplings. From the computations it is clear how they do generate also interactions between the Higgs boson and the W, Z and γ bosons. such as hVV' and $hhVV'$ vertices (cf appendix of [216] for the explicit couplings resulting from O_B and O_W).

Therefore the aTGCs are just one of the many low-energy signs of the Physics beyond the SM that EFT parametrizes. The EFT operators potentially modify and create couplings between all SM bosons and fermions, so that a Global analysis of all Electroweak Precision Data (EWPD), including Charged aTGC limits, as well as Higgs Data accumulated by the LHC, Fermilab, LEP and DIS experiments brings strong constraints on the coefficients of these operators. This is currently a very active field. The topic is heavily technical although conceptually quite clear. In the following, only few points from these analyses are briefly reviewed [200].

An early model for these Global analyses is the very comprehensive one performed in reference [217]. It combined all the EWPD collected up to LEP2 (see [208, 218] for more recent Global analyses of EWPD). With the discovery of the Higgs boson at the LHC, there has been an explosive multiplication of Global analyses of this, which adding the Higgs Data, allow to cover all the scope of the low-energy effects of EFT expanded up to dimension-6 [219–224].

These analyses show that the limits on aTGC allow to constrain very significantly effects affecting also the decays $h \to Vf\bar{f}$ and $h \to Z\gamma$ [200, 221]. The importance of the aTGC limits has been illustrated in an particularly illuminating way in the reference [225], where limits on Δg_1^Z and $\Delta\kappa_\gamma$ have been derived from Higgs Data only. These limits turn out to be of the same order, but, importantly, with a different correlation pattern, than those obtained directly at LHC, Fermilab and LEP (cf [209] for a similar but more recent analysis) [17].

The Global analyses work in the framework of the EFT involving all dimension-6 operators that one can form using all the SM fields before SSB, which are invariant under the full $SU(3)_C \times SU(2)_L \times U(1)_Y$ Gauge symmetry and which conserve B and L. These operators are vastly more numerous than the five listed in (A.33). A somewhat troubling issue is that more often than not, different Global analyses clearly use very different operators. Beside different approximations and simplifications which switch off some operators and the use of different names for identical operators, different Global analyses are rooted in reference set of operators, called Operators Bases, which can be authentically distinct. And this is perfectly right.

Indeed an operator can be shown to be equivalent to a combination of other operators up to some manipulations among which fields identities obtained from the equations of motion derived from the SM Lagrangian. In such a case it has been shown that the physical effects of this operator and of the operators combination to which in this sense it is equivalent are identical. This operator is therefore redundant with respect to the combined ones and can be put aside if one retains the others. An Operator Basis is a minimal set of non-redundant operators from which one can form combination equivalent to any operator.

There is an huge number of admissible Operator Bases. Three of them can be considered as standard since they have been repeatably used in the literature [18]: the Warsaw Basis [196, 228], the SILH Basis [229] and the HISZ Basis [154]. They differ mainly in their bosonic operators. The reference [200] gives a comparative table of the operators of these Bases.

---

[17] One finds in [208] some charges against the LHC aTGC limits published so far. Beside the blame for not publishing the correlations between the aTGCs parameters, it is argued that the data used to extract limits are in a kinematic regime where the EFT expansion fails. A similar statement is made in [226]. This very problematically point seems however to be not corroborated by other analyses [219].

[18] The nomenclature for these standard Bases used here is the one from reference [227]

Since the physical effects are identical, the choice of a particular Operator Basis is mainly an affair of convenience. Still there are important differences between and important consequences result from using one or another of these Bases.

There are tricky technical differences. For instance the Charged aTGCs relation (A.40) is a consequence of cutting the EFT expansion at dimension-6. This relation is valid in any Operator Basis and it can be derived in a quite direct way both in the SILH Basis [221] and in the HISZ Basis [222]. In the Warsaw Basis, the relation is retrieved through a somewhat convoluted path: only one operator contributes directly to $\Delta\kappa_Z$ and $\Delta\kappa_\gamma$ as if at first Δg_1^Z was null (cf equations (35) and (36) in [217]), but these aTGCs do get also indirect contributions from operators modifying the Fermi constant as for instance a 4-fermions operator modifying the muon decay rate (cf equations 20 and 21 in [217]). It is only when all contributions are gathered that the relation (A.40) is eventually retrieved.

A criteria has been advanced to weight the virtues of the different Operator Bases, which is motivated by considerations on the UV completion of the EFT, i.e on the underlying model of the Physics beyond the SM. Once such a model is assumed, some operators can be shown to appear at the tree level or at the loop level of the fundamental theory [230, 231]. In this perspective, an Operator Basis is to be preferred if its operators can be classified in one or the other of these categories since the relative strengths of the operators coefficients can be guessed [19]. The argument is at the disadvantage of the HISZ Basis. However the point seems controversial, being put forward by some [229, 232] but dismissed by others [200, 223, 233].

A most relevant argument is that a particular Operator Basis can obscure the actual constraints from the Data. For instance there can be "blind" directions in Operator space, i.e combinations of operators, which turn out to be very weakly constrained. An Operator Basis is to be preferred if such a direction corresponds to a single or at least few Basis operators. The Warsaw Basis seems the main target of this line of argumentation. However the issue arises only in analyses of the EWPD if the LEP2 $e^+e^- \to W^-W^+$ measurements are excluded. This exclusion has been claimed to be artificial in the recent reference [218] which indeed performs a very comprehensive EWPD analysis in the Warsaw Basis.

An argument somewhat related to the former is to prefer an Operator Basis which somehow links directly to the data. This line of argumentation had lead to the recent proposal of another Basis in [227], the "Higgs" Basis, which evolved from [232, 234, 235]. The idea is that an EFT operator leads to various interactions terms in the "physical" fields W, Z, γ and h, multiplied by couplings which are functions of the operator coefficient. In general, these couplings can depend on more than one operator coefficients. Example of this are the equations (A.35), (A.37), (A.39) and (A.42) which express the "physical" couplings appearing in the physical fields Lagrangian (A.29) as functions of the coefficients of the EFT operators listed in (A.33).

Since these "physical" couplings are more numerous than the operators coefficients, there are necessarily relations that one can form between the "physical" couplings exclusively. Example of such "necessary" relations are the relations (A.34), (A.36), (A.40) and (A.43). Crucially these relations are valid in any Operator Basis and results only from having neglected the operators of dimension greater than 6 in the expansion of the EFT Lagrangian.

The astute idea of the "Higgs" Basis is to focus on the "physical" couplings, i.e on the interactions terms in the physical fields, and to promote some of them, thusly called "independent couplings", as the parameters of interest. The other couplings, the "dependent couplings", are obtained from the independent couplings through the "necessary" relations. Actually these relations do render

---

[19] On a similar basis, one finds sometimes the statement that λ_Z in (A.35) can be neglected since the operator O_{WWW} is absent at tree level in most of the models of Physics beyond the Standard Model. However this looks to be an educated guess from Models builders since apparently no fundamental reason is put forward that would prevent such a model to exist.

Lagrangians built on after-SSB fields such as (A.29) invariant under the $SU(3)_C \times SU(2)_L \times U(1)_Y$ symmetry.

Clearly the independent couplings can be picked up arbitrary but this arbitrariness allows to do choices which make transparent the constraints brought by some Data sets (the actual proposed choice is very much Higgs Data oriented). Although secondarily, the independent couplings choice defines an Operator Basis. The authors of the proposal chose to express the Higgs Basis operators in terms of combination of operators of the Standard Bases above. In addition to the relations between the Bases, the reference [227] gives all the dependence relations. This allows for instance to see very directly the relations between the aTGCs parameters and the couplings driving the $h\gamma\gamma$, $hZ\gamma$ and hZZ vertices. By now an analysis program using the Higgs Basis is vigorously pursued by its promoters [202, 209, 220, 236]. It remains to be seen if this Basis is indeed the most appropriate way to tackle the Global EFT analyses or if it will be just yet another Basis pilling up with the others. In any instance, there is in this field an effort to ease the multiple Bases issue for example thanks to the automatic translation tool proposed recently in [237].

Most the EFT analyses have been performed by theorists groups using published results of Experimental collaborations (by now, there are just few ATLAS and CMS EFT analyses [180, 212, 238]). There are some points of concern which touch the experimental analyses proper.

The first point is that a proper EFT analysis should exclude quartic dependence on anomalous couplings of cross-sections but in case of SM forbidden effects.

For instance, in equation (A.15), the interferences of the anomalous amplitudes with the SM amplitude give terms linear in the anomalous couplings, while the squares of the anomalous amplitudes and the interferences of the anomalous amplitudes between themselves, give the bilinear terms. The linear terms are of the order $1/\Lambda^2$ in an EFT perspective. However, the quartic terms, which are perfectly right in the Effective Lagrangian and the Vertex function approaches, are of the order $1/\Lambda^4$ in the EFT perspective. So they are of the order of the interference of SM with EFT dimension-8 operators which have been neglected. Therefore the quartic terms should be excluded in a EFT dimension-6 analysis but if the SM amplitude is null.

This is not the experimentalist habit for aTGCs limits since most if not all limits are extracted with these quartic terms included. On the other hand, one finds sometimes the statements that the impacts on anomalous coupling limits of these quartic terms are nevertheless quantifying the sensitivity of the data to dimension-8 operator contributions. So it seems that it would be appropriate that the experiments do publish limits both with and without these terms.

An other point does concern a different aspect of the validity of the EFT expansion, namely the unitarity violation issue. It is very clear that form factors are bad from the point of view of EFT. But the form factor prescription has a least the advantage to be a fix simple and easy to implement. Beyond the confusing fact that, as we saw, there seems to be divergent opinions on a violation of the unitarity in the present LHC limits (see footnote 17), it is not anyway really clear what should be the proper way to deal with the issue in the context of an EFT analysis of raw Data at the LHC which involve a large range of actual energies in the center of mass, $\sqrt{\hat{s}}$, of the hard interactions. One finds in [216] an extensive analysis of the unitarity problem in the HISZ Basis. It gives the upper limits of the product $|\frac{C_i}{\Lambda^2}\hat{s}|$ beyond which unitarity is violated. However $\hat{s}$ is not always experimentally accessible. In the somewhat different context of an anomalous Quartic Gauge Bosons Couplings EFT analysis, CMS published limits obtained with no unitarity prescription at all, along the values of the couplings which violate unitarity at the clearly too high value of $\sqrt{\hat{s}} = 8TeV$ [239]. This is a very clean but crude procedure. One can hope that there are more sophisticated treatments of the issue, possibly by using more conveniently defined experimental observables which for the time being are still to be designed.

Appendix B

Linear-EFT Dimension-6 Operators

Hereafter are presented the expansions in the after-SSB fields, the W, Z and γ fields, of the EFT operators O_B and O_W defined in section A.3 by (A.33).

B.1 Definitions

One defines

$$W_\mu^\pm = (W_\mu^1 \mp W_\mu^2)/\sqrt{2}\ ,\ Z_\mu = c_w W_\mu^3 - s_w B_\mu,\ \text{and}\ A_\mu = s_w W_\mu^3 + c_w B_\mu,$$

$$\tan\theta_W = g'/g\ ,\ c_w = \cos\theta_W\ ,\ s_w = \sin\theta_W$$

$$\mathcal{D}_\mu = \partial_\mu + ig(s_w A_\mu + c_w Z_\mu),$$

v the vacuum expectation value of Higgs doublet and h the Higgs Boson field

$$m_W = \frac{1}{2}vg \text{ and } m_Z = \frac{1}{2}v\sqrt{g^2 + g'^2}$$

One has

$$\not{W}_{\mu\nu} = \frac{i}{2}g\sigma^i W_{\mu\nu}^i = \frac{i}{2}g\begin{pmatrix} W_{\mu\nu}^3 & W_{\mu\nu}^1 - iW_{\mu\nu}^2 \\ W_{\mu\nu}^1 + iW_{\mu\nu}^2 & -W_{\mu\nu}^3 \end{pmatrix}$$

$$= \frac{i}{2}g\begin{pmatrix} s_w A_{\mu\nu} + c_w Z_{\mu\nu} + ig(W_\mu^+ W_\nu^- - W_\nu^+ W_\mu^-) & \sqrt{2}(\mathcal{D}_\mu W_\nu^+ - \mathcal{D}_\nu W_\mu^+) \\ \sqrt{2}(\mathcal{D}_\mu^\dagger W_\nu^- - \mathcal{D}_\nu^\dagger W_\mu^-) & -(s_w A_{\mu\nu} + c_w Z_{\mu\nu} + ig(W_\mu^+ W_\nu^- - W_\nu^+ W_\mu^-)) \end{pmatrix}$$

and

$$\not{B}_{\mu\nu} = \frac{i}{2}g' B_{\mu\nu} = \frac{i}{2}g'(c_w A_{\mu\nu} - s_w Z_{\mu\nu}) = \frac{i}{2}(g s_w A_{\mu\nu} - \tan^2\theta_W g c_w Z_{\mu\nu})$$

In the unitary Gauge one has

$$H = \begin{pmatrix} 0 \\ \frac{1}{\sqrt{2}}(v+h) \end{pmatrix}$$

so that

$$\begin{aligned} D_\mu H &= (\partial_\mu + ig\frac{\sigma_i}{2}W_\mu^i + ig'\frac{1}{2}B_\mu)H \\ &= \partial_\mu H + \frac{i}{2}\begin{pmatrix} \sqrt{g^2+g'^2}[s_w B_\mu + c_w W_\mu^3] & g\sqrt{2}W_\mu^+ \\ g\sqrt{2}W_\mu^- & \sqrt{g^2+g'^2}[s_w B_\mu - c_w W_\mu^3] \end{pmatrix} H \\ &= \begin{pmatrix} i m_W W_\mu^+(1+\frac{h}{v}) \\ \frac{1}{\sqrt{2}}\partial_\mu h - i\frac{m_Z}{\sqrt{2}}Z_\mu(1+\frac{h}{v}) \end{pmatrix} \end{aligned}$$

B.2 O_B

One has

$$
\begin{aligned}
O_B &= (D_\mu H)^\dagger \not{B}^{\mu\nu}(D_\nu H) \\
&= \begin{pmatrix} i m_W W^+_\mu (1+\frac{h}{v}) \\ \frac{1}{\sqrt{2}}\partial_\mu h - i\frac{m_Z}{\sqrt{2}} Z_\mu (1+\frac{h}{v}) \end{pmatrix}^\dagger \frac{i}{2}(g s_w A^{\mu\nu} - \tan^2\theta_W g c_w Z^{\mu\nu}) \begin{pmatrix} i m_W W^+_\nu (1+\frac{h}{v}) \\ \frac{1}{\sqrt{2}}\partial_\nu h - i\frac{m_Z}{\sqrt{2}} Z_\nu (1+\frac{h}{v}) \end{pmatrix} \\
&= \frac{i}{2}(g s_w A^{\mu\nu} - \tan^2\theta_W g c_w Z^{\mu\nu}) \times \\
&\quad \Big[\frac{1}{2}\partial_\mu h \partial_\nu h + (m_W^2 W^-_\mu W^+_\nu + \frac{m_Z^2}{2} Z_\mu Z_\nu)(1+\frac{h}{v})^2 + i\frac{m_Z}{2}(Z_\mu \partial_\nu h - Z_\nu \partial_\mu h)(1+\frac{h}{v})\Big] \\
&= \frac{i}{2}(g s_w A^{\mu\nu} - \tan^2\theta_W g c_w Z^{\mu\nu})\Big[m_W^2 W^-_\mu W^+_\nu (1+\frac{h}{v})^2 + i m_Z Z_\mu \partial_\nu h (1+\frac{h}{v})\Big]
\end{aligned}
\tag{B.1}
$$

where in the last line it has been used that $A^{\mu\nu}$ and $Z^{\mu\nu}$ are antisymmetric while $\partial_\mu h \partial_\nu h$ and $Z_\mu Z_\nu$ are symmetric, and that $V^{\mu\nu}(Z_\mu \partial_\nu h - Z_\nu \partial_\mu h) = 2V^{\mu\nu} Z_\mu \partial_\nu h$ if $V^{\mu\nu}$ is antisymmetric.

So one reads

$$
\begin{aligned}
O_B = \quad & -i g s_w \frac{m_W^2}{2} A^{\mu\nu} W^+_\mu W^-_\nu (1+\frac{h}{v})^2 \text{ (vertices AWW + ...)} \\
& + i g c_w \tan^2\theta_W \frac{m_W^2}{2} Z^{\mu\nu} W^+_\mu W^-_\nu (1+\frac{h}{v})^2 \text{ (vertices ZWW + ...)} \\
& - \quad g s_w \frac{m_Z}{2} A^{\mu\nu} Z_\mu \partial_\nu h \quad (1+\frac{h}{v}) \text{ (vertices AZH + ...)} \\
& + \quad g c_w \tan^2\theta_W \frac{m_Z}{2} Z^{\mu\nu} Z_\mu \partial_\nu h \quad (1+\frac{h}{v}) \text{ (vertices ZZH + ...)}
\end{aligned}
$$

where "..." stands for vertices built from the precedding one with additional hs.

B.3 O_W

One has

$$
\begin{aligned}
O_W &= (D_\mu H)^\dagger \not{W}^{\mu\nu}(D_\nu H) \\
&= \begin{pmatrix} i m_W W^+_\mu (1+\frac{h}{v}) \\ \frac{1}{\sqrt{2}}\partial_\mu h - i\frac{m_Z}{\sqrt{2}} Z_\mu (1+\frac{h}{v}) \end{pmatrix}^\dagger \frac{i}{2} g \begin{pmatrix} W^{3\mu\nu} & W^{1\mu\nu} - iW^{2\mu\nu} \\ W^{1\mu\nu} + iW^{2\mu\nu} & -W^{3\mu\nu} \end{pmatrix} \begin{pmatrix} i m_W W^+_\nu (1+\frac{h}{v}) \\ \frac{1}{\sqrt{2}}\partial_\nu h - i\frac{m_Z}{\sqrt{2}} Z_\nu (1+\frac{h}{v}) \end{pmatrix}
\end{aligned}
\tag{B.2}
$$

The Gauge Bosons interactions from O_W are obtained directly setting $h = 0$

$$
\begin{aligned}
O_W^G &= \frac{i}{2} g \Big\{[-i m_W W^-_\mu]\Big[W^{3\mu\nu} i m_W W^+_\nu + [W^{1\mu\nu} - iW^{2\mu\nu}][-i\frac{m_Z}{\sqrt{2}} Z_\nu]\Big] \\
&\quad + [i\frac{m_Z}{\sqrt{2}} Z_\mu]\Big[[W^{1\mu\nu} + iW^{2\mu\nu}] i m_W W^+_\nu - W^{3\mu\nu}[-i\frac{m_Z}{\sqrt{2}} Z_\nu]\Big]\Big\} \\
&= \frac{i}{2}[g s_w A^{\mu\nu} + g c_w Z^{\mu\nu} + i g^2 (W^{+\mu} W^{-\nu} - W^{+\nu} W^{-\mu})] m_W^2 W^-_\mu W^+_\nu \\
&+ \frac{ig}{2\sqrt{2}} m_Z m_W \Big[W^+_\mu [W^{1\mu\nu} + iW^{2\mu\nu}] - W^-_\mu [W^{1\mu\nu} - iW^{2\mu\nu}]\Big] Z_\nu \\
&= \frac{i}{2}(g s_w A^{\mu\nu} + g c_w Z^{\mu\nu}) m_W^2 W^-_\mu W^+_\nu - \frac{g^2}{2}(W^{+\mu} W^{-\nu} - W^{+\nu} W^{-\mu}) m_W^2 W^-_\mu W^+_\nu \\
&+ \frac{ig}{2} m_Z m_W \Big[W^{+\mu}[\mathcal{D}^\dagger_\mu W^-_\nu - \mathcal{D}^\dagger_\nu W^-_\mu] - W^{-\mu}[\mathcal{D}_\mu W^+_\nu - \mathcal{D}_\nu W^+_\mu]\Big] Z^\nu
\end{aligned}
$$

where the antisymmetry of $A^{\mu\nu}$ and $Z^{\mu\nu}$ has been used to discard a $Z_\mu Z_\nu$ term and to do Lorentz indices substitution in a term containing a single Z.

Then since

$$\begin{gathered} W^{+\mu}[\mathcal{D}^\dagger_\mu W^-_\nu - \mathcal{D}^\dagger_\nu W^-_\mu] - W^{-\mu}[\mathcal{D}_\mu W^+_\nu - \mathcal{D}_\nu W^+_\mu] = \\ W^{+\mu}W^-_{\mu\nu} - W^{-\mu}W^+_{\mu\nu} - i(gs_w A^\mu + gc_w Z^\mu)[W^+_\mu W^-_\nu + W^-_\mu W^+_\nu] + i(gs_w A_\nu + gc_w Z_\nu)2W^{+\mu}W^-_\mu \end{gathered}$$

one reads

$$\begin{aligned} O^G_W = \; & -igs_w \frac{m_W^2}{2} A^{\mu\nu} W^+_\mu W^-_\nu && \text{(vertex AWW)} \\ - \; & igc_w \frac{m_W^2}{2} Z^{\mu\nu} W^+_\mu W^-_\nu && \text{(vertex ZWW)} \\ - \; & igc_w \frac{m_Z^2}{2} (W^+_{\mu\nu} W^{-\mu} - W^-_{\mu\nu} W^{+\mu}) Z^\nu && \text{(vertex ZWW)} \\ - \; & g^2 \frac{m_W^2}{2} (W^{+\mu}W^{-\nu} - W^{+\nu}W^{-\mu}) W^-_\mu W^+_\nu && \text{(vertex WWWW)} \\ + \; & (gc_w)(gs_w) \frac{m_Z^2}{2} [W^+_\mu W^-_\nu + W^-_\mu W^+_\nu] A^\mu Z^\nu && \text{(vertex ZAWW)} \\ - \; & (gc_w)(gs_w) m_Z^2 W^{+\mu} W^-_\mu A^\nu Z_\nu && \text{(vertex ZAWW)} \\ + \; & (gc_w)^2 \frac{m_Z^2}{2} [W^+_\mu W^-_\nu + W^-_\mu W^+_\nu] Z^\mu Z^\nu && \text{(vertex ZZWW)} \\ - \; & (gc_w)^2 m_Z^2 W^{+\mu} W^-_\mu Z^\nu Z_\nu && \text{(vertex ZZWW)} \end{aligned} \tag{B.3}$$

Appendix C

Coverage studies for Poisson Data when expectation depends quadratically on the parameter

Herafter, I document studies of Coverage probability of two methods for constructing Confidence Domains. In the studied case, the observation follows a Poisson law and the mean value depends on the parameter of interest quadratically. Both methods use the Likelihood Ratio test statistic. One of the method severely under covers sometimes while the other covers always.

This excercise is an oppotunity to work out in a simple context but in details statistical procedures very often discussed in the HEP field.

C.1 Introduction

The general case can be described as follows. Let's assume that we are interested in a set of some parameters noted $\vec{f}$. One wants to learn about $\vec{f}$ from the observed values of a set of some variables noted $\vec{x}$. One should model the connection between $\vec{f}$ and $\vec{x}$, and design a procedure to extract from $\vec{x}$ some knowledge on $\vec{f}$. The modeling of the observation consists in saying that $\vec{x}$ is a realization of a random variable $\vec{X}$ following the distribution $p\left(\vec{x};\vec{f}\right)$. The procedure consists in defining a region in the $\vec{f}$ space which depends on $\vec{x}$, a Confidence Domain $CD\left(\vec{x}\right)$.

The Coverage probability is a qualification of the construction of the Confidence Domains. It is the central Frequentist concept and the "exact" coverage has been even described as the Holly Grail of Frequentism [240].

The determination of the Coverage probabilty starts by choosing first a value of the parameters vector, $\vec{f_t}$. Then one generates, according to $p\left(\vec{x};\vec{f_t}\right)$, a set of pseudo-experiments $\{\vec{x}_i\}$. For each $\vec{x}_i$, one computes $CD\left(\vec{x}_i\right)$ and asks if $CD\left(\vec{x}_i\right)$ covers $\vec{f_t}$, i.e if $\vec{f_t}$ is within $CD\left(\vec{x}_i\right)$. One desires that this happens often but one is ready to accept that this fails from time to time due to large fluctuation allowed by $p\left(\vec{x};\vec{f_t}\right)$. In this way and in the limit of a very large number of pseudo-experiments, one estimates the probability that a Confidence Domain so produced to cover the values of the true parameters, $\vec{f_t}$. This probability qualifies the procedure of the construction of the Confidence Domains. It is the Coverage probability, $C\left(\vec{f_t}\right)$, of the Confidence Domain procedure for the particular value $\vec{f_t}$.

In the limit of a very large number of pseudo-experiments, one can imagine the pseudo-experiments arranged in the $\vec{x}$ space in small cells centered on $\vec{x}^c$ of volume $d\vec{x}$. One cell contains a fraction $p\left(\vec{x}^c;\vec{f_t}\right)d\vec{x}$ of the total number of the pseudo-experiments. The pseudo-experiments of this cell are counted as "successes" if $\vec{f_t} \in CD\left(\vec{x}^c\right)$. So the Coverage probability will be the sum of the fraction $p\left(\vec{x}^c;\vec{f_t}\right)d\vec{x}$ over the cells such that $\vec{f_t} \in CD\left(\vec{x}^c\right)$. Therefore one gets that the Coverage probability is the integral of the distribution law over the region of the observations space defined by the condition $\vec{f} \in CD\left(\vec{x}\right)$

$$C\left(\vec{f}\right) = \int_{\vec{x}/\vec{f}\in CD(\vec{x})} p\left(\vec{x};\vec{f}\right)d\vec{x} \tag{C.1}$$

If the Coverage is exact, i.e if the Coverage probability is a constant independent on $\vec{f}$, it is possible to speak about probability of an interval to contain the true parameter, avoiding to resort to such a concept as probability of the parameter, in strict compliance to the Frequentist doctrine. In practice, Coverage probability is rarely constant and one should be happy if it is limited from bellow, hopefully by a nominal Confidence Level that the procedure attaches to its Confidence Domains.

In the problem studied here, as in [240], we are concerned with the simple case of a counting experiment in a single bin without nuisance parameter. The observation is a number of counts noted n_o. Furthermore there is only one parameter of interest, a real number noted f. So the Confidence Domains are Confidence Intervals on f, $CI\left(n_o\right)$ and the equation (C.1) becomes

$$C\left(f\right) = \sum_{n_o\in A(f)} g\left(n_o;f\right) \text{ with } A\left(f\right) = \left\{n_o \mid f \in CI\left(n_o\right)\right\} \tag{C.2}$$

where $g\left(n_o;f\right)$ is a Poisson law

$$g(n_o;f) = \frac{e^{-\mu}\mu^{n_o}}{n_o!} \tag{C.3}$$

In addition unlike in [240], μ, the mean value of the law, is not here the parameter of interest, but depends quadratically on it

$$\mu = f^2 + C \tag{C.4}$$

where C is a known positive real constant.

A use case for such a dependence is the constuction Confidence Domains for the anomalous Triple Gauge Couplings in the production of bosons pairs at hadron colliders [241]. The amplitude of the reaction is the sum of the Standard Model amplitude plus anomalous amplitudes proportional to these couplings. So that the cross-section is a second degree polynomial of the couplings.

Hereafter we establish the Coverage performance of two procedures building Confidence Intervals. Both methods use the Likelihood Ratio. It should be noted that there is no need here to resort to generation of pseudo-experiments since the probability case is simple enough. All the computations are exact up to the precision to which, on one hand, one computes the repartition function of a χ^2 law and, on the other hand, one solves the equations defining the intervals ends. For the first we rely on the Root package [242] and the second can be reduced at will.

C.2 Confidence Interval Methods

In this problem, the Likelihood is

$$L(f;n_o) = g(n_o;f) \tag{C.5}$$

The Maximum Likelihood Estimators (MLE) of f, $\hat{f}$ are given by

$$\hat{f} = \begin{cases} 0 & \text{if } n_o < C \\ \pm\sqrt{n_o - C} & \text{if } n_o \geq C \end{cases} \tag{C.6}$$

Although there are 2 maxima when $n_o \geq C$, owing to the sign symmetry of the problem, there will be no ambiguity below in speaking of these maxima as if there was a single $\hat{f}$.

The Likelihood Ratio is the test statistic

$$R(f;n_o) \equiv \frac{L(f;n_o)}{L(\hat{f};n_o)} \tag{C.7}$$

By construction one has

$$0 \leq R(f;n_o) \leq 1 = R(\hat{f};n_o) \tag{C.8}$$

One defines the 2 derived test statistics

$$q(f;n_o) \equiv -ln\left(R(f;n_o)\right) \tag{C.9}$$

and

$$\chi(f;n_o) \equiv \sqrt{2q(f;n_o)} \tag{C.10}$$

The analytical expression of $q(f;n_o)$ is given in the Additional material section C.5. The figure C.1 shows typical examples of this function; when n_o is lower than C, the function has a single extremum, a minimum at $f = 0$; as soon as n_o is greater than C, the minimum drifts away to larger and larger value of f; a maximum appears at $f = 0$ and increases with n_o.

The Likelihood Ratio (C.1) is a mean to compare a test value f to $\hat{f}$, the value of the parameter the most compatible with the observation n_o. Somehow, the farthest f is from $\hat{f}$, the least f is compatible with the observation, the smallest $R(f;n_o)$ becomes. The determination of the ends of a Confidence Interval is the selection of some values of f away from $\hat{f}$ but somehow still acceptable. The point is to build a criteria to decide what "somehow" means.

In the following, two methods are considered which both uses the Likelihood Ratio.

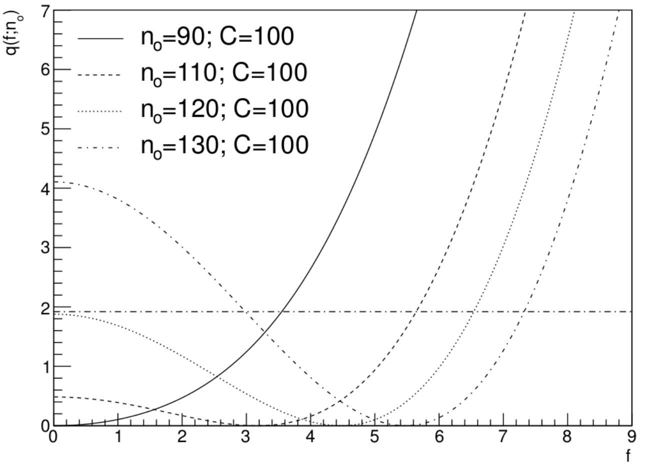

Figure C.1: Test statistic $q(f;n_o)$ as a function of f for various values of n_o. Since the functions are symmetric, only the $f \geq 0$ side is shown.

C.2.1 $\Delta \ln L$ method

In this method, the interval ends are found by solving in f_e the equation

$$R(f_e;n_o) = e^{-\frac{{n_\sigma}^2}{2}} \Leftrightarrow q(f_e;n_o) = \frac{{n_\sigma}^2}{2} \Leftrightarrow \chi(f_e;n_o) = n_\sigma \tag{C.11}$$

where n_σ is for instance 1.96 for a 95% Confidence Level Interval. For an interval of $(1-\alpha)100\%$ Confidence Level this condition can be reformulated as

$$\pi(f;n_o)=\alpha \text{ with } \pi(f;n_o)=1-\int_{-\chi(f;n_o)}^{\chi(f;n_o)}\frac{1}{\sqrt{2\pi}}e^{-\frac{x^2}{2}}dx \tag{C.12}$$

The principle of this method is to divide the f parameter space on the basis of the value $R(f;n_o)$: lower than a threshold, f is rejected from the Confidence Interval, higher f gets included.

This method, generalized to the Profile Likelihood Ratio, is basically the MINOS algorithm from the Minuit suite [166]. The rationale of the method is that this is indeed the appropriate thing to do if the underlying probability is Gaussian. In absence of nuisance parameters the method is known to perform poorly [240, 243]. Still with nuisance parameters it was found surprisingly good [244].

C.2.2 p-value method

The first step of this method is to compute a p-value for a test value f. The p-value is a real positive number lower than 1 depending both on f and n_o, $p(f;n_o)$.

The idea is to compare the value of $R(f;n_o)$ computed with the actual observation n_o, against a set of values $\{R(f;n_o^i)\}$ obtained generating a set of pseudo-experiments $\{n_o^i\}$ according to $g(n_o^i;f)$, i.e. as if the "true" value of the parameter was f.

Given these conditions of generation, the different n_o^i are expected to be vey often compatible with f. So the distribution of the $R(f;n_o^i)$ should show a large fraction of pseudo-experiments at high value. Now if one chooses f significantly different from $\hat{f}$ so that $R(f;n_o)$ is significantly low, such a low value will be "atypical" compared to the distribution of the $R(f;n_o^i)$. It will lie somewhere in the low values tail of the distribution.

One quantifies this by counting how many n_o^i have their $R(f;n_o^i)$ lower than $R(f;n_o)$, i.e. by computing the probability to get $R(f;n_o^i)$ lower than $R(f;n_o)$. Reasoning as one did for the Coverage probability, one gets that the p-value is also an integral/sum over a specific region of the observations space that one can write as

$$\begin{aligned} p(f;n_o) &= \sum_{n_o'\in W(f,n_o)} g(n_o';f) \text{ where } W(f,n_o)=\{n_o' \mid R(f;n_o')\le R(f;n_o)\} \\ &= 1-\sum_{n_o'\in B(f,n_o)} g(n_o';f) \text{ where } B(f,n_o)=\{n_o' \mid R(f;n_o') > R(f;n_o)\} \end{aligned} \tag{C.13}$$

where $B(f,n_o)$ ($W(f,n_o)=B(f,n_o)^{\complement}$) is the set of the integers "better-than-n_o-according-to-R-for-f" ("worse-or-as-bad-than-n_o-according-to-R-for-f"). A low value of $p(f;n_o)$ means that, assuming that the true value of the parameter is f, one has all reasons to be surprised to observe n_o since, according to the probability distribution of the Likelihood Ratio for this f, it is rare to get an observation with a so low value $R(f;n_o)$. Therefore we have good reasons to not accept such a f.

While the $\Delta\ln L$ method includes or rejects a particular value f on the basis of $R(f;n_o)$, the criteria of the p-value method is based on the value of $p(f;n_o)$: lower than a threshold, f is rejected from the Confidence Interval, higher f gets included.

The ends of the Confidence Interval are found by solving in f_e the equation

$$p(f_e;n_o)=\alpha \tag{C.14}$$

Due to discrete nature of the Poisson Data, the function $p(f;n_o)$ gets discontinuities in f and the above condition can not be met exactly. Some prescription is needed. Hereafter results will be presented using a prescription that turns out to guarantee coverage. An alternative prescription is discussed in the Additional material section C.5.

C.3 Results

C.3.1 $\Delta \ln L$ method

C.3.1.1 Interval Ends

As we saw the ends of the 95% Confidence Level Interval of the $\Delta \ln L$ method are found solving in f_e the equation

$$q(f; n_o) = \frac{1.96^2}{2} \sim 1.92 \tag{C.15}$$

As shown on figure C.1 depending on the value of n_o, one can find one or two disjunct intervals. If $n_o < C$, one gets one interval only since then $q(f; n_o)$ has only one minimum for $f = 0$. For $n_o \geq C$, $q(f; n_o)$ gets two minima and an extremum at $f = 0$. The value of the function at this extremum is itself an increasing function of n_o. So, there is a critical value for n_o greater than C [1] such that if n_o is below (above), $q(f = 0; n_o)$ is lower (greater) than $\frac{1.96^2}{2}$ and one has one (two) interval(s).

Since the function $\pi(f; n_o)$ is continuous, there is no particular issue in finding the solution of (C.12). Figures C.2 show two typical examples of $\pi(f; n_o)$: in figure C.2(a), n_o is low enough so that there is only one interval, in figure C.2(b), n_o is greater than the critical value discussed above and one gets two disjunct intervals.

The figure C.3 shows an example of the ends of the Confidence Intervals as a function of n_o. Again if n_o is low enough, one gets only one interval but two intervals when n_o is larger.

C.3.1.2 Coverage

One computes the Coverage probability using the equation (C.2).

Let's consider the figure C.3. It corresponds to the case $C = 6$ and shows the 95% Confidence Level intervals for the different possible observations. The equation (C.2) instructs to consider all possible observations one after an other and for a given observation n_o, to add its associated probability $g\left(n_o; f\right)$ if f belongs to its Confidence Interval $CI(n_o)$. This amounts to draw an horizontal line at $f = 0$ on the figure C.3 and to select the observations the Confidence Intervals of which are crossed by this line. For $f = 0$, one sees that this picks up the 12 integers from $n_o = 0$ to $n_o = 11$. Summing up their associated probabilities one gets $C(f = 0) \sim 98\%$. We report this value on the figure C.4(a) which shows the Coverage probability as a function of f for the case $C = 6$.

Now let's take a f slightly above 0. One sees in figure C.3, that if f is small enough, the horizontal line for this f still crosses the same Confidence Intervals that were crossed for $f = 0$. Therefore the sum in (C.2) still contains the 12 terms that it contains for $f = 0$. But the weights $g\left(n_o; f\right)$ have changed and it turns out that the sum is lower than $C\left(f = 0\right)$. So in figure C.4(a), the Coverage probability starts to decrease.

This continues up to $f \sim 0.65$. Then as we can see in figure C.3, the horizontal line for this f comes to cross the interval for $n_o = 12$. So the sum in (C.2) gets a new term and the Coverage probability in figure C.4(a) gets a discontinuity.

Continuing this game for a while, one understands that the Coverage probability in figure C.3 is an highly discontinuous function of f. The figure C.4(b) which displays the Coverage probability $C(f)$ for the case $C = 0.1$, shows the same discontinuous pattern. This feature of the Coverage probabilities results from the observations being discrete. It is found whatever the Confidence Interval method is. What is specific to the $\Delta \ln L$ method, is that there are many under-covered values of f specially for low values of C, i.e lower than announced by the Confidence Level of the intervals. For instance, the figure C.4(b) shows that Coverage probability values as low as 86% can be obtained while the face value of the Confidence Level of the intervals is 95%.

A global view of the situation is given by the figure C.5. It displays the coverage probability in the (C, f^2) plane with $f \geq 0$, in colors where it is greater than 95%. One notes a general dependence on

---

[1] If C is great enough, the critical value is $\sim C + 1.96\sqrt{C}$.

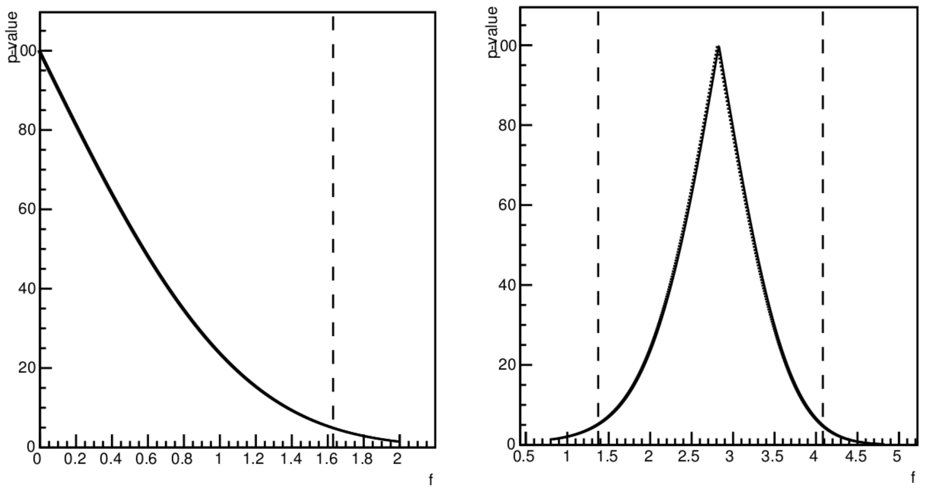

(a) $\pi(f; n_o)$ in % for $C = 6$ and $n_o = 2$ (b) $\pi(f; n_o)$ in % for $C = 6$ and $n_o = 14$

Figure C.2: $\pi(f; n_o)$ function in % for $C = 6$ and two values of n_o. The vertical lines are the locations of the ends of the 95 % Confidence Level intervals of the $\Delta \ln L$ method. Since the functions are symmetric, only the $f \geq 0$ side is shown.

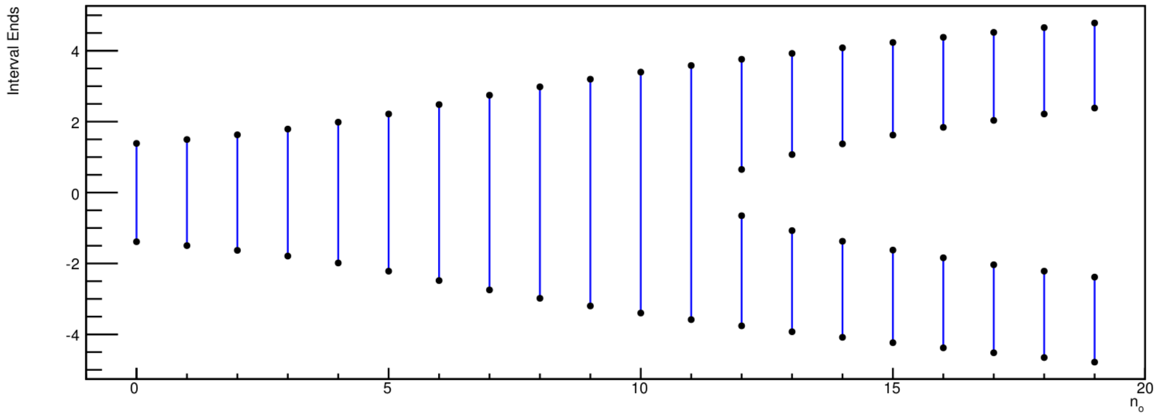

Figure C.3: Ends of the 95 % Confidence Level intervals of the $\Delta \ln L$ method for $C = 6$ as function of n_o.

$f^2 + C$, the expected bin counting, blurred in a troubled zone loosely comprised between the $f^2 \sim 2\sqrt{C}$ and $f^2 \sim \sqrt{C}$ curves. One sees that the method under-covers in a large fraction of the parameter space. The under-coverage is actually quite severe and Coverage probabilities as low as 85% are found in the area covered by the figure C.5. Finally, one notes a vast area, loosely defined by $f^2 < \sqrt{C}$, in which the method generally over-covers by few %.

So the $\Delta \ln L$ method, although easy to catch and to implement, does not ensure coverage. The p-value method discussed below is definitely more challenging but it has the definitive advantage to cover.

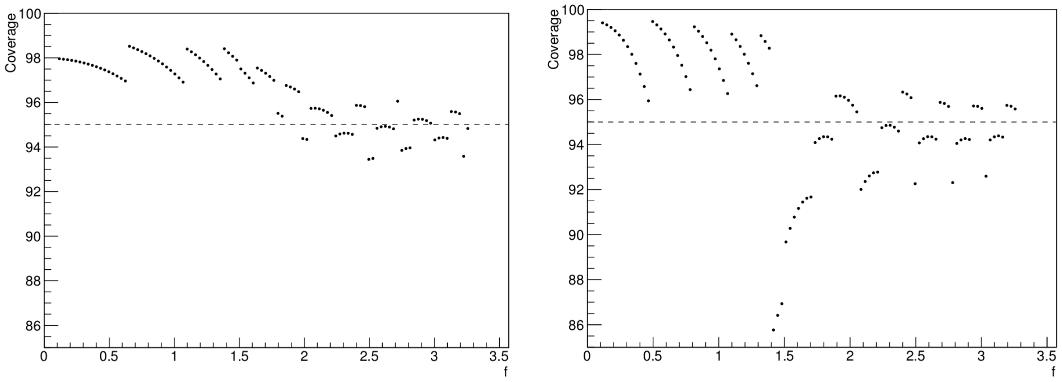

(a) Coverage probability for $C = 6$ (b) Coverage probability for $C = 0.1$

Figure C.4: Coverage probability in % as a function of f for 95% Confidence Level interval of the $\Delta \ln L$ method

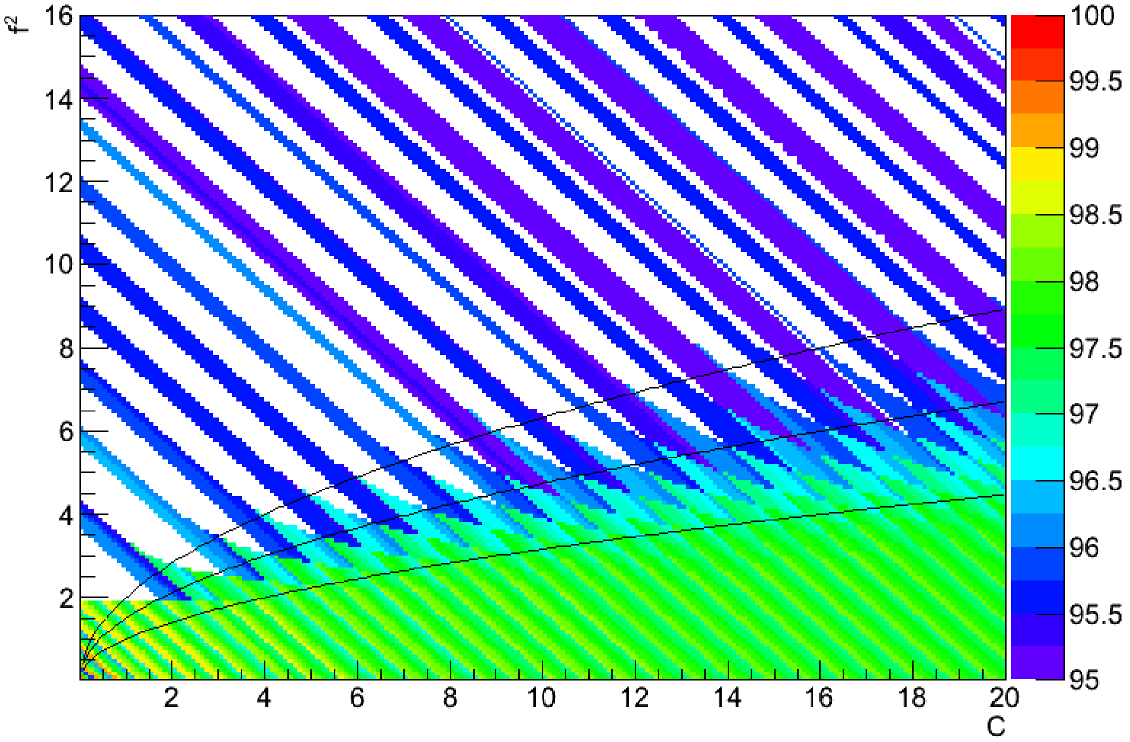

Figure C.5: Coverage probability in the (C, f^2) plane with $f \geq 0$ for the 95 % Confidence Level intervals of the $\Delta \ln L$ method. Only Coverage probabilities greater than 95% are shown. The three solid lines are the curves $f^2 = a\sqrt{C}$ for $a = 2, 1.5$ and 1.

C.3.2 p-value method

C.3.2.1 Interval Ends

The definition (C.13) makes the computation of the p-value, $p(f;n_o)$, a more complicated matter than the computation of the function $\pi(f;n_o)$.

A detailed analysis presented in the Additional material section C.5 shows that the composition of the set the integers “better-than-n_o-according-to-R-for-f”, $B(f,n_o)$ defined by (C.13), depends discontinuously on f. This makes the p-value a discontinuous function of f. Figures C.6 show two typical examples of the $p(f;n_o)$ function. Although the shape of $p(f;n_o)$ is globally similar to the one of $\pi(f;n_o)$ (cf figures C.2), there are many discontinuities as well as local inversions of the slope with respect to the general trend.

The discontinuities of $p(f;n_o)$ imply that the condition (C.14) can not be met strictly. One can at first decide to look for the f values fulfilling the condition as closely as possible and from below. This corresponds to consider all the f which have a p-value lower than α, i.e all the “bad” f, and among them to take as the interval end, the one which has the greater p-value. Its is shown in the Additional material section C.5 that this “Simple prescription” leads to performance far superior to the performance of the $\Delta \ln L$ method. Still there remains few under-coverage spots although less severe than in the $\Delta \ln L$ method.

Actually these under-coverage spots come from the fact that the “Simple prescription” can let outside the Confidence Interval few “good” f-ranges on which the p-values are bigger than α. A better prescription, named the “Proper prescription” in the Additional material section C.5 (cf C.5.2.5), is first to consider all the intervals such that any f outside them has a a p-value lower than α, and then to take the shortest of these intervals as the Confidence Interval. In short, outside the Confidence Interval every f is “bad”. Actually this is the core of the p-value method and this is what insures coverage.

For both prescriptions, there could be few “bad” f-ranges inside the Confidence Interval on which $p(f;n_o) < \alpha$. They lead to over-coverage with the “Proper prescription”. One could envision to remove this insider “bad” ranges. However this would lead to a bunch of disconnected intervals. It is much more convenient to buy a bit of over-coverage but to keep the Confidence Intervaks simply connected. As it is shown in the Additional material section C.5, this choice is closely related to a similar one advised in the Feldman-Cousins method [163].

Adopting the“Proper prescription”, one can determine the interval ends of the p-value method for any observation n_o. For instance for the case $C = 6$, one obtains the Confidence Intervals shown on figure C.7. Comparing this figure with the figure C.3, the intervals of the p-value method and of the $\Delta \ln L$ method look very similar.

This comparison can be made more precise by computing for the interval ends of the p-value method, the values of the test statistics, $\chi(f;n_o) = \sqrt{2q(f;n_o)}$. Indeed from the equation (C.11), one sees that these would be the value of the “effective” n_σ that one would have had to apply in the $\Delta \ln L$ method to find the same interval ends. For the case $C = 6$ the result is shown on the figure C.8. In this particular case, this effective n_σ varies from a value at low n_o apparently close to $\chi \sim 1.64$ definitevely lower than the 1.96 value of the $\Delta \ln L$ method, up to values slightly above 1.96 at high n_o. This pattern varies with the value of C and is studied in details in the Additional material section C.5 [2].

---

[2] The $\chi \sim 1.64$ is not accidental. In short, it results from the fact that the p-value can be shown to be the probability in the tails of a distribution as actually $\pi(f;n_o)$ is from its definition (C.12). However in the p-value case, it turns out that the tails can be asymmetrical up to the point for instance that the probability of one tail gives the main contribution to the p-value. In this case and if C is high enough, one gets $\chi \sim 1.64$ since the probability above 1.64σ is indeed 5% for a Gaussian distribution.

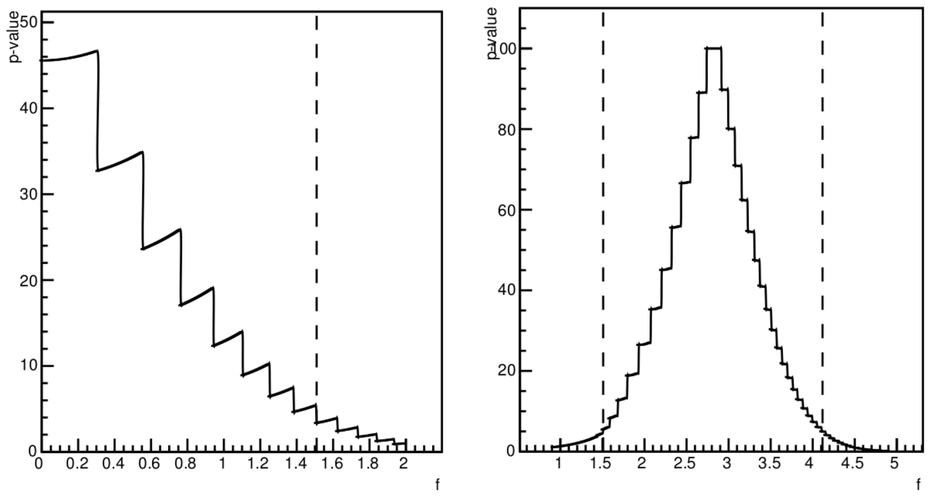

(a) $p(f; n_o)$ in % for $C = 6$ and $n_o = 2$ (b) $p(f; n_o)$ in % for $C = 6$ and $n_o = 14$

Figure C.6: $p(f; n_o)$ function in % for $C = 6$ and two values of n_o. The vertical lines are the locations of the ends of the 95 % Confidence Level intervals of the p-value method with the "Proper prescription" (cf C.5.2.5). Since the function is symmetric, only the $f \geq 0$ side is shown.

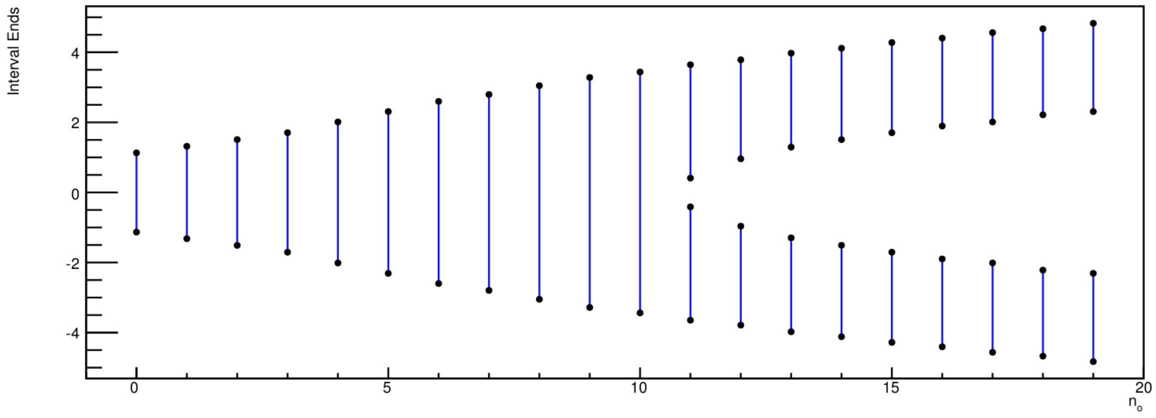

Figure C.7: Ends of the 95 % Confidence Level intervals of the p-value method with the "Proper prescription" (cf C.5.2.5) for $C = 6$ as a function of n_o.

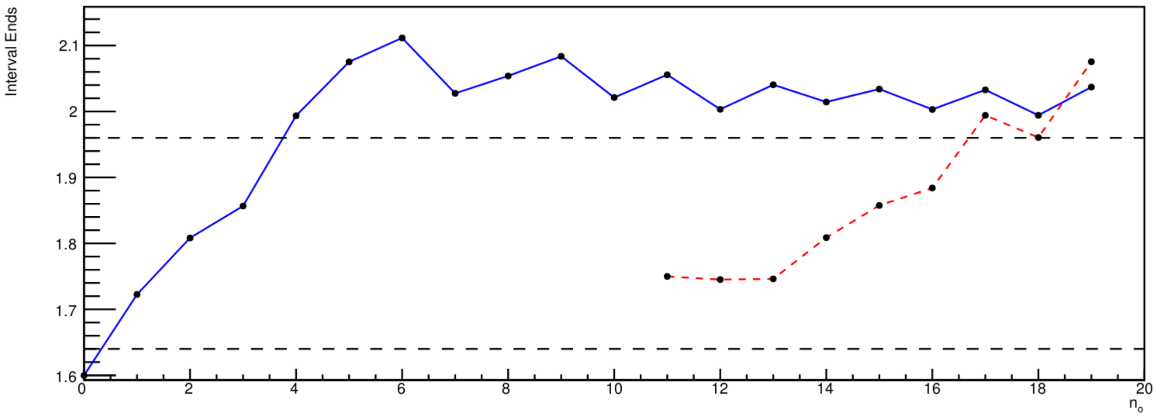

Figure C.8: $\chi(f; n_o) = \sqrt{2q(f; n_o)}$ for the ends of the 95 % Confidence Level intervals of the p-value method with the "Proper prescription" (cf C.5.2.5) for $C = 6$. The blue solid curve corresponds to the outermost interval ends. The red dashed curve corresponds to the innermost interval ends when two intervals are obtained. The black dashed lines are the curves $\chi = 1.96$ and $\chi = 1.64$.

C.3.2.2 Coverage

The computation of the Coverage probability for the p-value method follows the same track than for the $\Delta \ln L$ method.

For the same reasons the Coverage probability is a highly discontinuous function as illustrated for the cases $C = 6$ and $C = 0.1$ on the figures C.9. However comparing these figures to the figures C.4 of the $\Delta \ln L$ method, one sees that the Under-Coverage is no more an issue.

This is confirmed by the figure C.10 which shows the Coverage probability in the (C, f^2) plane with $f \geq 0$, in colours when it is greater than 95%. Comparing with figure C.5, one notes a total absence of Under-Coverage and a globally mitigated Over-Coverage.

As it is shown in the Additional material sections C.5.3 and C.5.4, the p-value method with the “Proper“ prescription does cover by construction and is equivalent to the Feldman-Cousins method [163].

C.4 Summary and conclusion

In this work one explored a simplified version of the problem of deriving Confidence Intervals for the anomalous Triple Gauge Couplings insisting on the rigor of the derivation and in particular on the Coverage probability.

Without nuisance parameters and with a single bin, our statistical problem is similar to the one addressed in [240] with the important difference that the mean value is not the parameter of interest but a second degree polynomial of it.

Among the two methods studied here, the $\Delta \ln L$ method is very commonly used. Its well known poor performance are confirmed in the context of our problem. The other method, the more challending p-value method, has far better performance and in particular covers by construction. As we have shown, to obtain these nice features, its application requires explicit prescription more precise than one could have guessed at first.

Increasingly complexity when many parameters of interest and bins are included as well as inclusion of nuisance effects make quickly impractical the analytical approach used here. One has to resort to sophisticated minimization tools as well as to pseudo-experiments to address the same questions. Still, the results of the simple case studied here can be of some help to understand more complex situations.

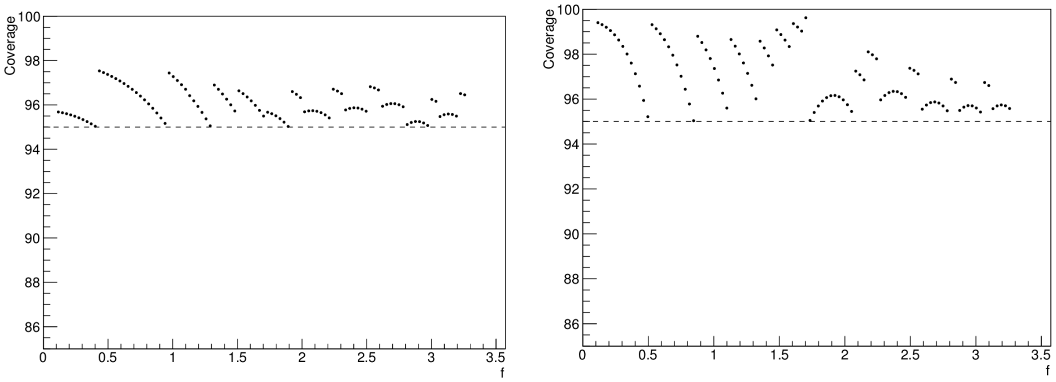

(a) Coverage probability for $C = 6$

(b) Coverage probability for $C = 0.1$

Figure C.9: Coverage probability in % as a function of f for 95% Confidence Level interval of the p-value method with the "Proper prescription" (cf C.5.2.5).

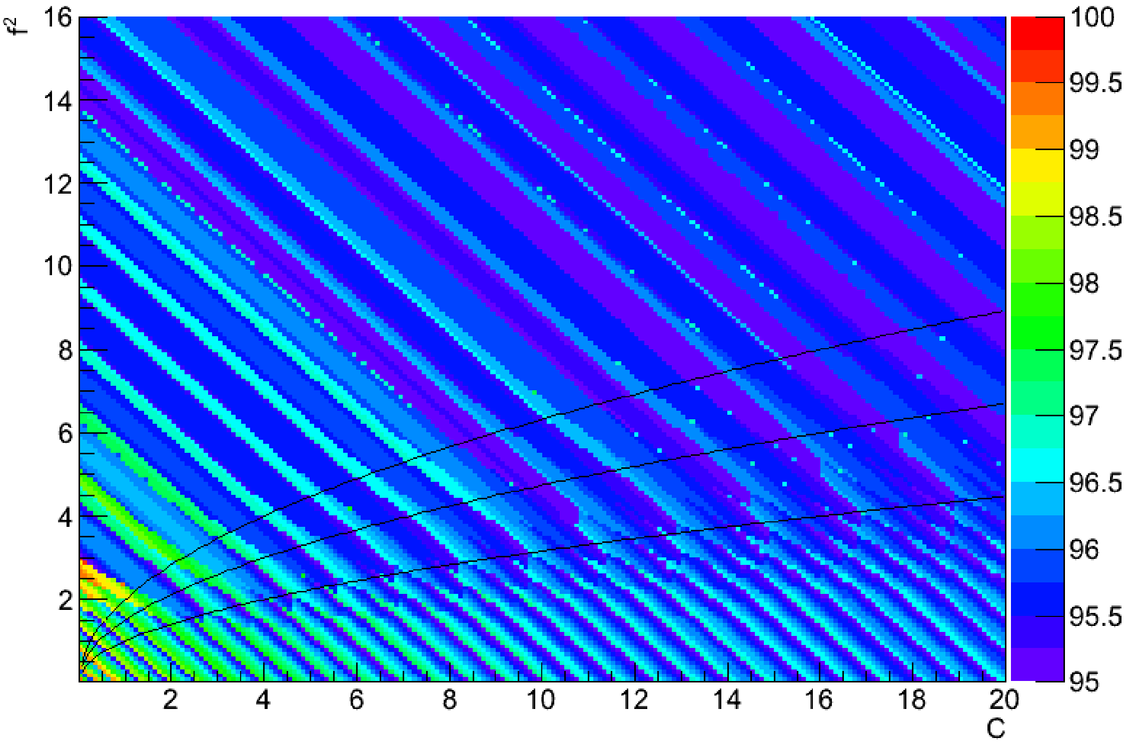

Figure C.10: Coverage probability in the (C, f^2) plane with $f \geq 0$ for the 95 % Confidence Level intervals of the p-value method with the "Proper prescription" (cf C.5.2.5). Only Coverage probabilities greater than 95% are shown. The three solid lines are the curves $f^2 = a\sqrt{C}$ for $a = 2, 1.5$ and 1.

C.5 Additional Material

C.5.1 Likelihood Ratio

The analytical form of the test statistics $q(f; n_o)$ defined by (C.9) is:

$$q(f;n_o) = \begin{cases} -n_o ln\left(\frac{f^2+C}{n_o}\right) + f^2 + C - n_o & \text{if } n_o \geq C \\ -n_o ln\left(\frac{f^2+C}{C}\right) + f^2 & \text{if } n_o < C \end{cases}$$

C.5.2 p-value method

C.5.2.1 Intersection of q functions

The definition of the p-value implies that one solves first the problem of finding τ such that

$$q(\tau; n_o') = q(\tau; n_o) \text{ for } n_o' \neq n_o$$

where n_o is the actual observation and n_o' an alternative hypothetical observation. The solution, $\tau(n_o'; n_o)$, does exist only if n_o or n_o' is greater than C. Defining n_c, as the integer such that $n_c \geq C > n_c - 1$, it comes

$$\begin{array}{llll} \text{if} & n_o \leq n_c - 1 \text{ and } n_c \leq n_o' & \text{then} & \tau(n_o'; n_o) = \sqrt{\left(\frac{{n_o'}^{n_o'} e^{C-n_o'}}{C^{n_o}}\right)^{\frac{1}{n_o'-n_o}} - C} \\ \text{if} & n_o' \leq n_c - 1 \text{ and } n_c \leq n_o & \text{then} & \tau(n_o'; n_o) = \sqrt{\left(\frac{{n_o}^{n_o} e^{C-n_o}}{C^{n_o'}}\right)^{\frac{1}{n_o-n_o'}} - C} \\ \text{if} & n_c \leq n_o \text{ and } n_c \leq n_o' & \text{then} & \tau(n_o'; n_o) = \sqrt{\frac{1}{e}\left(\frac{{n_o'}^{n_o'}}{{n_o}^{n_o}}\right)^{\frac{1}{n_o'-n_o}} - C} \end{array} \tag{C.16}$$

The set of the $\tau(n_o'; n_o)$ forms a suite increasing with n_o'. [3]

C.5.2.2 Categorization

From the definition (C.13), the different integers n_o' have to be sorted out in two categories: the category of the "worse-or-as-bad-than-n_o-according-to-R-for-f" such that $q(f; n_o') \geq q(f; n_o)$ and the category of the "better-than-n_o-according-to-R-for-f" such that $q(f; n_o') < q(f; n_o)$. So we have just to find how $q(f; n_o')$ evolves with n_o'.

All depends on whether n_o is lower or greater than C as shown on figures C.11 and C.12. It comes

- if $n_o \leq n_c - 1$
  - if $n_o' \leq n_o$ (cf figure C.11(a)) then $\forall f \; q(f; n_o') \geq q(f; n_o)$ and this n_o' is to be counted as "worse-or-as-bad"
  - if $n_o < n_o' \leq n_c - 1$ (cf figure C.11(b))
    - if $|f| = 0$ then $q(f; n_o') = q(f; n_o)$ and this n_o' is to be counted as "worse-or-as-bad"
    - $|f| \neq 0$ then $\forall f \; q(f; n_o') < q(f; n_o)$ and this n_o' is to be counted as "better"
  - if $n_c \leq n_o'$ (cf figure C.11(c)), then the curves $q(f; n_o')$ and $q(f; n_o)$ cross for $f = \tau(n_o'; n_o)$
    - if $|f| \leq \tau(n_o'; n_o)$ then $q(f; n_o') \geq q(f; n_o)$ and this n_o' is to be counted as "worse-or-as-bad"
    - if $|f| > \tau(n_o'; n_o)$ then $q(f; n_o') < q(f; n_o)$ and this n_o' is to be counted as "better"
- if $n_c \leq n_o$:

---

[3] One notes that if C is an integer, i.e $C = n_c$, then $\forall n_o < n_c \; \tau(n_c; n_o) = 0$.

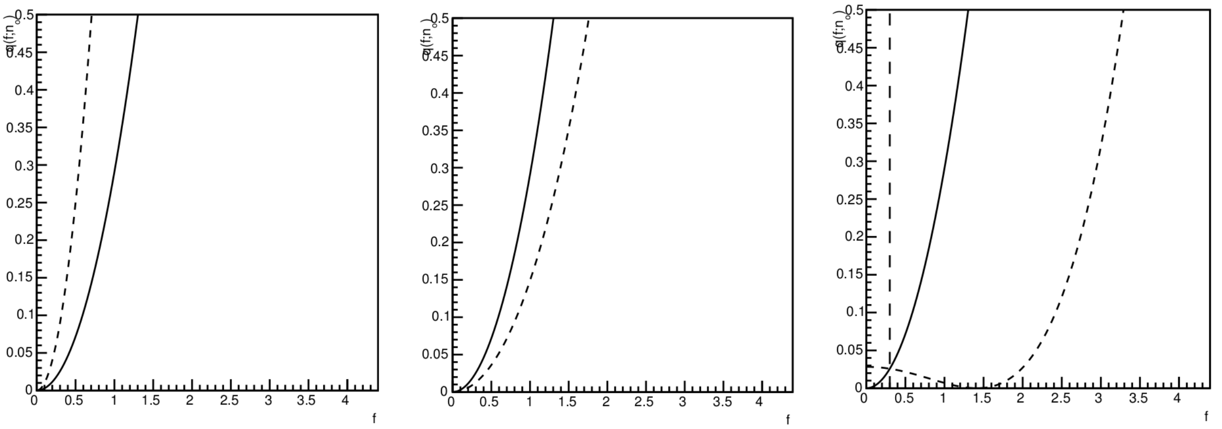

(a) Case $n_o' \leq n_o$ (b) Case $n_o < n_o' \leq n_c - 1$ (c) Case $n_c \leq n_o'$

Figure C.11: Cases $n_o \leq n_c - 1$. Solid line corresponds to $q(f;n_o)$, and dashed line to $q(f;n_o')$

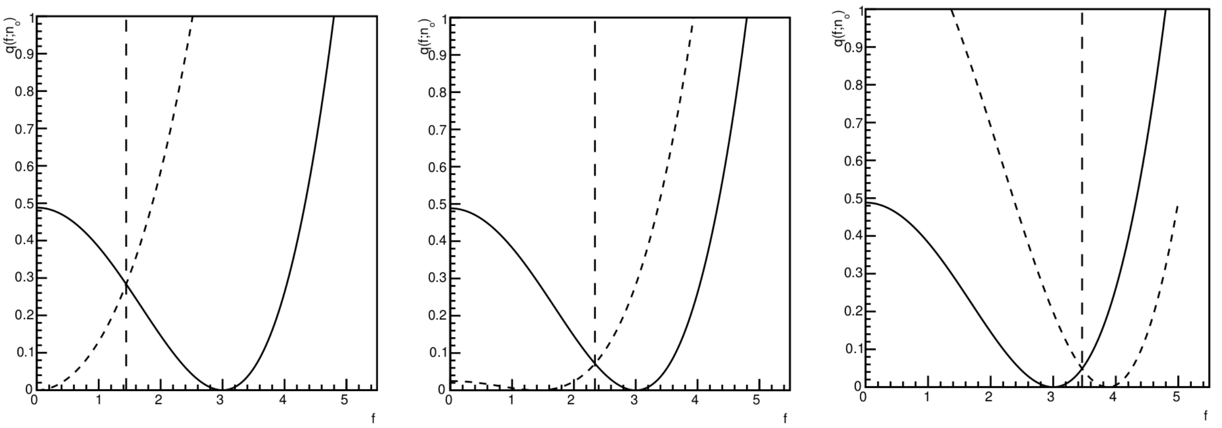

(a) Case $n_o' < n_o$ (b) Case $n_o' < n_o$ (c) Case $n_o < n_o'$

Figure C.12: Cases $n_c \leq n_o$. Solid line corresponds to $q(f;n_o)$, and dashed line to $q(f;n_o')$

- if $n_o' = n_o$, this n_o' is to be counted as "worse-or-as-bad"
- if $n_o' < n_o$, (cf figure C.12(a) and figure C.12(b)), the curves cross for $f = \tau(n_o'; n_o)$
  - if $|f| < \tau(n_o'; n_o)$ then $q(f;n_o') < q(f;n_o)$ and this n_o' is to be counted as "better"
  - if $|f| \geq \tau(n_o'; n_o)$ then $q(f;n_o') \geq q(f;n_o)$ and this n_o' is to be counted as "worse-or-as-bad"
- if $n_o < n_o'$ (cf figure C.12(c), the curves $q(f;n_o')$ and $q(f;n_o)$ cross for $f = \tau(n_o'; n_o)$
  - if $|f| \leq \tau(n_o'; n_o)$ then $q(f;n_o') \geq q(f;n_o)$ and this n_o' is to be counted as "worse-or-as-bad"
  - if $|f| > \tau(n_o'; n_o)$ then $q(f;n_o') < q(f;n_o)$ and this n_o' is to be counted as "better"

In the space (f, n_o'), the domains of the "worse-or-as-bad" and "better" categories display interesting patterns such as shown on figures C.13.

C.5.2.3 p-value computation

From previous results, one can compute the p-value in all cases. As illustrated by figures C.13, the set of the "better" n_o' turns out to be a single segment $[n_1; n_2]$ in such a way that the p-value can be

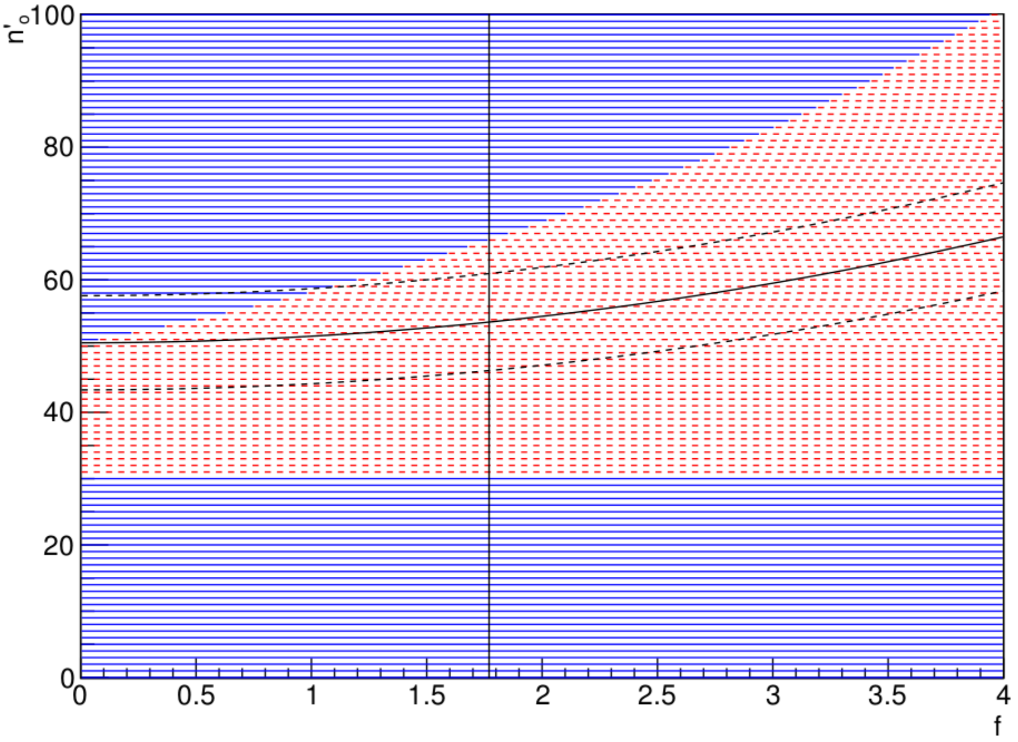

(a) For $C = 50.5$ and $n_o = 30$.

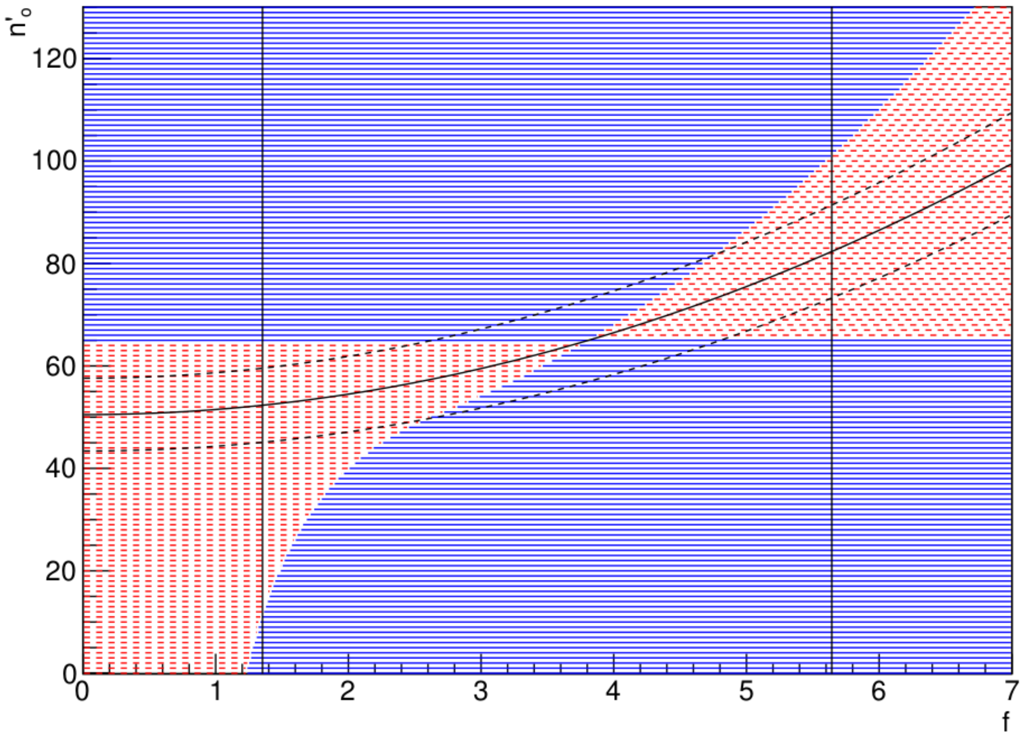

(b) For $C = 50.5$ and $n_o = 65$.

Figure C.13: For a given f, the solid blue lines mark the n_o' values such that $q(f; n_o') \geq q(f; n_o)$, i.e the "worse-or-as-bad" n_o', and the dashed red lines lines mark the n_o' values such that $q(f; n_o') < q(f; n_o)$, i.e the "better" n_o'. The solid black curve is the curve $n_o' = \mu$ where $\mu = f^2 + C$. and the dashed black curves are the curves $n_o' = \mu \pm \sqrt{\mu}$. The vertical lines are the locations of the interval ends of the p-value method according to the "Proper prescription" (cf C.5.2.5).

written in the simple form:

$$p(f;n_o) = 1 - \sum_{n'_o=n_1}^{n_2} g(n'_o;f)$$

Examining all the cases, it comes

- if $n_o \leq n_c - 1$
  - if $f = 0$ then
  $$p(f;n_o) = 1$$
  - if $0 < |f| \leq \tau(n_c;n_o)$ then
  $$p(f;n_o) = 1 - \sum_{n'_o=n_o+1}^{n_c-1} g(n'_o;f) \tag{C.17}$$
  which can be written as
  $$p(f;n_o) = 1 - F_{\chi^2}(2\mu;2(n_o+1)) + F_{\chi^2}(2\mu;2n_c) \tag{C.18}$$
  where $\mu = f^2 + C$ and $F_{\chi^2}(x;N_{dof})$ is the repartition function of a χ^2 law of N_{dof} number of degrees of freedom
  - if $\tau(n_c;n_o) < |f|$ then
  $$\begin{aligned} p(f;n_o) &= 1 - \textstyle\sum_{n'_o=n_o+1}^{\tilde{n}} g(n'_o;f) \text{ where } \tilde{n} \text{ is such that } \tau(\tilde{n};n_o) < |f| \leq \tau(\tilde{n}+1;n_o) \\ &= 1 - F_{\chi^2}(2\mu;2(n_o+1)) + F_{\chi^2}(2\mu;2(\tilde{n}+1)) \end{aligned}$$

  The $p(0;n_o) = 1$ result was expected since here the MLE is null, $\hat{f} = 0$.

  If $n_o = n_c - 1$ and $|f| \leq \tau(n_c;n_o)$ the limits of the sum in (C.17) appears to be inversed with respect to the normal order. In this case, the sum should be understood as being null. Then we have $p(f;n_o) = 1$ over the range $|f| \in [0;\tau(n_c;n_o)]$. Note that this result is obtained also from (C.18) without any particular prescription. At first sight, it could be strange that $p(f;n_o) = 1$ for $f \neq \hat{f}$. As shown on figure C.14, this comes from the fact that for this particular value of n_o, any alternative n'_o is “worse-or-as-bad” as long as $|f| \leq \tau(n_c;n_o)$. This illustrates the odd effects resulting from the discrete nature of the Poisson Law.

- if $n_c \leq n_o$
  - if $|f| < \tau(n_o-1;n_o)$ then
  $$\begin{aligned} p(f;n_o) &= 1 - \textstyle\sum_{n'_o=\tilde{n}+1}^{n_o-1} g(n'_o;f) \text{ where } \left\{ \begin{array}{ll} \text{if } |f| < \tau(0;n_o) & \tilde{n} = -1 \\ \text{if } |f| \geq \tau(0;n_o) & \tilde{n} \text{ is such that} \\ & \tau(\tilde{n};n_o) \leq |f| < \tau(\tilde{n}+1;n_o) \end{array} \right. \\ &= 1 - F_{\chi^2}(2\mu;2(\tilde{n}+1)) + F_{\chi^2}(2\mu;2n_o) \end{aligned}$$
  - if $\tau(n_o-1;n_o) \leq |f| \leq \tau(n_o+1;n_o)$ then
  $$p(f;n_o) = 1$$

  Again one finds a case where $p(f;n_o) = 1$ for $f \neq \hat{f} = \sqrt{n_o - C}$ [4]. The situation is illustrated on figure C.15 showing that for $|f| \in [\tau(n_o-1;n_o);\tau(n_o+1;n_o)]$, any alternative to n_o is “worse-or-as-bad”

---

[4] From equations (C.16), one can check that the MLE is within this interval, $\hat{f} = \sqrt{n_o - C} \in [\tau(n_o-1;n_o);\tau(n_o+1;n_o)]$

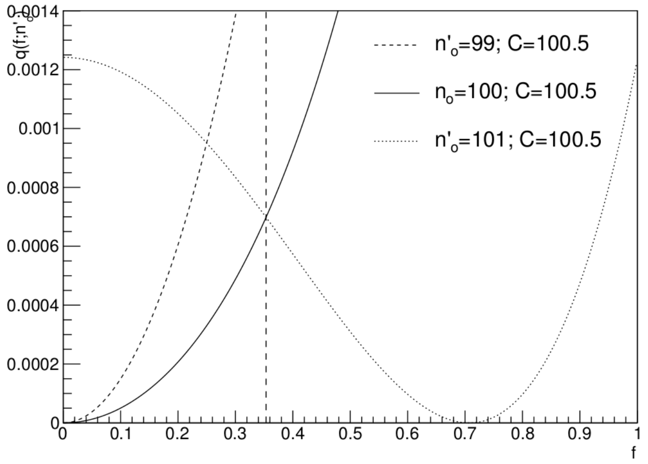

Figure C.14: Example of the $n_o = n_c - 1$ case. The vertical line is $f = \tau(n_c; n_o)$. In the range $|f| \in [0; \tau(n_c; n_o)]$, $\forall n'_o\ q(f; n'_o) \geq q(f; n_o)$ and so $p(f; n_o) = 1$

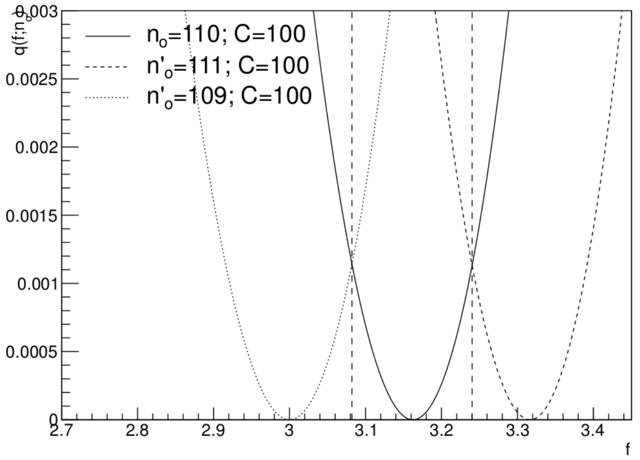

Figure C.15: Details of the $[\tau(n_o - 1; n_o); \tau(n_o + 1; n_o)]$ area. The vertical lines are $f = \tau(n_o - 1; n_o)$ and $f = \tau(n_o + 1; n_o)$. In the range $|f| \in [\tau(n_o - 1; n_o); \tau(n_o + 1; n_o)]$, $\forall n'_o\ q(f; n'_o) \geq q(f; n_o)$ and so $p(f; n_o) = 1$

- if $\tau(n_o + 1; n_o) < |f|$ then

$$\begin{aligned} p(f; n_o) &= 1 - \textstyle\sum_{n'_o = n_o+1}^{\tilde{n}} g(n'_o; f) \text{ where } \tilde{n} \text{ is such that } \tau(\tilde{n}; n_o) < |f| \leq \tau(\tilde{n}+1; n_o) \\ &= 1 - F_{\chi^2}(2\mu; 2(n_o + 1)) + F_{\chi^2}(2\mu; 2(\tilde{n} + 1)) \end{aligned}$$

C.5.2.4 p-value vs f function

So the p-value function $p(f; n_o)$ is defined by ranges and is discontinuous as illustrated on figures C.6. The general pattern of the domains of the “worse-or-as-bad” and “better” categories in the space (f, n'_o), as shown on figures C.13, as well as the location of the $n'_o = \mu$ and $n'_o = \mu \pm \sqrt{\mu}$ curves help to understand the shape of the p-value function. The p-value as defined by (C.13) is a sum of the probabilities of the “worse-or-as-bad” n'_o. It can be seen as the probability in the tails of the Poisson distribution the mean value of which can be followed on figures C.13.

When $n_o \leq n_c - 1$, one sees on figure C.13(a), that at very low $|f|$ the probability in the tails will be high. Thus one starts from a high $p(f; n_o)$ value as shown on figure C.6(a). When $|f|$ increases the mean value of the Poisson distribution increases. This decreases the probability in the lower tail the edge of which is constant with f. Since the edge of the upper tail increases faster than μ does, the probability in this tail decreases too. So globally the function $p(f;n_o)$ decreases. However locally the $p(f;n_o)$ can increase as shown on figure C.6(a) over a range over which the terms in (C.13) remains unchanged.

The case $n_c \leq n_o$ is different as one can see on figure C.13(b). At low $|f|$, one can start from a high or a low $p(f;n_o)$ value depending on whether n_c is close or not to n_o. In both cases however $p(f;n_o)$ increases with $|f|$, until $|f|$ is close to $\hat{f}$ where $p(f;n_o)$ reaches 1. Above $\hat{f}$, the situation is similar to the $n_o \leq n_c - 1$ case and $p(f;n_o)$ decreases. Again this is a global trend only.

From this description, it is clear that the condition (C.14) has no reason to be fulfilled by finding an equal amount of probability in the low and upper tails of the Poisson distribution. This is in net contrast with the logic behind the $\Delta \ln L$ method quite explicit in the equation (C.12). The comparison with the $\Delta \ln L$ will be explored in more details below.

C.5.2.5 Looking for ends of Confidence Interval

Because the p-value function $p(f;n_o)$ is discontinuous applying the condition (C.14) is not straightforward.

First, the discontinuities pose the problem of how to deal with the ends of the ranges. For instance, say that one is examining the values of f in one of such ranges, $]a,b]$; the limit of $f(a+\epsilon)$ for $\epsilon > 0$ when $\epsilon \to 0$ is defined but it is not equal to $f(a)$, $\lim_{\epsilon\to 0+} f(a+\epsilon) \neq f(a)$. A priori, this excludes the point $(a, \lim_{\epsilon\to 0+} f(a+\epsilon))$ when looking for the ends for Confidence Intervals. This does not look to be appropriate and we consider here such a point as a legitimate part of the curve. This means that all the ends of the ranges on which the function is defined, are treated as bi-valued.

Then due to the discontinuities, there could be that there is simply no f such that $p(f;n_o) = \alpha$. So one can think that the condition (C.14) should be replaced by a “as close as possible to α” criteria and after further thinking, by “as close as possible to α from below” criteria since one does not want to get interval of Confidence Level lower than $(1-\alpha)100\%$. This leads to the “Simple prescription” that the end interval f_l is such that:

$$\text{Simple Prescription: } f_l \mid \forall f \mid p(f;n_o) \leq \alpha,\, p(f;n_o) \leq p(f_l) \leq \alpha$$

This prescription leads to Coverage performance far better than the $\Delta \ln L$ method as illustrated by the figure C.16 showing the Coverage probability in the (C, f^2) plane for $f \geq 0$, with this prescription. Comparing to the figure C.5, it is clear that both Over-Coverage and Under-Coverage are reduced. Unfortunately some Under-Coverage spots remain although much smaller than in the $\Delta \ln L$ case: over the area covered by the figure C.16, the Coverage probability is nowhere found lower than 94%.

After inspection, the Under-Coverage spots of the “Simple prescription” look to be related to cases such as the one shown on figure C.17(a): above the choosen interval end, i.e here outside the Confidence Interval, there are values of f such that $p(f;n_o) > \alpha$.

So one gives up the “Simple prescription” and adopts the new “Proper prescription”: consider all the intervals verifying that any f outside the interval has a p-value lower than α and take the shortest of these intervals as the Confidence Interval. The result is shown on figure C.17(b). One notes that as shown on figure C.17(b), there could be some values of f inside the Confidence Interval such that $p(f;n_o) < \alpha$. To exclude them would lead to not simply connected segments.

As shown in the main text, the p-value method with the “Proper prescription” never under-covers.

C.5.2.6 Comparison with the $\Delta \ln L$ method

The most direct comparison of the Confidence Intervals obtained with the p-value method and the $\Delta \ln L$ method consists in asking, for a given interval obtained in the p-value method, what would be the n_σ that one would have to use to get the same interval in the $\Delta \ln L$ method (cf (C.11)). This amounts to compute the test statistics $\chi(f;n_o)$ at the interval ends. The figures C.18(a), C.18(b), and C.18(c) show $\chi(f;n_o)$ as a function of n_o for increasing values of C.

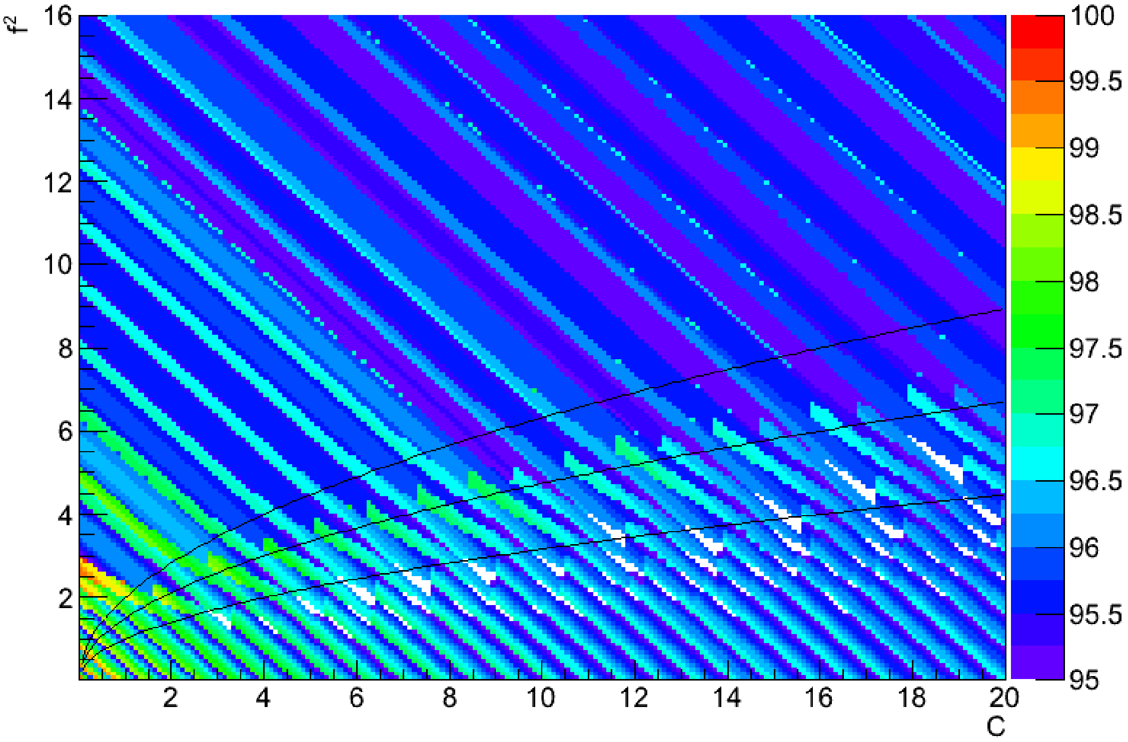

Figure C.16: Coverage probability in the (C, f^2) plane with $f \geq 0$ for the 95 % Confidence Level intervals of the p-value method with the "Simple Prescription". Only Coverage probabilities greater than 95% are shown. The three solid lines are the curves $f^2 = a\sqrt{C}$ for $a = 2, 1.5$ and 1.

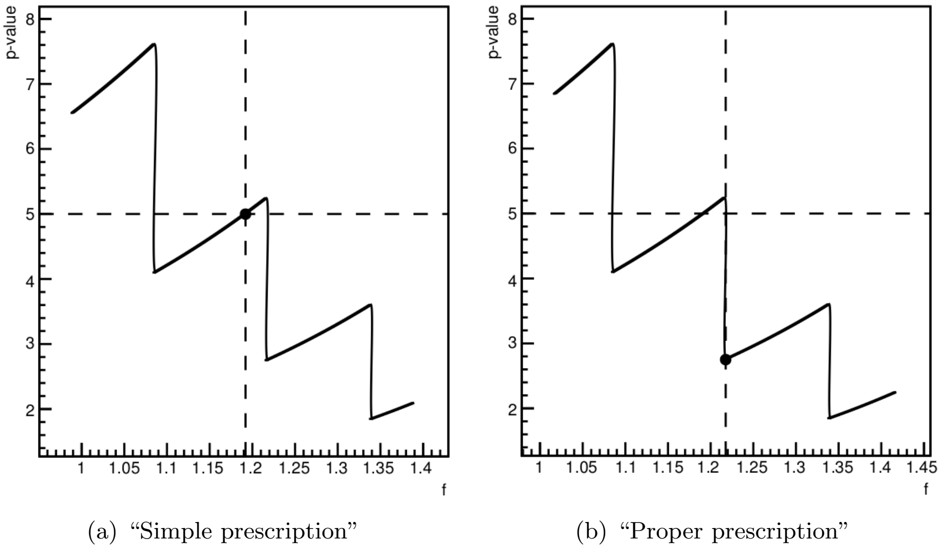

(a) "Simple prescription" (b) "Proper prescription"

Figure C.17: Example of locations of the intervals ends for the p-value method with the "Simple prescription" or the "Proper prescription". The vertical lines show the positions of the selected interval end. The horizontal line gives the targeted value, here 5% for a 95% Confidence Level Interval.

At low C, as on figure C.18(a), the equivalent n_σ of the outermost end is systematically greater than the 1.96 value of the $\Delta \ln L$ method. The equivalent n_σ of the innermost end in case of two intervals follows the same trend for high n_o. However for lower n_o, it is on the contrary much lower than 1.96. This implies that one obtains two disjunct intervals in the p-value method for lower n_o than in the $\Delta \ln L$ method.

When C increases, as on figure C.18(b). the equivalent n_σ of both the innermost and the outermost ends remains higher than 1.96 at high n_o. However at low n_o, the equivalent n_σ starts from lower and lower values, apparently closer and closer to 1.64.

At high C an asymptotic regime clearly sets in as shown on figure C.18(c). As n_o increases, both innermost and the outermost ends flip from a regime with $n_\sigma \sim 1.64$ to a regime with $n_\sigma \sim 1.96$.

This situation can be understood by studying two n_o values in the most simple case represented by the figure C.13(a) corresponding to $C = 50.5$.

For instance when $n_o = 30$ only one interval is obtained. The position of the interval end, close to 1.8, in the (f, n_o') plane is shown on the figure C.13(a). As it can be understood from the position of the mean value of the Poisson distribution, the p-value is mostly equal to the probability in the upper tail of the distribution. Then one understands that a value $\chi(f; n_o) \sim 1.64$ is found. Indeed, since the mean value is high enough, one can approximate the Poisson distribution by a Gaussian distribution and as it is known, a probability of 5% is found in an upper tail of a Gaussian law above 1.64 σ.

In a similar way when $n_o = 65$ two intervals are obtained. The outermost end is found close to 5.6 while the innermost end is close to 1.4. From the location of the innermost end in the (f, n_o') plane shown on the figure C.13(b), it is clear that for this end the situation is similar to the previous studied case: an asymmetric tails configuration leads to a value $\chi(f; n_o) \sim 1.64$. On the contrary the location of the outermost end shows that the tails will be symmetric. Following the same lines of reasoning, one understands then that a value $\chi(f; n_o) \sim 1.96$ is to be expected since a probability of 2.5% is indeed found in an upper tail of a Gaussian law above 1.96 σ.

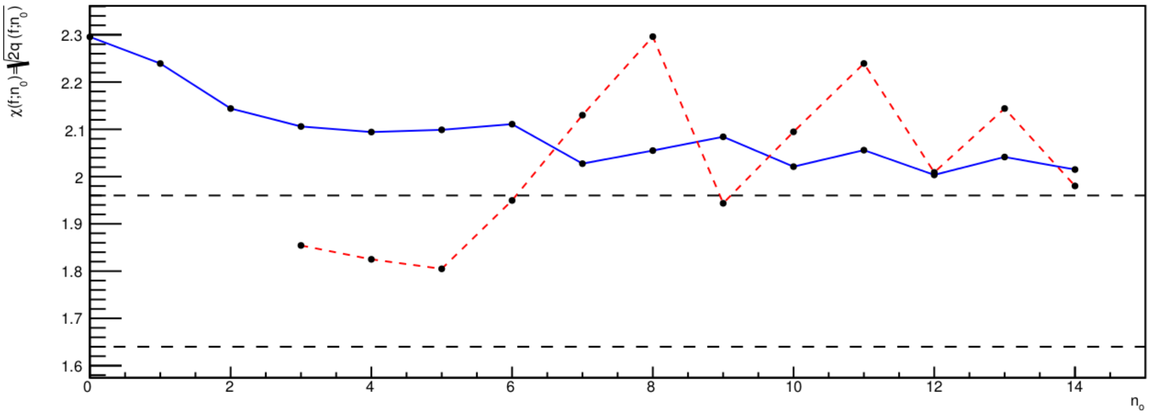

(a) $C = 0.5$

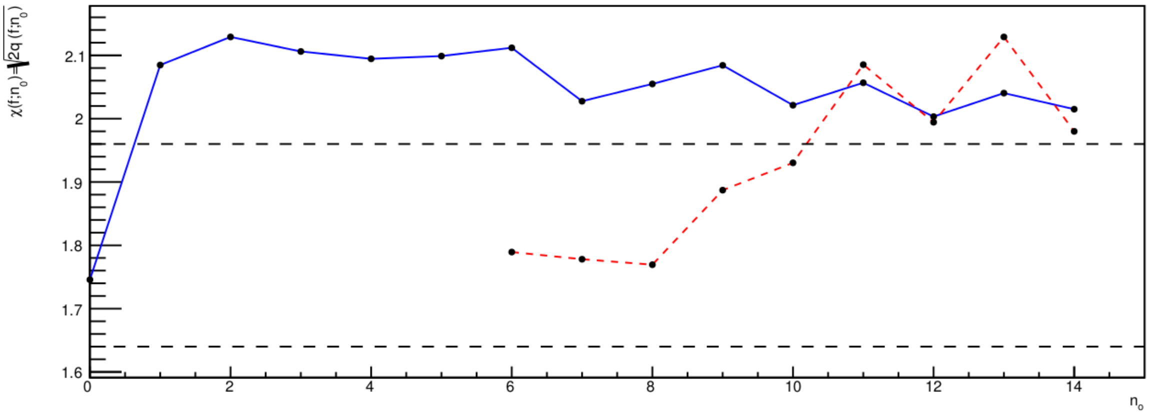

(b) $C = 2.5$

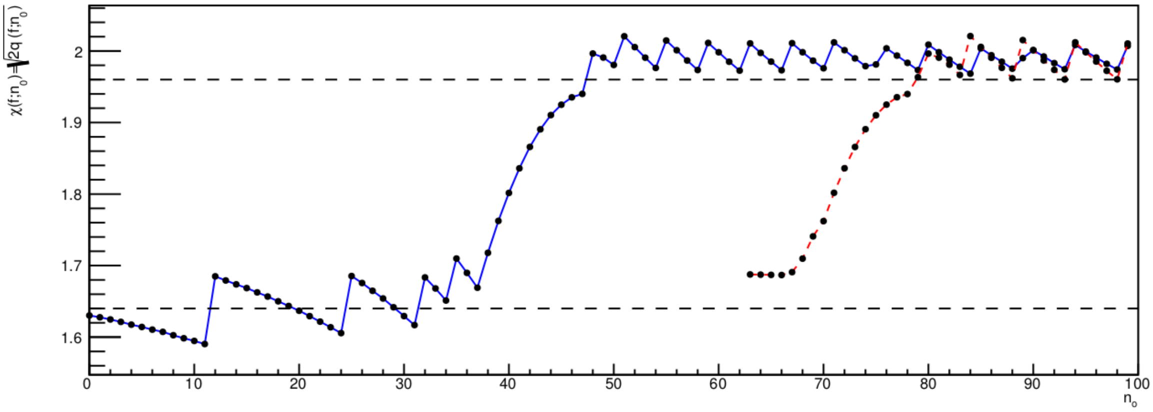

(c) $C = 50.5$

Figure C.18: $\chi(f;n_o) = \sqrt{2q(f;n_o)}$ for the ends of the 95 % Confidence Level intervals of the p-value method with the "Proper prescription", for $C = 0.5$. The blue solid curve corresponds to the outermost interval ends. The red dashed curve corresponds to the innermost interval ends when two intervals are obtained. The black dashed lines are the curves $\chi = 1.96$ and $\chi = 1.64$.

C.5.3 Coverage of the p-value method

Whatever the Confidence Interval method is, we have seen that the Coverage probability is given by the equation (C.2), i.e

$$C(f) = \sum_{n_o \in A(f)} g(n_o; f) \tag{C.19}$$

where $A(f)$ is the set of the observations for which f is in the Confidence Interval $CI(n_o)$

$$A(f) = \{n_o \mid f \in CI(n_o)\}$$

This divides the observations in two sets: a set of the "accepted" observations, $\{n_o^a\} = A(f)$, which enter in the sum (C.19), and the set of the "rejected" observations, $\{n_o^r\} = A(f)^{\complement}$ which do not.

Lets consider the "rejected" observations set. One orders these observations according to the values of their Likelihood ratios $R\,(f, n_o^r)$ and one picks up the "best-according-to-R-for-f" of them, $\tilde{n}_o^r$, i.e it is such that $R\,(f, \tilde{n}_o^r)$ is the greatest of the set of the $\{R\,(f, n_o^r)\}$ [5].

Now one looks for observations n_o strictly "better-according-to-R-for-f" than $\tilde{n}_o^r$, i.e. such that $R\,(f, n_o) > R\,(f, \tilde{n}_o^r)$. One has adopted a notation for this set when one defined the p-value in (C.13):

$$B(f, \tilde{n}_o^r) = \{n_o \mid R(f; n_o) > R(f; \tilde{n}_o^r)\}$$

By construction, these observations do not belong to the "rejected" set since $\tilde{n}_o^r$ is the "best-according-to-R-for-f" of the "rejected". So all observations n_o "better-according-to-R-for-f" than $\tilde{n}_o^r$ belong to the accepted set $\{n_o^a\}$, i.e $B(f, \tilde{n}_o^r) \subset A(f)$. So looking back to the sum in (C.19), one gets that

$$C(f) = \sum_{n_o \in A(f)} g(n_o; f) \geq \sum_{n_o \in B(f, \tilde{n}_o^r)} g(n_o; f)$$

so that using (C.13) one gets

$$C(f) > 1 - p(f; \tilde{n}_o^r) \tag{C.20}$$

In the general case, the result (C.20) does not bring too much. But in the case of the p-value method with the Proper prescription, it implies that the method covers. Indeed since by definition $\tilde{n}_o^r$ belongs to the "rejected" set, one has $\tilde{n}_o^r \notin A(f)$, i.e $f \notin CI(\tilde{n}_o^r)$. The latter condition, in the case of the p-value method with the Proper prescription, implies $p(f; \tilde{n}_o^r) < \alpha$. So the result (C.2) becomes

$$C(f) > 1 - \alpha$$

Therefore the p-value method with the Proper prescription covers.

---

[5] The existence of a finite $\tilde{n}_o^r$ is granted if the set $\{n_o^r\}$ is finite. If it is not, then to require that a finite $\tilde{n}_o^r$ exists possibly imposes a restriction on the admissible distributions $g(n_o; f)$ and Confidence Interval methods. Still this seems granted for the distributions of interest which verify $g(n_o; f) \to 0$ when $n_o \to \infty$, as the one considered here, and the Confidence Interval methods for which $A(f)$ is finite as those studied here.

C.5.4 Equivalence of the p-value and Feldman-Cousins methods

The Feldman-Cousins method [163] is a Neyman construction of Confidence Intervals with a specific ordering principle.

First the method starts by building intervals not over the parameter axis for a fixed observation n_o, but over the observations axis for a fixed f. Lets call these intervals Observation Intervals and note them $OI(f)$. For a given f, one builds $OI(f)$ by gathering the observations in the decreasing order of their Likelihood Ratios while summing up their probabilities, and we continue this up to getting a total sum just exceeding $1-\alpha$

$$\sum_{n'_o \in OI(f)} g(n'_o; f) \geq 1-\alpha \tag{C.21}$$

where the sum runs on the observations ordered by decreasing Likelihood Ratios.

Then the Confidence Interval $CI_{FC}(n_o)$ is formed by collecting all the f such that $n_o \in OI(f)$

$$CI_{FC}(n_o) = \{f | n_o \in OI(f)\} \tag{C.22}$$

Lets consider a f which does not belong to $CI_{FC}(n_o^X)$ for a given n_o^X, i.e from (C.22), such that $n_o^X \notin OI(f)$. Then lets consider the sum over the observations strictly "better-according-to-R-for-f" than n_o^X which enters in the definition of the p-value (C.13)

$$1 - p(f, n_0^X) = \sum_{n'_o \in B(f, n_0^X)} g(n'_o; f) \tag{C.23}$$

where by definition of $B(f, n_0^X)$ in (C.13), the sum runs over all the n'_o such that $R(f; n'_o) > R(f; n_0^X)$. By construction of $OI(f)$, one has $OI(f) \subset B(f, n_o^X)$. Therefore

$$\sum_{n'_o \in B(f, n_0^X)} g(n'_o; f) > \sum_{n_o \in OI(f)} g(n_o; f)$$

So from (C.21) and (C.23) one gets

$$f \notin CI_{FC}(n_o^X) \Leftrightarrow p(f, n_0^X) < \alpha \tag{C.24}$$

The Proper Prescription for the p-value method that we described in preceding sections is to take the shortest simply connected interval such that

$$f \notin CI(n_o^X) \Rightarrow p(f, n_0^X) < \alpha$$

Comparing this to (C.24), and noting the "$\Rightarrow$" and the "$\Leftrightarrow$", one sees that the intervals of the p-value method are larger that those of the Feldman-Cousins method.

One saw that in order to get simply connected intervals, the Proper Prescription allows f-ranges within the Confidence Interval which have p-value lower than α. These "bad" f-ranges are what enlarges the intervals of the p-value method with respect to those of the Feldman-Cousins method. Would these ranges be removed, the two methods would be identical.

Actually the Feldman-Cousins method advised in [163] is not exactly (C.24). Indeed one finds in this paper the same prescription touching simply connected intervals (p 3878 of [163]) than the one we used here. Therefore the two methods, the p-value method with Proper Prescription and the "real" Feldman-Cousins method are identical in all details.

Appendix D

Muon Momentum Resolution

In this appendix, I derive analytical formulas for rought estimates of the resolution on the measurement of the momentum of a muon in the ATLAS Muon Spectrometer using idealizations of the Magnetic Field and of the detection units.

In the first section D.1, I express position and direction changes of a point moving in a plane as integrals on curvature radius. In the second section D.2, I estimate the resolutions on the measurement of the position and the angle of a Segment of a muon Track crossing a MDT Station.

The results of the two first sections are used in the third section D.3 to compute the resolution on the measurement of the momentum of a muon from the local measurements of the angles and the positions of a muon trajectory intersecting a set of "Measurement" lines which idealize the Muon Spectrometer Stations. The contribution of the Multiple scattering effects to the momentum resolution is estimated in the fourth section D.4.

The sections D.3 and D.4 offer estimates of the momentum resolution using "archetypal" methods for the measurement of the momentum, the Three-Points, Angle-Point and Angle-Angle Methods, which are idealizations of the actual means by which the momentum is measured. They are convenient for the simple analytical treatment that they allow while still accurately reflecting the real instrumental conditions: the Three-Points Method corresponds to measurements in the Barrel Muon Spectrometer Toroid where three Stations provide trajectory measurements and the trajectory bending occurs between the first and the last Stations; the Angle-Point Method corresponds to measurements in the End Cap Muon Spectrometer Toroid where again three Stations measure the trajectory but the bending occurs only between the first and second Stations; the Angle-Angle Method correspond to various places in the Muon Spectrometer where, due to imperfect acceptance coverage, only Two Stations are measuring the trajectory.

Each of these Methods uses only a subset of the available local measurements, e.g. the Three-Points Method uses three position measurements but not the three angles measurements which nevertheless are performed together with the position measurements. They are simplifications of the actual reconstruction algorithm which builds from all the available measurements.

In the last section D.5, a generalization is discussed. It allows to obtain the covariance matrix of the measurement of the parameters of a Track, not just the momentum but the position and angle as well. Any number of local measurements can be included not just those retained by the archetypal methods.

It is found that the much simpler archetypal methods do capture already the most important instrumental effects for the moment resolution and do provide estimates almost unchanged when all local measurements are used. However only the generalized method allows to discuss correlations between the measurements of the parameters of a track. In particular, the incidence angle and the momentum of a track are found highly correlated.

D.1 Deflections in position and direction for a point moving in a plane

One considers a curve in the (x, y) plane extending from a “Begin” point $(x = x_B, y = 0)$ to an “End” point $(x = x_E, y = H)$.

One introduces the curvilinear coordinate l and parametrizes the coordinates of a point on the curve as functions of l, $(x(l), y(l))$, so that $l = 0$ and l_{max} correspond to “Begin” and “End” points.

We call $\alpha(l)$ the angle between the unit tangent vector $\vec{T}$ and the x axis, and α_B and α_E its values at “Begin” and “End” points, see figure D.1.

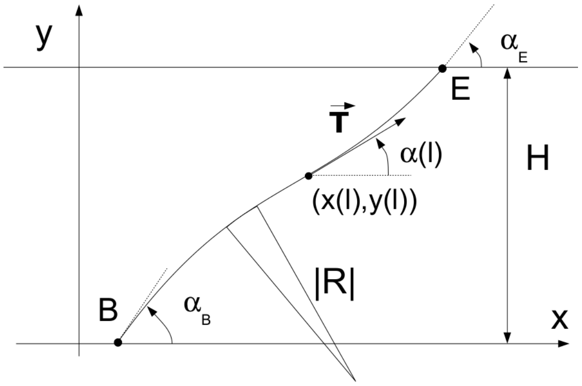

Figure D.1: 2D-curve extending from x-axis to $x = x_E$ straight line.

The aim is to express the variation of the x coordinate, $\Delta x = x_E - x_B$ and the variation of the α angle, $\Delta\alpha = \alpha_E - \alpha_B$, as integrals of the curvature radius R.

One has

$$\Delta x = \int_B^E \frac{dx}{dl} dl \quad \text{(D.1)} \qquad \Delta\alpha = \int_B^E \frac{d\alpha}{dl} dl \quad \text{(D.2)}$$

and by definition of α and R

$$\frac{dx}{dl} = \cot(\alpha)\frac{dy}{dl} \quad \text{(D.3)} \qquad \frac{d\alpha}{dl} = \frac{1}{R} \quad \text{(D.4)}$$

Using (D.3) in (D.1) and integrating by parts, it comes

$$\Delta x = \Delta x^o + \int_B^E (H - y)\frac{d\cot(\alpha)}{dl} dl \quad \text{(D.5)}$$

where $\Delta x^o \equiv H\cot(\alpha_B)$ is the change in x coordinate one gets when there is no deflection, i.e obtained performing a straight line extrapolation from the “begin” point.

Since $(H-y)\cot(\alpha)$ is the x difference between on one hand, the x coordinate at the actual position along the track and on the other hand, the extrapolation on the end line along the tangent from the same position, the second term in (D.5) collects the projections on the end line of each infinitesimal angular deflections.

Using (D.4) in (D.5) and in (D.2), it comes

$$\Delta x = \Delta x^o - \int_B^E (H - y)\frac{1}{\sin(\alpha)^2}\frac{1}{R} dl \quad \text{(D.6)} \qquad \Delta\alpha = \int_B^E \frac{dl}{R} \quad \text{(D.7)}$$

Under the approximation that the deflections are small, i.e $R >> H$, one gets:

$$\Delta x \sim \Delta x^o - \frac{1}{\sin(\alpha_B)}\int_B^E \frac{l_{max} - l}{R} dl \quad \text{(D.8)}$$

The expressions (D.6) and (D.7) are purely Geometry results. From here one takes that the deflections are induced by a Magnetic Field $\vec{B} = B.\vec{x} \wedge \vec{y}$ perpendicular to the (x, y) plane acting on a particle of momentum p and charge q. Therefore the curvature radius R is given for B in Tesla and p in GeV by:

$$\frac{1}{R} = -q\frac{0.3B}{p} \tag{D.9}$$

Using (D.9) in (D.6) and in (D.7), it comes

$$\Delta x = \Delta x^o + q\frac{0.3}{p}\int_B^E (H-y)\frac{B}{\sin(\alpha)^2}dl \tag{D.10}$$

$$\Delta\alpha = -q\frac{0.3}{p}\int_B^E Bdl \tag{D.11}$$

Under the approximation that the deflections are small, one gets:

$$\Delta x \sim \Delta x^o + q\frac{0.3}{p\sin(\alpha_B)}\int_B^E B(l_{max}-l)dl \tag{D.12}$$

If in addition, B is uniform one gets:

$$\Delta x \sim \Delta x^o + q\frac{0.3BH^2}{2p\sin(\alpha_B)^3} \tag{D.13}$$

$$\Delta\alpha \sim -q\frac{0.3BH}{p\sin(\alpha_B)} \tag{D.14}$$

It is interesting to estimate the deflections of the trajectory of a muon of $1TeV$ in the Barrel Muon Spectrometer Toroid. Considering a bending over a distance of $5m$ and taking a typical Magnetic Field of $0.5T$, one obtains a sagitta of $\sim 470\mu m$ for the arc formed by the trajectory and a total angular deflection of $\sim 750\mu rad$.

D.2 Local measurements in MDT

One wants to estimate the resolution on the measurements of the local position and angle in a MDT Station. In the bending plane, the wires of the drift tubes form a grid of points,$\{T_i\}$, see figure D.2. For a given tube one measures the impact parameter, μ_i of the trajectory with respect to the wire.

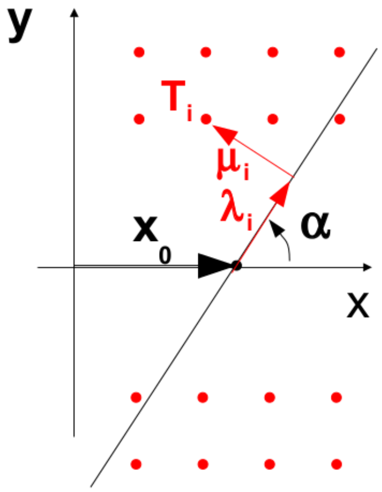

Figure D.2: Fit of a straight line in the plane orthogonal to MDT tube axes

One assumes that the Magnetic Field is weak enough and the momentum high enough for the trajectory to be approximately a straight line in the Station volume. Then an other quantity of interest is λ_i, the distance between the point on the trajectory the closest to T_i and the point where the trajectory crosses the mid-plane between the two MDT Multilayers. One assumes that the resolution of the μ_i measurements is the same for all tubes, σ_{tube}.

One wants to measure x_0 and α, the point where the trajectory crosses this mid-plane and its angle there.

Because the basic measurement is on μ_i, it is easier to work with the product $x_0 \sin(\alpha)$, i.e the projection of the length x_0 on an axis orthogonal to the track. It is then clear that the resolution on $x_0 \sin(\alpha)$ is the statistical combination of the measurements of all the μ_i's:

$$\frac{1}{\sigma(x_0 \sin(\alpha)^2} = \sum_i \frac{1}{\sigma(\mu_i)^2} \tag{D.15}$$

Therefore one has

$$\not\sigma_x \equiv \sigma(x_0 \sin(\alpha)) = \frac{\sigma_{tube}}{\sqrt{N_{tubes}}} \tag{D.16}$$

where N_{tubes} is the total number of crossed tubes.

Along the same lines, it comes that the resolution on α is:

$$\sigma(\alpha) = \frac{\sigma_{tube}}{\sqrt{\sum \lambda_i^2}} \tag{D.17}$$

We assume that the μ_i are small enough with respect to the Station thickness so that one can do the approximation $\lambda_i \sim y_i / \sin(\alpha)$. Therefore on has

$$\not\sigma_\alpha \equiv \sigma(\alpha / \sin(\alpha)) \sim \frac{\sigma_{tube}}{\sqrt{\sum y_i^2}} \tag{D.18}$$

It is convenient to write this as

$$\not\sigma_\alpha \sim \frac{\sigma_{tube}}{\sqrt{N_{tubes}}} \frac{2}{Y} \tag{D.19}$$

where $Y \equiv 2\sqrt{\frac{\sum y_i^2}{N_{tubes}}}$ is a measure of the distance between the MDT Multilayers.

Since N_{tubes} is approximately proportional to $1/\sin(\alpha)$, one has

$$\not\sigma_x \sim \not\sigma_x^0 \sqrt{\sin(\alpha)} \tag{D.20}$$

$$\not\sigma_\alpha \sim \not\sigma_\alpha^0 \sqrt{\sin(\alpha)} \tag{D.21}$$

with

$$\not\sigma_x^0 = \frac{\sigma_{tube}}{\sqrt{N_{tubes}^{\perp}}} \tag{D.22}$$

$$\not\sigma_\alpha^0 = \frac{\sigma_{tube}}{\sqrt{N_{tubes}^{\perp}}} \frac{2}{Y} \tag{D.23}$$

where $N_{tubes}^{\perp}$ is the number of tubes crossed at normal incidence.

Taking $N_{tubes}^{\perp} \sim 6$, $\sigma_{tube} \sim 100\mu m$ and $Y \sim 30cm$, one gets

$$\not\sigma_x^0 \sim 41\mu m \tag{D.24}$$

$$\not\sigma_\alpha^0 \sim 270\mu rad \tag{D.25}$$

Such an angular resolution is typical of the BMS Stations. The angular resolution is better for the BIL Stations due to their four Tube Layers per MDT Multilayer and for the BML, BOS and BOL Stations due to their larger distance between their MDT Multilayers. It is definitively worst for the BIS Stations due to the much shorter distance between their MDT Multilayers.

Hereafter we will use the values $\not\sigma_x^0 \sim 40\mu m$ and $\not\sigma_\alpha^0 \sim 300\mu rad$ for numerical estimates.

D.3 Momentum Measurement Methods

One considers the situation represented in figure D.3: a trajectory crosses three parallel “Measurement” lines on which its local position and angle can be measured. One calls H_{12}, H_{23} and H_{13}, the distances between the lines in the y direction and α_B, the angle of the trajectory when it crosses the first plane.

One assumes that the resolution of local position and angle measurements are the same for all the “Measurement” lines. From the results of the section D.2, we get that is appropriate to work with the resolution on $x_i \sin(\alpha)$, $\not\sigma_x$ and with the resolution on $\alpha/\sin(\alpha)$, $\not\sigma_\alpha$.

Finally, one assumes the conditions that lead to (D.13) and (D.14) do hold and one specializes to the $q = -1$ case.

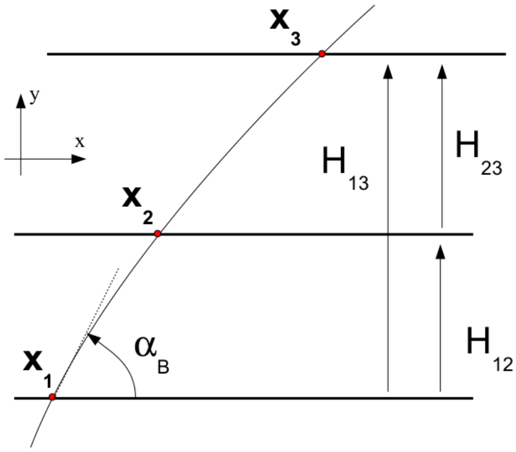

Figure D.3: Muon trajectory crossing three “Measurement” lines where its position and angle can be measured.

Hereafter one considers methods of momentum extraction under specific Magnetic Field and “Measurement” lines configurations and choice on which local measurements are actually used.

D.3.1 Three-Points Method

Here an uniform Magnetic Field applies between all three “Measurement” lines and one uses only the measurements of the local positions x_1, x_2 and x_3 of the trajectory when it crosses them. From (D.13), one gets

$$x_2 - x_1 \sim H_{12}\cot(\alpha_B) - \frac{0.3BH_{12}^2}{2p\sin(\alpha_B)^3} \tag{D.26}$$

$$x_3 - x_1 \sim H_{13}\cot(\alpha_B) - \frac{0.3BH_{13}^2}{2p\sin(\alpha_B)^3} \tag{D.27}$$

The quantity Δ_{3P} which isolates the p dependence and allows to compute it, is

$$\Delta_{3P} = (x_2 - x_1) - (x_3 - x_1)\frac{H_{12}}{H_{13}} \tag{D.28}$$

since indeed

$$\frac{1}{p_{3P}} \sim \frac{2}{0.3B}\frac{\sin(\alpha_B)^3}{H_{12}H_{23}}\Delta_{3P} \tag{D.29}$$

The quantity Δ_{3P} has a simple geometrical meaning illustrated on figure D.4: from the local position measurements on the first and last “Measurement” lines, one extrapolates on the middle “Measurement” line the position of the trajectory if no deflection would have happened; comparing with the actual position, one infers what the actual deflection has been.

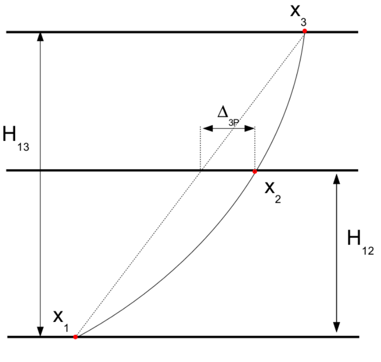

Figure D.4: Three-Points Method. The quantity Δ_{3P} contains all the information on the muon momentum.

Assuming that the most favorable solution $H_{12} = H_{23} = H_{13}/2$ is chosen, it comes that the resolution on p is:

$$\left.\frac{\sigma(p)}{p}\right._{3P} \sim \frac{8\not\sigma_x^0}{0.3BH_{13}^2}\sqrt{\frac{3}{2}}\,p\sin(\alpha_B)^{5/2} \tag{D.30}$$

Assuming that the "Measurement" lines represent the Barrel Stations of the Muon Spectrometer, i.e they are parallel to the beam-axis, then α_B is the polar angle θ and $p\sin(\alpha_B)$ is the transverse momentum p_T. One gets

$${\frac{\sigma(p_T)}{p_T}}_{3P} \sim \frac{8\not\sigma_x^0}{0.3BH_{13}^2}\sqrt{\frac{3}{2}}\,p_T\sin(\theta)^{3/2} \qquad \text{(Barrel)} \tag{D.31}$$

For a position resolution $\not\sigma_x^0 \sim 40\mu m$ and "Barrel" values of Magnetic Field and dimension, i.e $B \sim 0.5T$ and $H_{13} \sim 5m$, one gets for p_T in GeV

$${\frac{\sigma(p_T)}{p_T}}_{3P} \sim 10\%.\ \text{TeV}^{-1}\,p_T\sin(\theta)^{3/2} \qquad \text{(Barrel)} \tag{D.32}$$

There is a η range, intermediate between Barrel and End Cap areas, in which a Three-Points measurement is performed in the Muon Spectrometer (see figure 1.11). In this configuration the "Measurement" lines are orthogonal to the beam-axis and $\alpha_B = \theta + \pi/2$. One gets

$${\frac{\sigma(p_T)}{p_T}}_{3P} \sim \frac{8\not\sigma_x^0}{0.3BH_{13}^2}\sqrt{\frac{3}{2}}\,p_T\cos(\theta)^{3/2}\frac{1}{\tan(\theta)} \qquad \text{(Transition)} \tag{D.33}$$

D.3.2 Angle-Point Method

On considers the case where there is an uniform Magnetic Field between the two first "Measurement" lines but no Magnetic Field between the two last lines. From (D.13) and (D.14), one gets

$$x_2 - x_1 \sim H_{12}\cot(\alpha_B) - \frac{0.3BH_{12}^2}{2p\sin(\alpha_B)^3} \tag{D.34}$$

$$x_3 - x_2 \sim H_{23}\cot(\alpha_B + \Delta\alpha) \text{ with } \Delta\alpha \sim \frac{0.3BH_{12}}{p\sin(\alpha_B)} \tag{D.35}$$

The quantity $\Delta_{\alpha P}$ which isolates the p dependence and allows to compute it, is

$$\Delta_{\alpha P} = (x_2 - x_1) - (x_3 - x_2)\frac{H_{12}}{H_{23}} \tag{D.36}$$

since indeed

$$\frac{1}{p}_{\alpha P} \sim \frac{2}{0.3B}\frac{\sin(\alpha_B)^3}{H_{12}^2}\Delta_{\alpha P} \tag{D.37}$$

The quantity $\Delta_{\alpha P}$ has a simple geometrical meaning illustrated in figure D.5: from the local position measurements on the middle and last "Measurement" lines, one extrapolates on the first "Measurement" line the position of the trajectory would no deflection have happened; comparing with the actual position, one infers what the actual deflection has been.

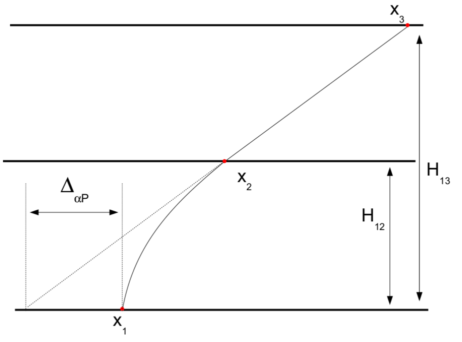

Figure D.5: Angle-Point Method. The quantity $\Delta_{\alpha P}$ contains all the information on the muon momentum.

Assuming that the configuration $H_{12} = H_{23} = H_{13}/2$ has been chosen, it comes:

$${\frac{\sigma(p)}{p}}_{\alpha P} \sim \frac{8\not\sigma_x^0\sqrt{6}}{0.3BH_{13}^2}\,p\sin(\alpha_B)^{5/2} \tag{D.38}$$

The Angle-Point Method is only relevant for the Muon Spectrometer in the End Cap region.

Therefore using $\alpha_B = \theta + \pi/2$, one gets

$$\left.\frac{\sigma(p_T)}{p_T}\right._{\alpha P} \sim \frac{8\not{\sigma}_x^0\sqrt{6}}{0.3BH_{13}^2}\, p_T \cos(\theta)^{3/2} \frac{1}{\tan(\theta)} \tag{D.39}$$

The dependence on the incidence angle on the Tubes Layers of the Barrel resolution (D.31) and of End Cap resolution (D.39) differs by the term $\frac{1}{\tan(\theta)}$. In order to fairly compare the Barrel and End Cap resolutions, it is appropriate to choose a reference angle θ_0 and then to compare Barrel resolution at $\frac{\pi}{2} - \theta_0$ and End Cap resolution at θ_0. Since, apart the term $\frac{1}{\tan(\theta)}$, the dependence of the resolutions on the incidence angle is the same, this is equivalent to write

$$\left.\frac{\sigma(p_T)}{p_T}\right._{\alpha P} \sim \frac{8\not{\sigma}_x^0\sqrt{6}}{0.3BH_{13}^2\tan(\theta_0)}\, p_T \cos(\theta)^{3/2} \frac{\tan(\theta_0)}{\tan(\theta)} \tag{D.40}$$

and to look at the numerical value of the multiplicative factor $\frac{8\not{\sigma}_x^0\sqrt{6}}{0.3BH_{13}^2\tan(\theta_0)}$

For a reference angle corresponding to the pseudo-rapidity ~ 2.2, i.e $\theta_0 \sim 12.6^o$, a position resolution $\not{\sigma}_x^0 \sim 40\mu m$ and "End Cap" values of Magnetic Field and size, i.e $B \sim 1T$ and $H_{13} \sim 11m$, one gets for p_T in GeV

$$\left.\frac{\sigma(p_T)}{p_T}\right._{\alpha P} \sim 10\%.\ \mathrm{TeV}^{-1}\, p_T \cos(\theta)^{3/2} \frac{\tan(\theta_0)}{\tan(\theta)} \tag{D.41}$$

A more complete treatment takes into account the variation of Magnetic Field with the distance to the beam. For the choice of reference angle above, it turns out that one retrieves (D.40) and (D.41) but without the term $\frac{\tan(\theta_0)}{\tan(\theta)}$

D.3.3 Angle-Angle Method

On considers the case where there is an uniform Magnetic Field between all the "Measurement" lines but only the local measurements on two "Measurement" lines, called here lines a and b are available. The momentum measurement will rely then on the capability of the "Measurement" line to measure also local angle. The distance between the two available "Measurement" lines is called here H_{ab}.

In the Angle-Angle Method, one uses only the measurements of the two local angles. From (D.14), one gets

$$\left.\frac{1}{p}\right._{\alpha\alpha} \sim \frac{\sin(\alpha_B)}{0.3BH_{ab}}\Delta\alpha \tag{D.42}$$

which gives

$$\left.\frac{\sigma(p)}{p}\right._{\alpha\alpha} \sim \frac{\sqrt{2}\not{\sigma}_\alpha^0}{0.3BH_{ab}} p \sin(\theta)^{5/2} \tag{D.43}$$

It is convenient to compare the momentum resolution of the Angle-Angle Method to the one that could have been obtained if the Three-Points Method could have been applied, cf (D.30)

$$R_{\alpha\alpha/3P} \equiv \left.\frac{\sigma(p)}{p}\right._{\alpha\alpha} \Big/ \left.\frac{\sigma(p)}{p}\right._{3P} \sim \frac{1}{4\sqrt{3}} \frac{\not{\sigma}_\alpha^0}{\not{\sigma}_x^0} \frac{H_{13}^2}{H_{ab}} \tag{D.44}$$

For position resolution $\not{\sigma}_x^0 \sim 40\mu m$, angular resolution $\not{\sigma}_\alpha^0 \sim 300\mu rad$, "Barrel" value $H_{13} \sim 5m$, and that it is the Medium Station that is missing, i.e $H_{ab} = H_{13}$, one gets

$$R_{\alpha\alpha/3P} \sim 5 \tag{D.45}$$

This indicates a strong degradation of the momentum resolution when only two Stations can be used. Actually this is a quite optimistic estimate since not only it could happen that the missing Station is not the Medium one, but we also considered equal angular resolutions. More realistic estimates are obtained if one considers the possible Stations pairs cases as well as more realistic angular resolutions, i.e $\not\sigma^0_\alpha \sim 500\mu rad$ for BIS Stations, $\not\sigma^0_\alpha \sim 300\mu rad$ for BMS Stations and $\not\sigma^0_\alpha \sim 200\mu rad$ for BIL, BML, BOS and BOL Stations. Noting $\not\sigma_{\alpha^0,a}$ and $\not\sigma_{\alpha^0,b}$ the angular resolution on the two "Measurement lines, the momentum resolution is given by

$$ {\frac{\sigma(p)}{p}}_{\alpha\alpha} \sim \frac{\sqrt{\not\sigma^2_{\alpha^0,a} + \not\sigma^2_{\alpha^0,b}}}{0.3BH_{ab}} p\sin(\theta)^{5/2} \tag{D.46} $$

$$ \text{i.e } R_{\alpha\alpha/3P} \sim \frac{1}{4\sqrt{6}} \frac{\sqrt{\not\sigma^2_{\alpha^0,a} + \not\sigma^2_{\alpha^0,b}}}{\not\sigma^0_x} \frac{H^2_{13}}{H_{ab}} \tag{D.47} $$

One gets the results of the table D.1: all configurations gives degradation by more than a factor 5 but the BIL-BOL case owing to the good angular resolutions of these Stations.

Configuration	$\not\sigma_{\alpha^0,a}(\mu rad)$	$\not\sigma_{\alpha^0,b}(\mu rad)$	$H_{ab}(m)$	$R_{\alpha\alpha/3P}$
BIS-BMS	500	300	2.5	15
BMS-BOS	300	200	2.5	9
BIS-BOS	500	200	5	7
BIL-BML	200	200	2.5	7
BML-BOL	200	200	2.5	7
BIL-BOL	200	200	5	4

Table D.1: Ratio of momentum resolutions of the Angle-Angle and Three-Points Methods for different scenarios

D.3.3.1 Trying to rescue the Angle-Angle Method: the Angle-Two-Points Method

In view of the degradation of the momentum resolution when only two "Measurement" line are available and only the two local angles are measured, see D.3.2, one can wonder if the addition of some local point measurement could help.

Hereafter we look for the momentum resolution when two points and one angle are measured. Latter, in section D.5, we will consider the case where all local angle and position measurements are used, but for now, in the approach of the simple methods explored here, we restrict our computations to three local measurements at most.

One assumes that the local angle is measured on the "Measurement" line b. One has

$$ x_b - x_a \sim H_{ab}\cot(\alpha_B) - \frac{0.3BH^2_{ab}}{2p\sin(\alpha_B)^3} \tag{D.48} $$

$$ \alpha_b \sim \alpha_B + \frac{0.3BH_{ab}}{p\sin(\alpha_B)} \tag{D.49} $$

The quantity $\Delta_{\alpha 2P}$ which isolates the p dependence and allows to compute it, is

$$ \Delta_{\alpha 2P} = (x_b - x_a) - H_{ab}\cot\alpha_b \tag{D.50} $$

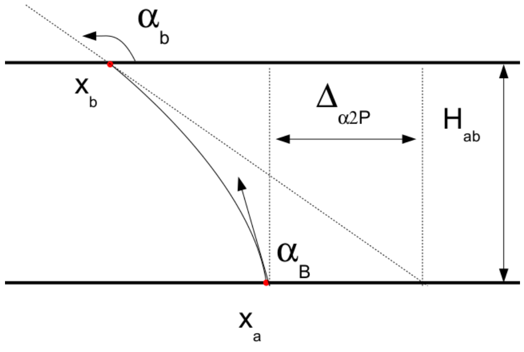

Figure D.6: Angle-Two-Points Method. The quantity $\Delta_{\alpha 2P}$ contains all the information on the muon momentum.

since indeed

$$ \frac{1}{p}_{\alpha 2P} \sim \frac{2}{0.3B} \frac{\sin(\alpha_B)^3}{H^2_{ab}} \Delta_{\alpha 2P} \tag{D.51} $$

The quantity $\Delta_{\alpha 2P}$ has a simple geometrical meaning illustrated in figure D.6: from the measurement of the local position and angle on the "Measurement" line b, one extrapolates to the "Measurement" line a the position of the trajectory as if no deflection would have happened; comparing with the actual position, one infers what the actual deflection has been.

It comes:

$$\frac{\sigma(p)}{p}_{\alpha 2P} \sim \frac{2\sqrt{2\not\sigma^2_{x^0,b} + H^2_{ab}\not\sigma^2_{\alpha^0,b}}}{0.3BH^2_{ab}}\, p\sin(\alpha_B)^{5/2} \tag{D.52}$$

i.e

$$R_{\alpha 2P/\alpha\alpha} \equiv {\tfrac{\sigma(p)}{p}}_{\alpha 2P} \Big/ {\tfrac{\sigma(p)}{p}}_{\alpha\alpha} \sim 2\frac{\not\sigma_{\alpha^0,b}}{\sqrt{\not\sigma^2_{\alpha^0,a} + \not\sigma^2_{\alpha^0,b}}}\sqrt{1+2\epsilon^2_{x\alpha}} \tag{D.53}$$

or

$$R_{\alpha 2P/3P} \equiv {\tfrac{\sigma(p)}{p}}_{\alpha 2P} \Big/ {\tfrac{\sigma(p)}{p}}_{3P} \sim \frac{1}{2\sqrt{6}}\frac{\not\sigma_{\alpha^0,b}}{\not\sigma^0_x}\sqrt{1+2\epsilon^2_{x\alpha}}\frac{H^2_{13}}{H_{ab}} \tag{D.54}$$

with

$$\epsilon_{x\alpha} = \frac{\not\sigma_x}{H_{ab}\not\sigma_\alpha} \tag{D.55}$$

For position resolution $\not\sigma^0_x \sim 40\mu m$, angular resolution $\not\sigma^0_\alpha \sim 300\mu rad$ and "Barrel" value $H_{ab} \sim 5m$, i.e $\epsilon_{x\alpha} \sim 0.027$, one gets

$$R_{\alpha 2P/\alpha\alpha} \sim 1.41 \text{ and } R_{\alpha 2P/3P} \sim 8 \tag{D.56}$$

Clearly in these conditions, the Angle-Two-Points Method is the worst of all. The result $R_{\alpha 2P/\alpha\alpha} \sim \sqrt{2}$, indicates that, in these conditions, the Angle-Two-Points Method exploits a single local angle measurement while the Angle-Angle Method exploits two of equal qualities.

However if the angular resolutions are unequal, since the Angle-Two-Points Method can exploit the best of the local angle measurements while the Angle-Angle Method can be spoiled by the worst of them, the Angle-Two-Points Method can turn out to be better than the Angle-Angle Method, as it is actually clearly possible from (D.53), .

Considering the "realistic" scenarios of the preceding section and using for each of them, the best measured local angle for the Angle-Two-Points Method, one gets the results of the table D.2. One sees that, since all the Stations in the large sectors have the same angular resolution no gain in to be expected from the Angle-Two-Points Method. However due to the very different angular resolutions involved in the BIS-BOS scenario, the Angle-Two-Points Method performs slightly better. There is not such an improvement for the BIS-BMS and BMS-BOS scenarios since the angular resolutions are not different enough. However in these scenarios, a better use of the best angular measurement is made in the Angle-Two-Points Method since one finds for them $R_{\alpha 2P/\alpha\alpha} < \sqrt{2}$.

Configuration	$\not\sigma_{\alpha^0,a}(\mu rad)$	$\not\sigma_{\alpha^0,b}(\mu rad)$	$H_{ab}(m)$	$R_{\alpha 2P/\alpha\alpha}$	$R_{\alpha 2P/3P}$
BIS-BMS	500	300	2.5	1.03	15
BMS-BOS	300	200	2.5	1.12	10
BIS-BOS	500	200	5	0.74	5
BIL-BML	200	200	2.5	1.42	10
BML-BOL	200	200	2.5	1.42	10
BIL-BOL	200	200	5	1.42	5

Table D.2: Ratio of momentum resolutions of the Angle-Two-Points, Angle-Angle and Three-Points Methods for different scenarios

D.4 Multiple Scattering contribution

One considers that the effect of the Multiple Scattering effects in the situation represented in figure D.1, can be described by a set of “Multiple Scattering” lines parallel to the x axis on which the trajectory angle is deflected by random angles α_i^{Sc}. Under the approximations that all deflections are small, it comes that the Multiple Scattering contributes to the position and angular deflections by adding to the Magnetic Field deflections (D.13) and (D.14), the terms

$$\Delta^{Sc}x = \frac{1}{\sin(\alpha_B)^2}\sum_i (H - y_i)\alpha_i^{Sc} \tag{D.57}$$

$$\Delta^{Sc}\alpha = \sum_i \alpha_i^{Sc} \tag{D.58}$$

where the sums run on the “Multiple Scattering” lines and the y_i’s are their y coordinates

D.4.1 Application to the Three-Points Method

One looks for the effects of Multiple Scattering on the quantity Δ_{3P} defined by (D.28). It comes that the Multiple Scattering effect adds the term:

$$\delta\Delta_{3P} = \frac{1}{\sin(\alpha_B)^2}\Big[\sum_{12}\alpha_i^{Sc}\big[(H_{12}-y_i)-(H_{13}-y_i)\frac{H_{12}}{H_{13}}\big] - \sum_{23}\alpha_i^{Sc}(H_{13}-y_i)\frac{H_{12}}{H_{13}}\Big] \tag{D.59}$$

where the first sum runs on the “Multiple Scattering” lines between the first and second “Measurement” lines and the second sum runs between the second and last “Measurement” ones. It comes

$$\delta\Delta_{3P} = -\frac{H_{12}H_{23}}{H_{13}\sin(\alpha_B)^2}\Big(\sum_{12}\alpha_i^{Sc}\big[1-\frac{|d_i|}{H_{12}}\big] + \sum_{23}\alpha_i^{Sc}\big[1-\frac{|d_i|}{H_{23}}\big]\Big) \tag{D.60}$$

where $d_i = y_i - H_{12}$ is the distance between the “Multiple Scattering” line and the middle “Measurement” line. The equation (D.60) shows that a “Multiple Scattering” line contributes more if closer to the middle “Measurement” line and not at all if located on the first or on the last “Measurement” line. Then the contribution to the momentum resolution is:

$$\frac{\sigma(p)}{p}\Big|_{3P}^{Sc} \sim \frac{2}{0.3B}\frac{\sin(\alpha_B)}{H_{13}}p\sqrt{\sum_{12}\sigma(\alpha_i^{Sc})^2\big[1-\frac{|d_i|}{H_{12}}\big]^2 + \sum_{23}\sigma(\alpha_i^{Sc})^2\big[1-\frac{|d_i|}{H_{23}}\big]^2} \tag{D.61}$$

where $\sigma(\alpha_i^{Sc})$ is the width of the Gaussian distribution of the angles α_i^{Sc}.

We take that a “Multiple Scattering” line corresponds to a certain amount of matter counted in radiation lengths, X_0^i, in the y direction such that for p in GeV , one has

$$\sigma(\alpha_i^{Sc}) = \frac{0.0136}{p}\sqrt{\frac{X_0^i}{\sin(\alpha_B)}} \tag{D.62}$$

Assuming that the configuration $H_{12} = H_{23} = H_{13}/2$ has been chosen, it comes

$$\frac{\sigma(p)}{p}\Big|_{3P}^{Sc} \sim \frac{2\times 0.0136}{0.3BH_{13}}\sqrt{\sin(\alpha_B)}\sqrt{\sum X_0^i\big[1-\frac{|d_i|}{H_{13}/2}\big]^2} \tag{D.63}$$

In the Muon Spectrometer the matter of each Station amounts for about $\sim 0.3X_0$. Assuming that there is a single “Multiple Scattering” line with such an amount of matter, located on the middle

"Measurement" line, $B \sim 0.5T$, and $H_{13} \sim 5m$, one gets

$$ {\frac{\sigma(p)}{p}}^{Sc}_{3P} \sim 2.0\%\sqrt{\sin(\alpha_B)} \tag{D.64} $$

D.4.2 Application to the Angle-Point Method

One looks for the effects of Multiple Scattering on the quantity $\Delta_{\alpha P}$ defined by (D.36). It comes that the Multiple Scattering effect adds the term:

$$ \delta\Delta_{\alpha P} = -\frac{H_{12}}{\sin(\alpha_B)^2}\Big(\sum_{12}\alpha_i^{Sc}[1-\frac{|d_i|}{H_{12}}] + \sum_{23}\alpha_i^{Sc}[1-\frac{|d_i|}{H_{23}}]\Big) \tag{D.65} $$

The equation (D.65) shows that again, a "Multiple Scattering" line contributes more if closer to the middle "Measurement" line and not at all if located on the first or on the last "Measurement" line. Then the contribution to the momentum resolution of the Multiple Scattering effect is:

$$ {\frac{\sigma(p)}{p}}^{Sc}_{\alpha P} \sim \frac{2}{0.3B}\frac{\sin(\alpha_B)}{H_{12}}p\sqrt{\sum_{12}\sigma(\alpha_i^{Sc})^2[1-\frac{|d_i|}{H_{12}}]^2 + \sum_{23}\sigma(\alpha_i^{Sc})^2[1-\frac{|d_i|}{H_{23}}]^2} \tag{D.66} $$

Assuming that the configuration $H_{12} = H_{23} = H_{13}/2$ has been chosen, it comes

$$ {\frac{\sigma(p)}{p}}^{Sc}_{\alpha P} \sim \frac{4 \times 0.0136}{0.3BH_{13}}\sqrt{\sin(\alpha_B)}\sqrt{\sum X_0^i[1-\frac{|d_i|}{H_{13}/2}]^2} \tag{D.67} $$

Assuming that there is a single "Multiple Scattering" line, amounting for $\sim 0.3X_0$, located on the middle "Measurement" line, and using "End Cap" values $B \sim 1T$ and $H_{13} \sim 11m$, one gets

$$ {\frac{\sigma(p)}{p}}^{Sc}_{\alpha P} \sim 0.9\%\sqrt{\sin(\alpha_B)} \tag{D.68} $$

D.4.3 Application to the Angle-Angle Method

From (D.42) it is clear that the Multiple Scattering effects contributes as

$$ {\frac{\sigma(p)}{p}}^{Sc}_{\alpha\alpha} \sim \frac{\sin(\alpha_B)}{0.3BH_{13}}p\sqrt{\sum\sigma(\alpha_i^{Sc})^2} \sim \frac{0.0136}{0.3BH_{13}}\sqrt{\sin(\alpha_B)}\sqrt{\sum X_0^i} \tag{D.69} $$

Comparing to the result for the Three-points Method (D.63), one gets

$$ R_{3P/\alpha\alpha} \equiv {\frac{\sigma(p)}{p}}^{Sc}_{3P} \Big/ {\frac{\sigma(p)}{p}}^{Sc}_{\alpha\alpha} \sim 2\sqrt{\frac{\sum X_0^i[1-\frac{|d_i|}{H_{13}/2}]^2}{\sum X_0^i}} \tag{D.70} $$

If the total amount of radiation lengths is put on the middle "Measurement" line it comes

$$ R_{3P/\alpha\alpha} \sim 2 \tag{D.71} $$

If the total amount of radiation lengths is distributed uniformly over all the space between the first and last "Measurement" lines, one gets

$$ R_{3P/\alpha\alpha} \sim 2/\sqrt{3} \sim 1.15 \tag{D.72} $$

D.5 Generalization

The preceding results were obtained by first expressing the momentum as a function of the local measurements and then propagating the measurements errors and multiple scattering effects in this expression. This approach becomes difficult, or even impossible, if much more measurements are used. One can expect that there is a way to combine any number of local measurements. This is what is tempted in this section.

D.5.1 General case

One considers N "Measurement" lines indexed by k, on which one measures the trajectory local positions and angles x_k and α_k, and a reference line located before the first "Measurement" line, on which one defines the parameters of the trajectory that we want to measure, x_B, α_B and $\rho = 1/p$, its position, angle and inverse momentum.

First one considers the case with no Multiple Scattering effects. The x_k and α_k quantities are functions of x_B, α_B and $\rho = 1/p$. The variations of x_k and α_k are obtained from those of x_B, α_B and ρ by

$$\begin{pmatrix} \delta x_k \\ \delta \alpha_k \end{pmatrix} = t^k \begin{pmatrix} \delta x_B \\ \delta \alpha_B \\ \delta \rho \end{pmatrix} \text{ with } t^k = \begin{pmatrix} \frac{\partial x_k}{\partial x_B} & \frac{\partial x_k}{\partial \alpha_B} & \frac{\partial x_k}{\partial \rho} \\ \frac{\partial \alpha_k}{\partial x_B} & \frac{\partial \alpha_k}{\partial \alpha_B} & \frac{\partial \alpha_k}{\partial \rho} \end{pmatrix} \tag{D.73}$$

One defines the vector $\vec{\mu}$ to store all the x_k and α_k and the vector $\vec{\tau}$ to store x_B, α_B and ρ so that

$$\mu_{2k-1} = x_k \ , \ \mu_{2k} = \alpha_k \ , \ \tau_1 = x_B \ , \ \tau_2 = \alpha_B \text{ and } \tau_3 = \rho \tag{D.74}$$

Therefore the variations of $\vec{\mu}$ is obtained from the variation of $\vec{\tau}$ by

$$\delta\vec{\mu} = T\delta\vec{\tau} \tag{D.75}$$

where the matrix T is defined by

$$T_{j,i} = \frac{\partial \mu_j}{\partial \tau_i}, \text{ i.e } T_{2k-1,i} = t^k_{1,i} = \frac{\partial x_j}{\partial \tau_i} \text{ and } T_{2k,i} = t^k_{2,i} = \frac{\partial \alpha_j}{\partial \tau_i} \tag{D.76}$$

Then one writes the χ^2 function as:

$$\chi^2 = \sum_k^N \{\epsilon^x_k \frac{\delta x_k^2}{\sigma_x^2} + \epsilon^\alpha_k \frac{\delta \alpha_k^2}{\sigma_\alpha^2}\} = \delta\vec{\mu}^\top W^{\vec{\mu}} \delta\vec{\mu} \tag{D.77}$$

where σ_x and σ_α are some reference local position and angle resolutions and the positive parameters ϵ^s and ϵ^α_k allow for performance differences between the local measurements done on the different "Measurement" lines, and the diagonal matrix $W^{\vec{\mu}}$ is

$$W^{\vec{\mu}}_{i,j} = \delta_{i,j} W^{\vec{\mu}}_{i,i} \text{ with } W^{\vec{\mu}}_{2k-1,2k-1} = \frac{\epsilon^x_k}{\sigma_x^2} \text{ and } W^{\vec{\mu}}_{2k,2k} = \frac{\epsilon^\alpha_k}{\sigma_\alpha^2} \tag{D.78}$$

Using (D.75) in (D.77), one gets

$$\chi^2 = \delta\vec{\tau}^\top W^{\vec{\tau}} \delta\vec{\tau} \text{ with } W^{\vec{\tau}} = T^\top W^{\vec{\mu}} T \tag{D.79}$$

with

$$W^{\vec{\tau}}_{i,j} = \sum_l T_{l,i} T_{l,j} W_{l,l} = \sum_l \frac{\partial \mu_l}{\partial \tau_i} \frac{\partial \mu_l}{\partial \tau_j} W_{l,l} = \sum_{k=1}^N \{T_{2k-1,i} \frac{\epsilon^x_k}{\sigma_x^2} T_{2k-1,j} + T_{2k,i} \frac{\epsilon^\alpha_k}{\sigma_\alpha^2} T_{2k,j}\}$$

i.e

$$W^{\vec{\tau}} =$$

$$\begin{pmatrix} \sum_k \frac{\partial x_k}{\partial x_B}\frac{\epsilon_k^x}{\sigma_x^2}\frac{\partial x_k}{\partial x_B} + \frac{\partial \alpha_k}{\partial x_B}\frac{\epsilon_k^\alpha}{\sigma_\alpha^2}\frac{\partial \alpha_k}{\partial x_B} & \sum_k \frac{\partial x_k}{\partial x_B}\frac{\epsilon_k^x}{\sigma_x^2}\frac{\partial x_k}{\partial \alpha_B} + \frac{\partial \alpha_k}{\partial x_B}\frac{\epsilon_k^\alpha}{\sigma_\alpha^2}\frac{\partial \alpha_k}{\partial \alpha_B} & \sum_k \frac{\partial x_k}{\partial x_B}\frac{\epsilon_k^x}{\sigma_x^2}\frac{\partial x_k}{\partial \rho} + \frac{\partial \alpha_k}{\partial x_B}\frac{\epsilon_k^\alpha}{\sigma_\alpha^2}\frac{\partial \alpha_k}{\partial \rho} \\ \sum_k \frac{\partial x_k}{\partial \alpha_B}\frac{\epsilon_k^x}{\sigma_x^2}\frac{\partial x_k}{\partial x_B} + \frac{\partial \alpha_k}{\partial \alpha_B}\frac{\epsilon_k^\alpha}{\sigma_\alpha^2}\frac{\partial \alpha_k}{\partial x_B} & \sum_k \frac{\partial x_k}{\partial \alpha_B}\frac{\epsilon_k^x}{\sigma_x^2}\frac{\partial x_k}{\partial \alpha_B} + \frac{\partial \alpha_k}{\partial \alpha_B}\frac{\epsilon_k^\alpha}{\sigma_\alpha^2}\frac{\partial \alpha_k}{\partial \alpha_B} & \sum_k \frac{\partial x_k}{\partial \alpha_B}\frac{\epsilon_k^x}{\sigma_x^2}\frac{\partial x_k}{\partial \rho} + \frac{\partial \alpha_k}{\partial \alpha_B}\frac{\epsilon_k^\alpha}{\sigma_\alpha^2}\frac{\partial \alpha_k}{\partial \rho} \\ \sum_k \frac{\partial x_k}{\partial \rho}\frac{\epsilon_k^x}{\sigma_x^2}\frac{\partial x_k}{\partial x_B} + \frac{\partial \alpha_k}{\partial \rho}\frac{\epsilon_k^\alpha}{\sigma_\alpha^2}\frac{\partial \alpha_k}{\partial x_B} & \sum_k \frac{\partial x_k}{\partial \rho}\frac{\epsilon_k^x}{\sigma_x^2}\frac{\partial x_k}{\partial \alpha_B} + \frac{\partial \alpha_k}{\partial \rho}\frac{\epsilon_k^\alpha}{\sigma_\alpha^2}\frac{\partial \alpha_k}{\partial \alpha_B} & \sum_k \frac{\partial x_k}{\partial \rho}\frac{\epsilon_k^x}{\sigma_x^2}\frac{\partial x_k}{\partial \rho} + \frac{\partial \alpha_k}{\partial \rho}\frac{\epsilon_k^\alpha}{\sigma_\alpha^2}\frac{\partial \alpha_k}{\partial \rho} \end{pmatrix} \quad (D.80)$$

Result (D.79) tells that the matrix $W^{\vec{\tau}}$ is the inverse of the covariance matrix, $C^{\vec{\tau}}$, for the x_B, α_B and ρ parameters. Therefore the result (D.80) allows to compute all errors and correlations factors for the measurements of these parameters. For instance the square of the error on ρ is given by:

$$\sigma(\rho) = \sqrt{\frac{W^{\vec{\tau}}_{1.1}W^{\vec{\tau}}_{2,2} - {W^{\vec{\tau}}_{2,2}}^2}{D}} \quad (D.81)$$

where D is the determinant of $W^{\vec{\tau}}$.

In this approach the inclusion of Multiple-scattering effects is straightforward. One introduces N^{Sc} angles of scattering, α_i^{Sc} and considers them as parameters of the trajectory along the parameters x_B, α_B and ρ. To incorporate the α_i^{Sc}, the vector $\vec{\mu}$ is extended to become a $2N + N^{sc}$ vector and the vector $\vec{\tau}$ becomes a $3 + N^{sc}$ vector:

$$\mu_{2N+i} = \alpha_i^{Sc} \text{ and } \tau_{3+i} = \alpha_i^{Sc} \quad (D.82)$$

The elements of matrix T are still given by $T_{j,i} = \frac{\partial \mu_j}{\partial \tau_i}$ but T is now a $(2N + N^{Sc}) \times (3 + N^{Sc})$ matrix. Taking into account that $\frac{\partial \alpha_l^{Sc}}{\partial \alpha_m^{Sc}} = \delta_{l,m}$, $\frac{\partial \alpha_l^{Sc}}{\partial x_B} = 0$, $\frac{\partial \alpha_l^{Sc}}{\partial \alpha_B} = 0$, and $\frac{\partial \alpha_l^{Sc}}{\partial \rho} = 0$, the elements of T are explicitly given by:

$$\forall k \leq N \quad T_{2k-1,i} = \frac{\partial x_k}{\partial \tau_i} \text{ and } T_{2k,i} = \frac{\partial \alpha_k}{\partial \tau_i}$$

$$\text{and } \forall l > 2N, \quad T_{l,i} = \delta_{l-2N,i-3}\mathcal{H}_{4,i} \text{ where } \mathcal{H}_{l,m} = 0 \text{ if } l > m \text{ and } \mathcal{H}_{l,m} = 1 \text{ if } l \leq m \quad (D.83)$$

To weight the likelihood of a given set of α_i^{Sc}, the χ^2 function is modified by adding the term $\sum(\frac{\alpha_i^{Sc}}{\sigma(\alpha_i^{Sc})})^2$ where the sum runs on all the angles of scattering. The matrix $W^{\vec{\mu}}$ is still diagonal, i.e $W^{\vec{\mu}}_{i,j} = \delta_{i,j}W^{\vec{\mu}}_{i,i}$, but it is now a $(2N + N^{Sc}) \times (2N + N^{Sc})$ matrix. The diagonal elements are:

$$\forall k \leq N \quad W^{\vec{\mu}}_{2k-1,2k-1} = \frac{\epsilon_k^x}{\sigma_x^2} \text{ and } W^{\vec{\mu}}_{2k,2k} = \frac{\epsilon_k^\alpha}{\sigma_\alpha^2}, \text{ and } W^{\vec{\mu}}_{2N+i,2N+i} = \frac{1}{\sigma(\alpha_i^{Sc})^2} \quad (D.84)$$

The elements of the matrix $W^{\vec{\tau}}$ are still given by $\sum_l T_{l,i}T_{l,j}W_{l,l}$ but $W^{\vec{\tau}}$ is now a $(3+N^{Sc}) \times (3+N^{Sc})$ matrix. Explicitly they are:

$$W^{\vec{\tau}}_{i,j} = \sum_{k=1}^{N} \{\frac{\partial x_k}{\partial \tau_i}\frac{\epsilon_k^x}{\sigma_x^2}\frac{\partial x_k}{\partial \tau_j} + \frac{\partial \alpha_k}{\partial \tau_i}\frac{\epsilon_k^\alpha}{\sigma_\alpha^2}\frac{\partial \alpha_k}{\partial \tau_j}\} + \frac{1}{\sigma(\alpha_{i-3}^{Sc})^2}\delta_{i,j}\mathcal{H}_{4,i} \quad (D.85)$$

D.5.2 Special case

One specializes the previous general results to the kind of idealized situations we have considered up to now. The “Measurement” lines are parallel to the reference line. The reference line coincides with the first “Measurement” line. One calls h_k the distance between the “Measurement” lines k and $k-1$ and one takes $h_1 = 0$. The Magnetic Field between the “Measurement” lines k and $k-1$, B_k, is taken uniform and small, and one takes $B_1 = 0$. Unless stated otherwise, one does not include multiple scattering effects. One gets

$$x_k = x_B + \cot(\alpha_B) H_k - \frac{0.3\rho}{2\sin(\alpha_B)^3} \not{B}_a^k H_k^2 \tag{D.86}$$

$$\alpha_k = \alpha_B + \frac{\rho}{\sin(\alpha_B)} \not{B}_b^k H_k \tag{D.87}$$

with

$$\not{B}_a^k \equiv \frac{2}{H_k^2} \sum_{k'=2}^{k} B_{k'} \left[H_k h'_k - \frac{1}{2}(H_{k'}^2 - H_{k'-1}^2) \right] \text{ and } \not{B}_b^k \equiv \frac{1}{H_k} \sum_{k'=1}^{k} B_{k'} h_{k'} \tag{D.88}$$

$$\text{with } H_k \equiv \sum_{k'=1}^{N} h_{k'} \tag{D.89}$$

Then the matrix t^k is

$$t^k = \begin{pmatrix} 1 & -\frac{H_k}{\sin(\alpha_B)^2} \mathbb{1}_{\not{a}} & \frac{-0.3\not{B}_a^k H_k^2}{2\sin(\alpha_B)^3} \\ 0 & \mathbb{1}_{\not{b}} & \frac{0.3\not{B}_b^k H_k}{\sin(\alpha_B)} \end{pmatrix} \tag{D.90}$$

$$\text{where } \mathbb{1}_{\not{a}} = 1 - \frac{0.9\not{B}_a^k H_k \rho}{2\sin(\alpha_B)\tan(\alpha_B)} \text{ and } \mathbb{1}_{\not{b}} = 1 - \frac{0.3\not{B}_b^k H_k \rho}{\sin(\alpha_B)\tan(\alpha_B)} \tag{D.91}$$

Finally it comes [1]

$$\frac{\sigma(p)}{p^2} \frac{0.3}{\sin(\alpha_B)^2} = \sqrt{\frac{\frac{1}{\not{\sigma}_x^2}\left[\sum_k \epsilon_k^x \sum_k \epsilon_k^x H_k^2 - (\sum_k \epsilon_k^x H_k)^2 \right] + \frac{1}{\not{\sigma}_\alpha^2} \sum_k \epsilon_k^x \sum_k \epsilon_k^\alpha}{\mathbb{D}}} \tag{D.92}$$

with

$$\mathbb{D} = \begin{vmatrix} \sum_k \epsilon_k^x & -\sum_k \epsilon_k^x H_k & -\sum_k \frac{\epsilon_k^x \not{B}_a^k H_k^2}{2} \\ -\sum_k \frac{\epsilon_k^x H_k}{\not{\sigma}_x^2} & \sum_k \frac{\epsilon_k^x H_k^2}{\not{\sigma}_x^2} + \frac{\epsilon_k^\alpha}{\not{\sigma}_\alpha^2} & \sum_k \frac{\epsilon_k^x \not{B}_a^k H_k^3}{2\not{\sigma}_x^2} + \frac{\epsilon_k^\alpha \not{B}_b^k H_k}{\not{\sigma}_\alpha^2} \\ -\sum_k \frac{\epsilon_k^x \not{B}_a^k H_k^2}{2\not{\sigma}_x^2} & \sum_k \frac{\epsilon_k^x \not{B}_a^k H_k^3}{2\not{\sigma}_x^2} + \frac{\epsilon_k^\alpha \not{B}_b^k H_k}{\not{\sigma}_\alpha^2} & \sum_k \frac{\epsilon_k^x \not{B}_a^{k2} H_k^4}{4\not{\sigma}_x^2} + \frac{\epsilon_k^\alpha \not{B}_b^{k2} H_k^2}{\not{\sigma}_\alpha^2} \end{vmatrix} \tag{D.93}$$

The equations (D.92) and (D.93) may be the most compact form of the general result. Specializing to the "only local position measurements" condition, i.e $\forall k, H_k \not{\sigma}_\alpha \gg \not{\sigma}_x$, does not improve the expression. However specializing to "only local angle measurements" conditions, i.e $\forall k, H_k \not{\sigma}_\alpha \ll \not{\sigma}_x$, gives:

$$\frac{\sigma(p)}{p^2} \frac{0.3}{\sin(\alpha_B)^2}_{\alpha\text{-Only}} = \not{\sigma}_\alpha \sqrt{\frac{\sum_k \epsilon_k^\alpha}{\sum_k \epsilon_k^\alpha \sum_k \epsilon_k^\alpha \not{B}_b^{k2} H_k^2 - (\sum_k \epsilon_k^\alpha \not{B}_b^k H_k)^2}} \tag{D.94}$$

This procedure does combine all the local position and angle measurements available and it can give the full covariance matrix of the track parameters measurements. However the result (D.92) leads to tedious algebraic computations even for the simple configurations of the methods that we examined. Still it shows that $\frac{\sigma(p)}{p^2}$ does not depend on p and is proportional to $\sin(\alpha_B)^2$, the proportionality factor being independent of the track parameters.

The approach can cope with a Magnetic Field continuously varying in y: one imagines an infinite number of fictitious "Measurement" lines, all "silenced" by setting their ϵ_k^x and ϵ_k^α at 0, but on a finite

---

[1] Since $\mathbb{D}$ is first order in $B_k B_{k'}$, the quantities $\mathbb{1}_{\not{a}}$ and $\mathbb{1}_{\not{b}}$ are effectively set to 1

set of true “Measurement” lines. Then one finds back (D.92) with

$$\not{B}_a^k \equiv \frac{2}{H_k^2}\int_0^{H_k} B(y)(H_k - y)dy \text{ and } \not{B}_b^k = \frac{1}{H_k}\int_0^{H_k} B(y)dy \tag{D.95}$$

Finally since nothing prevents the denominator of (D.92) to be null, there can be certain configuration that could lead to infinite momentum resolution, i.e to an impossible measurement of the momentum. The most obvious of these critical configurations is when all the $\not{B}_a^k$ and $\not{B}_b^k$ are null or extremely small. As indicated by (D.95) if the Magnetic Field is trivially small all along the trajectory, this is only possible if the Magnetic Field changes sign along the trajectory canceling or almost canceling its deflection effects on the trajectory.

D.5.3 Momentum Resolution with all measurements

In this section we use the results of the section D.5.2 to improve on the resolutions obtained in section D.3. It is very easy to code the result (D.92) to compute numerical estimates in any local measurements and Magnetic Fields configurations. This allows not only to check the results of section D.3, but also to evaluate how much they improve when one adds local measurements which were not used.

D.5.3.1 Three-Points Method vs Three-Angles-Three-Points Method

For instance in the Three-Points Method configuration, see section D.3.1, one can wonder what would be the improvement if local angle measurements are added to the three local position measurements used, i.e what is gained with a Three-Angles-Three-Points Method with respect to the Three-Points Method. For position resolution $\not{\sigma}_x \sim 40\mu m$, angular resolution $\not{\sigma}_\alpha \sim 300\mu rad$, and “Barrel“ values $B \sim 0.5T$ and $H_{13} \sim 5m$, one gets that $\frac{\sigma(p)}{p^2}\frac{1}{\sin(\alpha_B)^2}$ is $10.5\% Tev^{-1}$ without the local angle measurements and improves to only $10.3\% Tev^{-1}$ when one adds local angle measurements.

D.5.3.2 Angle-Point Method vs Three-Angles-Three-Points Method

Similarly for the Angle-Point Method configuration, see section D.3.2, one gets that for position resolution $\not{\sigma}_x \sim 40\mu m$, angular resolution $\not{\sigma}_\alpha \sim 300\mu rad$, and ”End Cap“ values $B \sim 1.T$ and $H_{13} \sim 11m$, $\frac{\sigma(p)}{p^2}\frac{1}{\sin(\alpha_B)^2}$ changes from $9.7\% Tev^{-1}$ without local angle measurements to $9.6\% Tev^{-1}$ with them. Again the improvement is marginal.

D.5.3.3 Angle-Angle Method vs Two-Angles-Two-Points Method

Turning now to the case of the Angle-Angle Method configuration, see section D.3.3, it appears that, if the angular resolutions on the measured local angles are identical, the addition of the two local position measurements to the two local angle measurements used has strictly no effect on the resolution.

This intriguing result can be understood considering the figure D.7. Are represented the two “Measurement” lines, the local positions and angles x_1, x_2, α_1 and α_2 being measured, the center of curvature C, the curvature radius R and the trajectory which is a segment of circle since the Magnetic Field is uniform. Since one has seen

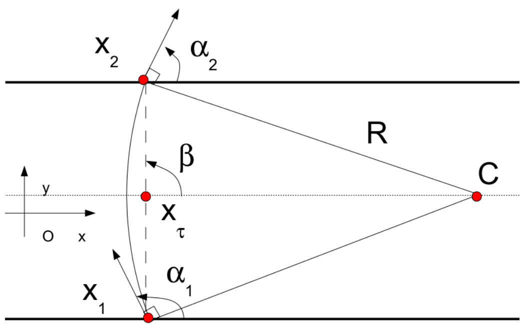

Figure D.7: Two-Angles-Two-Points Method. The track can be represented by the three parameters x_τ, β and $1/p$ rather than by the three parameters x_B, α_B and $1/p$.

that $\frac{\sigma(p)}{p^2}\frac{1}{\sin}(\alpha_B)^2$ is independent of the track parameters, one can work with the particular configuration where C is on the mid-line between the two "Measurement" lines, as represented in D.7.

One defines the position parameter $x_{\mathcal{T}}$ as the x coordinate of the middle of the two points where the trajectory crosses the "Measurement" lines and the angle β the angle between the line joining these two last points and the x axis. Instead of representing the trajectory by the parameters x_B, α_B and $1/p$, one uses the parameters $x_{\mathcal{T}}$, β and $1/p$. Then one examines the variations of the local quantities to be measured as function of the variations of the parameters of this new track representation. Variations of $x_{\mathcal{T}}$ induces correlated variations of x_1 and x_2. Variations of β induces anti-correlated variations of x_1 and x_2 and correlated variations of α_1 and α_2. Finally variations of $1/p$ induces anti-correlated α_1 and α_2. Therefore the track parameters and local quantities to be measured, separate in two groups: on one hand $x_{\mathcal{T}}$ and β in relation with the set $\{\Sigma_x = \frac{\delta(x_1+x_2)}{\sqrt{2}}, \Delta_x = \frac{\delta(x_1-x_2)}{\sqrt{2}}, \Sigma_\alpha = \frac{\delta(\alpha_1+\alpha_2)}{\sqrt{2}}\}$ and on the other hand $1/p$ in relation with $\Delta_\alpha = \frac{\delta(\alpha_1-\alpha_2)}{\sqrt{2}}$. If the angular resolutions on the measured local angles α_1 and α_2 are identical, then the variables Σ_α and Δ_α are non-correlated. This makes the above two groups statistically independent. In this case the resolution on $1/p$ depends exclusively on the resolution on Δ_α and is completely independent on position measurements

However if the angular resolutions of the two "Measurement" lines differ, the addition of local position measurements can help somewhat the momentum measurement. One can compute the performance of the method using two local angles and two local position measurements, the Two-Angles-Two-Points Method, in the scenarios considered in sections D.3.3 and D.3.3.1. This performance is compared to the performance of the Angle-Angle Method and Three-Points Method in the table D.3. Comparing with the performance of the Angle-Angle Method listed in the table D.1, one sees that the improvements are inexistent in the large sectors, owing to the equality of angular resolutions of the stations there, and that they are small in the small sectors and consistent with the indications of small improvements from the Angle-Two-Points Method listed in the table D.2.

Configuration	$\not\sigma_{\alpha^0,a}(\mu rad)$	$\not\sigma_{\alpha^0,b}(\mu rad)$	$H_{ab}(m)$	$R_{2\alpha 2P/\alpha\alpha}$	$R_{2\alpha 2P/3P}$
BIS-BMS	500	300	2.5	0.88	13
BMS-BOS	300	200	2.5	0.92	9
BIS-BOS	500	200	5	0.69	5
BIL-BML	200	200	2.5	1.00	7
BML-BOL	200	200	2.5	1.00	7
BIL-BOL	200	200	5	1.00	4

Table D.3: Ratio of momentum resolutions of Two-Angles-Two-Points and Three-Angles-Three-Points Methods for different scenarios

D.5.3.4 Conclusions on the effects of adding local measurements in the basic Methods

The three archetypal methods, Three-Points, Angle-Point and Angle-Angle Methods, give a fair account of the momentum measurement capabilities of the Muon Spectrometer. Taking into account that other local measurements exist than the ones they used, does not bring major changes [2].

For the Angle-Angle Method, one can even ignore the detailed angular resolutions, the main effect being due to lever arm variations. Using a "mean" angular resolution of $\sim 300\mu rad$, one gets a degradation with respect to the potential Three-Points resolution by a factor ~ 5 (cf equation (D.45)) if the two most distant stations are used and ~ 10 if the Medium station is paired with the innermost or outermost station, and this is a fair summary, even if a severe one, of the results of the table D.3.

---

[2] Even if one can say that the measurement is more of the Angle-Two-Points type for the BIS-BOS scenario, more of the Angle-Angle type for the BMS-BOS scenario while both methods contribute equally for the BIS-BMS scenario, the improvements with respect to pure Angle-Angle performances are not changing the global picture.

D.5.4 Measuring all the Track parameters

The result (D.80) allows to estimate not only momentum resolution but also resolutions on the Track position and angle measurement as well as all correlations between these measurements. In this section, we deal with the same idealized situations used the section D.5.2 but we do consider the measure of all the Track parameters. We also allow Multiple Scattering effect although only for the Three-Points and Angle-Point Methods. For these computations, the "Measurement" lines will be assumed to have identical local measurements resolutions.

D.5.4.1 Three-Points Method

Specializing to the "only local position measurements" conditions using the three "Measurement" lines configuration of the Three-Points Method, it comes that the matrix $W^{\vec{\tau}}_{3P}$ is:

$$W^{\vec{\tau}}_{3P} = \frac{1}{\not{\sigma}_x^2} \begin{pmatrix} 3\sin(\alpha_B)^2 & -H_{13}\left[\beta+1\right] & \frac{-0.3BH_{13}^2}{\sin(\alpha_B)}\frac{\beta^2+1}{2} \\ -H_{13}\left[\beta+1\right] & \frac{H_{13}^2}{\sin(\alpha_B)^2}\left[\beta^2+1\right] & \frac{0.3BH_{13}^3}{\sin(\alpha_B)^3}\frac{\beta^3+1}{2} \\ \frac{-0.3BH_{13}^2}{\sin(\alpha_B)}\frac{\beta^2+1}{2} & \frac{0.3BH_{13}^3}{\sin(\alpha_B)^3}\frac{\beta^3+1}{2} & \frac{0.3^2B^2H_{13}^4}{\sin(\alpha_B)^4}\frac{\beta^4+1}{4} \end{pmatrix} \tag{D.96}$$

where $\beta = H_{12}/H_{13}$. Inversing $W^{\vec{\tau}}_{3P}$ and assuming the choice $H_{12} = H_{23} = H_{13}/2$, one gets the momentum resolution (D.30), and the position and angle resolutions

$$\sigma(x_B)_{3P} = \frac{\not{\sigma}_x}{\sin(\alpha_B)} \tag{D.97}$$

$$\sigma(\alpha_B)_{3P} = \frac{\not{\sigma}_x \sin(\alpha_B)}{H_{13}}\sqrt{26} \tag{D.98}$$

as well as the Correlation matrix

$$\mathscr{C}_{3P} = \begin{pmatrix} 1 & \frac{-3}{\sqrt{26}} \sim -0.59 & \frac{-1}{\sqrt{6}} \sim -0.41 \\ \frac{-3}{\sqrt{26}} \sim -0.59 & 1 & \frac{6}{\sqrt{39}} \sim 0.96 \\ \frac{-1}{\sqrt{6}} \sim -0.41 & \frac{6}{\sqrt{39}} \sim 0.96 & 1 \end{pmatrix} \tag{D.99}$$

For position resolution $\not{\sigma}_x^0 \sim 40\mu m$ and "Barrel" value $H_{13} \sim 5m$, one gets

$$\sigma(x_B)_{3P} \sim \frac{40\mu m}{\sin(\alpha_B)^{1/2}} \tag{D.100}$$

$$\sigma(\alpha_B)_{3P} \sim 41\mu rad\ \sin(\alpha_B)^{3/2} \tag{D.101}$$

D.5.4.2 Angle-Point Method

If instead one uses the Magnetic Field and "Measurement" lines configurations of the Angle-Point Method, it comes that the $W^{\vec{\tau}}_{\alpha P}$ matrix is:

$$W^{\vec{\tau}}_{\alpha P} = \frac{1}{\not{\sigma}_x^2} \begin{pmatrix} 3\sin(\alpha_B)^2 & -H_{13}\left[\beta+1\right] & \frac{-0.3BH_{13}^2}{\sin(\alpha_B)}\frac{\beta^2+\beta(2-\beta)}{2} \\ -H_{13}\left[\beta+1\right] & \frac{H_{13}^2}{\sin(\alpha_B)^2}\left[\beta^2+1\right] & \frac{0.3BH_{13}^3}{\sin(\alpha_B)^3}\frac{\beta^3+\beta(2-\beta)}{2} \\ \frac{-0.3BH_{13}^2}{\sin(\alpha_B)}\frac{\beta^2+\beta(2-\beta)}{2} & \frac{0.3BH_{13}^3}{\sin(\alpha_B)^3}\frac{\beta^3+\beta(2-\beta)}{2} & \frac{0.3^2B^2H_{13}^4}{\sin(\alpha_B)^4}\frac{\beta^4+\beta^2(2-\beta)^2}{4} \end{pmatrix} \tag{D.102}$$

where β is defined as in section D.5.4.1 Inversion of $W^{\vec{\tau}}_{\alpha P}$, with the choice $H_{12} = H_{23} = H_{13}/2$, gives the momentum resolution (D.38), and the position and angle resolutions

$$\sigma(x_B)_{\alpha P} = \frac{\not{\sigma}_x}{\sin(\alpha_B)} \tag{D.103}$$

$$\sigma(\alpha_B)_{\alpha P} = \frac{\not{\sigma}_x \sin(\alpha_B)}{H_{13}} 2\sqrt{14} \tag{D.104}$$

The Correlation matrix is

$$\mathscr{C}_{\alpha P} = \begin{pmatrix} 1 & \frac{-2}{\sqrt{14}} \sim -0.53 & \frac{-1}{\sqrt{6}} \sim -0.41 \\ \frac{-2}{\sqrt{14}} \sim -0.53 & 1 & \frac{9}{2\sqrt{21}} \sim 0.98 \\ \frac{-1}{\sqrt{6}} \sim -0.41 & \frac{9}{2\sqrt{21}} \sim 0.98 & 1 \end{pmatrix} \tag{D.105}$$

For position resolution $\not{\sigma}^0_x \sim 40\mu m$ and "End Cap" value $H_{13} \sim 11m$, one gets

$$\sigma(x_B)_{\alpha P} \sim \frac{40\mu m}{\sin(\alpha_B)^{1/2}} \tag{D.106}$$

$$\sigma(\alpha_B)_{\alpha P} = 27\mu rad\ \sin(\alpha_B)^{3/2} \tag{D.107}$$

D.5.4.3 Angle-Angle Method

To apply (D.80) to the Angle-Angle Method, it is convenient to add the measurements of the local positions on the two "Measurement" lines. These measurements are needed to get a determination of all the track parameters together. Since we will assume that the angular resolutions of the two local angles measurements are identical, we already know that they are not changing the momentum resolution. It comes that the $W^{\vec{\tau}}_{\alpha\alpha}$ matrix is:

$$W^{\vec{\tau}}_{\alpha\alpha} = \begin{pmatrix} \frac{2}{\not{\sigma}^2_x} \sin(\alpha_B)^2 & -\frac{H_{ab}}{\not{\sigma}^2_x} & -\frac{0.3B}{2\sin(\alpha_B)} \frac{H^2_{ab}}{\not{\sigma}^2_x} \\ -\frac{H_{ab}}{\not{\sigma}^2_x} & \frac{1}{\sin(\alpha_B)^2} \left[\frac{H^2_{ab}}{\not{\sigma}^2_x} + \frac{2}{\not{\sigma}^2_\alpha}\right] & \frac{0.3B}{\sin(\alpha_B)^3} \left[\frac{H^3_{ab}}{2\not{\sigma}^2_x} + \frac{H_{ab}}{\not{\sigma}^2_\alpha}\right] \\ -\frac{0.3B}{2\sin(\alpha_B)} \frac{H^2_{ab}}{\not{\sigma}^2_x} & \frac{0.3B}{\sin(\alpha_B)^3} \left[\frac{H^3_{ab}}{2\not{\sigma}^2_x} + \frac{H_{ab}}{\not{\sigma}^2_\alpha}\right] & \frac{0.3^2 B^2}{\sin(\alpha_B)^4} \left[\frac{H^4_{ab}}{4\not{\sigma}^2_x} + \frac{H^2_{ab}}{\not{\sigma}^2_\alpha}\right] \end{pmatrix} \tag{D.108}$$

Inversion of $W^{\vec{\tau}}_{\alpha\alpha}$ gives the momentum resolution (D.43), and the position and angle resolutions

$$\sigma(x_B)_{\alpha\alpha} = \frac{\not{\sigma}_x}{\sin(\alpha_B)} \sqrt{\frac{1 + 2\epsilon^2_{x\alpha}}{1 + 4\epsilon^2_{x\alpha}}} \tag{D.109}$$

$$\sigma(\alpha_B)_{\alpha\alpha} = \frac{\not{\sigma}_\alpha \sin(\alpha_B)}{\sqrt{2}} \sqrt{\frac{1 + 8\epsilon^2_{x\alpha}}{1 + 4\epsilon^2_{x\alpha}}} \tag{D.110}$$

$$\text{with } \epsilon_{x\alpha} = \frac{\not{\sigma}_x}{H_{ab}\not{\sigma}_\alpha} \tag{D.111}$$

The Correlation matrix is

$$\mathscr{C}_{\alpha\alpha} = \begin{pmatrix} 1 & \frac{\epsilon_{x\alpha}\sqrt{2}}{\sqrt{(1+8\epsilon^2_{x\alpha})(1+2\epsilon^2_{x\alpha})}} & 0 \\ \frac{\epsilon_{x\alpha}\sqrt{2}}{\sqrt{(1+8\epsilon^2_{x\alpha})(1+2\epsilon^2_{x\alpha})}} & 1 & \sqrt{\frac{1+4\epsilon^2_{x\alpha}}{1+8\epsilon^2_{x\alpha}}} \\ 0 & \sqrt{\frac{1+4\epsilon^2_{x\alpha}}{1+8\epsilon^2_{x\alpha}}} & 1 \end{pmatrix} \tag{D.112}$$

For position resolution $\not\sigma_x^0 \sim 40\mu m$, angular $\not\sigma_\alpha^0 \sim 300\mu rad$ and "Barrel" value $H_{ab} \sim 5m$, i.e $\epsilon_{x\alpha} \sim 0.027$, one gets

$$\sigma(x_B)_{\alpha\alpha} \sim \frac{40\mu m}{\sin(\alpha_B)^{1/2}} \tag{D.113}$$

$$\sigma(\alpha_B)_{\alpha\alpha} \sim 210\mu rad\ \sin(\alpha_B)^{3/2} \tag{D.114}$$

and

$$\mathscr{C}_{\alpha\alpha} = \begin{pmatrix} 1 & \sim 0.0376 & 0 \\ \sim 0.0376 & 1 & \sim 0.999 \\ 0 & \sim 0.999 & 1 \end{pmatrix} \tag{D.115}$$

D.5.4.4 Three-Points Method with Multiple Scattering

We address again the Three-Points Method configuration allowing this times a Multiple Scattering angle, α^{Sc}, on the medium station. We proceed as explained in section D.5.1 adding α^{Sc} to the representation of the track and constraining it in the χ^2 function. One ends up with the 4×4 W matrix $W^{\vec{\tau},4}_{3P+Sc}$

$$W^{\vec{\tau},4}_{3P+Sc} = \frac{1}{\not\sigma_x^2} \begin{pmatrix} 3\sin(\alpha_B)^2 & -H_{13}\big[\beta+1\big] & \frac{-0.3BH_{13}^2}{\sin(\alpha_B)}\frac{\beta^2+1}{2} & -H_{13}[1-\beta] \\ -H_{13}\big[\beta+1\big] & \frac{H_{13}^2}{\sin(\alpha_B)^2}\big[\beta^2+1\big] & \frac{0.3BH_{13}^3}{\sin(\alpha_B)^3}\frac{\beta^3+1}{2} & \frac{H_{13}^2}{\sin(\alpha_B)^2}[1-\beta] \\ \frac{-0.3BH_{13}^2}{\sin(\alpha_B)}\frac{\beta^2+1}{2} & \frac{0.3BH_{13}^3}{\sin(\alpha_B)^3}\frac{\beta^3+1}{2} & \frac{0.3^2B^2H_{13}^4}{\sin(\alpha_B)^4}\frac{\beta^4+1}{4} & \frac{0.3BH_{13}^3}{\sin(\alpha_B)^3}\frac{1-\beta}{2} \\ -H_{13}[1-\beta] & \frac{H_{13}^2}{\sin(\alpha_B)^2}[1-\beta] & \frac{0.3BH_{13}^3}{\sin(\alpha_B)^3}\frac{1-\beta}{2} & \frac{H_{13}^2[1-\beta]^2}{\sin(\alpha_B)^2}\frac{1}{\kappa} \end{pmatrix} \tag{D.116}$$

where β is defined as in section D.5.4.1 and $\frac{1}{\kappa} \equiv 1 + \frac{1}{\Gamma}$ with

$$\Gamma \equiv \left(\frac{H_{13}\sigma(\alpha^{Sc})}{\not\sigma_x \sin(\alpha_B)}[1-\beta]\right)^2 \tag{D.117}$$

Inversing $W^{\vec{\tau},4}_{3P+Sc}$ and removing the row and column involving α^{Sc}, one gets the 3×3 covariance matrix, $C^{\vec{\tau},3}_{3P+Sc}$, for the (x_B, α_B, ρ) parameters. There exist simple formulas for this dimensional reduction that allow to get the inverse of $C^{\vec{\tau},3}_{3P+Sc}$, the matrix $W^{\vec{\tau},3}_{3P+Sc}$, directly from $W^{\vec{\tau},4}_{3P+Sc}$. Using them, one gets

$$W^{\vec{\tau},3}_{3P+Sc} = \frac{1}{\not\sigma_x^2} \begin{pmatrix} (2+\gamma)\sin(\alpha_B)^2 & -H_{13}\big[\beta+\gamma\big] & \frac{-0.3BH_{13}^2}{\sin(\alpha_B)}\frac{\beta^2+\gamma}{2} \\ -H_{13}\big[\beta+\gamma\big] & \frac{H_{13}^2}{\sin(\alpha_B)^2}\big[\beta^2+\gamma\big] & \frac{0.3BH_{13}^3}{\sin(\alpha_B)^3}\frac{\beta^3+\gamma}{2} \\ \frac{-0.3BH_{13}^2}{\sin(\alpha_B)}\frac{\beta^2+\gamma}{2} & \frac{0.3BH_{13}^3}{\sin(\alpha_B)^3}\frac{\beta^3+\gamma}{2} & \frac{0.3^2B^2H_{13}^4}{\sin(\alpha_B)^4}\frac{\beta^4+\gamma}{4} \end{pmatrix} \tag{D.118}$$

where $\frac{1}{\gamma} \equiv 1 + \Gamma$. Inversing $W^{\vec{\tau},3}_{3P+Sc}$ and assuming the choice $H_{12} = H_{23} = H_{13}/2$, one finds

$$\sigma(x_B)_{3P+Sc} = \sigma(x_B)_{3P} \tag{D.119}$$

$$\sigma(\alpha_B)_{3P+Sc} = \sqrt{\big(\sigma(\alpha_B)_{3P}\big)^2 + \big(\sigma(\alpha_B)^{Sc}_{3P}\big)^2} \tag{D.120}$$

where $\sigma(\alpha_B)_{3P}$ is given by (D.98) and the Multiple Scattering contribution, $\sigma(\alpha_B)^{Sc}_{3P}$, is given by

$$\sigma(\alpha_B)^{Sc}_{3P} = \sigma(\alpha^{Sc})(1-\beta) \tag{D.121}$$

One gets also

$$\sigma(\rho)_{3P+Sc} = \sqrt{\left(\frac{1}{p}\frac{\sigma(p)}{p}_{3P}\right)^2 + \left(\frac{1}{p}\frac{\sigma(p)}{p}^{Sc}_{3P}\right)^2} \tag{D.122}$$

with $\frac{\sigma(p)}{p}_{3P}$ given by (D.30) and $\frac{\sigma(p)}{p}^{Sc}_{3P}$ given by (D.61), and the Correlation matrix

$$\mathscr{C}_{3P+Sc} = \begin{pmatrix} 1 & \frac{-3}{\sqrt{26}}\frac{1}{\sqrt{1+\frac{\Gamma}{26}}} & \frac{-1}{\sqrt{6}}\frac{1}{\sqrt{1+\frac{\Gamma}{6}}} \\ \frac{-3}{\sqrt{26}}\frac{1}{\sqrt{1+\frac{\Gamma}{26}}} & 1 & \frac{6}{\sqrt{39}}\frac{1+\frac{\Gamma}{12}}{\sqrt{1+\frac{\Gamma}{26}}\sqrt{1+\frac{\Gamma}{6}}} \\ \frac{-1}{\sqrt{6}}\frac{1}{\sqrt{1+\frac{\Gamma}{6}}} & \frac{6}{\sqrt{39}}\frac{1+\frac{\Gamma}{12}}{\sqrt{1+\frac{\Gamma}{26}}\sqrt{1+\frac{\Gamma}{6}}} & 1 \end{pmatrix} \tag{D.123}$$

One notes that the Multiple Scattering effect renders the correlation matrix momentum dependent.

For position resolution $\not\sigma^0_x \sim 40\mu m$, "Barrel" value $H_{13} \sim 5m$, $\sigma(\alpha^{Sc})$ given by (D.62) for an amount of matter equivalent to $\sim 0.3X_0$ put on the Medium "Measurement" line and assuming a Barrel configuration of the "Measurement" lines, i.e $\alpha_B = \theta$, one gets for p_T in GeV

$$\sigma(\alpha_B)_{3P+Sc} \sim \sqrt{\left(41\mu rad\ \sin(\theta)^{3/2}\right)^2 + \left(\frac{4\mu rad.\ \text{TeV}}{p_T}\sqrt{\sin(\theta)}\right)^2} \tag{D.124}$$

$$\frac{\sigma(p)}{p}_{3P+Sc} \sim \sqrt{\left(10\%.\ \text{TeV}^{-1}\, p_T \sin(\theta)^{3/2}\right)^2 + \left(2\%\ \sqrt{\sin(\theta)}\right)^2} \tag{D.125}$$

D.5.4.5 Angle-Point Method with Multiple Scattering

We address the Angle-Point Method configuration allowing a Multiple Scattering angle, α^{Sc}, on the medium station. We repeat the procedure of the previous section and get the 4×4 matrix $W^{\vec{\tau},4}_{\alpha P+Sc}$

$$W^{\vec{\tau},4}_{\alpha P+Sc} = \frac{1}{\not\sigma^2_x}\begin{pmatrix} 3\sin(\alpha_B)^2 & -H_{13}\left[\beta+1\right] & \frac{-0.3BH_{13}^2}{\sin(\alpha_B)}\frac{\beta^2+\beta(2-\beta)}{2} & -H_{13}[1-\beta] \\ -H_{13}\left[\beta+1\right] & \frac{H_{13}^2}{\sin(\alpha_B)^2}\left[\beta^2+1\right] & \frac{0.3BH_{13}^3}{\sin(\alpha_B)^3}\frac{\beta^3+\beta(2-\beta)}{2} & \frac{H_{13}^2}{\sin(\alpha_B)^2}[1-\beta] \\ \frac{-0.3BH_{13}^2}{\sin(\alpha_B)}\frac{\beta^2+\beta(2-\beta)}{2} & \frac{0.3BH_{13}^3}{\sin(\alpha_B)^3}\frac{\beta^3+\beta(2-\beta)}{2} & \frac{0.3^2B^2H_{13}^4}{\sin(\alpha_B)^4}\frac{\beta^4+\beta^2(2-\beta)^2}{4} & \frac{0.3BH_{13}^3}{\sin(\alpha_B)^3}\frac{\beta(2-\beta)(1-\beta)}{2} \\ -H_{13}[1-\beta] & \frac{H_{13}^2}{\sin(\alpha_B)^2}[1-\beta] & \frac{0.3BH_{13}^3}{\sin(\alpha_B)^3}\frac{\beta(2-\beta)(1-\beta)}{2} & \frac{H_{13}^2(1-\beta)^2}{\sin(\alpha_B)^2}\frac{1}{\kappa} \end{pmatrix} \tag{D.126}$$

where β is defined as in section D.5.4.1 and κ as in section D.5.4.4, and

$$W^{\vec{\tau},3}_{\alpha P+Sc} = \frac{1}{\not\sigma^2_x}\begin{pmatrix} (2+\gamma)\sin(\alpha_B)^2 & -H_{13}\left[\beta+\gamma\right] & \frac{-0.3BH_{13}^2}{\sin(\alpha_B)}\frac{\beta^2+\beta(2-\beta)\gamma}{2} \\ -H_{13}\left[\beta+\gamma\right] & \frac{H_{13}^2}{\sin(\alpha_B)^2}\left[\beta^2+\gamma\right] & \frac{0.3BH_{13}^3}{\sin(\alpha_B)^3}\frac{\beta^3+\beta(2-\beta)\gamma}{2} \\ \frac{-0.3BH_{13}^2}{\sin(\alpha_B)}\frac{\beta^2+\beta(2-\beta)\gamma}{2} & \frac{0.3BH_{13}^3}{\sin(\alpha_B)^3}\frac{\beta^3+\beta(2-\beta)\gamma}{2} & \frac{0.3^2B^2H_{13}^4}{\sin(\alpha_B)^4}\frac{\beta^4+\beta^2(2-\beta)^2\gamma}{4} \end{pmatrix} \tag{D.127}$$

where γ is defined as in section D.5.4.4. Inversing $W^{\vec{\tau},3}_{\alpha P+Sc}$ and assuming the choice $H_{12} = H_{23} = H_{13}/2$, one finds

$$\sigma(x_B)_{\alpha P+Sc} = \sigma(x_B)_{\alpha P} \tag{D.128}$$

$$\sigma(\alpha_B)_{\alpha P+Sc} = \sqrt{\left(\sigma(\alpha_B)_{\alpha P}\right)^2 + \left(\sigma(\alpha_B)^{Sc}_{\alpha P}\right)^2} \tag{D.129}$$

where $\sigma(\alpha_B)_{\alpha P}$ is given by (D.104) and the Multiple Scattering contribution, $\sigma(\alpha_B)^{Sc}_{\alpha P}$, is given by

$$\sigma(\alpha_B)^{Sc}_{\alpha P} = \sigma(\alpha^{Sc}) \tag{D.130}$$

One gets also

$$\sigma(\rho)_{\alpha P+Sc} = \sqrt{\left(\frac{1}{p}\frac{\sigma(p)}{p}_{\alpha P}\right)^2 + \left(\frac{1}{p}\frac{\sigma(p)}{p}^{Sc}_{\alpha P}\right)^2} \tag{D.131}$$

with $\frac{\sigma(p)}{p}_{\alpha P}$ given by (D.38) and $\frac{\sigma(p)}{p}^{Sc}_{\alpha P}$ given by (D.66), and the Correlation matrix

$$\mathscr{C}_{\alpha P+Sc} = \begin{pmatrix} 1 & \frac{-2}{\sqrt{14}}\frac{1}{\sqrt{1+\frac{\Gamma}{14}}} & \frac{-1}{\sqrt{6}}\frac{1}{\sqrt{1+\frac{\Gamma}{6}}} \\ \frac{-2}{\sqrt{14}}\frac{1}{\sqrt{1+\frac{\Gamma}{14}}} & 1 & \frac{9}{2\sqrt{21}}\frac{1+\frac{\Gamma}{9}}{\sqrt{1+\frac{\Gamma}{14}}\sqrt{1+\frac{\Gamma}{6}}} \\ \frac{-1}{\sqrt{6}}\frac{1}{\sqrt{1+\frac{\Gamma}{6}}} & \frac{9}{2\sqrt{21}}\frac{1+\frac{\Gamma}{9}}{\sqrt{1+\frac{\Gamma}{14}}\sqrt{1+\frac{\Gamma}{6}}} & 1 \end{pmatrix} \tag{D.132}$$

One notes again that the Multiple Scattering effect renders the correlation matrix momentum dependent.

For position resolution $\not{\sigma}_x^0 \sim 40\mu m$, "End cap" value $H_{13} \sim 11m$, $\sigma(\alpha^{Sc})$ given by (D.62) for an amount of matter equivalent to $\sim 0.3X_0$ put on the Medium "Measurement" line and assuming End cap configuration for the "Measurement" line, i.e $\alpha_B = \theta + \pi/2$, one gets for p_T in GeV

$$\sigma(\alpha_B)_{\alpha P+Sc} \sim \sqrt{\left(27\mu rad\ \cos(\theta)^{3/2}\right)^2 + \left(\frac{2\mu rad.\ \text{TeV}}{p_T}\sqrt{\cos(\theta)}\frac{\tan(\theta)}{\tan(\theta_0)}\right)^2} \tag{D.133}$$

$$\frac{\sigma(p)}{p}_{\alpha P+Sc} \sim \sqrt{\left(10\%.\ \text{TeV}^{-1}\ p_T \cos(\theta)^{3/2}\frac{\tan(\theta_0)}{\tan(\theta)}\right)^2 + \left(0.9\%\ \sqrt{\cos(\theta)}\right)^2} \tag{D.134}$$

where, as done in section D.3.2, $\theta_0 = 12.6^o$ has been introduced to allow fair comparison between Barrel and End cap resolutions.

D.5.4.6 Comment on angle-momentum correlation

One notes in (D.99), (D.105) and (D.115), that there is an important correlation between the momentum and angle measurements. One notes also from (D.123) and (D.132), that the Multiple Scattering decreases all correlations between track parameters measurements but the correlation between momentum and angle.

This indicates that there is a potential gain on the momentum resolution that could be obtained in combining this track measurement with a measurement of a point on the trajectory far away from the Muon Spectrometer, i.e in the Inner Detector, since improvement of the trajectory angle resolution alone would lead to a momentum resolution improvement. However this mechanism compete with the angle blurring induced by the Multiple scattering effects when crossing the calorimeters.